

Time-Resolved Scanning Ion Conductance Microscopy and Single-Molecule Spectroscopy

Présentée le 14 septembre 2023

Faculté des sciences et techniques de l'ingénieur
Laboratoire de bio- et nano-instrumentation
Programme doctoral en biotechnologie et génie biologique

pour l'obtention du grade de Docteur ès Sciences

par

Samuel MENDES LEITÃO

Acceptée sur proposition du jury

Prof. M. Dal Peraro, président du jury
Prof. G. Fantner, directeur de thèse
Prof. L. Baker, rapporteur
Prof. P. Actis, rapporteur
Prof. T. Zambelli, rapporteur

The gull sees farthest who flies highest.
— Richard Bach

Acknowledgments

Ambitious science projects demand expertise from different scientific fields that can be met with great success when people from various cultural and scientific backgrounds work together. During my doctoral thesis work, I most appreciated working in a creative and engaging environment with people who promoted open communication where ideas were generated and shaped together into the scientific output described in the thesis. This rich environment profoundly impacted my Ph.D. journey at EPFL, where I met people who motivated me and shaped my path as a scientist and human being who values the diversity in people and science.

First, I extend profound gratitude to Prof. Georg Fantner, my doctoral thesis supervisor, whose mentorship has molded my scientific trajectory. My adventure in science started when I met Georg as a master's student from Portugal during an exchange program in Switzerland. His dedicated guidance extended beyond supervision, as he journeyed to Lisbon to contribute to my master's defense - a gesture reflecting his exceptional commitment. His support and role model qualities have established the principles of mentorship that I will uphold throughout my future career. As a Ph.D. supervisor, he inspired me to pursue challenging projects of an interdisciplinary nature and work with scientists and engineers from diverse backgrounds, fundamental for the scientific output of my thesis. His guidance, creative insights driven by a passion for designing and building instruments, and remarkable analytical insights were pivotal in my growth as a Ph.D. student and scientist.

I am also deeply thankful to my esteemed collaborators, Prof. Aleksandra Radenovic and her former Ph.D. student Vytautas Navikas, who have provided me with an enriching research experience. Aleksandra is an exceptional supportive and nurturing mentor, always providing guidance and vision that have greatly shaped my research endeavors. Her curiosity and excitement for science are contagious and an example of a scientist I aspire to be. Vytautas, an extraordinary scientist (and artist), was a constant companion on my Ph.D. journey. Our shared curiosity, learning, and accomplishments have created the most cherished and enjoyable memories of my doctoral pursuit.

I express my gratitude to the members of my thesis committee, Prof. Tomaso Zambelli, Prof. Lane Baker, Prof. Paolo Actis, and Prof. Matteo Dal Peraro, for evaluating my thesis and providing constructive suggestions, motivating me to pursue an academic path as the next step of my career.

I would also like to express my gratitude to all members of our laboratory - LBNI - who have been a continuous source of inspiration and support throughout my Ph.D. journey. I extend my heartfelt appreciation to Barney Drake for all his support in building instruments

from concept to prototype. His dedicated work and cheerful personality were always a constant motivation for me. I am equally thankful to Adrian Nievergelt, who provided invaluable guidance when I first joined the lab. I am grateful for his great mentorship and teachings in developing scanning probe microscopy instrumentation. A very special thank you goes to Santiago Andany, with whom I shared the highs and lows of our research journey since our days as master's students. Gratitude also extends to all my fellow lab members, whose collaborative spirit and contributions have enriched multiple projects and fostered cherished friendships. My appreciation goes to Mustafa Kangul, Navid Asmari, Matthias Neuenschwander, Marcos Penedo, Asal Ayar, Veronika Cencen, Esther R ath, M elanie Hannebelle, Charl une Brillard, Soma Biswas, Gustavo Rocha, Luis Fernando Hill, Augoustina Economou, Nahid Hosseini, Prabhu Swain, Bahareh Ghadiani, Amanda Kl ager, Federica Teodoro, Yiwei Zheng, Ingrid Margot, Anouk Hein, and Lena Ong. Your collective support has genuinely enriched my academic journey.

I would also like to thank the dedicated collaborators from Radenovic's lab. Thank you to Sanjin Marion and Sebastien Davies for introducing me to the captivating nanopore research field. My appreciation also extends to Helena Milkovich, Kristin S Grussmayer, Simon Meyer, Nathan Ronceray, and Kalid Ibrahim, who have contributed to our joint projects.

Additionally, I wish to thank the numerous collaborators within EPFL and beyond whose invaluable contributions to our shared research endeavors. I want to thank Katarina Pinjusic, Xavier Pierrat, Denis Djekic, Jens Anders, Alexander Persat, Daniel Constam, Pistoletti Blanchet, Kaikai Chen, Alexandre Kuhn, and Ulrich Keyser, for the opportunity to engage in interdisciplinary projects together.

Finally, I am grateful to my parents Rosa and Joao, and my siblings Tiago and Marta Leitao, for their constant support and nurturing creativity within my personal and professional life. Lastly, to my beloved Kate who brings endless joy to my life, and accompanies me on every step of my journey. I am looking forward to embarking on our next adventure together.

Samuel Mendes Leitao

Lausanne, August 6 2023

Abstract

The evolution of the 3D morphology is at the center of many relevant biological processes ranging from cellular differentiation to cancer invasion and metastasis. Microscopy techniques, such as electron microscopy (EM), super-resolution (SR) optical microscopy, and atomic force microscopy (AFM), have been applied to image the structure of cells in great detail. The major challenge is to obtain 3D information at nanometer resolution without affecting the viability of the cells and avoiding interference with the process.

The thesis presents the development of a time-resolved scanning ion conductance microscope (SICM), from concept to prototype, capable of resolving spatiotemporal biological processes with unprecedented resolution and imaging speed. By integrating advances in nanopositioning, controls theory, microelectronics, and nanopore fabrication, the time-resolved SICM system enabled sub-5 nm resolution, performed high-speed imaging of 0.5 s per pixel, and allowed large imaging volumes. Moreover, the stability of the system enabled performing live cell imaging over 48 h without perturbations. We applied time-resolved SICM to dynamic processes on cell membranes that included: Structural evolution of circular dorsal ruffles (CDRs), shedding light on their mechanisms of formation; Morphological changes in human melanoma cells upon treatment with a drug known to reduce resistance to immunotherapy; And mechanisms of bacteria-host infection in the human cell membrane.

Furthermore, we combined time-resolved SICM with super-resolution fluorescence optical fluctuation microscopy (SOFI). By optimizing the SOFI computational approach and fluorophore's properties, high-speed correlative 3D imaging with mitigated phototoxic effects was achieved. The complementary capabilities of time-resolved SICM and SOFI provided comprehensive information on cell membrane morphology and cytoskeleton protein architecture, offering sub-diffraction resolution in living cells. This combined method holds promise as a routine tool for studying membrane processes.

In addition to imaging, time-resolved SICM was successfully adapted for single-molecule spectroscopy using nanopores, creating a new technique called scanning ion conductance spectroscopy (SICS). SICS overcame limitations in nanopore technology by controlling the nanopores' position and the translocation speed of individual molecules. The ability to control the speed and average multiple readings of the same molecule has resulted in two orders of magnitude increase in signal-to-noise ratio compared to conventional free translocation. In our glass nanopore experiments, we detected a 3.4 angstroms single nucleotide missing in a long strand of dsDNA. Moreover, we utilized SICS to successfully identify and analyze intricate topological features within complex DNA structures, including DNA-dCas9 complexes, hairpins, molecular rulers, and dsDNA gaps. The increased detection capability with SICS has the potential to be transferable to other solid-

state and biological nanopore methods, significantly improving diagnostic and sequencing applications.

Keywords: Scanning ion conductance microscopy, super-resolution optical microscopy, live-cell imaging, Biomembrane dynamics, Melanoma cells, Bacterial Infection, nanopores, single-molecule detection, DNA systems.

Résumé

L'évolution de la morphologie en 3D est au centre de nombreux processus biologiques importants, allant de la différenciation cellulaire à l'invasion et à la métastase du cancer. Des techniques de microscopie, telles que la microscopie électronique (EM), la microscopie optique à super-résolution (SR) et la microscopie à force atomique (AFM), ont été utilisées pour imager en détail la structure des cellules. Le défi majeur consiste à obtenir des informations en 3D avec une résolution nanométrique sans affecter la viabilité des cellules et en évitant toute interférence avec le processus.

La thèse présente le développement d'un microscope à conductance ionique à balayage (SICM) résolu dans le temps, de la conception au prototype, capable de résoudre des processus biologiques spatiotemporels avec une résolution et une vitesse d'imagerie sans précédent. En intégrant les avancées en nanopositionnement, en théorie du contrôle, en microélectronique et en fabrication de nanopores, le système SICM résolu dans le temps a permis d'obtenir une résolution inférieure à 5 nm, de réaliser une imagerie à haute vitesse de 0.5 s par pixel et de permettre de grands volumes d'imagerie. De plus, la stabilité du système a permis de réaliser une imagerie en direct de cellules pendant 48 heures sans perturbations. Nous avons appliqué le SICM résolu dans le temps à des processus dynamiques sur les membranes cellulaires, notamment: l'évolution structurale des plis dorsaux circulaires (CDR), éclairant leurs mécanismes de formation; les changements morphologiques dans les cellules de mélanome humain lors du traitement par un médicament connu pour réduire la résistance à l'immunothérapie; et les mécanismes d'infection bactérienne-hôte dans la membrane cellulaire humaine.

De plus, nous avons combiné le SICM résolu dans le temps avec la microscopie de fluctuation optique de fluorescence à super-résolution (SOFI). En optimisant l'approche computationnelle de la SOFI et les propriétés des fluorophores, nous avons pu obtenir une imagerie 3D corrélacionnelle à haute vitesse avec des effets phototoxiques atténués. Les capacités complémentaires du SICM résolu dans le temps et de la SOFI ont fourni des informations complètes sur la morphologie de la membrane cellulaire et l'architecture des protéines du cytosquelette, offrant une résolution en dessous de la limite de diffraction optique sur les cellules vivantes. Cette méthode combinée présente des perspectives prometteuses en tant qu'outil courant pour l'étude des processus membranaires.

En plus de l'imagerie, le SICM résolu dans le temps a été adapté avec succès pour la spectroscopie de molécule unique en utilisant des nanopores, créant ainsi une nouvelle technique appelée spectroscopie de conductance ionique à balayage (SICS). Le SICS a surmonté les limitations de la technologie des nanopores en contrôlant la position des nanopores et la vitesse de translocation des molécules individuelles. La capacité de contrôler la vitesse et de réaliser des lectures multiples de la même molécule a entraîné une augmentation de deux ordres de grandeur du rapport signal sur bruit par rapport à la translocation libre conventionnelle. Dans nos expériences avec des nanopores en verre,

nous avons détecté l'absence d'un seul nucléotide d'une longue chaîne d'ADN double brin, avec une précision de 3,4 angströms. De plus, nous avons utilisé le SICS pour identifier avec succès et analyser des caractéristiques topologiques complexes au sein de structures d'ADN, telles que les complexes d'ADN-dCas9, les épingle à cheveux, les règles moléculaires et les lacunes d'ADN double brin. L'augmentation de la capacité de détection avec le SICS a le potentiel d'être transférable à d'autres méthodes de nanopores à l'état solide et biologiques, améliorant ainsi considérablement les applications de diagnostic et de séquençage.

Mots-clés: Microscopie à conductance ionique balayante, microscopie optique de super-résolution, imagerie en direct des cellules, dynamique des biomembranes, cellules de mélanome, infection bactérienne, nanopores, détection de molécules uniques, systèmes d'ADN.

Contents

1. Introduction	1
1.1. Spatiotemporal scales in live cell imaging.....	1
1.2. Scanning probe microscopy (SPM).....	3
1.3. SPM instrumentation	5
1.4. Live cell imaging with AFM	7
1.5. Scanning ion conductance microscopy (SICM).....	9
1.5.1. SICM principle.....	9
1.5.2. SICM resolution	10
1.5.3. SICM scanning modes.....	11
1.5.4. Live cell imaging and applications with SICM.....	13
1.6. Thesis structure	15
2. Advances in High-Speed SICM.....	17
2.1. Introduction to advances in high-speed SICM	17
2.2. Thesis approach to high-speed SICM to study spatiotemporally processes in live cells	19
3. Time-Resolved Scanning Ion Conductance Microscopy for Three-Dimensional Tracking of Nanoscale Cell Surface Dynamics.....	23
3.1. Abstract	24
3.2. Introduction.....	24
3.3. Results	25
3.3.1. Time-resolved SICM setup.....	25
3.3.2. Live cell imaging with time-resolved SICM.....	27
3.3.3. Tracking dynamic processes on cell membranes	29
3.3.4. High-speed imaging with time-resolved SICM	29
3.3.5. Study of morphological changes in cancer cells.....	31
3.3.6. Study of host-pathogen infection mechanisms in human cell.....	32
3.4. Discussion	34
3.5. Methods	35
3.5.1. Cell lines and cell culture.....	35
3.5.2. Time-resolved SICM instrumentation	35

3.5.3.	Time-resolved SICM measurements	36
3.5.4.	Data processing and analysis	37
3.6.	Supporting information.....	38
4.	Combined Fluorescence Microscopy with SICM.....	60
4.1.	Introduction to combined fluorescence microscopy with SICM.....	60
4.2.	Thesis approach to combined SICM with SR fluorescence microscopy.....	61
5.	Correlative 3D Microscopy of Single Cells using Super-Resolution and Scanning Ion-Conductance Microscopy	63
5.1.	Abstract	64
5.2.	Introduction	64
5.3.	Results	65
5.3.1.	Combined SICM/SOFI system.....	65
5.3.2.	Optimizing 2D resolution of fluorescence imaging with SOFI.....	67
5.3.3.	Optimizing 3D resolution of fluorescence imaging with SOFI.....	69
5.3.4.	Correlative SICM and 3D SOFI imaging of cytoskeletal cell structures	70
5.3.5.	Live cell imaging with combined SICM/SOFI	72
5.4.	Discussion.....	73
5.5.	Methods	75
5.5.1.	2D widefield fluorescence imaging setup	75
5.5.2.	Multiplane SOFI setup.....	75
5.5.3.	Scanning ion-conductance microscopy setup.....	76
5.5.4.	Combined 2D widefield fluorescence /SICM setup	76
5.5.5.	Coverslip fabrication	76
5.5.6.	Cell culture	77
5.5.7.	Sample fixation and staining	77
5.5.8.	Two-color sample staining	77
5.5.9.	Imaging buffers	78
5.5.10.	Two-color SOFI imaging	78
5.5.11.	SICM imaging and processing	79
5.5.12.	SOFI Image analysis and image alignment	79
5.5.13.	Live-cell SOFI/SICM imaging.....	79

5.5.14.	Correlative 3D SICM/SOFI data rendering.....	80
5.6.	Supporting information	81
6.	Molecular Sensing with Nanopores	99
6.1.	Introduction molecular sensing with nanopores	99
6.2.	Thesis approach to molecular sensing with nanopores	100
7.	Spatially Multiplexed Single-Molecule Translocations through a Nanopore at Controlled Speeds.....	102
7.1.	Abstract	103
7.2.	Introduction.....	103
7.3.	Results	104
7.3.1.	Single-molecule translocations controlled by nanopositioner.....	104
7.3.2.	Controlled translocations of molecular rulers.....	106
7.3.3.	Spatial addressability and spatial multiplexing of single molecules	108
7.3.4.	Single base gap detection in dsDNA.....	110
7.4.	Discussion	111
7.5.	Methods	113
7.5.1.	SICS system and controlled translocation measurements	113
7.5.2.	Data processing and analysis.....	113
7.5.3.	Fabrication and characterization of nanocapillaries	114
7.5.4.	Nanocapillary filling procedure	114
7.5.5.	Lambda DNA preparation.....	115
7.5.6.	gRNA preparation and immobilization	115
7.5.7.	dCas9-DNA complex formation	115
7.5.8.	DNA ruler construct.....	116
7.5.9.	DNA gap construct.....	116
7.5.10.	Oligonucleotide-DNA gap template construct	116
7.5.11.	Imaging chambers for DNA immobilization	117
7.5.12.	Surface immobilization.....	117
7.5.13.	Single-molecule fluorescence imaging.....	117
7.6.	Supporting information	118

8. Conclusion and Future Developments	130
8.1. Time-resolved SICM instrumentation for high-speed imaging	130
8.2. Time-resolved SICM for studying live cell biology at the nanoscale.....	131
8.3. Combined super-resolution optical imaging with time-resolved SICM	131
8.4. Single-molecule spectroscopy with time-resolved SICM	132
8.5. Future developments.....	132
9. Scientific Contributions.....	134
Bibliography	137
Curriculum Vitae	156

Chapter 1

Introduction

1.1. Spatiotemporal scales in live cell imaging

Life involves intricate processes, from protein interactions to cell systems that lead to the formation of tissues and organs (Figure 1.1). Live-cell imaging is vital to understand the molecular mechanisms that govern those complex cellular processes, such as cell communication, cell motility, differentiation, and membrane trafficking¹⁻⁴. Most of our knowledge in cell biology derives from utilizing microscopy technologies, yet the methods currently available to biologists present many technical challenges to observing those processes at the nanoscale⁵.

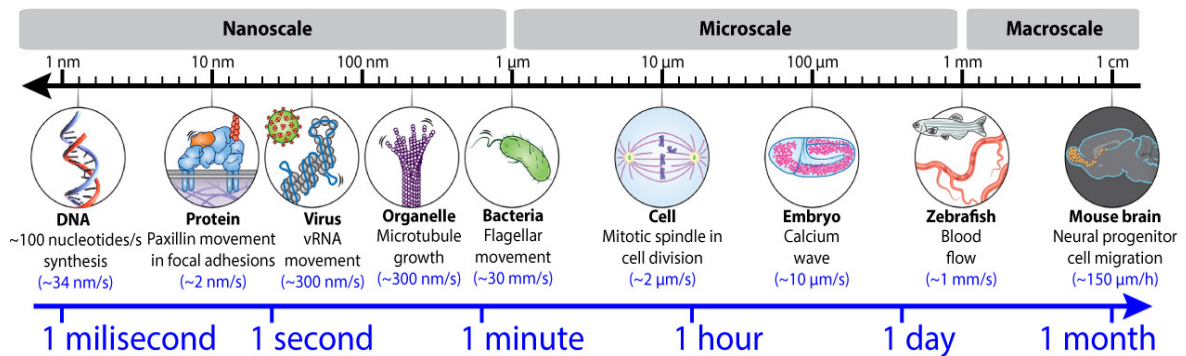


Figure 1.1. The Spatiotemporal range of relevant biological phenomena that occur over the nanometer to centimeter spatial scale and over timescales ranging from milliseconds to days. Reproduced from ⁶.

Optical fluorescence microscopy technology comprises a plethora of modalities that enable observing biological processes in living samples across different spatial scales and speeds (Figure 1.1)⁶⁻¹². Optical microscopy remains the gold standard for high-speed live cell imaging, offering the ability to acquire data typically at speeds up to 200 frames/s over a wide field (Figure 1.2a). However, the light diffraction limit restricts the resolution to hundreds of nanometers, around 500 nm and 200 nm, in the axial and lateral directions, respectively. Super-resolution (SR) microscopy, such as localization microscopy, allows imaging beyond the diffraction limit¹³, but the dose of photons required to perform fluorescence imaging causes cell damage and interferes with the processes^{14,15}. Moreover, in SR normally spatial resolution comes at the cost of long acquisition time, typically in the range of minutes per frame, and the axial resolution required to resolve processes on the cell membrane is still limited to tens of nanometers. In addition, fluorescence microscopy requires prior knowledge of the molecule being tracked, modifying that molecule and cells

with fluorescent tags. Furthermore, it tracks the position of fluorescent probes instead of the target molecules, which may produce artifacts.

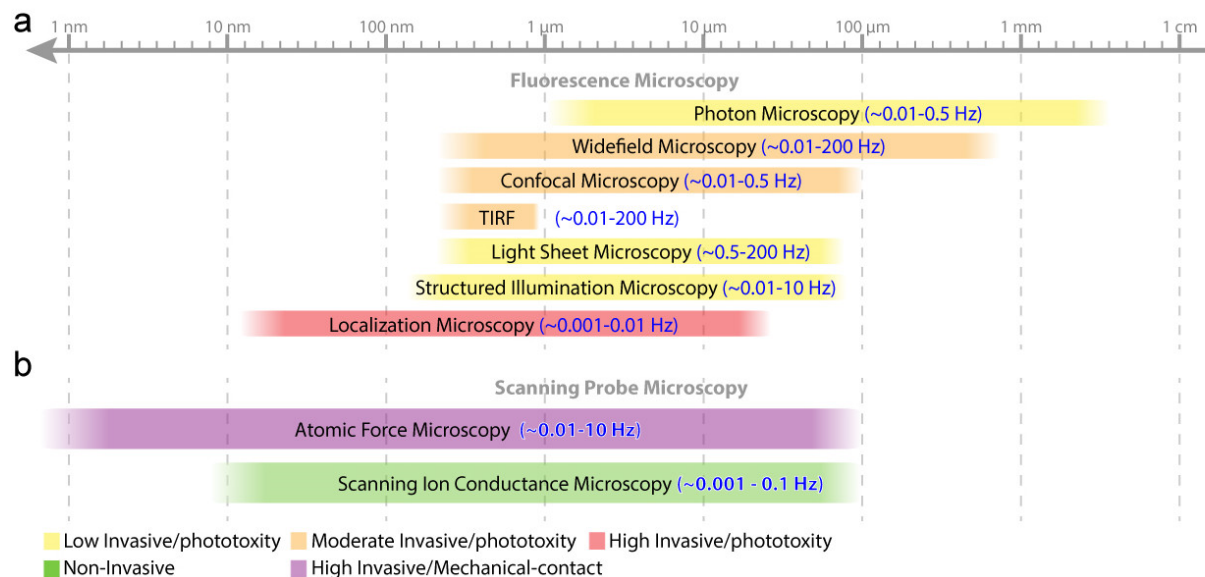


Figure 1.2. The spatiotemporal scale of several microscopy modalities across biological processes. a) Typical fluorescence microscopy methods used in living samples over indicated spatiotemporal scales with approximated resolution range. Reproduced from ⁶. b) Scanning probe microscopy methods. The frame acquisition rate in Hertz indicates the typical image acquisition rates. Colors in a and b denote the invasiveness of the method for live cells.

Scanning probe microscopy (SPM), such as atomic force microscopy (AFM)¹⁶ and scanning ion conductance microscopy (SICM)¹⁷, are label-free microscopy modalities that perform imaging with resolution in the nanometer range (Figure 1.2b). AFM is the only microscopy that allows live cell imaging with sub-nanometer resolution but is detrimental to live cells due to the mechanical contact of the probe with the soft membrane surface¹⁸. Alternatively, SICM is a true non-contact SPM ideal for live cell imaging¹⁹. However, the spatial and temporal resolution is lower than in AFM, hindering its use to study many biological processes, which is vital to resolve nanoscale structures and track them in time (Figure 1.1).

The major challenge in biological imaging is to obtain 3D information at nanometer resolution without affecting the viability of the cells and avoiding interference with the involved processes under study. Thus, the invention and advancement of microscopy methods that can image cells and tissues at high spatiotemporal resolution without interfering with cellular functions are vital to progress our knowledge. The thesis aims to develop a non-invasive microscope based on SICM that can image biological processes across different spatial and temporal scales, from cell systems such as neural networks to single molecules such as DNA (Figure 1.3). Moreover, the thesis aims to combine SICM

with SR fluorescence for complementary imaging information about molecular activity (Figure 1.3v). Ultimately, the thesis aims to use SICM to detect single molecules such as DNA structures (Figure 1.3vii).

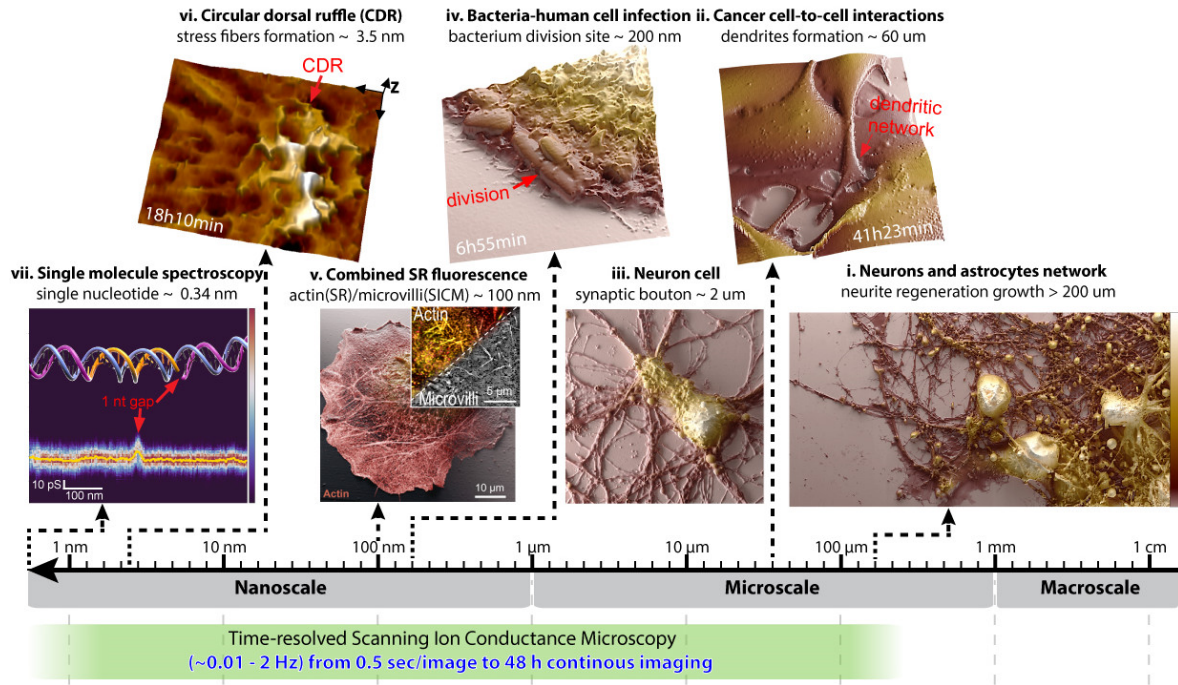


Figure 1.3. The spatiotemporal scale of time-resolved SICM across several biological processes.

1.2. Scanning probe microscopy (SPM)

Scanning probe microscopy (SPM) is a type of microscopy that uses a physical probe to generate topography images of surfaces^{16,20,21}. SPM was first established with the invention of scanning tunneling microscopy (STM) by Gerd Binnig and Heinrich Rohrer at IBM Zurich in 1981, winning the Nobel prize in 1986^{20,21}. The STM principle consists of a current originating from the quantum tunneling effect of electrons when a potential between is applied between a conductive probe and a conductive sample separated by a few angstroms. An exquisite resolution is possible as the tunneling current increases exponentially when the probe-sample distance decreases. STM is a non-contact SPM modality that uses tunneling current as a feedback signal to generate topography images. Nevertheless, it relies on conductive surfaces, making it unsuitable for applications to biological samples (which are insulators to some degree).

To image non-conductive samples and envisioning biological applications, atomic force microscopy (AFM) was invented by Binnig, Calvin Quate, and Christoph Gerber in 1986¹⁶. The AFM principle comprises a contact force between a microcantilever and a

surface, measured by the deflection of the cantilever in contact with the sample through the change in the angle of the cantilever end related to the surface. Usually, the deflection angle is measured with a four-quadrant photodiode that converts photons of a reflected laser beam into electric current, later converted into voltage to be operated by the scanning controller. The contact force, dependent on the cantilever tip-surface distance, can be approximated by Hook's law as

$$F(d) = -K_c d, \quad (1.1)$$

where K_c is the spring constant of the cantilever in N/m, and d is the cantilever deflection of the cantilever when interacting with the surface.

The principle of SPM lies in the physical or chemical interaction between the probe and the surface, and the measured interaction is always a convolution of the sample affecting the probe and the probe affecting the sample. Thus, in SPM, the image generated is a reconstruction of the object from the complex probe-surface interaction while performing raster scanning (Figure 1.4a). In SPM, the image is formed through a controller that keeps a constant probe-surface interaction (setpoint), while the change in topography generates a change in the measured signal to which the controller needs to react in real-time during raster scanning. In the case of STM and AFM, a proportional–integral–derivative (PID) controller is often used to keep the constant interaction (setpoint) and generate the image (Figure 1.4b and c), while in SICM is a trigger system (Figure 1.4d). Therefore, implementing a controller that can detect and track the setpoint accurately for high-speed raster scanning and link the XY coordinates where the probe is at a given time to a measured quantity at a given time are key challenges in SPM to generate accurate topography images of a sample.

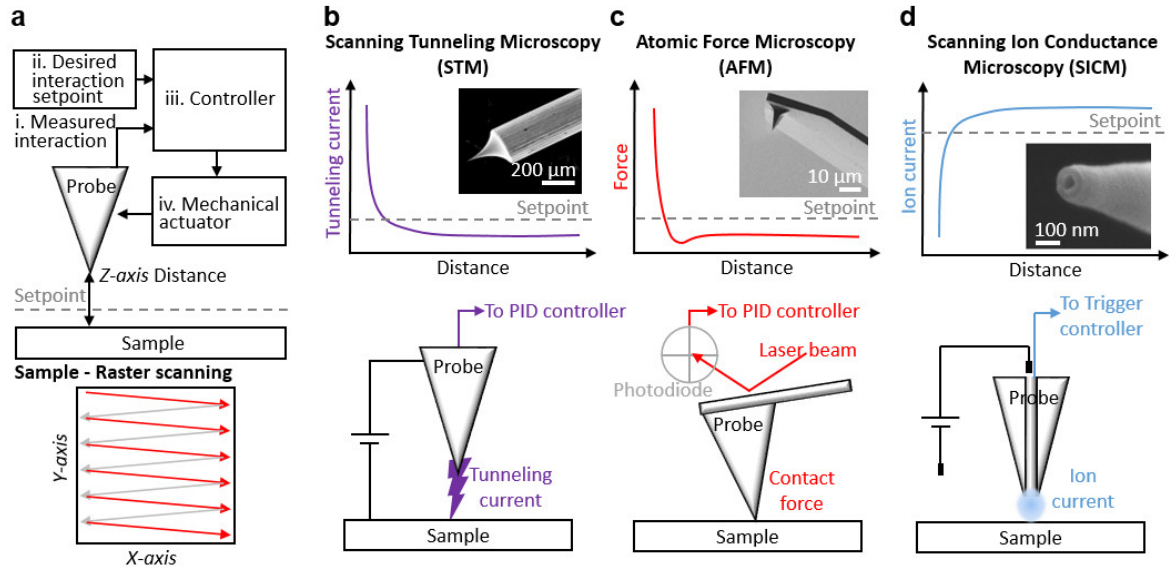


Figure 1.4. Principle of scanning probe microscopy (SPM). a) Basic components of a SPM setup based on raster scanning imaging. b) Principle of scanning tunneling microscopy (STM) that uses a conductive tip as a probe, usually made of tungsten²² or platinum iridium (PtIr), and the corresponding interaction curve (tunneling current versus probe-surface distance). c) Principle of AFM that uses a microcantilever as a probe, usually made of silicon or silicon nitride (Si₃N₄), and the corresponding interaction curve (force versus probe-surface distance). d) Principle of scanning ion conductance microscopy (SICM) that uses a borosilicate or quartz nanopore²³ as a probe (ion current versus probe-surface distance).

1.3. SPM instrumentation

In a SPM system, the probe-sample interaction is transduced into an electrical signal (Figure 1.3a-i). This signal is compared to the desired interaction setpoint (Figure 1.3a-ii) by the controller (Figure 1.3a-iii), moving the probe's position relative to the surface (Figure 1.3a-iv) to keep the interaction setpoint constant. The sample is then moved in XY (Figure 1.3a-v) while the probe detects the topographical changes while keeping constant interaction. To generate a topography image, the Z position (Z signal generated to keep the setpoint constant) of the probe at a given time is synchronized and linked to the raster scanning XY coordinates. Therefore, the critical components of an SPM microscope are the physical probe characteristics, probe-sample interaction transduction, the probe mechanical-actuator characteristics, and the scanning controller.

The physical probe depends on the type of application and corresponding SPM modality. For instance, STM uses a conductive probe to measure the tunneling current between the probe and a conductive surface (Figure 1.4b)^{20,21}. On the other hand, AFM

uses a microcantilever that measures the tip-sample interaction forces (Figure 1.4c)¹⁶. SICM uses ion currents through a nanopore in an electrolyte solution to probe surfaces (Figure 1.4d). The type of probe and SPM modality can provide a topography map of the surface and other physical quantities, such as surface charge density (SICM)²⁴ or mechanical properties of materials (AFM)²⁵. However, the interpretation of the real topography and physical quantities measured is extremely difficult because the image generated is a convolution between the probe-sample interactions that are affected by the physicochemical heterogeneity of the surfaces being imaged with SPM.

The probe-sample interaction is transduced into an electrical signal to be compared with the desired setpoint by the controller. Depending on the interaction being measured, the input noise and bandwidth of the conversion to a readable electrical signal critically impact the image resolution and speed of the scanning^{26,27}.

The characteristics of the mechanical actuator that move the probe position are critical for controlled probe motion during scanning. In many SPM applications, the mechanical actuator consists of piezoelectric elements and mechanical elements such as flexures²⁸⁻³². The challenge in performing high-speed imaging is that when the probe is moved fast, the resonances of the mechanical elements can be excited leading to the uncontrolled motion of the probe. Additionally, during actuation, the mass of the components creates an inertia leading to a delay in the actuator response.

The scanning controller and imaging modes are similar among SPM modalities, adapted to different implementations for the used transduced signal. STM is often performed with a “constant current mode” to keep the tunneling current constant while tracking the surface, yielding high-resolution images of conductive surfaces³³. AFM often utilizes an “intermittent contact mode” to keep a constant oscillation amplitude of the cantilever deflection while tracking the surface³⁴. “Intermittent contact mode” is critical to image soft biological samples in AFM as it applies lower tip-sample forces³⁵⁻³⁷. These modes are implemented with PID controllers that have a delay response limiting the speed of the imaging.

The challenge in SPM systems is tracking the probe-surface interaction setpoint accurately while scanning the sample at fast speeds, and minimizing artifact effects from mutual probe-sample interferences. Optimizing all these elements individually and integrating them together is fundamental to improving the image resolution and acquisition speed in any SPM modality.

1.4. Live cell imaging with AFM

Among SPM techniques, AFM is a microscopy that yields sub-nanometer resolution and is capable of scanning living cells in solution. With the development of high-speed AFM, it has become possible to study temporal changes in biological samples and processes that occur in short temporal ranges. Thus, AFM has been extensively used to study membrane processes in prokaryotes and eukaryotes. Examples of AFM applications include Dufrene et al used AFM to characterize the surface ultrastructure and molecular interactions of living fungal spores at the nanometer scale³⁸. Alsteens *et al* used AFM to probe the localization and interactions of chemical and biological sites on living cells at high speed and high resolution³⁹. Schneider et al. recorded plasma membrane structures involved in exocytosis in pancreatic cells⁴⁰. Dupres et al measured the specific binding forces of individual adhesins, mapping their distribution on the surface of living bacteria⁴¹. Andre et al. imaged the architecture and assembly of peptidoglycan in Gram-positive bacteria⁴². Fantner et al. imaged the action of the antimicrobial peptide on Escherichia coli cells⁴³. Eskandarian et al. and Hannebelle et al. studied bacteria cell division with long time-lapse AFM imaging^{44,45}. Odermatt et al. combined super-resolution fluorescence with AFM to track mammalian cell dynamics⁴⁶. Recently, Penedo et al. created a nanoendoscopy-AFM method that enabled the visualization of nanodynamics of the eukaryotic membrane inner scaffold⁴⁷. Many applications also included mechanical properties studies using the force the AFM cantilever applied to deform the cells^{25,48–54}. Other AFM applications on live cells included modifying the cantilever with a microfluidic system (FluidAFM) by Zambelli et al. for several biological studies^{55–57}.

Although AFM has enabled breakthrough studies in cell membrane, the forces applied by the cantilever tip deform the fragile cell structures (Figure 1.5a), and interfere with cell viability (Figure 1.5b). Thus, soft and suspended structures such as microvilli are challenging to resolve¹⁸. In addition, while visualization of bacterial growth and division for several days has been possible with AFM, maintaining such long imaging times on sensitive eukaryotic cells such as neurons is challenging due to the complexity and time variance of the tip-sample force interaction. Being able to image continuously at the nanoscale over long periods (days) without affecting the cell's viability is still one of the main challenges in live cell microscopy.

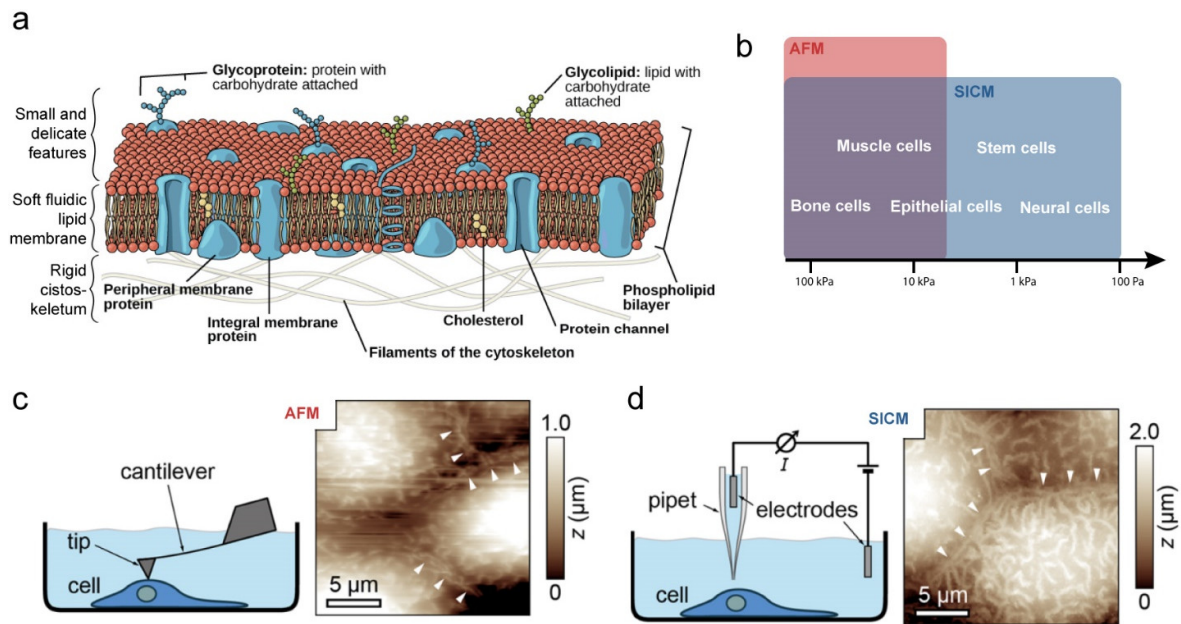


Figure 1.5. Cell membrane structures resolved by SICM. a) Composition of the cell membrane, comprising soft features. Reproduced from⁵⁸. b) Cells sensitive to a different range of pressure. c) AFM deforms suspended features on the cell membrane such as microvilli. d) SICM can resolve soft structures and microvilli. Reproduced from¹⁸.

In summary, AFM is an SPM modality that uses the interaction forces between the mechanical cantilever probe and the sample's surface, to image dynamic biological processes (See equation 1.1). However, the mechanical contact between the AFM probe creates artifacts, and interacts with the cell structures affecting them (Figure 1.5c). Therefore, an alternative non-contact SPM modality, SICM, has emerged as the ideal tool for live cell imaging in mammalian and human cells. SICM is a non-contact method that uses an ionic current to image biological samples without mechanical interference (Figure 1.5d).

1.5. Scanning ion conductance microscopy (SICM)

1.5.1. SICM principle

Scanning ion conductance microscopy (SICM) was invented by Hansma, Drake, Marti, Gould and Prater in 1989¹⁷ and further developed by Korchev *et al.* to image live cells⁵⁹. The principle of SICM is based on an ion current induced through an electrolyte-filled nanopipette (Figure 1.6a), when a voltage is applied between one electrode inside the pipette and another in bath solution (Figure 1.6b). The current decreases when the pipette pore approaches the surface as the flow of ions through the pore is reduced, thus providing a measure of the pipette-sample distance (Figure 1.6c).

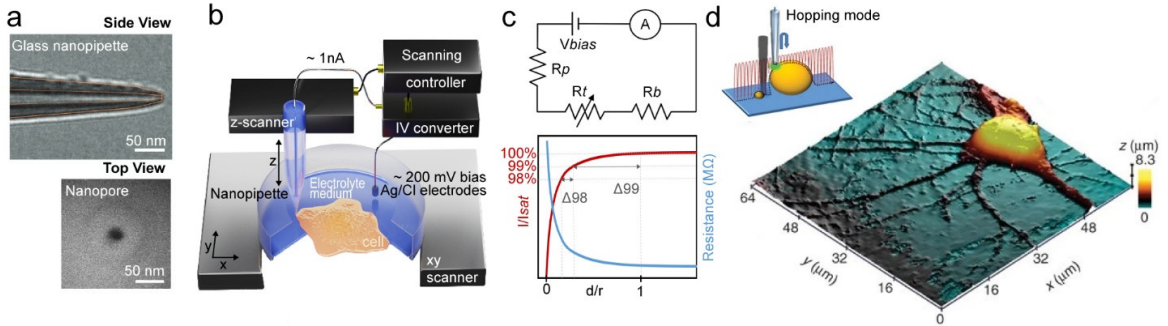


Figure 1.6. Principle of a scanning ion conductance microscope (SICM). *a*) SICM probe: TEM image showing the nanocapillary geometry at the tip⁶⁰. *b*) An ion current is generated through a glass nanopore by applying a voltage between two electrodes. I_{sat} is the current when the pipette is far from the surface. *c*) The corresponding electric circuit and the current-distance curve when the pipette moves towards the surface. *d*) Topography image (3D image of the surface) of a cortical neuron. Reproduced from¹⁹.

The electrical pipette resistance opposing the flow of the ionic current through the electrolyte is divided into three regions^{61,62,63}: The pipette resistance from the pipette tip base to the tip opening R_p ; the distance-dependent access resistance between the pipette tip and the sample surface R_t ; and resistance from the tip region to the bath electrode R_b that can be neglected as it is much smaller than R_p (Figure 1.6c, top panel).

The constant resistance R_p depends on the geometry of the pipette and the conductivity of the electrolyte solution. It can be calculated analytically when modeling the pipette as a hollow cone⁶⁴:

$$R_p = \frac{1}{\kappa} \frac{h}{\pi r_i r_e} \approx \frac{1}{\kappa} \frac{h}{\pi r_i \tan(\theta)}, \quad (1.2)$$

where κ is the conductivity of the electrolyte, r_i is the inner radius of the tip pore, r_e is the inner radius of the pipette base, and θ is the cone angle of the pipette wall with the vertical axis (usually around 3°), and h is the pipette height to base. The quantity r_o/h can be

approximated by $\tan(\theta)$, considering that the length of the conical part of the pipette is much larger than the tip.

The variable access resistance R_t that depends on the distance between the tip and the sample (d) and the d/r_o ratio, was estimated by Johannes Rheinlaender and Tilman Schaeffer with FEM analysis⁶¹. For a given range of d/r_o ratio the R_t was estimated as:

$$R_t(d/r_o \leq 0.2) \approx \frac{1}{\kappa} \frac{\ln(r_o/r_i)}{2\pi d}; \quad (1.3)$$

$$R_t(d/r_o \geq 0.2) \approx \frac{1}{4\kappa r_i} \left[1 + 0.2 \left(\frac{r_o}{d} \right)^{1.2} \right]. \quad (1.4)$$

where r_o is the outer radius of the tip opening (typically $2r_i$). Therefore, the ion current-distance relationship can be observed in the form of an approach curve (Figure 1.6c, bottom panel) given by Ohm's law as:

$$I_{pore}(d) \approx \frac{V_{bias}}{R_p + R_t}, \quad (1.5)$$

where V_{bias} is the voltage applied between the two electrodes. The ion current is transduced into an electric signal used by the controller to detect the surface and create a topographical map of cell structures (Figure 1.6d).

1.5.2. SICM resolution

The axial resolution of SICM depends on the pore geometry, and is mainly limited by the electrical noise in the measurement of the ionic current through the glass nanopore⁶⁵. In the low-frequency regime below 100 Hz, noise power spectral density is dominated by flicker noise arising from fluctuations in the ionic conductance through the pore⁶⁶. In frequencies ranging from 100 to 10,000 Hz, noise is influenced by sources of white noise in the pore or measurement electronics⁶⁷. At higher frequencies above 10,000 Hz the dominant noise source is the amplifier's voltage noise and the total capacitance at the input⁶⁸. In this regime, the root-mean-square value of the current noise I_{RMS} is given by

$$I_{RMS}(B) = (2\pi/\sqrt{3})B^{3/2}C_t v_n, \quad (1.6)$$

with B corresponding to the measurement bandwidth, v_n is the intrinsic voltage noise density (V/\sqrt{Hz}) of the input amplifier, and C_t represents the total input capacitance that includes the capacitance of the pipette (usually ~ 10 pF), the parasitic capacitance of the wiring, and the input capacitance of the current amplifier⁶⁸⁻⁷⁰.

The axial resolution in hopping mode imaging, which is the most used mode in SICM cell measurements, can be estimated by considering the minimal detectable current

drop in the current-distance curve¹⁹. This is highly affected by the signal-to-noise ratio (SNR) given by I_{pore}/I_{RMS} and for 100 nm pore diameter pipettes has been estimated to be in the sub-10 nm range, while 30 nm pore diameter pipette have achieved sub-5 nm resolution⁶⁵. On the other hand, the lateral resolution of SICM depends mainly on the pore geometry and was estimated by Johannes Rheinlaender and Tilman Schaeffer through simulations and experimental reports. They showed that the limit of lateral resolution in SICM is about three times the pore inner radius^{61,71}.

SICM resolution enables the study of structures in the sub-100 nm range, such as microvilli, and proteins and supported lipid bilayers in the sub-5 nm range⁷²⁻⁷⁴. However, compared to AFM, which uses a stiff probe, SICM uses a fragile glass nanopore probe that easily breaks and clogs in the physiological medium, hampering the use of small pores to achieve higher resolution. In addition, small pores mean the probe will interact with the surface at shorter ranges and are more prone to break. In addition, in live cell imaging, we aim to resolve structures that are located over a large axial range (usually above 10 μm in eukaryotic cells), causing small nanopipettes to break easily when they encounter a large cell edge, which is frequently encountered when scanning mammalian cells. Thus, the way the probe is actuated and the scanning mode implemented in a SICM system is critical to resolve structures in live cells accurately over long periods.

1.5.3. SICM scanning modes

The SICM was invented in Hansma's lab, a group dedicated to designing and building AFM systems. Therefore, the first imaging modes were implemented with an adapted AFM controller that used the current as the feedback signal to control the probe position and image surfaces¹⁷.

In constant current mode (DC mode), the probe moves laterally while maintaining a predefined setpoint. This setpoint is used as a feedback signal to control the vertical position of the probe while tracking the surface contour. The topography is generated by measuring the relative movement of the piezo actuator that holds the pipette while keeping a constant current (Figure 1.7a). While this mode enables high-speed imaging on flat surfaces, it struggles to counter large slopes leading to pipette breakage. Moreover, it does not account for current drifts during imaging that leads to tip-surface distance variations and can cause artifacts^{17,75}.

In alternating current mode (AC mode), the pipette moves laterally while oscillating the pipette vertically in the 100–10,000 Hz range at a fixed amplitude⁷⁵⁻⁷⁷. The amplitude of the alternating current signal is used as feedback to control the z-position of the probe while tracking the surface contour (Figure 1.7b). Other variations of the AC mode use bias or

phase modulation instead^{78,79}. Although the AC mode is less affected by current drifts, it still struggles with steep slopes characteristic of eukaryotic cells^{76,77,80}.

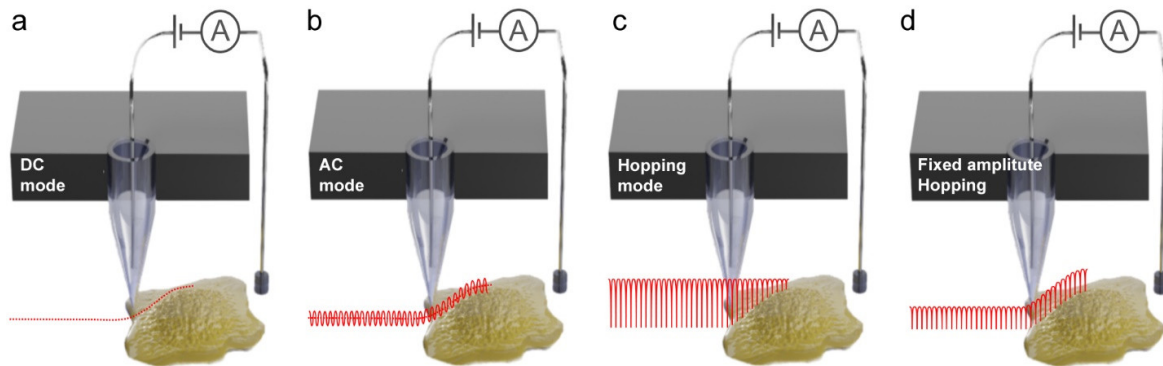


Figure 1.7. SICM scanning modes. a) Constant current scanning mode. b) Alternating current scanning mode. c) Hopping scanning mode. d) Modified Hopping mode to increase imaging speed.

Envisioning a SICM system that can perform stable live cell imaging, the backstep/hopping mode was pioneered and developed by the groups of Dietzel, Happel, and Yuri Korshev^{19,81,82}. In hopping mode, the pipette is moved vertically from a safe distance, usually a couple of micrometers. When the pipette is lowered towards the surface, it detects a change in a current from the interaction with the surface. At a defined current setpoint (Usually 99% of the normalized current far from the surface), the controller triggers the pipette retraction, and the z-position at the setpoint is recorded. This is the ideal mode for live cell imaging as it can overcome large cell edges leading to stable measurements (Figure 1.7c). However, the time required to move up and down large distances, makes hopping mode extremely slow. Therefore, several approaches and modifications to the hopping mode scanning were developed, such as retracting a defined distance (fixed amplitude) instead of retraction to the initial position (Figure 1.7d).

As the hopping mode is a slow imaging process, several modifications have been made to reduce imaging acquisition time. For example, Happel et al. implemented a pre-scan method to adjust the hopping retract distance according to the sample topography, reducing hopping time per pixel in flat regions⁸³. Following the same principle, Novak et al. implemented a pre-scan that imaged different regions at different resolutions depending on surface roughness. Cell regions were scanned in high resolution, while flat regions were scanned with low resolution to reduce the scanning time⁸⁴. Other approaches avoid pre-scanning, such as the TSFM mode by Zhuang et al. which adjusts the hopping retract amplitude based on information from the previous line (maximum surface amplitude)⁸⁵. Takahashi et al. implemented a scanning algorithm to adapt the hopping retract amplitude when the probe encounters steeper slopes, also reducing the hop/pixel time in flat regions⁸⁶. Ultimately, the hopping mode proved capable of resolving temporally biological processes and has become the most common mode for live cell imaging in SICM.

1.5.4. Live cell imaging and applications with SICM

Due to the non-contact nature of probe-surface interaction with SICM and the creation of stable imaging modes that can resolve spatiotemporally cellular processes, the application of SICM for live cell imaging has remarkably increased and diversified over the last decade. Several biological processes have been imaged since the first demonstration of live cell imaging using SICM by Korchev et al.⁵⁹. Novak et al. observed networks of hippocampal neurons and mechanosensory stereocilia cochlear hair cells¹⁹. Takahashi et al. imaged the dendritic spine and synaptic boutons, cargo transport, synapse formation, and rearrangement of the cytoskeleton at the growth cone in hippocampal neurons⁸⁷. Zhang et al. observed the morphology of amyloid fibrils and studied the nucleation and growth mechanisms behind amyloid self-assembly⁸⁸. Ushiki et al. observed collagen fibrils⁸⁹. Zhou et al. resolved primary cilia⁹⁰. Nakajima et al. imaged trachea and renal glomerulus⁹¹. Gorelik et al. used SICM to observe changes in cell area correlated with microvilli density in kidney epithelial cells⁷². Simeonov et al. imaged cardiomyocyte contractions by combining scanning ion conductance microscopy with a microelectrode array⁹². Remarkably, Shevchuk et al. imaged proteins in membranes of living cells using high-resolution SICM⁷³. Many other investigations were conducted using SICM for live cell imaging⁹³.

SICM imaging extends beyond topography, enabling mechanical properties and surface charge characterization. Sanchez et al. and Pellegrino et al. devised a SICM method to measure surface mechanical properties by applying a hydrostatic pressure^{94,95}. Rheinlaender and Schäffer further developed this method to apply a constant pressure during hopping mode, generating multiparametric topography and young modulus maps at high resolution⁹⁶. To avoid using an external pressure system, Clarke et al. showed that SICM could measure mechanical properties by indenting a cell at low stress using the intrinsic interaction forces between the glass nanopipette and the cell membrane⁹⁷. These pioneering works showed that SICM could measure the mechanical properties of soft cell membranes without direct contact force, in contrast to AFM, which often deteriorates the soft cell structures. Several cell types and biological studies were conducted using SICM for mechanical mappings, such as fibroblasts⁹⁶, blood platelets^{98,99}, cardiomyocytes¹⁰⁰, cancer cells¹⁰¹, and β -amyloid aggregate formation¹⁰².

Regarding surface charge mapping with SICM, Sa and Baker studied the electrical double layer (EDL) interaction between the nanocapillary tip and the surface, influencing the ion current through the pore¹⁰³. Unwin and coworkers demonstrated the application of SICM to create surface charge maps on polymer surfaces¹⁰⁴. Baker and coworkers devised a method based on a differential approach to ion current rectification (ICR), measuring surface charge in silane-functionalized PDMS microdomains²⁴. In biomembrane microdomains, Dong and coworkers showed surface charge measurements on supported lipid bilayers^{74,105}. Page et al. and Perry et al. showed surface charge measurements on

eukaryotic cells^{106,107}. Cremin et al. measured surface charge in prokaryotic cells to differentiate Gram-negative *Escherichia coli* and the Gram-positive *Bacillus subtilis*¹⁰⁸.

SICM can also be combined with other sensing methods for applications on live cells. Actis et al. developed SICM nanocapillaries with integrated carbon nanoelectrodes for intracellular electrochemical recordings in single cells¹⁰⁹. Takahashi and coworkers combined SICM with scanning electrochemical microscopy (SECM) on live cells to record topography and electrochemical responses of enzymes simultaneously¹¹⁰. Baker and coworkers, in the same year as Unwin and coworkers, showed that SICM could be used to measure pH^{111,112}. Korchev and coworkers recently demonstrated the application of SICM to generate maps of measured extracellular pH in living cells¹¹³.

SICM provides a unique topographical, mechanical, and chemical characterization of live cells, yet, improving the spatiotemporal resolution of SICM would unlock more detailed studies of intricate biological processes such as cancer invasion and host cell infection. However, the requirements to perform high-speed imaging on live cells create constraints on the SICM design and performance. Addressing these constraints was the primary motivation in my thesis (See **Chapters 2 and 3**), followed by the combination of SICM with super-resolution fluorescence (**Chapters 4 and 5**) and the development of a new method for single-molecule detection using SICM (**Chapters 6 and 7**).

1.6. Thesis structure

According to EPFL regulations defined by the doctoral commission (CDoct) decision, this thesis is structured in **Article format** accordingly to CDoct 109 (November 2015). Thus, the thesis main body consists of the compilation of the three main articles published during my doctoral studies as first author, followed by a conclusion and future directions. An **Introduction-Chapter** is given before each **Article-Chapter**, providing context for the challenges addressed in the thesis.

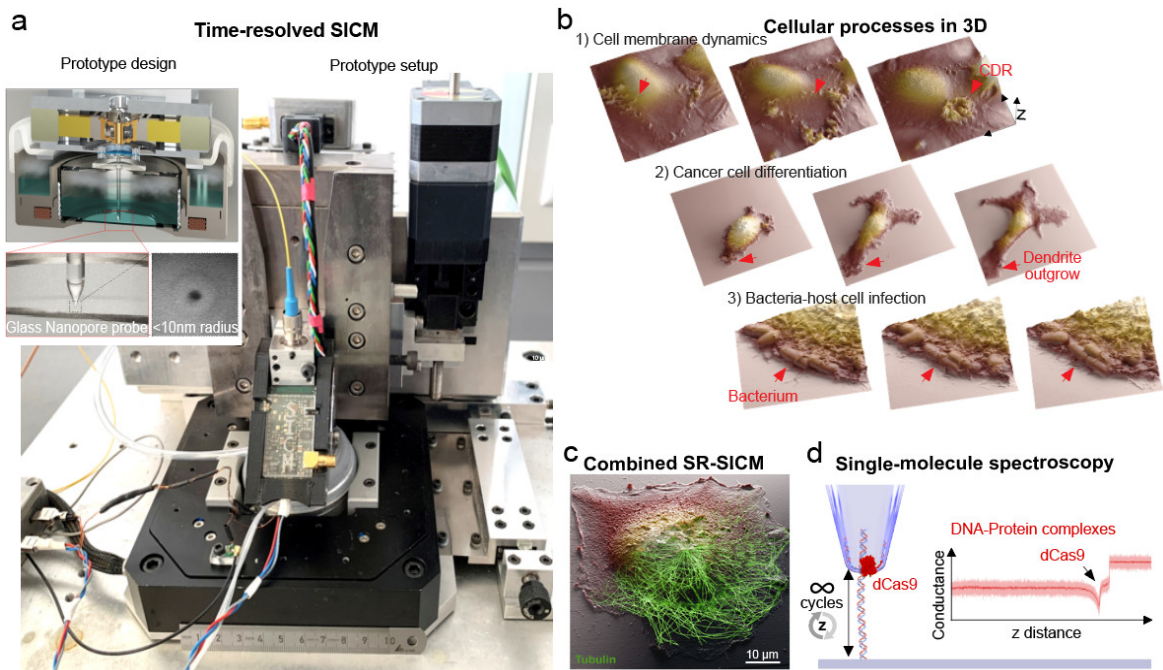


Figure 1.8. Summary of thesis projects and main achievements. a) Development of a time-resolved SICM setup. b) Applications to cellular processes. c) Correlative super-resolution fluoresce microscopy with SICM. d) Single-molecule spectroscopy with a novel method dubbed scanning ion conductance spectroscopy (SICS).

- **Chapter 2** introduces advances and challenges in high-speed SICM, followed by the development of the time-resolved SICM and its application to cellular processes, shown in **Article-Chapter 3** (Figures 1.8a and b),
- **Chapter 4** introduces correlative SICM and fluorescence imaging, followed by integrating super-resolution fluorescent microscopy into the time-resolved SICM system in **Article-Chapter 5** (Figure 1.8c).
- **Chapter 6** introduces challenges in single-molecule detection with nanopores, followed by developing the new SICS method for single-molecule spectroscopy in **Article-Chapter 7** (Figure 1.8d).

- **Chapter 8** summarizes the main findings and contributions of the thesis, followed by future directions.
- **Chapter 9** lists individual contributions to published and under review research articles during the thesis work.

Chapter 2

Advances in High-Speed SICM

2.1. Introduction to advances in high-speed SICM

The time resolution of conventional SICM imaging with hopping mode is slow, taking minutes to hours for image acquisition in living cells. This drawback hampers SICM applications to study dynamic processes that require high temporal resolution, such as endocytosis¹¹⁴, viral infection¹¹⁵, and morphodynamics¹¹⁶. The limiting factor is the overshoot time at the trigger setpoint (Figure 2.8a), leading to an overshoot distance that breaks the pipette in contact with the sample. The overshoot time arises from the resonances and the inertial mass of the moving components that constitute the mechanical actuator, the limited power output of the piezo amplifier, the pipette capacitance, and the detection bandwidth of the current signal with the transimpedance amplifier¹¹⁷.

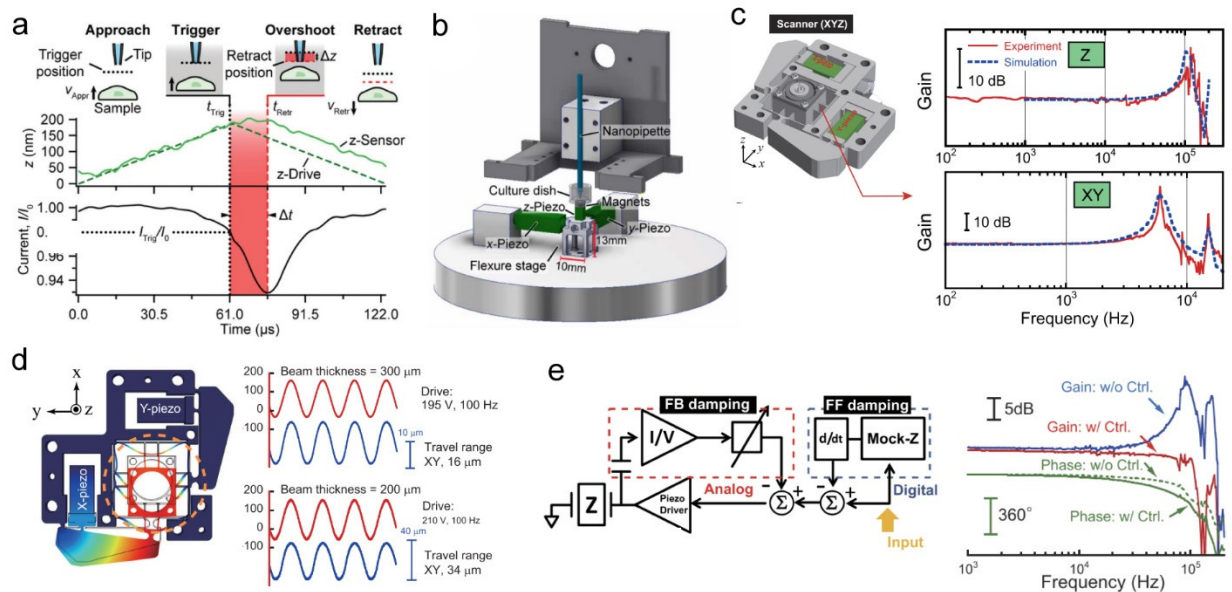


Figure 2.1. High-speed SICM elements. a) Time sequence of the probe z-position (upper plot) and the ion current (lower plot) during an approach curve in the hopping mode. When the setpoint is detected (t_{Trig}) the controller inverts the slope of the z-piezo drive signal (dashed black line) to retract the nanopipette as fast as possible. However, the probe continues approaching for a certain time (t_{Retr}) due to the finite response time of the z-piezo and signal delay, generating an overshoot time ($\Delta t_{\text{overshoot}} = t_{\text{Retr}} - t_{\text{Trig}}$)¹¹⁷. b) and c) Illustration of a mechanical design for high-speed SICM with high-resonance characteristics^{117,118}. d) Flexure design allowing for mechanical amplification in SICM¹¹⁹.

*e) Schematic of a damping controller to compensate resonances of the nanocapillary actuator*¹¹⁸.

Many initial high-speed SICM methodologies were based on reducing the number of hops per area or the hopping retract distance to save imaging time (Described in SICM imaging modes, chapter 1.5.3), rather than improving the hopping velocity. To improve the approach and retract velocity that determines the hopping rate and ultimately the image acquisition speed, researchers have addressed several limitations in SICM hopping actuation to reduce the $\Delta t_{overshoot}$ (Figure 2.1). These methods are based on increasing the resonance frequency and response of the nanocapillary actuator, and reducing the inertia at the trigger setpoint.

Shevchuk et al. developed a high-speed SICM setup consisting of a large-range piezo actuator (with low-resonance) for hopping actuation, combined with a small-range piezo (150 kHz resonance) to retract the nanocapillary probe with a reduced overshoot at the trigger, avoiding probe collision^{114,120}. This method enabled an image acquisition time of 7 s per frame to track clathrin-mediated endocytosis, a process that occurs within 20 – 40 seconds. Other approaches, such as the ARS mode by Jung et al. used a closed-loop system to decelerate the pipette near the surface, also reducing the overshoot time¹²¹. However, those SICM systems were built with low resonance frequency actuators that can originate undesired displacement oscillations for high-speed hopping rates.

To improve the resonance frequency in high-speed SICM systems Simeonov et al. and Watanabe et al. developed custom-designed mechanical actuators (Figure 2.1b and c)^{117,118}. Such implementations enabled moving the nanocapillary probe at high velocity during hopping actuation and retracting the probe with reduced uncontrolled oscillations from the resonances. Additional methods for damping control of the resonances have been implemented (Figure 2.1d)¹¹⁸. These custom-designed high-speed SICM systems enabled acquisition times in the second and sub-second range for the first time, tracking microvilli dynamics and lamellipodia^{117,118}. However, designing high-resonance actuators comes at the cost of reduced actuation range necessary for cell imaging as they can spread on surfaces over 100 μm x 100 μm area and a height above 10 μm .

To improve the actuation range, Ando's group developed an actuator design enabling mechanical amplification in the XY direction for high-speed AFM and later adapted it to high-speed SICM, improving the XYZ range to 34 μm x 34 μm x 6 μm (Figure 3.1e)^{31,119}. However, these extended imaging volume capabilities are still behind the ideal requirements for imaging processes over the full area of a single-cell surface. Moreover, these compact high-speed designs are not ideal for cell viability which need to be in a closed environment with temperature, humidity, and gas infusion control that interferes with the performance of piezo actuators under these conditions. Thus, challenges persist in performing reliable time-lapse SICM imaging for an extended time, high-resolution

imaging with small nanocapillaries, and single-cell volume imaging with high-speed hopping capabilities to resolve processes in the millisecond range.

2.2. Thesis approach to high-speed SICM to study spatiotemporally processes in live cells

Our approach to high-speed SICM is the development of a system that can resolve spatiotemporally processes in eukaryotic cells, from sub-second to days, with the highest resolution and cell viability possible, and enabling large imaging volumes. The integration of all these capabilities in the same system is addressed as follows:

- Enable cell viability during high-speed measurements. The nanocapillary actuator is integrated into a custom-designed mini-incubator, providing optimal cell culture conditions with temperature, gas infusion, and humidity. The environmental chamber is insulated through a silicon membrane to minimize interference with the probe actuator. This approach does not affect the hopping rate performance (Up to 2.5 kHz) and allows keeping cell viability for long time-lapse imaging (48h), tested in several eukaryotic cell lines (kidney, melanoma, cervical cancer, and neuroblastoma cells) and Bacteria cells (*Escherichia coli* and *Mycobacteria smagmatis*).
- Design a high-resonance probe actuator for high-speed hopping. The Z-axis actuator that moves the nanocapillary is decoupled from the XY-axis actuator that moves the sample. This design prevents resonances from the sample actuator (lower resonance – it moves a Petri dish with a sample in 5 ml medium over a large 100 μm range) from interfering with the probe z piezo actuator's response. It also keeps a lower inertial mass on the probe actuator to lower the overshoot time.
- Extend the probe actuator range. The probe Z-axis actuator is designed with a flexure configuration that enables mechanical amplification by a factor of 2.2. This design extends the range in the axial direction to 22 μm while keeping a high-frequency resonance of 13 kHz. The extended range enables a total imaging volume of 100 μm x 100 μm x 23 μm in XYZ, which meets the requirements for imaging the full area of a single-cell surface.
- Reduce the piezo-drive delay at the trigger setpoint. The system uses a custom-made high-current piezo amplifier with high bandwidth¹²². In this SICM integration, the piezo amplifier converts the low-voltage input from the time-resolved SICM controller in FPGA (-10 to 10 V) to the high-voltage (0 – 140 V) used to operate the piezoelectric stack actuator. The conversion delay at the trigger with the adaptive hopping waveform is about 1 μs (even with the large capacitance of the prize actuator), thus reducing the overshoot time.

- Improve the performance of the overall achievable high-speed rate. An adaptive hopping mode controller is implemented in FPGA. While probing the surface, applies a variable gain to the probe actuator motion in the function of the measured current. The reduced velocity near the surface increases the setpoint detection accuracy and yields a faster trigger retraction response. However, the fast retraction time originates uncontrolled oscillations from the resonances. To eliminate probe motion oscillations, the resonances of the actuator are re-shaped by a data-driven controller originally developed for AFM¹²³. In this SICM integration with the adaptive hopping mode, the data-driven controller is implemented as a 16th-order discrete-time filter that compensates for the resonances of the electromechanical actuator. Compared to the conventional hopping mode, the adaptive hopping performance shows a five times improvement in the achievable hopping rate while tracking the interaction setpoint.
- Increase the bandwidth of the detected current signal during high-speed hopping. The system uses a custom-tailored complementary metal oxide semiconductor (CMOS) amplifier with high bandwidth^{124–126}. In this SICM integration, the CMOS-based TIA is adapted for current-to-voltage conversion with 1 GOhm transimpedance gain, input noise of $2.93 \text{ fA}/\sqrt{\text{Hz}}$, and bandwidth up to 600kHz. This improvement in the detected current SNR and bandwidth improves current setpoint tracking, showing stable hopping rates of 2.5 kHz on live cells.
- Increase the image resolution while performing high-speed imaging. Small nanocapillary probes are fabricated with high SNR, using an electron beam procedure that shapes and shrinks the pore to a desired size under 30 nm¹²⁷. The pore geometries are optimized for wider angles between the pore wall and the vertical axis yielding a lower resistance (higher conductance signal and SNR). The increased SNR with small pores enables a higher resolution and achievable hopping rate. The resolution is tested on supported a supported lipid bilayer (SLB) of 6 nm height, showing an estimated axial resolution of $3 \pm 1 \text{ nm}$ with the adaptive hopping mode.
- Ensure current signal stability over long imaging periods and overcome pore contamination. Although small nanocapillaries wield high-resolution imaging, using them in cell medium is extremely unreliable as they easily clog. Moreover, sudden changes in the current signal cause unstable hopping setpoint detection leading to breaking the nanocapillary. To overcome those problems, an additional trigger system is implemented to retract the pipette from the medium when a shift in current is detected with a pre-defined amplitude. Retracting the pore from the medium generates capillaries forces that successfully remove the contamination. After, the scanning is resumed ensuring a long-lasting and stable imaging performance.

- Demonstrate time-resolved SICM performance for long time-lapse imaging. Spatiotemporal resolution of biological processes is tested for long imaging periods, up to 48 hours. For example, tracking formation and dynamics of circular dorsal ruffles (CDR) structures, that are mediated by actin filaments (ranging from 3.5 nm to 100 nm)
- Demonstrate time-resolved SICM performance for large imaging volumes. Single-cells and cell networks processes are imaged over 100 μm x 100 μm and 80 μm x 80 μm areas. For example, the morphology of transformed melanoma cells.
- Demonstrate time-resolved SICM performance for high-speed imaging with adaptive hopping mode. After single-cell scanning, we focus the imaging area on small-cell regions to track specific processes. For example, tracking the formation of clathrin-mediated endocytosis at 500 ms/frame in a 3.6 μm x 3.6 μm area. These fast frame times show that high-speed SICM on cells is getting close to the performance of high-speed AFM on biomolecules (31 – 147 ms on Myosin V for example^{35,128})
- Demonstrate time-resolved SICM application to study processes in cancer cells. We conduct imaging experiments to observe the impact of an immunoresistance suppressor molecule on melanoma cells. Morphological changes in melanoma cells are characterized with SICM after induced differentiation with forskolin, added to the medium. Importantly, we show that our integrated perfusion system into the mini-incubator does not affect the high-speed hopping performance while releasing the drugs diluted in the medium.
- Demonstrate time-resolved SICM application to study processes of bacteria infection. We image host-cell infection processes on human cells by *E. Coli*. We follow infection processes of adhesion, proliferation, and membrane engulfment that are related to the geometrical shape of individual bacteria. Importantly, we show the compatibility of the time-resolved SICM system to fluorescence microscopy, imaging fluorescently labeled HeLa cell membrane (host infected cells) and *Escherichia coli* (pathogen) cytosol while performing SICM.
- Multidimensional visualization of SICM data, to highlight topographical features on cell membranes during biological processes. We have a pipeline to display SICM and SICM/Fluorescence images in 3D. The pipeline uses an edge detection process from the slope between pixels that is overlaid with a topography colormap and displayed with 3D render software.

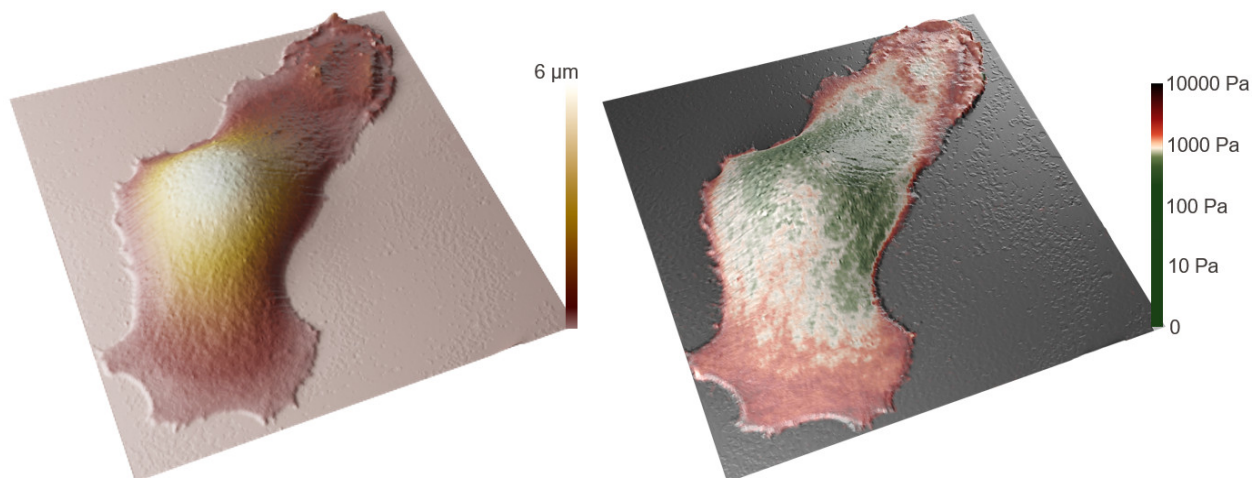


Figure 2.2. Time-resolved SICM for multiparametric measurements of live cells. $60\ \mu\text{m}$ range: 256×256 pixels. Left) Topography image of a live melanoma cell. Right) Young modulus map projected on the topography. The young modulus was calculated for each pixel from the slope of the current-distance curve between 99% and 98% of the baseline current with a method developed by Rheinlaender et al.⁹⁶. The intrinsic force applied by the nanocapillary was estimated from a calibration method developed by Kolmogorov et al.¹²⁹.

- Demonstrate that time-resolved SICM is a modular platform that can be adapted and combined with other measurements. The time-resolved SICM controller implemented in FPGA is modular and versatile, therefore enabling the easy integration of multiparametric SICM modes. The image below shows live cell imaging with combined topography and mechanical mapping on a melanoma cell (Figure 2.2). Time-resolved SICM is a platform for live cell topography imaging, and it was created to be potentially combined with other measurements, such as mechanical properties, surface charge density, pH sensing, and SECM.

The development of the time-resolved SICM, including biological applications, is described in the following **Article-Chapter 3**.

Chapter 3

Time-Resolved Scanning Ion Conductance Microscopy for Three-Dimensional Tracking of Nanoscale Cell Surface Dynamics

This is a verbatim copy of an article published in ACS Nano, 2021.

<https://pubs.acs.org/doi/10.1021/acsnano.1c05202>

Leitao, M. S.¹; Drake, B.¹; Pinjusic, K.²; Pierrat, X.³; Navikas, V.⁴; Nievergelt, A.¹; Brillard, C.¹; Djekic, D.⁵; Radenovic, A.⁴; Persat, A.³; Constam, S.²; Anders, J.⁵; Fantner, E. G.^{1,6}

1: Laboratory for Bio- and Nano-Instrumentation, Institute of Bioengineering, School of Engineering, Swiss Federal Institute of Technology Lausanne (EPFL); Lausanne, Switzerland. 2: Laboratory of Developmental and Cancer Cell Biology, Institute for Experimental Cancer Research, School of Life Sciences, Swiss Federal Institute of Technology Lausanne (EPFL); Lausanne, Switzerland. 3: Laboratory of Microbial Mechanics, Institute of Bioengineering and Global Health, School of Life Sciences, Swiss Federal Institute of Technology Lausanne (EPFL); Lausanne, Switzerland. 4: Laboratory of Nanoscale Biology, Institute of Bioengineering, School of Engineering, Swiss Federal Institute of Technology Lausanne (EPFL); Lausanne, Switzerland. 5: Institute of Smart Sensors, Universität Stuttgart; Stuttgart, Germany. 6: Corresponding author.

Author contribution: I conceived the idea with Prof. Georg Fantner and Barney Drake. I developed the time-resolved SICM instrument with Barney Drake, who designed and built microscope mechanical parts. I developed an adaptive hopping mode in the open-source AFM controller created by Dr. Adrien Nievergelt and Charlene Brillard. I created a pipeline for 3D data visualization from SICM topography and SICM/fluorescence with Dr. Vytautas Navikas. I characterized and integrated a high-bandwidth CMOS transimpedance amplifier designed by Dr. Denis Djekic and Prof. Jen Anders. I developed and characterized nanocapillaries with small pores diameter and high SNR with protocols developed by Dr. Vytautas Navikas and Prof. Aleksandra Radenovic originally for nanopores single-molecule detection. I did the mechanical and electrical characterization of the different elements of the system and built electronic interfaces, integrating all the components that constitute the time-resolved SICM system. After, I tested the system performance for high-speed hopping, long time-lapse imaging, and several biological applications. I designed experiments and prepared samples in collaboration with molecular biologists (Dr. Katarina Pinjusic and Prof. Daniel Constam) and microbiologists (Dr. Xavier Pierrat and Prof. Alexander Persat). I analyzed data, made figures, and wrote the original manuscript.

3.1. Abstract

Nanocharacterization plays a vital role in understanding the complex nanoscale organization of cells and organelles. Understanding cellular function requires high-resolution information about how cellular structures evolve over time. A number of techniques exist to resolve static nanoscale structure of cells in great detail (super-resolution optical microscopy, EM, AFM). However, time-resolved imaging techniques tend to either have lower resolution, are limited to small areas, or cause damage to the cells thereby preventing long-term time-lapse studies. Scanning probe microscopy methods such as atomic force microscopy (AFM) combine high-resolution imaging with the ability to image living cells in physiological conditions. The mechanical contact between the tip and the sample, however, deforms the cell surface, disturbs the native state, and prohibits long-term time-lapse imaging. Here, we develop a scanning ion conductance microscope (SICM) for high-speed and long-term nanoscale imaging of eukaryotic cells. By utilizing advances in nanopositioning, nanopore fabrication, microelectronics, and controls engineering we developed a microscopy method that can resolve spatiotemporally diverse three-dimensional (3D) processes on the cell membrane at sub-5nm axial resolution. We tracked dynamic changes in live cell morphology with nanometer details and temporal ranges of sub-second to days, imaging diverse processes ranging from endocytosis, micropinocytosis, and mitosis, to bacterial infection and cell differentiation in cancer cells. This technique enables a detailed look at membrane events and may offer insights into cell-cell interactions for infection, immunology, and cancer research.

3.2. Introduction

Visualizing dynamic structural changes in live eukaryotic cells at the nanoscale is essential to understand the mechanisms by which cellular components fulfill their function in key cellular processes. The time frame of those processes ranges from seconds/minutes for events such as endocytosis, to hours/days for cell differentiation. To study long-term biological mechanisms, light-based time-lapse microscopy (TLM) methods have been implemented, capturing a sequence of images at regular intervals^{130,131}. Among the plethora of TLM techniques on eukaryotic cells, phase-contrast, differential interference contrast, and fluorescence microscopy are the most relevant. Visualizing morphological changes in the cell membrane, however, is challenging as they involve dynamic nanostructures with dimensions below the diffraction limit of light^{132,133}. Super-resolution microscopy methods have become invaluable in studying live cells¹³⁴. Yet, due to the axial resolution, photobleaching, and phototoxic effects it remains challenging to resolve the membrane surface of a living cell using light-based TLM techniques. In particular, determining the exact boundary of the cell membrane is often impossible at the nanometer scale¹³⁵. Atomic force microscopy offers excellent axial resolution and can be used to image live cells.

However, the forces applied by the cantilever tip deform the cell, thereby revealing the cytoskeleton, rather than the native shape of the cell membrane¹³⁶. In addition, the tip-sample forces deform soft structures such as microvilli, making them difficult to resolve¹⁸. Maintaining long imaging times with AFM on mammalian cells is technologically very difficult due to the complexity and time variance of the tip-sample force interaction. This drastically decreases the viability of cells, in particular those of mammalian origin. High-speed AFM imaging is limited to relatively small imaging ranges, and the need for small AFM cantilevers limits the height of the samples that can be imaged. The ultimate method for single-cell biology would combine the high-resolution 3D information of scanning probe microscopy, with the imaging range, the long-time time-lapse capability, and the high temporal resolution of optical microscopy.

Scanning Ion Conductance Microscopy (SICM)¹⁷ has been shown to be particularly well suited for imaging soft samples^{18,19,59}. By measuring the distance-dependent current through a nanopipette, SICM yields high-resolution images of fragile membrane features, without touching the cell. Together with the high axial resolution from scanning probes, the label-free characteristic of SICM is a crucial benefit over other optical methods such as super-resolution microscopies. Possibly the most notable evolution in SICM was the development of backstep/hopping mode by Happel⁸² and the seminal work by Novak and Korchev¹⁹, making SICM an ideal starting point for long time-lapse imaging of mammalian cells. However, hopping mode SICM is traditionally a rather slow technique with acquisition times in the order of tens of minutes per image, which prevents the study of fast dynamic events.

Here we develop a high-performance SICM system for high-speed and long time-lapse imaging by implementing recent advances in nanopositioning¹²², nanopore fabrication¹²⁷, microelectronics¹²⁶, and controls engineering¹²³. In order to demonstrate the capabilities of our system, we selected a diverse set of three-dimensional biological processes as test cases.

3.3. Results

3.3.1. Time-resolved SICM setup

The imaging speed in SICM is largely determined by the hopping rate¹⁹ and pipette velocity at which the pipette approaches the surface and retracts when the drop in ion current reaches a certain set point threshold (Figure 3.1a in red). Usually, a set point below 2% of the baseline current is used to avoid pipette/sample crashing. The hopping rate is limited by the speed at which the piezo scanner can retract the pipette without leading to excessive overshoot. Once the current drop reaches the set point, the SICM controller tries to retract the pipette as fast as possible. This motion creates an inertia that excites the resonance frequency of the piezo actuator. The larger the pipette velocity is at the time the current reaches the set point, the stronger is this parasitic excitation of the scanner

resonances. The resonances are also excited stronger the closer the hopping rate is to the resonance frequency of the piezo actuator. To overcome the second issue, previous efforts have been made in designing SICM scanners with high resonance frequencies which unfortunately goes at the expense of the Z-range^{117,118}. Imaging of Eukaryotic cells, however, requires piezo actuators with long-range (>10-20 μm). This traditionally leads to a tradeoff between resonance frequency and range of the actuator. In addition to using a custom high-bandwidth, large-range actuator (Figure 3.1b,c,d and Figure S3.1,2), we overcame this tradeoff in our instrument on the one hand by adaptively slowing down the pipette velocity already before it reaches the trigger setpoint¹³⁷. We use an adaptive gain applied to the piezo motion as a function of the current interaction curve (Figure S3.2a,b). In addition, the motion dynamics of the actuator are re-shaped by a data-driven controller¹²³, implemented in a 16th-order discrete-time filter that compensates for the resonances of the electromechanical actuators (Figure S3.2c-e and Supplementary Note 3.1). The adaptive hopping mode and the data-driven controller increased the achievable hopping rate by a factor of 5 (Figure 3.1c,d).

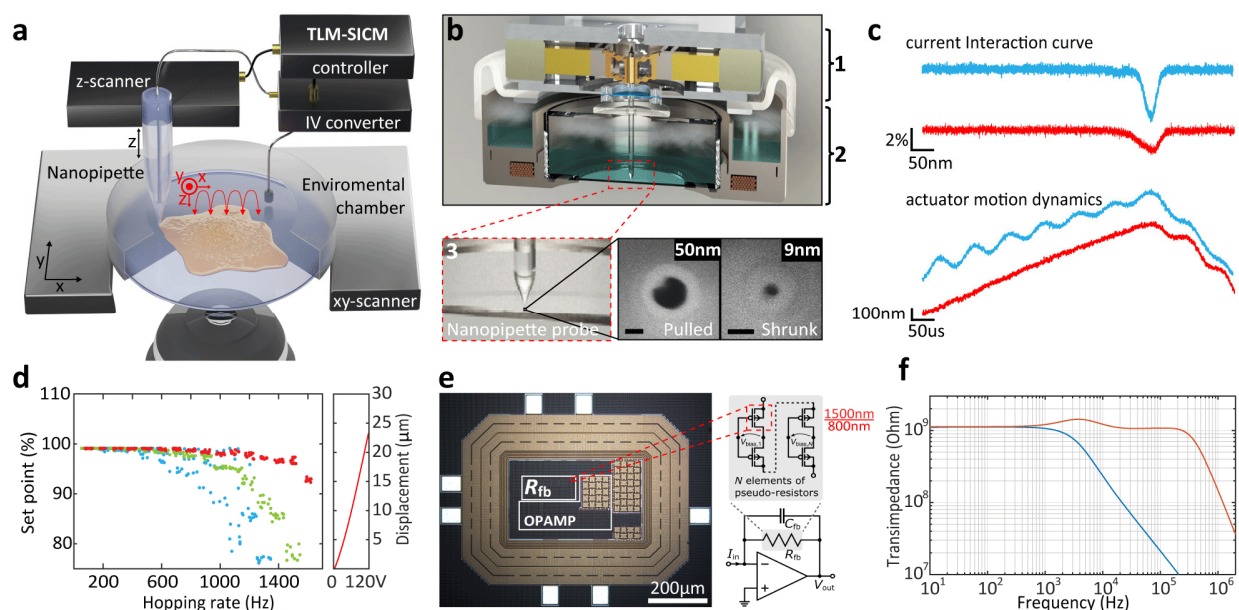


Figure 3.1. Time-resolved SICM principle and implementation. (a) Illustration of the SICM principle. (b) Schematic rendering of a cross-section of the time-resolved SICM system based on a high-bandwidth large-range SICM actuator (1), integrated into a miniature incubator (2). Nanopipettes are fabricated through laser pulling (50nm radius); and successively shrunk through SEM radiation to sub-10 nm pore radius, SEM images (3). Scale bars, 50 nm. (c) SICM interaction curve (top), and actuator motion dynamics (bottom) with conventional hopping mode in blue and with the time-resolved SICM implementation (adaptive hopping mode and data-driven controller) in red. 1 kHz hopping rate (1.25 mm s^{-1} approach velocity), $1 \mu\text{m}$ hopping height and 98% set point. (d) Actuator hopping rate performance with the conventional hopping mode (blue), adaptive hopping

mode (green), and adaptive hopping mode together with data-driven controller (red). 1 μm hopping height and 99% set point. (e) Die micrograph of custom TIA composed of a low-noise operational amplifier and a pseudo-resistor in its feedback. The pseudo-resistor consists of N series-connected pMOS transistor pairs with specific biasing to achieve a large and precise resistance value. (f) Transimpedance measurements of the 1st stage TIA (blue) and the overall transimpedance using the subsequent amplifier stage for bandwidth extension (red).

Another essential aspect for fast and accurate feedback response is the bandwidth of the low noise current to voltage conversion. Rosenstein et al. have demonstrated that increased performance in nanopore sensing platforms is obtainable by integrating custom tailored complementary metal oxide semiconductor (CMOS) amplifiers⁶⁸. We developed a custom, bandwidth-extended transimpedance amplifier (BE-TIA), which was manufactured in a 180-nm CMOS silicon-on-insulator technology for decreased parasitic well capacitances and leakage currents. It has a subsequent discrete amplifier stage to further increase the overall bandwidth¹²⁶. The TIA's feedback resistor is set to a very large value of 1 G Ω to achieve low noise and is composed of a multi-element pseudo-resistor (Figure 3.1e), i.e., a large number of series-connected small-sized p-channel MOS transistors of W/L = 1500/800 nm with inherent linearization and a specific biasing circuit that facilitates a precise and tunable high-value resistance (Figure 3.1e, Figure S3.4 and Supplementary Note 3.2). The subsequent amplifier increases the overall bandwidth from 10 kHz to 600 kHz (Figure 3.1f). The BE-TIA multiplied the achievable hopping rate in our time-resolved SICM by a factor of 8 (Figure S3.5).

3.3.2. Live cell imaging with time-resolved SICM

Maintaining cell viability during long-term time-lapse imaging requires accurate control of temperature, humidity and CO₂ levels in the sample area, without adversely affecting the SICM performance. We integrated our time-resolved SICM with a custom miniature incubator (Figure 3.2a and Figure S3.6), which ensured cell viability for well over 48h (Figure 3.2b). Figure 3.2c shows a 28 hours continuous time-lapse imaging sequence of kidney cells revealing highly dynamic protrusions on the apical cell surface such as lamellipodia ("LP" in Figure 3c-1,2), and ruffles ("R" in Figure 3.2c-1,3), which play a major role in cell motility (Figure S3.7). Furthermore, we observed filopodia, which are finger-like protrusions that cells use for probing the environment ("FL" in Figure 3.2c-1, and Figure S3.7). We also identified stress fibers that have an essential role in cell adhesion, migration, and mechanotransduction ("SF" in Figure 3.2c-1,3). Additionally, we observed cell-to-cell contacts that play a fundamental role in cell-communication and the development of multicellular organisms ("CC" in Figure 3.2c-1,2,4,5, and Figure S3.7). Figures 3.2d-4,5, and Figure S3.8 reveal how the interfaces of two cells fuse in syncytium. Of particular interest is the appearance and disappearance of circular dorsal ruffles

(“CDR1” and “CDR2” in Figure 3.2c-5 to 10, and Figure S3.9 and 3.10). Being able to observe the dynamics of these diverse structures within one long experiment lets us correlate the seemingly independent structures and investigate possible interdependencies.

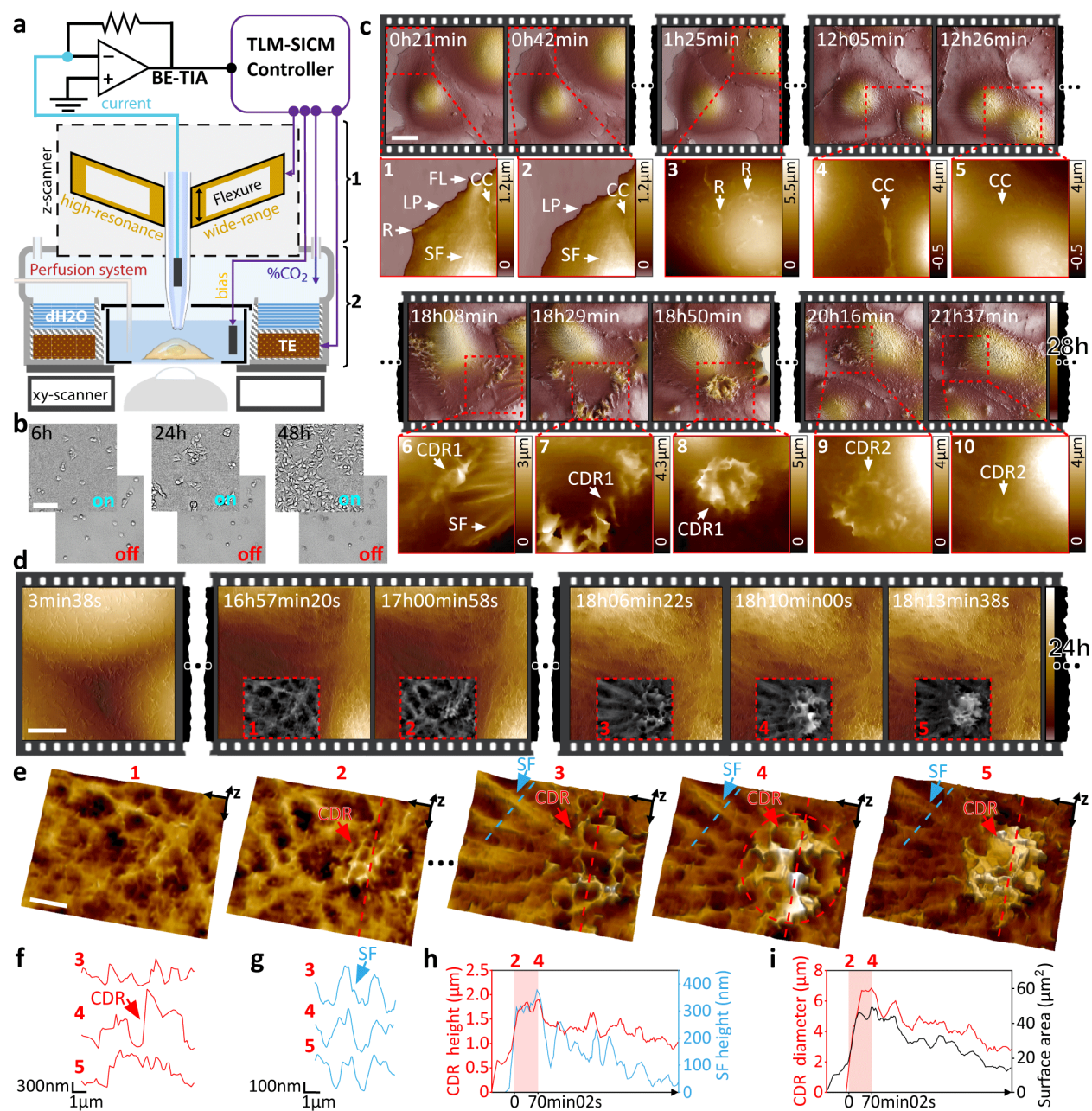


Figure 3.2. Time-resolved allows long-term 3D visualization of the eukaryotic cell membrane and the tracking of dynamic structures at nanometer resolution. (a) High-performance pipette z-actuator (1) is integrated into a miniature incubator (2). (b) Demonstration of cell viability and proliferation over 48 hours in our time-resolved SICM system, with controlled atmosphere ON vs OFF. (c) 28 hours time-lapse scanning of live

kidney cells (COS-7) in DMEM-Hi glucose medium. Scale bar, 20 μm . Several membrane structures can be visualized: ruffles (R), lamellipodia (LP), filopodia (FL), cell-cell contacts (CC), stress fibers (SF), and CDR. (d) 24 hours time-lapse scanning of live kidney cells tracking the formation of a CDR structure. Scale bar, 5 μm . (e) 3D view of the CDR with the Initiation spot in panels 1-2, and maximum expansion in panels 3-5. Scale bar, 2 μm . (f) Height-profile of the CDR ring (red arrow in F). (g) Height-profile of a nearby SF protruding the cell surface (blue arrow in F). (h) Plot of CDR and SF max-height, showing a strong correlation during the expansion period (2-4); (i) Plot of CDR ring diameter and surface area; over 130 frames.

3.3.3. Tracking dynamic processes on cell membranes

Circular dorsal ruffles (CDR) are elusive dynamic structures, likely related to cell migration, macropinocytosis, and internalization of membrane receptors¹³⁸. These important roles are receiving increasing attention in the scientific community due to their involvement in cancer progression and the facilitation of the pathogen infection¹³⁹. While most studies report that CDRs appear in cells stimulated with mitogenic and/or motogenic factors, our long time-lapse measurements on kidney cells show that these transient structures can appear in optimal culture conditions without external stimulation (Figure 3.2c-6 to 10, and Figure 3.2d). With time-resolved SICM we tracked a CDR that appeared at 17h00min of scanning with the maximum expansion of the wave reached at 18h10min (Figure 3.2d,e). Recently, Bernitt et al have modeled the appearance of CDRs and associated them with actin polymerization¹⁴⁰ using confocal microscopy. Our time-resolved SICM data corroborate their findings, adding three-dimensional details of the process at sub-100 nm lateral and sub-10 nm axial resolution. Figure 3.2e clearly shows the proximity of the ring-shaped actin mediated wave (CDR) (Figure 3.2f) to stress fibers (SF) (Figure 3.2g). The polymerization of the stress fibers extrudes the cell membrane and correlates with the formation of the CDR ring (Figure 3.2h, i). After expansion, these fibers gradually fade from the surface topography whilst CDR decreases in height and diameter, suggesting their interdependence.

3.3.4. High-speed imaging with time-resolved SICM

Many of the processes on the level of whole cells occur at a time scale of minutes or hours and can therefore be tracked easily with time-lapse SICM. Sub-cellular events such as endocytosis or infection, however, often occur much faster. Increasing the imaging speed of SICM has thus far been at the expense of imaging volume^{117,118} to only 7'000 μm^3 . This makes studying natural processes on live cells impractical. Our technique combines the ability to address large imaging volumes up to 220'000 μm^3 at moderately fast speeds with high-speed SICM imaging of small details on live cells (Figure 3.3a and Figure S3.11-13). The small-scale, high-speed data can thus be put in the context of the overall cell morphology and growth patterns. Figure 3.3a shows a large area 80 \times 80 μm overview scan

of a kidney cell. Subsequent zooming-in increased the temporal resolution to frame periods of 0.5 s/image at hopping rates of 2.5 kHz. We tracked protrusions at the cell periphery and on top of the cell membrane (Figure 3.3a, b, c). Figure 3.2d,e show endocytic pit formation on live kidney cells. We also observed endocytosis on modified melanoma cells (SKMEL) that co-express clathrin-RFP and dynamin-GFP (Figure 3.3f). Figure 3.3g depicts larger area scans (3 μm field of view) with higher resolution (100 \times 100 pixels) on the cell membrane to identify endocytic pits, and to extract dynamic key parameters such as pit depth and pit area and plot them as a function of time (Figure 3.3h). Another endocytic event imaged at 0.5 s/image, but a smaller size scale and lower number of pixels is shown in Figure 3.3i,j. The large dynamic range of the measurements in terms of scan size (500 \times 500 nm to 100 \times 100 μm), imaging speed (0.5 s/image to 20 min/image), number of pixels per image (1 kilopixel to 1 Megapixel), and a depth of view (22 μm with axial resolution below 10 nm) greatly enhances the type of biological questions that can be studied with time-resolved SICM.

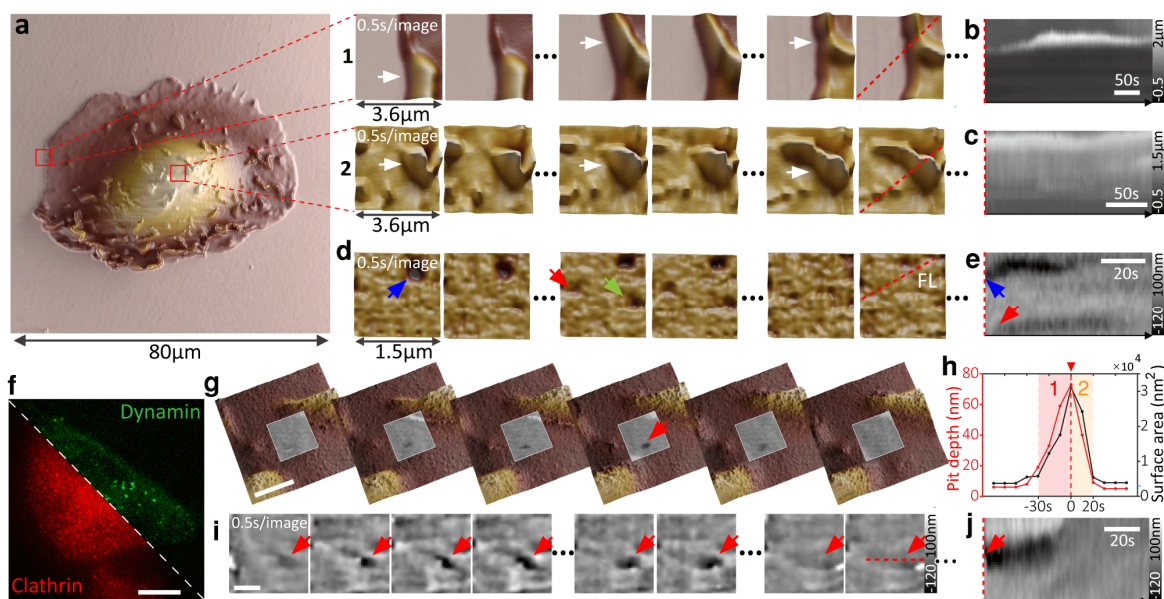


Figure 3.3. Time-resolved SICM allows a large dynamic scan range essential for long-term monitoring of cells and high-speed performance to track transient biological events at the nanoscale. (a) Large area scanning of a single kidney cell (80 μm : 512 \times 512 pixels). Fast image acquisition at 0.5 s/image (2.5 kHz hopping rate) on the cell periphery (1), and on top of the cell (2). Arrows point to dynamic ruffles. (b) and (c), Kymogram showing the dynamics of ruffles over time (red dashed lines in a, 1 and 2). (d), Fast image acquisition of 0.5 s/image of the kidney cell membrane with arrows pointing to several endocytic events; with the respective kymogram in e. (f), Fluorescence image of a transformed melanoma cell that co-expresses clathrin-RFP and dynamin-GFP. Scale bar, 20 μm . (g) Fast image acquisition of a larger area (3 μm : 100 \times 100 pixels) at 10 s/image (1 kHz hopping rate) detecting the formation of an endocytic pit (red arrow) within 50 s over 5 data points. Scale bar, 1 μm . (h) Plot of endocytic pit depth and surface area. 1: growing;

and 2: closing. (i) Fast image acquisition at 0.5 s/image of an endocytic pit (red arrow) within 50 seconds and 100 data points a 15 nm radius pipette. Scale bar, 500 nm; with the respective kymogram in (j).

3.3.5. Study of morphological changes in cancer cells

Time-resolved SICM is particularly well suited for biological questions that relate either to a change in 3D cell morphology, or where membrane trafficking plays a major role. Morphological changes of transformed cells, for example, are essential in cancer diagnosis and treatment decision-making¹⁴¹, but are difficult to track over long durations. Knowledge about associated events on cell membranes, their dynamics and roles in tumor evolution is limited by a lack of tools for long-term imaging. In cultured melanoma cells (B16-F1), important morphological changes linked to cell differentiation and motility are induced by 3'-5'-cyclic adenosine monophosphate (cAMP) signaling, which is implicated in mediating resistance to BRAF inhibitor therapy¹⁴², and which can be activated in vitro by treatment with the adenylate cyclase (ADCY) agonist forskolin (FSK)¹⁴³ (Figure S3.14). To evaluate the spatiotemporal resolution of time-resolved SICM to reveal cAMP-induced changes, we monitored melanoma cell morphology during 48 hours of sustained FSK treatment¹⁴⁴ (Figure 3.4a). Within this time frame, FSK treatment drastically increased the outgrowth and branching of interwoven cell dendrites that were frequently suspended >5 μm above the substrate (Figure 3.4b, c).

The high spatial resolution afforded by time-resolved SICM imaging revealed that FSK treatment rapidly increased the width of dendrites (Figure 3.4d,e, and Figure S3.15 and 3.16), and revealed the presence of membrane protrusions already during the earliest time points examined (Figure 3.4f, and Figure S3.17). Prolonged FSK treatment resulted in a gradual increase in cell surface area with no significant change in cell volume (Figure 3.4g, h, and Figure S3.18a, b). Curiously, these changes were accompanied by a rise in cell height skewness (Figure S3.18c), decreased cell height (Figure 3.4i and Figure S3.18d), and by a long-term decrease in membrane roughness (Figure 3.4j and Figure S3.18e). The roughness measured is associated with the presence of membrane protrusions, a feature related to focal adhesions that are mediated by rearrangement in actin cytoskeleton¹⁴⁵ and increased invasiveness in cancer¹⁴⁶.

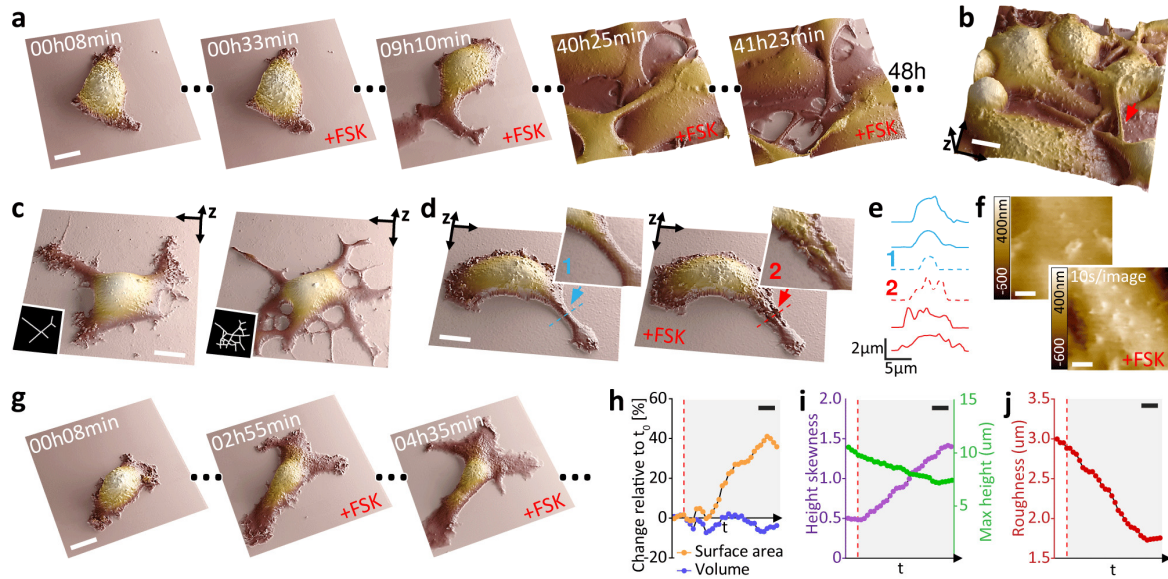


Figure 3.4. Time-resolved SICM enables a large dynamic scan range of cells and suspended structures, allowing long-term visualization of differentiation and morphological changes in melanoma cells. (a) 48 hours time-lapse scanning of melanoma cell (B16-F1) differentiation during prolonged treatment with 20 μM forskolin (FSK). Scale bar, 10 μm . (b) The long actuation range allows the nanoscale visualization of dendrites (branched cytoplasmic protrusions), suspended 5 μm above the substrate (red arrow). Scale bar, 10 μm . (c) FSK-induced dendrite outgrowth. Scale bar, 10 μm . (d) Tracking a single dendrite before (blue arrow) and after adding FSK (red arrow). Scale bar, 10 μm . (e) Height profile of the dendrite over a time sequence with 1 and 2 shown in panel d. (f) Visualization of the real-time effect of FSK on the cell membrane with fast image acquisition at 10 s/image (1 kHz hopping rate). Scale bar, 1 μm . (g) Visualization of long-term morphological changes associated with FSK-induced melanoma cells differentiation. Scale bar, 20 μm . (h) Surface area and volume percentage change relative to the first frame. (i) Maximal height and height skewness. (j) Membrane roughness. Scale bar, 50 minutes. The dashed line in red represents the addition of FSK.

3.3.6. Study of host-pathogen infection mechanisms in human cell

We also applied time-resolved SICM to investigate the mechanisms of bacterial adhesion of mammalian host cells, a first step towards infection by many pathogens. We monitored the binding of E.coli to epithelial cells through the display of synthetic adhesins (on bacteria) that mimic a pathogenic context. These bacterial cells display anti-GFP nanobodies (VHH) and bind to GFP anchored to the plasma membrane of HeLa cells¹⁴⁷. Interestingly, we observed an increase in the GFP signal around bacteria suggesting a local accumulation of the VHH-GFP bonds that represents an increase in the overall affinity of the bacterium to the host cell membrane over time (Figure 3.5,a,b,c and Figure S3.19). In addition, time-resolved SICM revealed bacteria dividing directly on the host cell membrane, proving that the attachment to the mammalian cell does not prevent bacterial

proliferation (Figure 3.5d, Figure S3.20). Occasionally, the binding of the bacterium tightened to the point it triggered its internalization by the mammalian cell (Figure 3.5e, Figure S3.21), as confirmed also by confocal microscopy (Figure S3.22).

Complementary to fluorescence microscopy, time-resolved SICM reveals the precise topography and position of the bacteria relative to the membrane, as well as the pathogen-membrane interactions. SICM is label-free and does not suffer from phototoxicity and photobleaching that could prevent the long-term visualization of these processes with fluorescence microscopy. In contrast to AFM, SICM is a truly non-contact measurement that prevents detachment of the settled bacteria or artificially perturbs their weak interactions with the host cell body that govern infection. SICM imaging did not prevent adhesion and invasion and was able to monitor the infection process over long imaging times. Due to the non-contact nature and minimized perturbations, we will be able to investigate a broad range of infection mechanisms and internalization processes in the future.

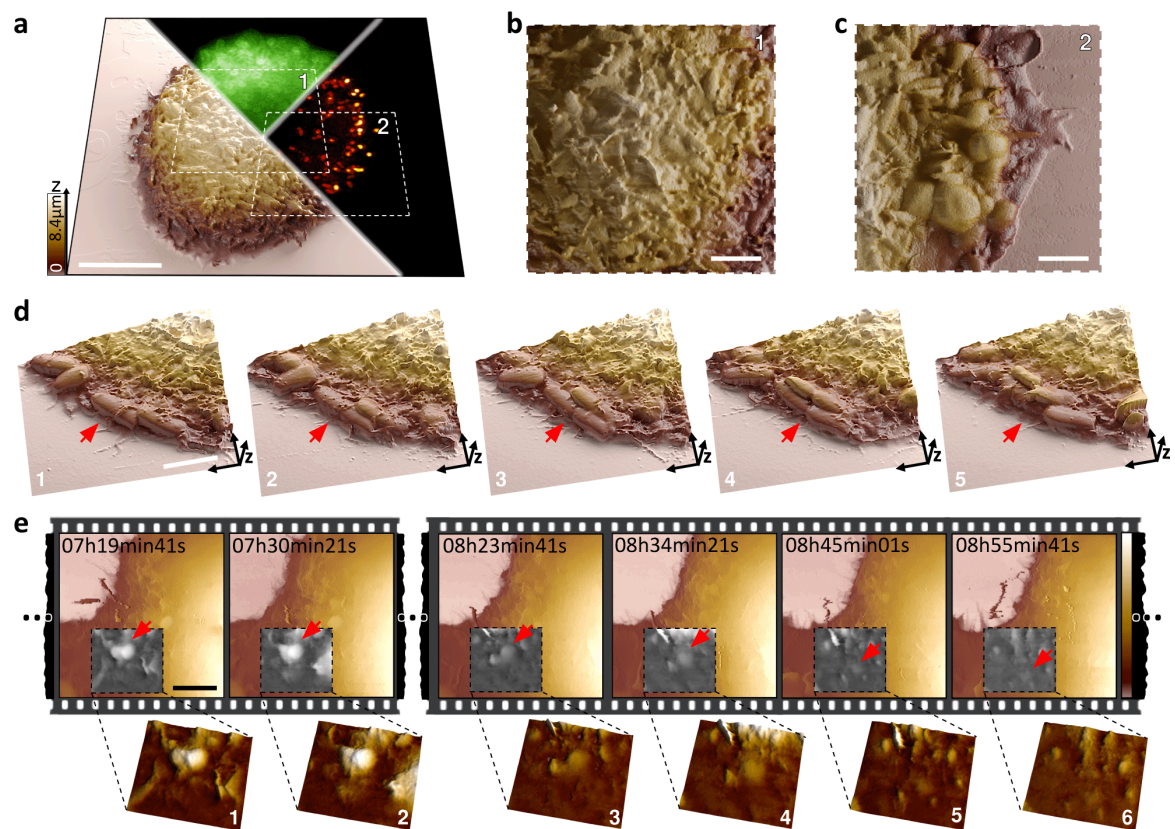


*Figure 3.5. Long-term visualization of infection mechanisms in bacterial adhesion and entry into host cells using time-resolved SICM. (a) Correlated three-dimensional representation of the live cell membrane surface with SICM. HeLa cells displaying a synthetic GFP receptor enabling its direct visualization (GFP, green channel) sequestered by its ligand: VHH expressed by *E. coli* (red channel). Scale bar, 10 μm . (b) *E. coli* can be resolved on top of the host cell body (area 1 marked in a); (c) and on the host cell edge*

(area 2 marked in a). Scale bar, 4 μm . (d) 3D visualization of bacteria infecting a mammalian cell. The red arrow points to a bacterium adhered to the cell, elongating (1-2) and dividing (3-5) on the mammalian cell membrane. Scale bar, 4 μm . (e) Live monitoring of bacteria engulfment and internalization; the red arrow points to a bacterium adhered to the host (1, 2) and being internalized (3-6). Scale bar, 4 μm .

3.4. Discussion

We have demonstrated in this work some of the benefits of time-resolved SICM for studying nanoscale processes in cell biology. However, some technological hurdles still need to be overcome for time-resolved SICM to become a routine tool in cell biology. One key requirement for good quality SICM imaging is a high-quality nanopipette with an appropriate aperture diameter for the specific application. While high-speed imaging generally benefits from a lower resistance pipette (i.e. a larger opening), high-resolution requires a small opening¹¹⁸. The resolution in SICM is determined by the pipette pore dimensions⁸⁰, with a lateral resolution of approximately three times the pore radius⁷¹. In terms of axial resolution, pipettes with pore dimensions of $\sim 15\text{nm}$ radius have been used to resolve features $\sim 5\text{nm}$ height⁷³. Obtaining reproducible and robust capillaries at small and precise diameters is still a challenge for many groups starting to use SICM. For SICM to reach its full potential, a reliable off-the-shelf source of SICM probes would be beneficial (similar to what is available for AFM cantilevers).

While time-resolved SICM can obtain unprecedented characterization of the cell shape and surface characteristics, these aspects often need to be correlated with biochemical information and changes to the internal organization of the cells. The combination of SICM with high-performance optical microscopy is a very promising area¹⁴⁸. The SICM is integrated with an inverted optical microscope (Figure S3.23) and can thus be used with many of the recently developed super-resolution microscopy techniques¹⁴⁹.

The SICM field has developed rapidly in recent years, with many additional measurement capabilities being added, such as sample stiffness⁹⁷, surface charge⁷⁴, and local pH¹¹³. Combining these developments with time-resolved SICM or high-speed SICM will provide unprecedented insights into eukaryotic membrane processes with three-dimensional nanometer detail.

3.5. Methods

3.5.1. Cell lines and cell culture

In this study, we used monkey kidney fibroblast-like cells COS-7, SKMEL human melanoma cells, B16-F1 mouse melanoma cells (ATCC), and HeLa ovarian cancer cells. COS-7 and SKMEL cells, modified to co-express dynamin-GFP and clathrin-RFP¹⁵⁰ were cultured in DMEM high glucose without phenol red medium (Gibco, Thermo Fisher Scientific), containing 10% of fetal bovine serum (Gibco, Thermo Fisher Scientific), 1% penicillin-streptomycin (Gibco, Thermo Fisher Scientific) and 4 mM L-glutamine (Gibco, Thermo Fisher Scientific). B16-F1 mouse melanoma cells were maintained in DMEM (Sigma) supplemented with 10% fetal bovine serum, 50 µg/ml gentamicin (Gibco, Thermo Fisher Scientific), and 1% GlutaMAX (Gibco, Thermo Fisher Scientific). Cells were regularly tested negative for *Mycoplasma* (SouthernBiotech 13100-01). HeLa cells were stably engineered to display a doxycycline-inducible GFP fused to a mouse CD80 transmembrane domain using standard second-generation lentivector production protocols and the plasmids pMD2G (Addgene 12259), pCMVR8.74 (Addgene 22036), and pXP340¹⁵¹ [eGFP(N105Y, E185V, Y206F)_mCD80_C-terminal into pRRLSIN.cPPT.GFP.WPRE (Addgene 12252)]. Before co-culture experiments, HeLa cells were seeded at 50,000 cells/ml on 35 mm glass dishes (Ibidi) in 400 µL Fluorobrite supplemented with 10% FBS and 1% Glutamax (Life Technologies). After 4-6 hours of attachment, the medium was renewed and supplemented with 500 ng/ml doxycycline (HiMedia) for the induction of GFP display, and with 3 µL of Deglycosylation Mix II (New England Biolab) to digest the glycocalyx and ease the access of bacteria to the cell membrane. *E. coli* K12 (BW25113), a flagellated (deltaFliCDST) and stably expressing mScarlet were retransformed with pDSG339 for tetracycline-inducible VHH anti-GFP display¹⁵². Stationary precultures of bacteria were diluted 1:3000 and induced overnight with 250 ng/ml tetracycline (Sigma) in LB.

3.5.2. Time-resolved SICM instrumentation

The time-resolved SICM setup consists of a custom-built pipette Z-actuator integrated into a controlled-atmosphere device, critical for cell viability during imaging (Figure S3.6e). The temperature is regulated with a temperature controller from THORLABS (TC200), and the percentage and flow rate of CO₂ gas infusion is regulated with a gas mixer from Life Imaging Services (The Brick). While keeping optimal cell culture conditions of 37 °C and 5 % CO₂ for several days, the high-performance Z-actuator configuration achieves a wide mechanical displacement amplification of 22 µm scanning range on the cell surface; and preserved high-speed SICM performance with the first resonance at above 13 kHz; The Z-actuator is driven by a custom made low-phase lag piezo controller¹²², and integrated with

a stepper-motor stage for sample approach. The XY-scanner used was a Piezo-Nanopositioning stage with 100 μm x-y travel range on the sample (P-733 Piezo NanoPositioner, Physik Instrumente), driven by a low-voltage piezo amplifier (E-500 Piezo Controller System, Physik Instrumente). The XY-scanner is assembled in a custom-built micro translation stage, mounted atop an inverted Olympus IX71 microscope body. Therefore the system offers correlative SICM capabilities with fluorescence microscopy¹⁴⁹. For fluorescence excitation, we used a four-color (405 nm, 488 nm 561 nm, 647 nm) pigtailed Monolithic Laser Combiner (400B, Agilent Technologies), controlled by a custom-written LabVIEW software. Images were acquired with a sCMOS camera (Photometrics, Prime 95B) and Micromanager software. The nanopipettes used as a probe in SICM were made of Borosilicate (Sutter Instrument) and quartz (Hilgenberg GmbH). They were fabricated with a CO₂ laser puller (Model P-2000, Sutter Instruments) with a radius from 60 nm to 20 nm sizes. Afterward, quartz capillaries can be shrunk to a sub-10 nanometer radius using electron beam irradiation^{127,153}. The pipette current was amplified by a transimpedance amplifier NF-SA-605F2 (100M Ω gain, NF corporation) and a 1G Ω custom-made TIA (Supplementary Note 2) for high-speed current to voltage conversion¹²⁶ (Figure 3.3a,g). A low-pass filter setting between 10-100 kHz was implemented after the pre-amplifier (Stanford SR560). A custom SICM controller (Supplementary Note 1) consisting of a data-driven scan engine^{123,154} and adaptive hopping mode was implemented in LabVIEW on a NI USB-7856R OEM R Series (National Instruments, Austin, TX, USA) in the framework of a home-built extensible high-performance scanning probe controller.

3.5.3. Time-resolved SICM measurements

The time-resolved SICM measurements were performed in the optimal culture conditions mentioned above at 37 °C and 5 % CO₂, COS-7 and SKMEL cells were seeded at 30,000 cells/ml in 35 mm glass dishes (Ibidi) for the long time-lapse experiments and 50,000 cells/ml for the high-speed measurements. For transfected SKMEL cells, the surface was coated with poly-D-lysine (Gibco, Thermo Fisher Scientific). Coverslips were washed with PBS before seeding the cells in 2 ml of DMEM medium. Prior to the experiments, the cells were grown overnight (12-16 h) at 37 °C and 5 % CO₂. In experiments using B16-F1 mouse melanoma cells, 50,000 cells/ml were seeded in 35 mm glass dishes (Ibidi) in 2ml volume of completed culture medium. After overnight culture (13-16 hours), cells were used for scanning. Forskolin (10-2073 Focus Biomolecules) was added to the cells through a perfusion system integrated with the environmental mini-chamber to a final concentration in the cell medium of 20 μM FSK. In the cell infection co-culture measurements, HeLa cell supernatant was renewed to 2 ml medium and 200 μL of stationary bacterial culture was added for 30 minutes (Figure 3.5a,b,c) and 15 minutes (Figure 3.5d), before co-culture. The samples were intensively washed 5 times with PBS. 2 ml of DMEM high glucose without phenol red medium (Gibco, Thermo Fisher Scientific) containing 10 % fetal bovine serum

(Gibco, Thermo Fisher Scientific) was added prior to imaging. In the long time-lapse experiments (Figure 3.5e), stationary bacteria (100 μ L) were added to the medium through a perfusion system integrated into the environmental mini-chamber after 1 hour of scanning. A DC voltage bias in a range of +150 to +300 mV was applied to the pipette. The current setpoint used in the hopping actuation was 99 % of the normalized current recorded (98 % for high-speed imaging). SICM image sequence in Figure 3.2c was acquired at 200 Hz hopping rate and 6 μ m hopping height, 512 \times 256 pixels. Image sequence in Figure 3.2d was acquired at 200 Hz hopping rate and 3 μ m hopping height, 256 \times 128 pixels. Image sequence in Figure 3.3a,d,e were acquired at 2.5 kHz hopping rate and 200 nm hopping height, 40 \times 25 pixels. Image sequence in Figure 3.3g was acquired at 1 kHz hopping rate and 500 nm hopping height, 100 \times 100 pixels. Image sequence in Figure 3.4a,b,g were acquired at 125 Hz hopping rate and 6 μ m hopping height, 300 \times 200 pixels. Figure 3.4c was acquired at 200 Hz hopping rate and 5 μ m hopping height, 256 \times 256 pixels. Image sequence in Figure 3.5 at 125 Hz hopping rate and 5 μ m hopping height, 512 \times 512 pixels (Figure 3.5a,b,c) and 256 \times 256 pixels (Figure 3.5d,e).

3.5.4. Data processing and analysis

SICM images were further processed using Gwyddion¹⁵⁵. Images were corrected for scanline mismatch with a median of differences row alignment and line artifacts characteristic of SPM were corrected. Afterward, a 2-pixel conservative denoise filter was applied. Images were exported with uniform pixels aspect ratios in 16 bit Portable Network Graphics format. For better visibility, the topography channel is merged with the slope channel to highlight the surface structures in all the data sets shown in panels with a video frame. In SICM images with a greyscale color map the background was flattened with a subtraction of a median level. To generate the three-dimensional shape of cells we used the advanced open-source 3D rendering tool Blender 3D for data visualization. Normalized topographical SICM data was imported as a height map and scaled in the axial direction. The corresponding SICM colormap was used as a color, projected on the topography. Videos were generated in ffmpeg format in Fiji¹⁵⁶.

3.6. Supporting information

Figure S3.1. Long-range actuator with preserved high bandwidth for wide axial scanning range on the cell surface.

Figure S3.2. Working principle of the time-resolved SICM controller.

Figure S3.3. Schematics of the time-resolved SICM setup implementation.

Figure S3.4. Schematic of the implemented multi-element pseudo-resistor (MEPR).

Figure S3.5. Custom monolithic bandwidth-extended transimpedance amplifier (BE-TIA) for high-speed current-to-voltage conversion.

Figure S3.6. Time-resolved SICM system composed of a high-performance SICM actuator integrated into an environmental chamber with temperature and CO₂ control.

Figure S3.7. Time-resolved SICM revealing dynamic protrusions on the apical cell surface.

Figure S3.8. Time-resolved SICM revealing two cells fusing in syncytium.

Figure S3.9. Time-resolved SICM revealing the appearance and disappearance of circular dorsal ruffles (CDR1).

Figure S3.10. Time-resolved SICM revealing the appearance and disappearance of two circular dorsal ruffles CDR2, CDR3.

Figure S3.11. High dynamic range of XYZ-actuation with SICM high-speed performance.

Figure S3.12. High dynamic range of XYZ-actuation with SICM high-speed performance and long time-lapse SICM capabilities.

Figure S3.13. Increased temporal resolution on detected events of interest.

Figure S3.14. Effect of Forskolin (FSK) on melanoma cells.

Figure S3.15. Time-resolved SICM imaging sequence showing dendrites outgrowth overtime by a melanoma cell treated with FSK.

Figure S3.16. Topography profiles of dendrites outgrowth on a melanoma cell protrusions after the indicated duration of FSK treatment.

Figure S3.17. Real-time effect of FSK on a melanoma cell membrane with fast SICM image acquisition.

Figure S3.18. Tracking morphological changes on melanoma cell treated with FSK with time-resolved SICM.

Figure S3.19. Fluorescence image of the bacterium affinity (*E. coli*) to the host mammalian cell membrane (HeLa), correlated with SICM topography.

Figure S3.20. Time-resolved SICM showing a HeLa cell being infected by *E. coli* bacteria.

Figure S3.21. Time-resolved SICM showing an E. coli being internalized by HeLa cell membrane over time.

Figure S3.22. Fluorescence image of an E. coli internalized by HeLa cell membrane.

Figure S3.23. Correlative fluorescence and scanning ion conductance microscopy.

Figure S3.24. Time-resolved SICM setup with an environmental control chamber for live cell imaging.

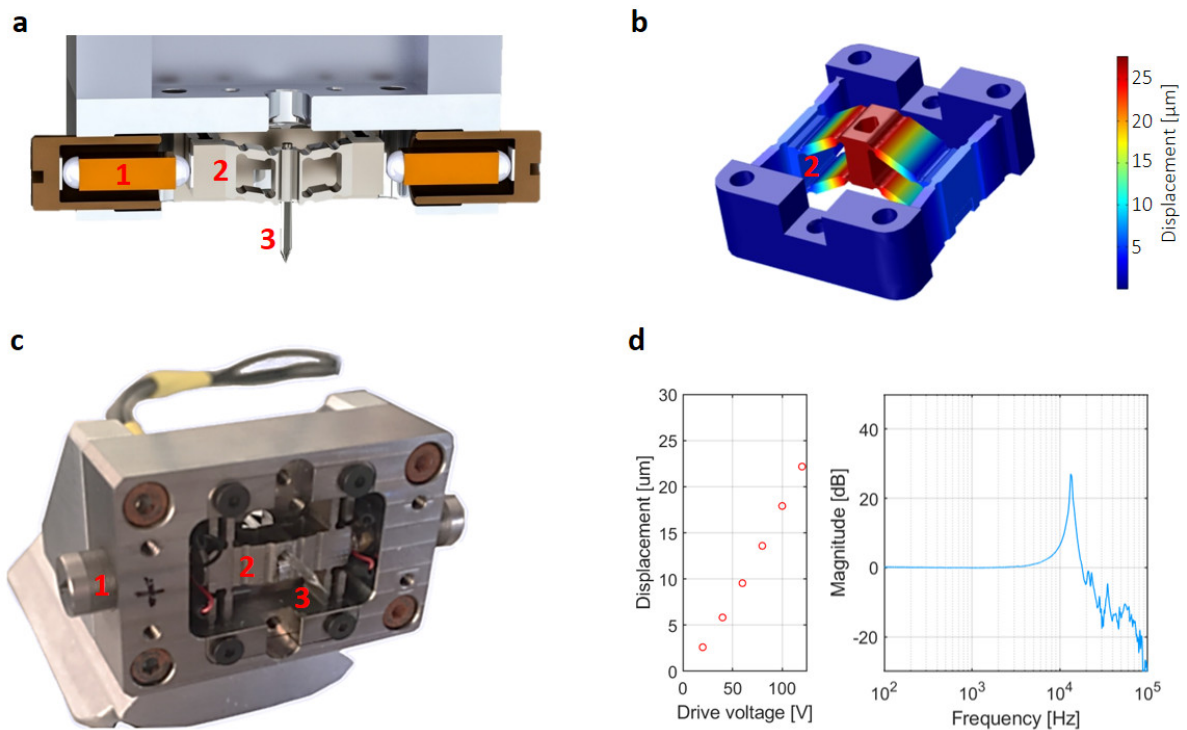


Figure S3.1. Long-range actuator with preserved high bandwidth for wide axial scanning range on the cell surface. (a) 3D rendering of a cross-section of the SICM pipette actuator. 1 shows the piezoelectric element, 2 shows the titanium flexure, and 3 the silicate nanopipette. (b) Finite element simulation of the motion of the actuator configuration allowing for a mechanical amplification with high-resonance. (c) Implementation of custom-built pipette actuator to perform cell topography imaging. (d) Mechanical displacement range of 22.17 μm for 120 V drive voltage (on the left in red). (e) and the actuator frequency response curve with the first resonance at 13.5 kHz (on the right in blue).

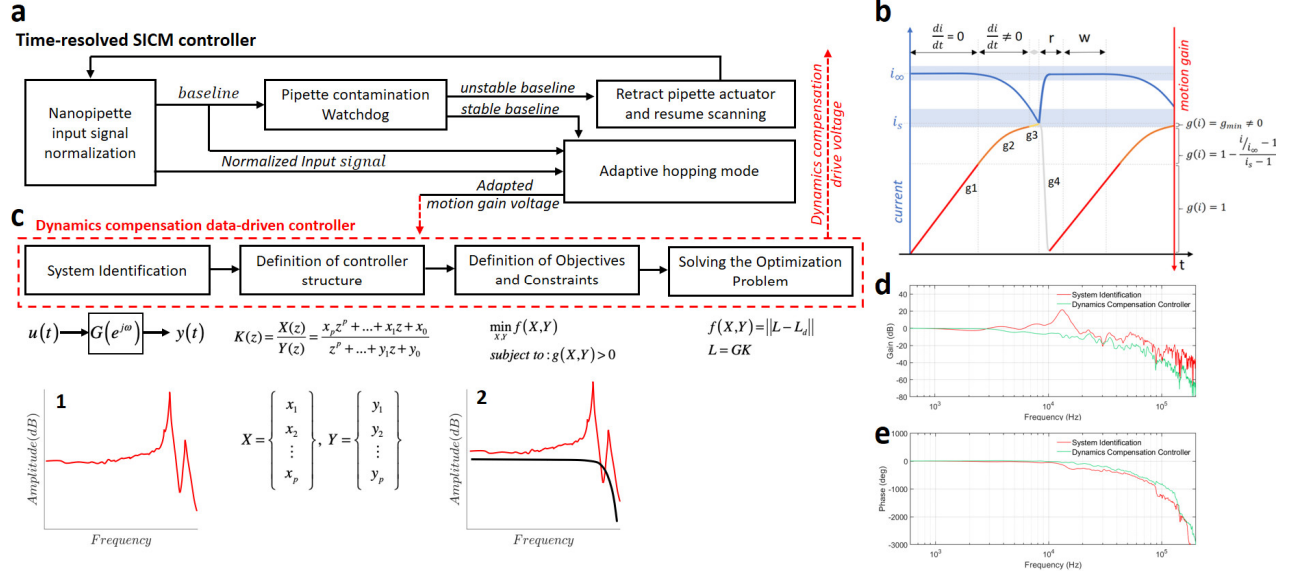


Figure S3.2. Working principle of the time-resolved SICM controller. (a) Wiring diagram of the controller highlighting the main features: Adaptive hopping mode, a data-driven controller, and a pipette contamination watchdog. (b) The principle of the adaptive hopping mode with an illustration showing the relationship between the current over time (blue) and piezo motion gain (red). The gain (g_1 and g_2) is proportional to the change in current (di/dt), converging to a minimal gain (g_3) until set point is reached, triggering the piezo retraction (g_4). The baseline is calculated by recording and averaging data over a time window size (w) after a time delay (r). (c) The data-driven controller¹²³ is composed of four steps: System identification, Definition of controller structure, Definition of objectives and constraints, and Solving the optimization problem. (d) System identification of the SICM actuator (Red) and its response after the implementation of the data-driven controller (Green). (e) Phase plot showing the system's response before (Red) and after (Green) the data-driven controller implementation.

Supplementary Note 3.1: Time-resolved SICM controller implementation.

The time-resolved SICM controller consists of three main features (Figure S3.2a): Adaptive hopping mode, a data-driven controller, and a pipette contamination watchdog. The adaptive mode is characterized by an adaptive gain applied to the piezo motion in the function of the measured current slope. The model used in the adaptive gain is described as $g(i) = 1 - \frac{i/i_{\infty} - 1}{i_s - 1}$, where i is the measured current, i_{∞} is the baseline current (current when the pipette is far from the surface), i_s is the current set point, and g_{\min} is the minimum gain (Figure S3.2b). The adaptive hopping mode is an adaptation of the closed-loop approach-retract-scanning (ARS) model¹³⁷.

The data-driven controller design consists of four main steps (Figure S3.2c). In the first step, a pseudo-random-binary-sequence signal is applied to the input ($u(t)$) of the piezo-actuator and the motion is recorded ($y(t)$). The acquired input-output data is used to

construct a non-parametric frequency response ($G(e^{j\omega})$) of the piezo-actuator which represents its dynamics (c1). Afterward, a structure is defined for the controller based on the available resources. Here, a parametric 16th-order discrete-time filter is chosen, $K(z) = \frac{X(z)}{Y(z)} = \frac{x_p z^p + \dots x_1 z + x_0}{z^p + \dots y_1 z + y_0}$; where X and Y are the parameters that shape the controller dynamics. In order to optimally select these parameters, a set of objectives ($f(X, Y)$) and constraints ($g(X, Y)$) are defined such that the combined behavior of the system (controller and actuator) satisfies our performance expectations. These optimization specifications determine the bandwidth of the system while guaranteeing its stability. For this configuration, the open-loop of the dynamics ($L = GK$) is shaped based on a desired dynamic response (L_d). In this regard, the area between the two frequency responses ($\|L - L_d\|_2$) is minimized (c2). A convex optimization method is utilized to design the controller such that it attenuates the high-amplitude dynamics of the piezo-actuator (Figure S3.2d,e). This whole design process is executed once and the selected controller parameters are used through the rest of the process to prepare the drive signal of the SICM actuator.

In addition, nanopipette pore contamination is a frequent event in long-term SICM measurements that lead to a decrease in the image quality and often breaks the glass pipette. Therefore, in order to perform long-term imaging a current signal monitoring controller (Pipette contamination watchdog in Figure S3.2a) triggers upon pipette contamination is detected and retracts the pipette from the medium. Capillaries forces successfully remove the contamination and the scanning is resumed, ensuring a long-lasting imaging performance.

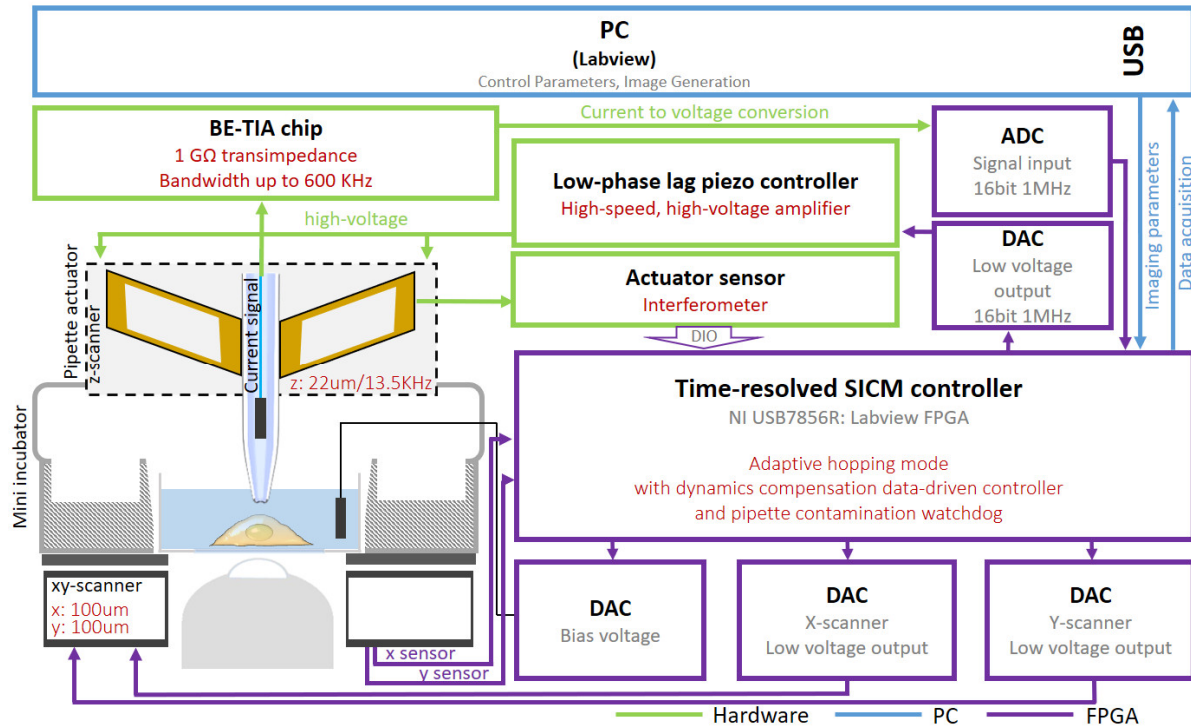


Figure S3.3. Schematics of the time-resolved SICM setup implementation. The current generated through the pipette nanopore is converted to voltage (BE-TIA) and amplified with a transimpedance of $1 \text{ G}\Omega$ used as input feedback control signal in the SICM controller (Time-resolved SICM controller). The response of the system is shaped with motion dynamics information from the interferometer (Actuator sensor), such that it attenuates the high-amplitude resonances. The piezoelectric actuators (z-scanner) are driven by a custom-made high-voltage amplifier¹²² with very low-phase lag (Low-phase lag piezo controller), ensuring a fast piezo-actuation response.

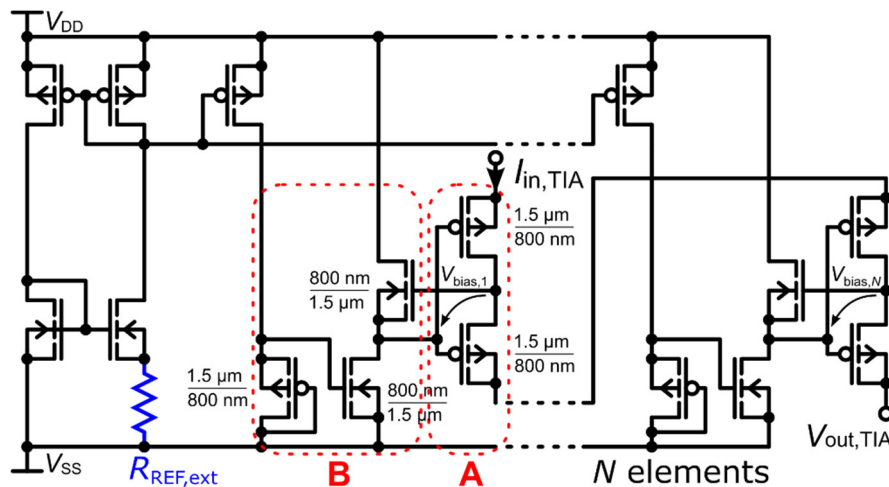


Figure S3.4. Schematic of the implemented multi-element pseudo-resistor (MEPR). I_{in} is the TIA current input, V_{out} is the TIA voltage output, and $R_{REF,ext}$ is the external reference

resistor, which sets the MEPR's large resistance value. A, p-channel MOS transistor pairs. B, Biasing circuit based on a pseudo current mirror.

Supplementary Note 3.2: Multi-element pseudo-resistor (MEPR) implementation.

The feedback resistor used in the TIA consists of p-channel MOS transistor pairs, which are biased in weak inversion and operated in the linear regime (A). Such devices are also named as pseudo-resistors due to their resistive behavior for drain-source voltages V_{DS} below the thermodynamic voltage $U_T = kT/q$, of which k is the Boltzmann constant, T the absolute temperature, and q the elementary charge. To linearize the I/V characteristic, a large number of N pseudo-resistor elements are connected in series so that V_{DS} does not exceed U_T even for the TIA's maximum output voltage. Since the pseudo-resistors in A are operated in weak inversion, they exhibit exponential dependencies on absolute temperature and threshold voltage. A specific biasing circuit (B) renders the exponential dependencies on absolute parameters to exponential dependencies on the mismatch between those parameters of the pseudo-resistors and the biasing circuit's transistors¹²⁴. The large number of elements further averages the transistor's mismatch and, hence, the resistance value is precise and robust against variations of temperature and process parameters¹²⁶. Furthermore, the biasing circuit facilitates the pseudo-resistors to be floating due to its current source, which provides the floating biasing voltage V_{bias} via the source follower. The entire device of Figure S3.4 is referred to as multi-element pseudo-resistor (MEPR)¹²⁵. The MEPR's resistor value can be tuned using an external reference resistor R_{REF} . A large tuning range from $1M\Omega$ to $1G\Omega$ has been reported¹²⁴. Moreover, it has been shown in that the MEPR features a noise floor similar to the Johnson noise of an equivalent ideal ohmic resistor¹²⁵. To minimize the noise, we have implemented the TIA with its maximum gain of $1G\Omega$.

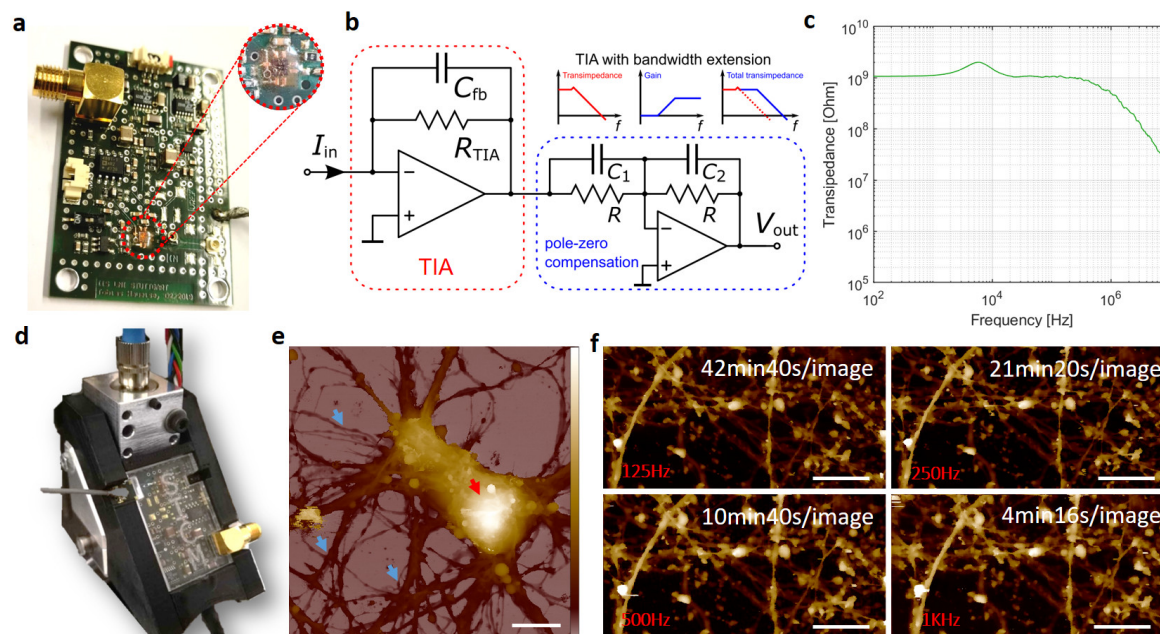


Figure S3.5. Custom monolithic bandwidth-extended transimpedance amplifier (BE-TIA) for high-speed current-to-voltage conversion. (a) Printed circuit board and a zoom-in of the BE-TIA. (b) Schematic of the TIA (red) and the succeeding pole-zero compensation circuit for bandwidth extension (blue). (c) Measured transimpedance vs. frequency of the BE-TIA. (d) Integration of the BE-TIA circuit in the SICM setup. (e) To demonstrate the performance of the system, we acquired a $60\ \mu\text{m}$ area image of a single mouse cortical neuron, fixed in 4% PFA in PBS solution. The red arrow shows the cell body and the blue arrows show the intricate network of neurites. Scale bar, $20\ \mu\text{m}$. Z scale, $0\text{--}8\ \mu\text{m}$. (f) To demonstrate the improvement in frame rate acquisition (512×256 pixels) with the integrated BE-TIA circuit, we performed SICM imaging of fixed cortical neurons. This panel shows no loss in the image quality of the neurites for higher hopping rates. Images were acquired at 125 Hz, 250 Hz, 500 Hz, and 1 kHz hopping rate ($500\ \text{nm}$ hopping height). Scale bar, $10\ \mu\text{m}$. Z scale, $0\text{--}2\ \mu\text{m}$.

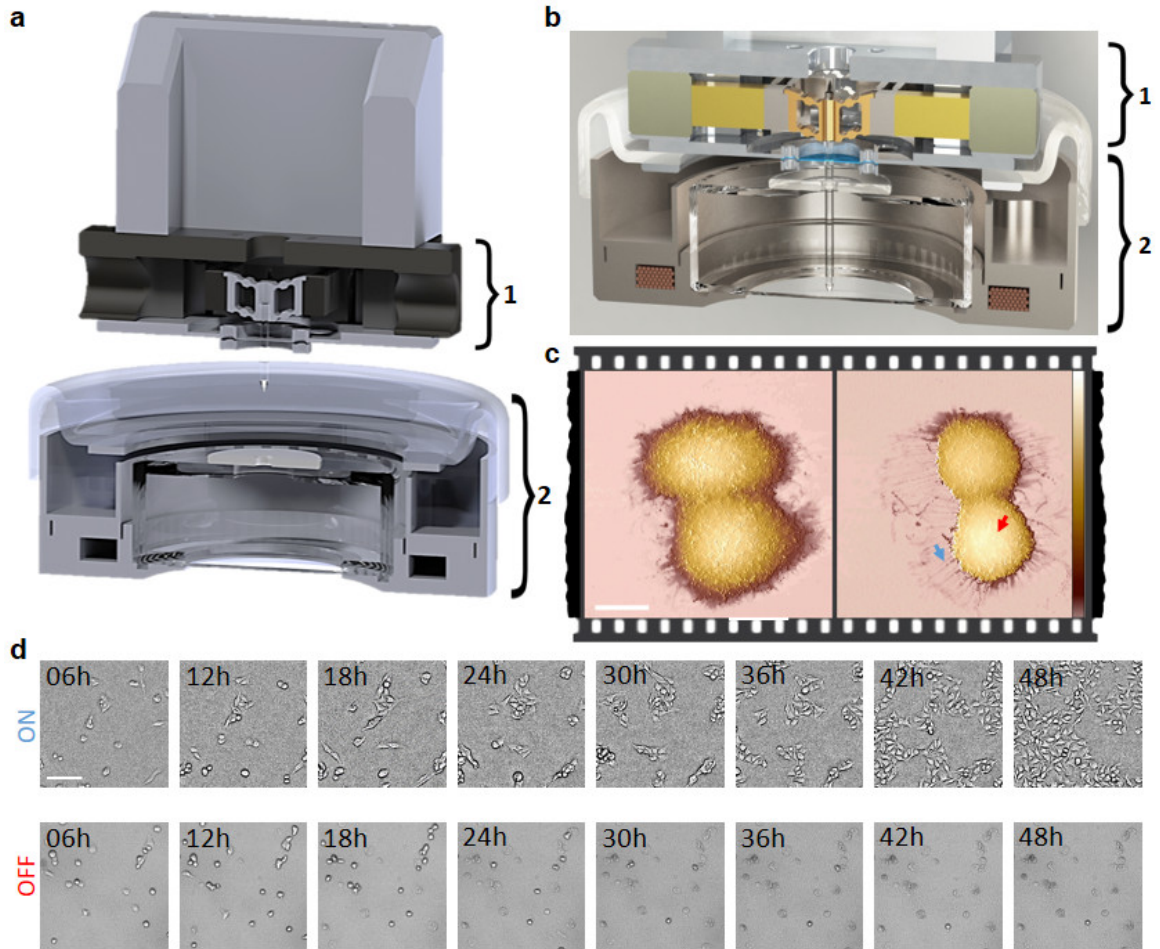


Figure S3.6. Time-resolved SICM system composed of a high-performance SICM actuator integrated into an environmental chamber with temperature and CO₂ control. (a) 3D rendering of a cross-section of the SICM actuator (1) apart from the miniature incubator (2). (b) 3D rendering of a cross-section of the enclosed SICM system (1 and 2 together). (c) Without the appropriate culture environment during the scanning, cells tend to undergo apoptosis within a few hours. This SICM topography image shows HeLa cells detaching from the surface after 6 hours without temperature and CO₂ diffusion in cell medium. The red arrow shows the cell body rounding and the blue arrow points to retracted adhesions where the cells were previously attached. Scale bar, 20 μm . Z scale, 0–12 μm . (d) Upper row: Brightfield microscopy of cell growth under conditions of a controlled atmosphere, demonstrating cell viability and proliferation over 48 hours. Bottom row: Cell growth without environmental control.

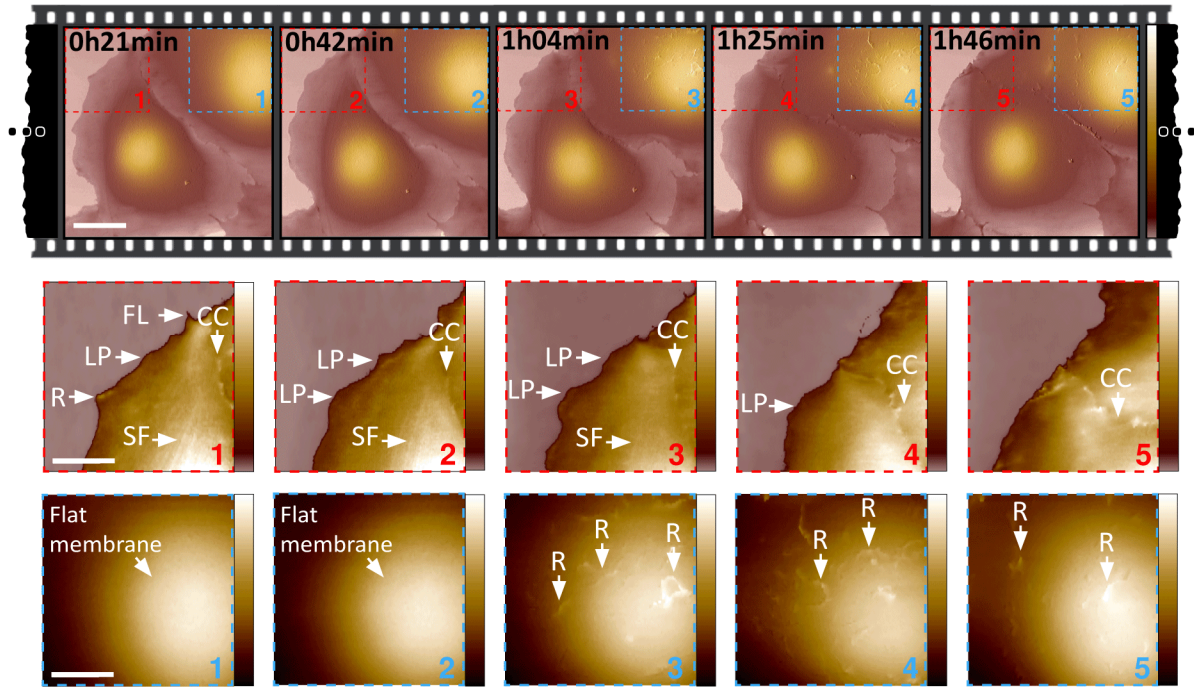


Figure S3.7. Time-resolved SICM revealing dynamic protrusions on the apical cell surface. Scale bar, 20 μm . Z scale, 0–8.5 μm . The sequence of zoom-in in red (1-5) shows motility on the cell periphery, with arrows identifying ruffles (R), lamellipodia (LP), filopodia (FL), cell-cell contact (CC), and stress fibers (SF). Scale bar, 10 μm . Z scale, 0–1.2 μm . The sequence of zoom-in in blue (1-5) shows the sudden appearance of dynamic ruffles (R) on the top of the cell membrane. Scale bar, 10 μm . Z scale, 0–5.2 μm .

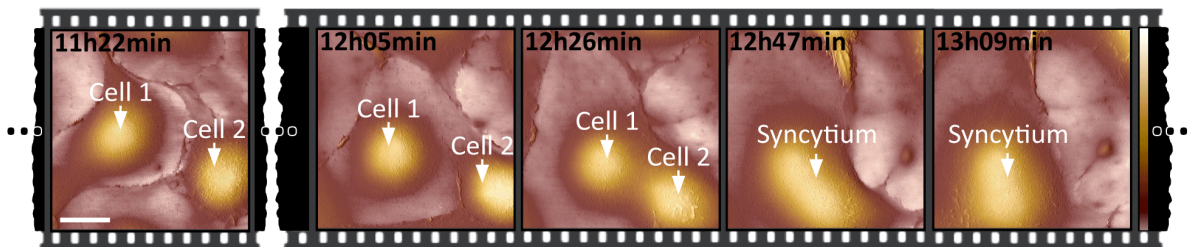


Figure S3.8. Time-resolved SICM revealing two cells fusing in syncytium. Arrows point to the top of two cells moving towards each other, fusing in syncytium. Scale bar, 20 μm . z scale, 0–7 μm .

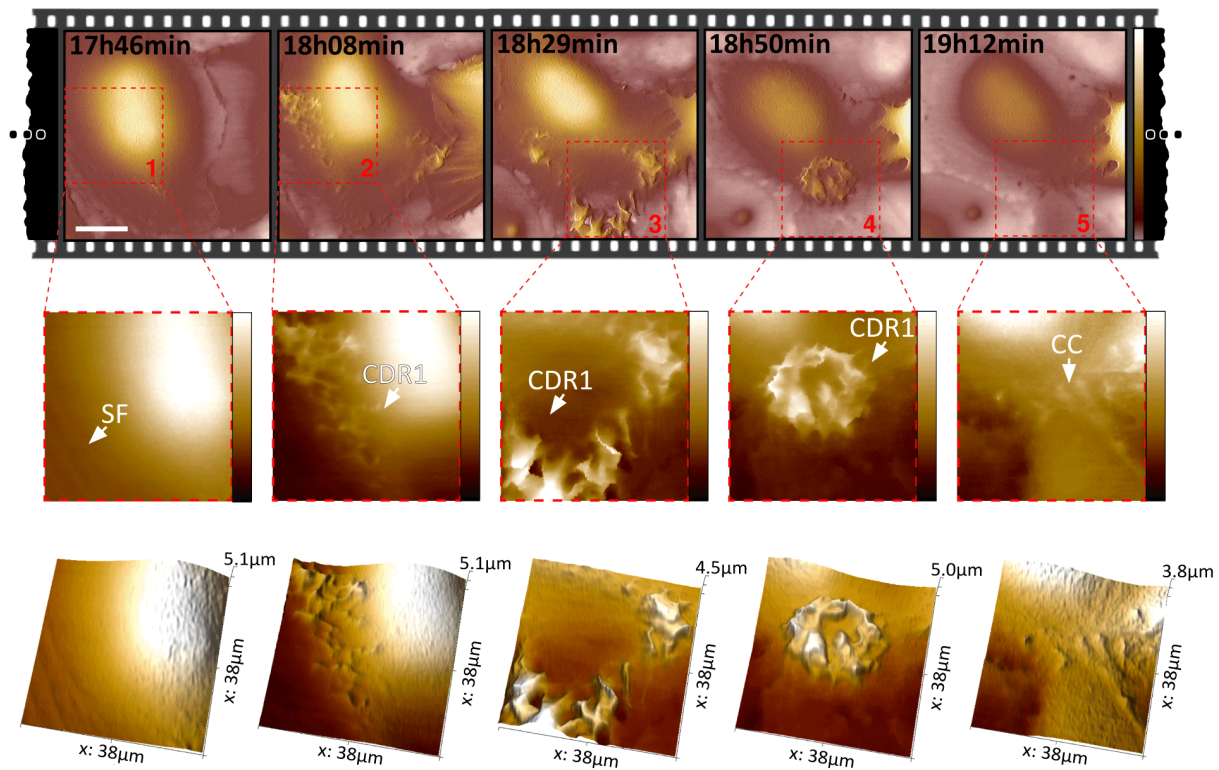


Figure S3.9. Time-resolved SICM revealing the appearance and disappearance of circular dorsal ruffles (CDR1). Scale bar, $20\ \mu\text{m}$. Z scale, $0\text{--}7\ \mu\text{m}$. The sequence of zoom-in in red (1-5) shows the sudden formation of a CDR. Z scale, $0\text{--}5\ \mu\text{m}$, $0\text{--}5\ \mu\text{m}$, $0\text{--}4\ \mu\text{m}$, $0\text{--}5\ \mu\text{m}$, $0\text{--}3\ \mu\text{m}$. Three-dimensional view of the sequence on the bottom.

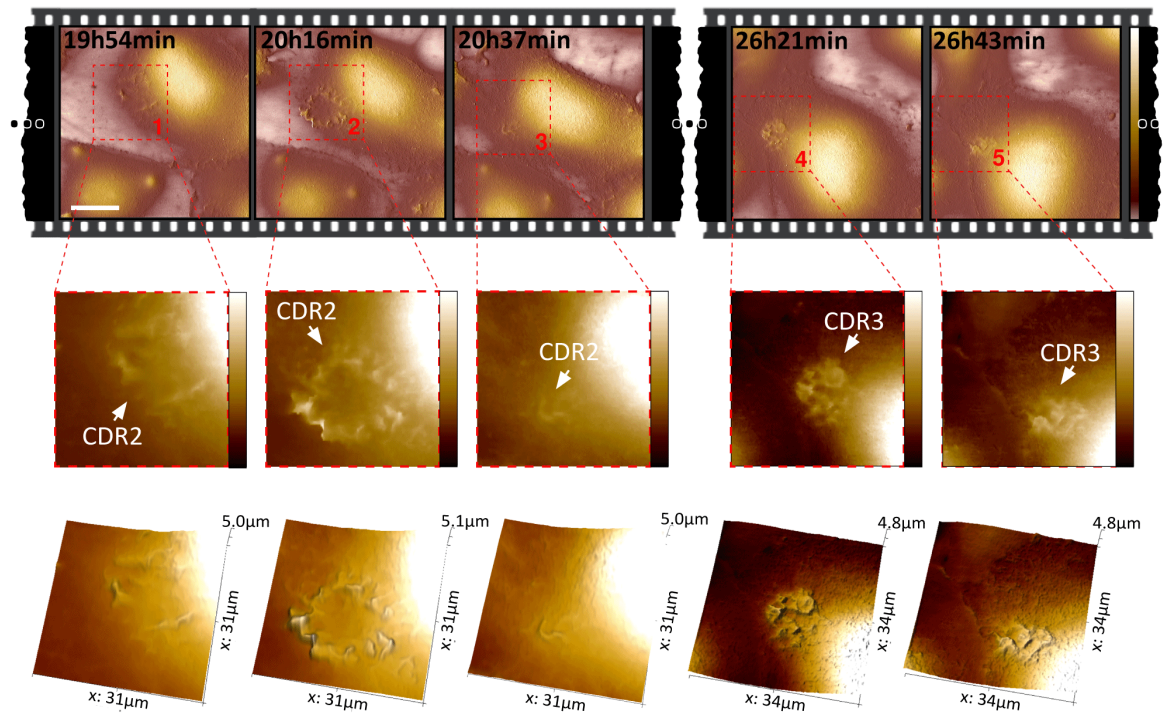


Figure S3.10. Time-resolved SICM revealing the appearance and disappearance of two circular dorsal ruffles CDR2, CDR3. Scale bar, 20 μm . Z scale, 0–7 μm . The sequence of zoom-in in red shows the sudden formation of two CDRs, CDR2 (1-3) and CDR3 (4-5). Z scale, -1–4 μm and 0–4 μm for 1-3 and 4-5 respectively. Three-dimensional view of the sequence on the bottom.

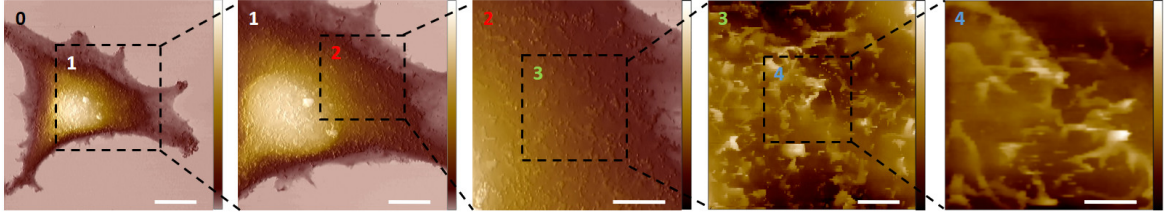


Figure S3.11. High dynamic range of XYZ-actuation with SICM high-speed performance. The first image shows the topography of an entire melanoma cell body on an area of 100 μm width. Acquired at 125 Hz hopping rate and 5 μm hopping height, 512 \times 256 pixels. Z scale, 0-12 μm . Scale bar, 20 μm . 1: Topography image on a smaller area of 50 μm width. Acquired at 200 Hz hopping rate and 3 μm hopping height, 512 \times 256 pixels. Scale bar, 10 μm . Z scale, 0-12 μm . 2: Topography image on a smaller area of 20 μm width. Acquired at 285 Hz hopping rate and 2 μm hopping height, 256 \times 128 pixels. Scale bar, 5 μm . Z scale, 0-10 μm . 3: Topography image on a smaller area of 10 μm width. Acquired at 500 Hz hopping rate and 1 μm hopping height, 256 \times 128 pixels. Scale bar, 2 μm . Z scale, 0-1.5 μm . 4: Topography image on a smaller area at 10 s/image. From a sequence of images acquired at 1 kHz hopping rate and 800 nm hopping height, 100 \times 100 pixels. Scale bar, 1 μm . Z scale, 0-1.2 μm . For better visualization, images 0-2 were merged with the slope, and 3-4 were leveled by a mean plane subtraction.

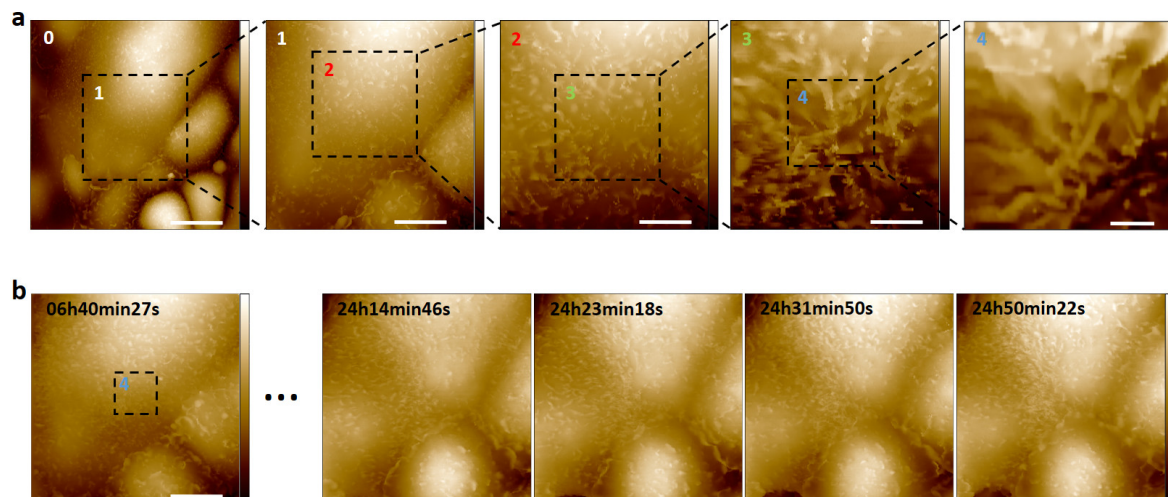


Figure S3.12. High dynamic range of XYZ-actuation with SICM high-speed performance and long time-lapse SICM capabilities. (a) The first image shows the topography of kidney cells on an area of $80\ \mu\text{m}$ width. Acquired at 200 Hz hopping rate and $3\ \mu\text{m}$ hopping height, 512×256 pixels. Scale bar, $20\ \mu\text{m}$. Z scale, $0\text{-}7.5\ \mu\text{m}$. 1: Topography image on a smaller area of $40\ \mu\text{m}$ width. Acquired at 250 Hz hopping rate and $2.5\ \mu\text{m}$ hopping height, 512×256 pixels. Scale bar, $10\ \mu\text{m}$. Z scale, $0\text{-}7\ \mu\text{m}$. 2: Topography image on a smaller area of $20\ \mu\text{m}$ width. Acquired at 285 Hz hopping rate and $2\ \mu\text{m}$ hopping height, 256×128 pixels. Scale bar, $5\ \mu\text{m}$. Z scale, $0\text{-}4.5\ \mu\text{m}$. 3: Topography image on a smaller area of $10\ \mu\text{m}$ width. Acquired at 500 Hz hopping rate and $1\ \mu\text{m}$ hopping height, 256×128 pixels. Scale bar, $2.5\ \mu\text{m}$. Z scale, $0\text{-}2.5\ \mu\text{m}$. 4: Topography image on a smaller area. From a sequence of images acquired at 670 Hz hopping rate and $800\ \text{nm}$ hopping height, 128×64 pixels. Scale bar, $1\ \mu\text{m}$. Z scale, $0\text{-}2\ \mu\text{m}$. (b) Zoom-out scanning from a4 followed by a 24 hours time-lapse sequence. Acquired at 250 Hz hopping rate and $2.5\ \mu\text{m}$ hopping height, 512×256 pixels. Scale bar, $10\ \mu\text{m}$. Z scale, $0\text{-}7\ \mu\text{m}$ for the frame at 06h 40min 27s and $0\text{-}5.5\ \mu\text{m}$ for the four frames after 24 hours.

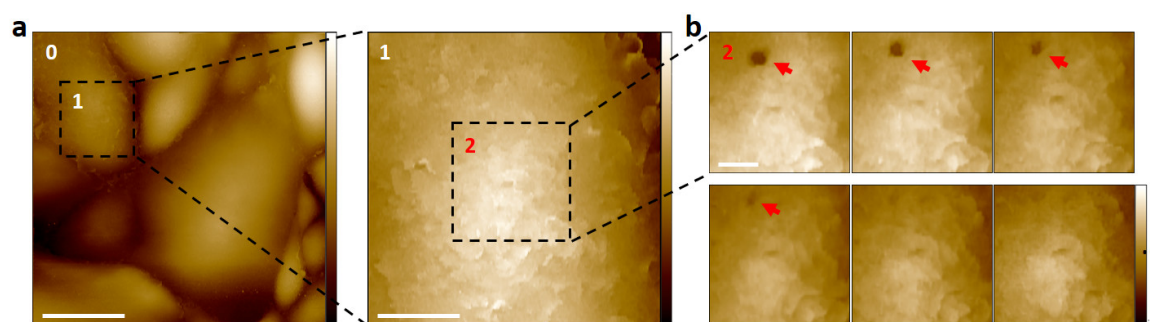


Figure S3.13. Increased temporal resolution on detected events of interest. (a) The first image shows the topography of kidney cells on a large area. Acquired at 125 Hz hopping rate and $5\ \mu\text{m}$ hopping height, 512×256 pixels. Scale bar, $16\ \mu\text{m}$. Z scale, $0\text{-}10\ \mu\text{m}$. 1: Topography image on a smaller area, marked in 0. Acquired at 250 Hz hopping rate and $2\ \mu\text{m}$ hopping height, 256×128 pixels. Scale bar, $4\ \mu\text{m}$. Z scale, $0\text{-}5\ \mu\text{m}$. (b) By decreasing the scanning area and focusing on detected events of interest (area marked in 1), we can increase the temporal resolution. Processes such as endocytosis can be visualized on kidney cells (Red arrow). Acquired at 285 Hz hopping rate and $2\ \mu\text{m}$ hopping height, 128×64 pixels. Scale bar, $2\ \mu\text{m}$. Z scale, $0\text{-}3\ \mu\text{m}$.

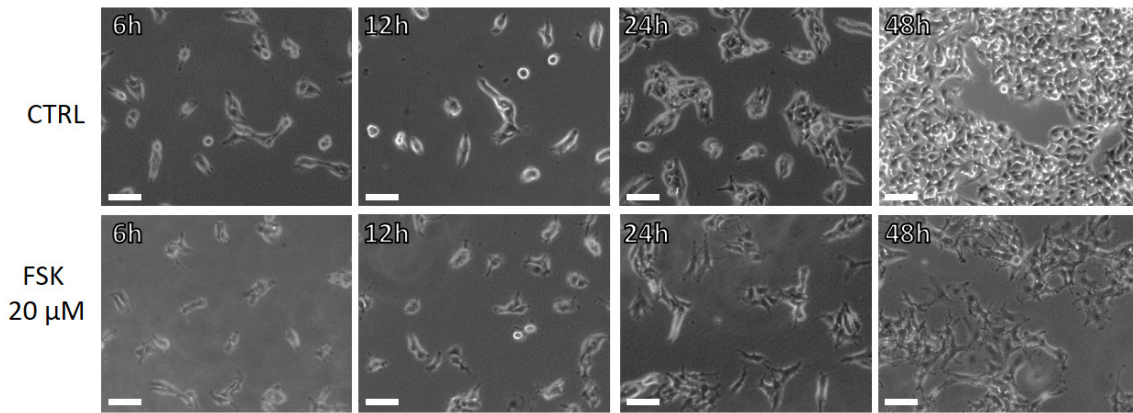


Figure S3.14. Effect of Forskolin (FSK) on melanoma cells. 50'000 cells were seeded on a glass-bottom petri-dish followed by an attachment period of 6 hours. Then cells were treated with 20 μM FSK (Bottom panel) and compared with the control (Top panel). Image show cells at 6, 12, 24, and 48 hours after cell seeding imaged with a phase-contrast microscope. Scale bar, 200 μm .

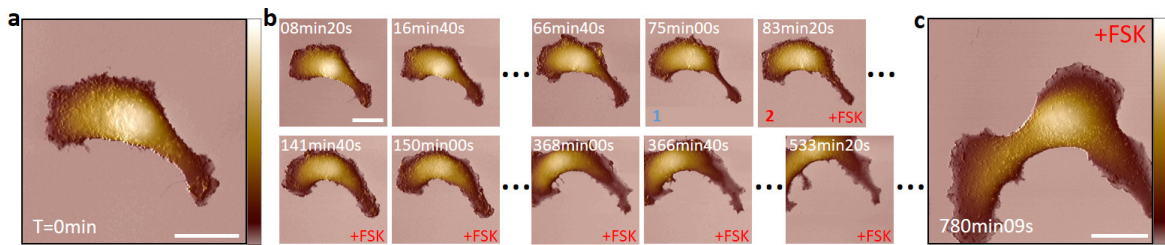


Figure S3.15. Time-resolved SICM imaging sequence showing dendrites outgrowth overtime by a melanoma cell treated with FSK. (a) The first image of the sequence before FSK treatment. Scale bar, 10 μm . Z scale, 0–9 μm . (b) Several time points of the sequence over 780 minutes showing the effect of 20 μM FSK (final concentration in the medium) on a single dendrite (1) before and (2) after treatment. (c) The last image of the sequence after 780 minutes highlighting morphological changes induced by FSK treatment, characterized by an increase in the width of the dendrite. Acquired at 125 Hz hopping rate and 6 μm hopping height, 300 \times 200 pixels. Scale bar, 10 μm . Z scale, 0–9 μm .

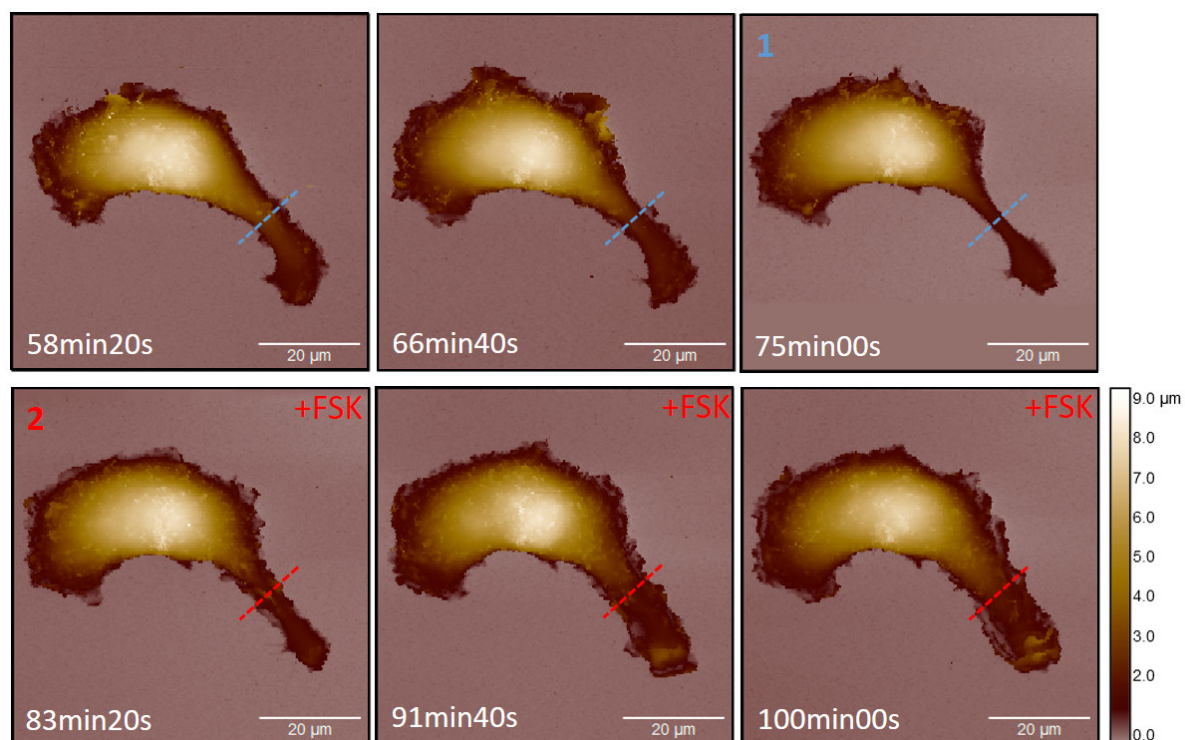


Figure S3.16. Topography profiles of dendrites outgrowth on a melanoma cell protrusions after the indicated duration of FSK treatment. Height profile of the dendrite (Figure 3.4e) over a time sequence. 1 shows a cell dendrite before treatment and 2 after adding 20 μM FSK.

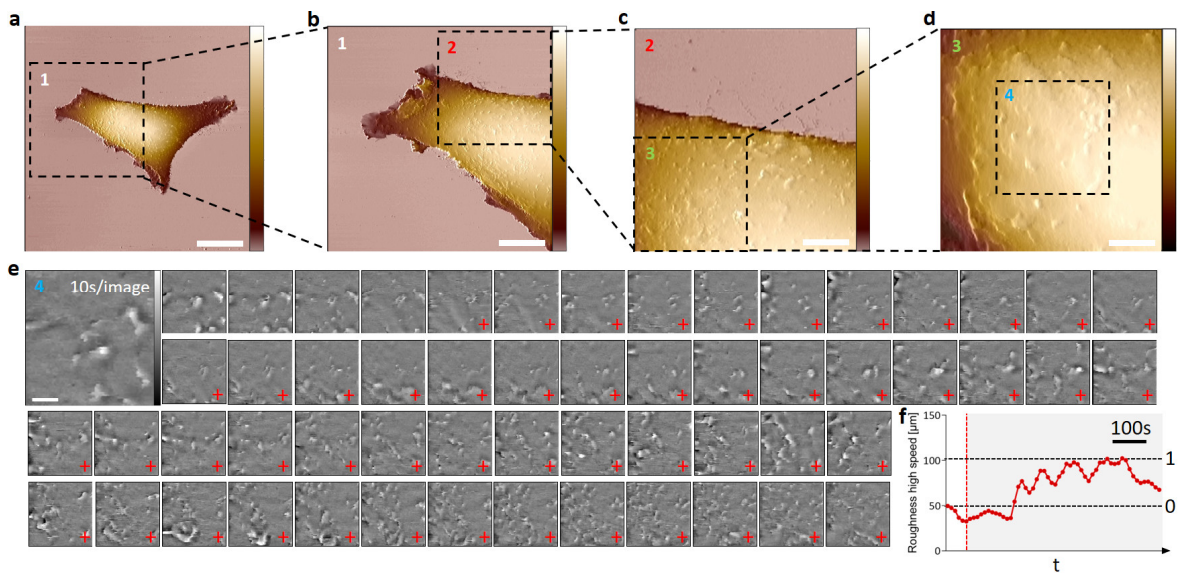


Figure S3.17. Real-time effect of FSK on a melanoma cell membrane with fast SICM image acquisition. (a) Topography image of a melanoma cell on an area of $100\ \mu\text{m}$. Acquired at $125\ \text{Hz}$ hopping rate and $5\ \mu\text{m}$ hopping height, 512×256 pixels. Scale bar, $20\ \mu\text{m}$. Z scale, $0\text{-}11\ \mu\text{m}$. (b) Topography image of the area 1 marked in a. Acquired at $200\ \text{Hz}$ hopping rate and $3\ \mu\text{m}$ hopping height, 512×256 pixels. Scale bar, $10\ \mu\text{m}$. Z scale, $0\text{-}9\ \mu\text{m}$. (c) Topography image of the area 2 marked in b. Acquired at $285\ \text{Hz}$ hopping rate and $2\ \mu\text{m}$ hopping height, 256×128 pixels. Scale bar, $5\ \mu\text{m}$. Z scale, $0\text{-}8\ \mu\text{m}$. (d) Topography image of the area 3 marked in c. Acquired at $500\ \text{Hz}$ hopping rate and $1\ \mu\text{m}$ hopping height, 256×128 pixels. Scale bar, $2.5\ \mu\text{m}$. Z scale, $0\text{-}6\ \mu\text{m}$. (e) Real-time effect of FSK (+) on the melanoma cell membrane of the area 4 marked in d at $10\ \text{s}/\text{image}$. From a sequence of images acquired at $1\ \text{kHz}$ hopping rate and $500\ \text{nm}$ hopping height, 100×100 pixels. Scale bar, $1\ \mu\text{m}$. Z scale, -300 to $+300\ \text{nm}$. For better visualization and quantification, the images were flattened and fixed to median zero, followed by a 2-pixel conservative denoise filter. (f) Plot of the surface roughness as a measure to quantify protrusion activity on the cell membrane over time after adding $20\ \mu\text{M}$ FSK (red dashed line). (0) Max roughness before FSK treatment at the beginning as a baseline. (1) Maximal roughness level after FSK treatment. Roughness is defined as the root mean square of height irregularities, computed from 2nd central moment of data values.

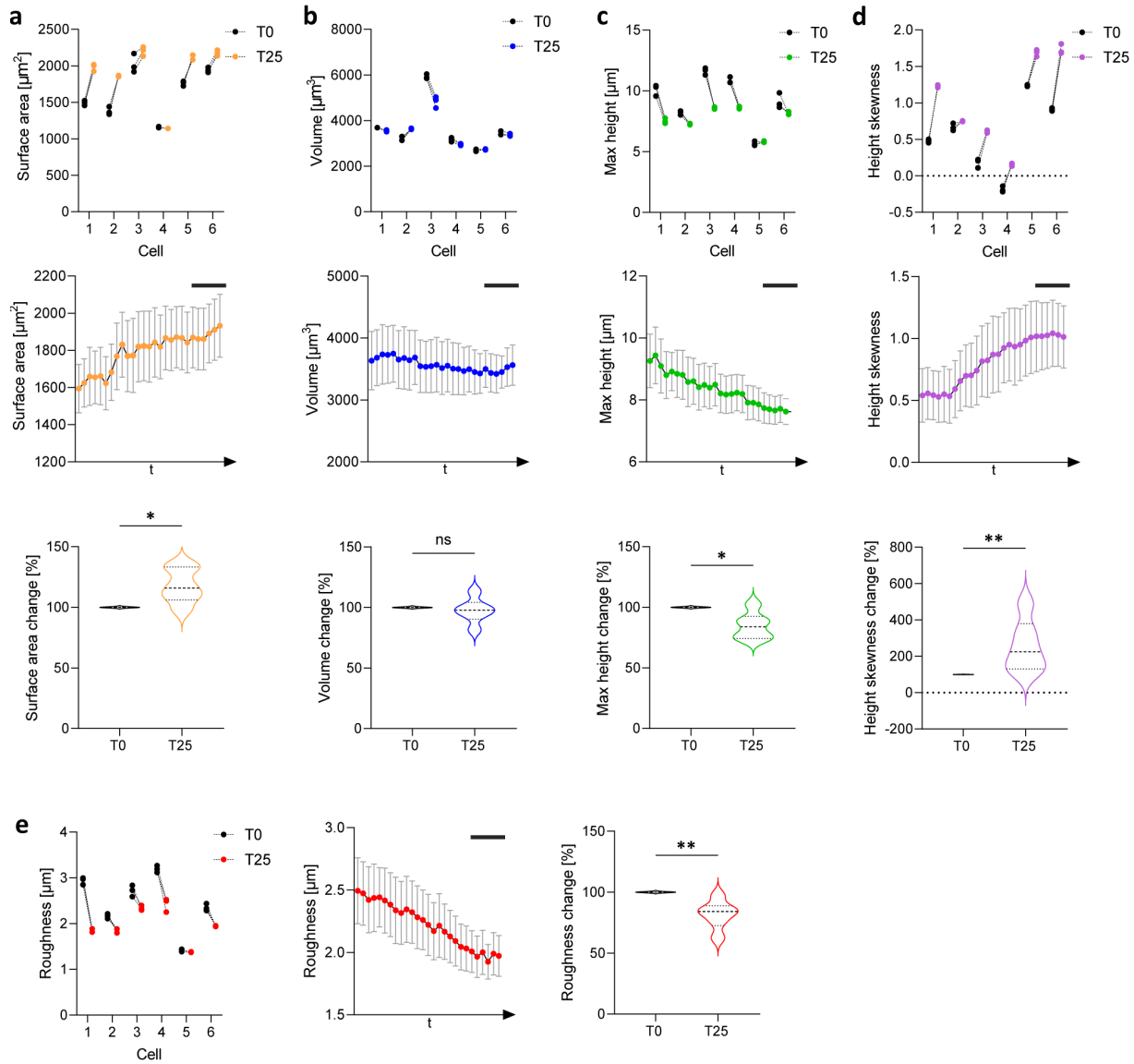


Figure S3.18. Tracking morphological changes on melanoma cell treated with FSK with time-resolved SICM. (a) Change in surface area; (b) volume change; (c) max height change; (d) Height skewness change; and (e) roughness change. Each parameter was measured in 6 different cells. First graph shows measured value in the first three frames of scanning (T0), related to the values measured at frames 25-27 of the same cell (T25). Graph below shows the change in the measurement over time. Violin plots represent percentage of the parameter change at T25 relative to T0. Error bars represent SEM, $n=6$. * $P < 0.05$, ** $P < 0.01$. Data compared using two-tailed Mann-Whitney test. Scale bar 50 minutes. The surface area is computed by triangulation of neighboring pixels and the volume is calculated as the integral of the surface height over the covered area. Height skewness is computed from the third central moment of data values.

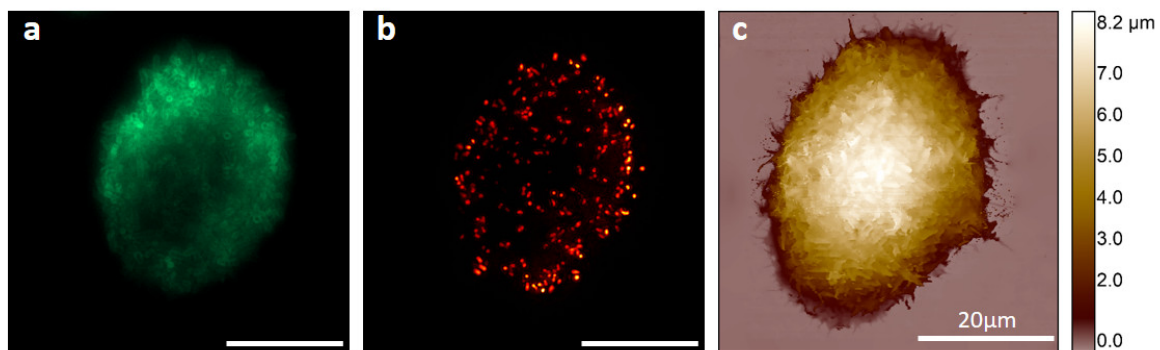


Figure S3.19. Fluorescence image of the bacterium affinity (*E. coli*) to the host mammalian cell membrane (HeLa), correlated with SICM topography. (a) *cd80* based GFP display in HeLa cells for direct visualization of the ligand (GFP) sequestered by VHH-intimin expressed by *E. coli* K12. Scale bar, 10 μm. (b) Visualization of *E. coli* K12 expressing *mScarlet* in the cytosol. Scale bar, 10 μm. (c) Three-dimensional representation of the live cell membrane surface with SICM. Acquired at 125 Hz hopping rate and 5 μm hopping height, 512 × 512 pixels.

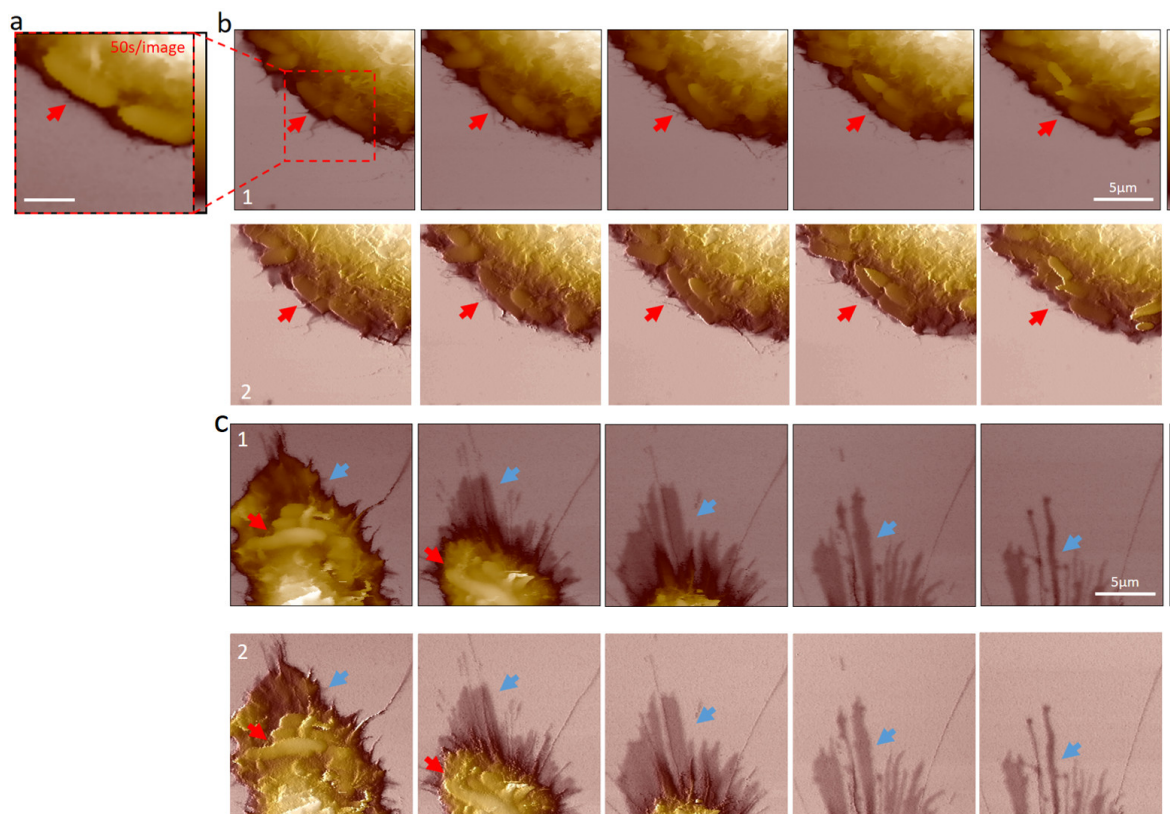


Figure S3.20. Time-resolved SICM showing a HeLa cell being infected by *E. coli* bacteria. (a) Topography image resolving *E. coli* dividing on the host HeLa cell membrane on a small area of $7.5 \mu\text{m}$. Acquired at 250 Hz hopping rate and $2 \mu\text{m}$ hopping height, 100×100 pixels. Scale bar, $2 \mu\text{m}$. Z scale, $0\text{--}3.2 \mu\text{m}$. (b) Topography of *E. coli* on a $15 \mu\text{m}$ area adhering and proliferating on the host cell membrane periphery (1). Red arrows point to the bacteria dividing on the membrane. Acquired at 125 Hz hopping rate and $4 \mu\text{m}$ hopping height, 256×256 pixels. Scale bar, $5 \mu\text{m}$. Z scale, $0\text{--}6 \mu\text{m}$. (c) Topography of *E. coli* adhered on the host cell membrane dendrite (1). Red arrows point to bacteria on the membrane and blue arrows point to the dendrite retracting. Acquired at 125 Hz hopping rate and $4 \mu\text{m}$ hopping height, 256×256 pixels. For better visualization, the topography channel was merged with the slope channel to enhance the surface edges (2). Scale bar, $5 \mu\text{m}$. Z scale, $0\text{--}3 \mu\text{m}$.

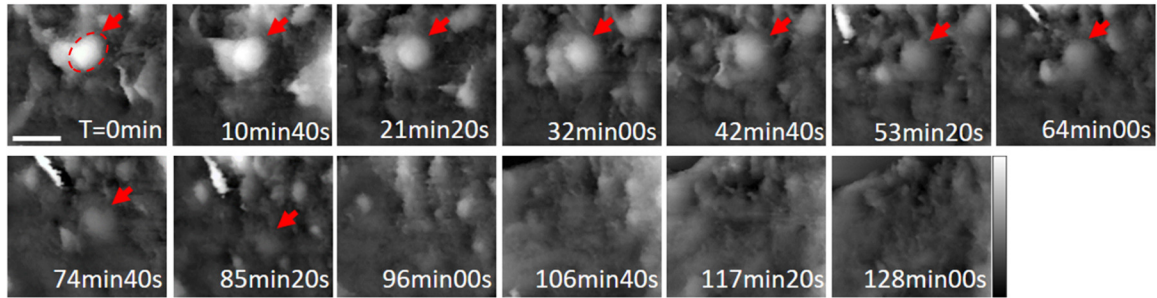


Figure S3.21. Time-resolved SICM showing an *E. coli* being internalized by HeLa cell membrane over time. Arrows point to a bacterium being internalized over 85 minutes. Zoom-in cut on an area from the long time-lapse shown in Figure 3.5e. Acquired at 125Hz hopping rate and 4 μm hopping height, 256 \times 256 pixels. For better visualization, the membrane surface was flattened. Scale bar, 2 μm . Z scale, 0-1.1 μm .

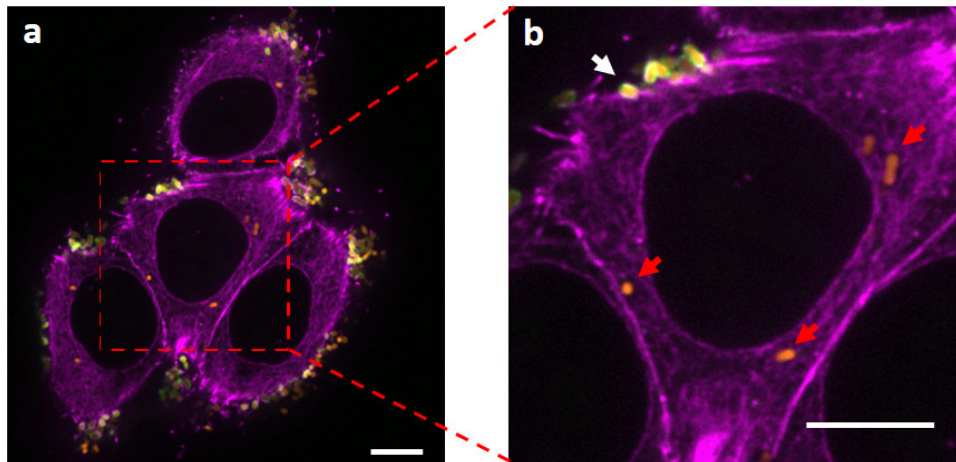


Figure S3.22. Fluorescence image of an *E. coli* internalized by HeLa cell membrane. (a) Infected cell showing bacteria adhered on the membrane and locally accumulating GFP signal (cd80 based GFP display). Cells were fixed in 4% paraformaldehyde for 20 minutes, permeabilized with 0.1% Triton X-100 for 5 minutes, and washed twice with PBS. Phalloidin-Atto 655 (Sigma) was used to stain actin at 500 nM for 15 minutes (purple). Data collected with a spinning disk confocal microscope and 100x oil immersion objective. Scale bar, 10 μm . (b) Zoom in on an area showing bacteria that were internalized and lost the GFP signal (red arrows), potentially due to lysosomal pH. The white arrow shows bacteria that were not internalized and kept the GFP signal. Scale bar, 10 μm .

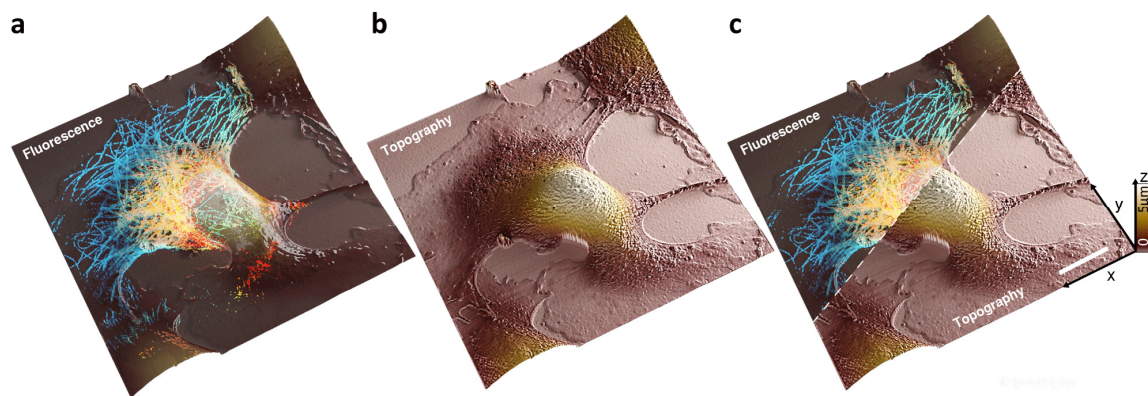


Figure S3.23. Correlative fluorescence and scanning ion conductance microscopy. (a) Fluorescence image of microtubules. (b) SICM topography image of the cell membrane. (c) Correlative fluorescence/topography image of a mammalian cell (COS7). Scale bar, 10 μm .

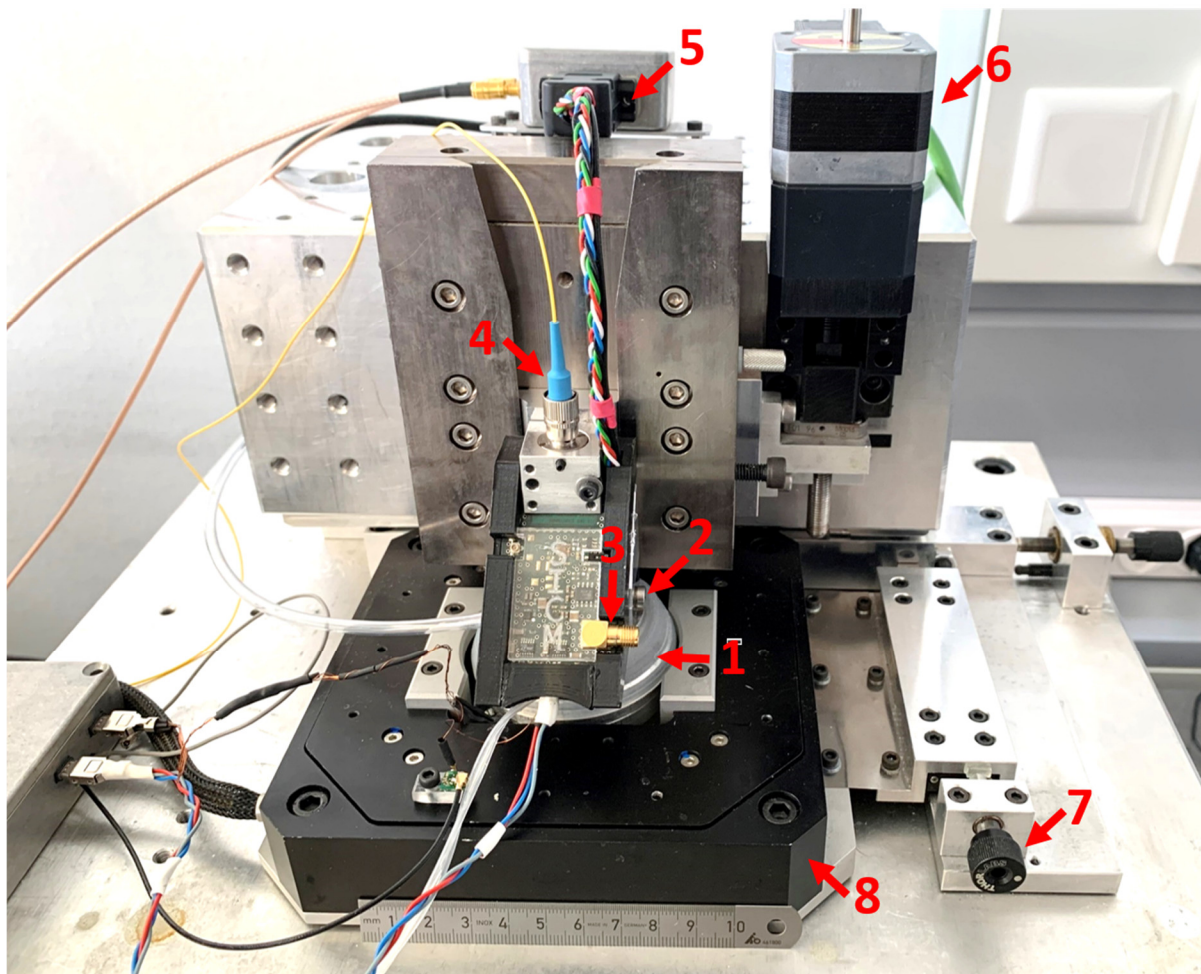


Figure S3.24. Time-resolved SICM setup with an environmental control chamber for live cell imaging. 1) Mini-incubator for environmental control; 2) High-performance Z scanner; 3) BE-TIA output; 4) Optical fiber (interferometer); 5) Z scanner drive-voltage; 6) Stepper motor for axial positioning; 7) XY translation stage; 8) XY scanner. Detailed information about the high-performance Z scanner is in Figure S3.2.

Chapter 4

Combined Fluorescence Microscopy with SICM

4.1. Introduction to combined fluorescence microscopy with SICM

Optical fluorescence microscopy is a powerful tool in cell biology, enabling researchers to gain valuable insights into various biomolecular processes occurring within cells, such as intracellular transport¹⁵⁷, organelle dynamics¹⁵⁸, and gene expression¹⁵⁹. It utilizes fluorescence-labeled molecules that emit photons in response to excitation by a light source. The emitted photons from the fluorescent tags are then captured and detected by highly sensitive cameras, generating detailed images of the biomolecules. By visualizing and analyzing these images, researchers can decipher biomolecules' spatial distribution and dynamics within the cellular environment.

To study molecular activity involved in cell membrane processes, researchers have used SICM in combination with fluorescence microscopy. For example, Korchev and coworkers used SICM to study the topography and shape of endocytosis pits over time sequences, co-localizing them with the presence of clathrin and caveolae proteins in fluorescence¹⁶⁰. Novak et al. imaged nanoparticle uptake in lung cells, involving protrusion processes imaged by SICM, co-localizing actin with fluorescence microscopy¹²⁰. Recently, Shevchuk and coworkers used SICM and fluorescence to show that the kinetics of virus-like particle assembly can vary on different plasma membrane domains¹¹⁵.

Although conventional fluorescence microscopy enables detecting the presence of specific proteins in a region of a cell membrane, the diffraction limit of light prevents resolving molecular arrangements involved in critical cellular processes, such as cytoskeleton rearrangement of actin mesh during viral or bacterial infection (as they can be as small as 3.5 nm). The diffraction limit of light was described by Ernst Abbe in 1873. Accordingly to Abbe's principle, the minimum resolvable distance between two points (d) is determined by the wavelength of light (λ) and the numerical aperture of the optical system (NA) as $d = \lambda / 2NA$. Therefore, the lateral resolution in a typical fluorescence microscopy experiment is limited to 200-300 nm laterally and 500-700 nm axially, depending on the wavelength, for the highest oil immersion objectives (~1.4 - 1.5 NA).

To overcome the light diffraction limit of light, Super-resolution (SR) microscopy techniques have been created. SR techniques utilize intricate optical designs, fluorophore properties, or computational algorithms to achieve higher resolution and retrieve finer subcellular details¹⁶¹. Among SR fluorescence techniques, localization microscopy is a

valuable tool for live cell imaging, exploiting the temporal separation of overlapped blinking fluorophores signals tagged to the molecule of interest. By activating a small fraction of molecules within a field of view, the positions of non-overlapping emitters can be computationally estimated with precision beyond the diffraction limit. After image reconstruction, the result is a high-resolution image (~10-20 nm lateral resolution) of molecular structures, such as microtubule networks (Figure 1.10b)¹⁶².

SR allows the visualization of specific proteins performing their function in relevant biological processes with sub-diffraction resolution. To go beyond the diffraction limit of light, Happel and coworkers combined SICM with a super-resolution fluorescence (SR) modality called stimulated emission depletion (STED)¹⁴⁸. This combination of SICM/STED was used to visualize cell morphology and tubulin network with a STED lateral resolution of 75 nm. However, in this approach limited to fixed cells, phototoxic effects prevent the study of many mechanisms occurring in living cells. Moreover, the 2D data lacks a spatial relationship to the global cell structure at the nanometer scale.

4.2. Thesis approach to combined SICM with SR fluorescence microscopy

Our approach to combining SICM with SR fluorescence microscopy is to integrate a SR method that yields less phototoxic effects and provides 3D information during combined imaging. Therefore, we found localization microscopy with the stochastic optical fluctuation imaging (SOFI) approach as the ideal method. The computational SOFI method and the fluorophores are optimized to perform 3D imaging with mitigated phototoxic effects, requiring low laser intensity and acquisition time. While SOFI provides the visualization of the cytoskeleton protein architecture, TR-SICM provides structural information about cell membrane morphology such as microvilli and filopodia. The integration of the combined system is addressed as follows:

- Custom-made 3D SOFI system for SR imaging with lower phototoxicity. SOFI is a computational imaging method that reduces acquisition times and phototoxic effects in live cell imaging¹⁶³. SOFI is applied to samples with high-fluorophore density and requires low-illumination power, yielding high-resolution images from statistical analysis of spatiotemporal fluctuations in blinking fluorophores. SOFI is computed from the spatiotemporal cross-cumulants of a sequence of blinking fluorophores in XYZ directions, generating virtual pixels and planes that yield high-resolution images in all three dimensions¹⁶⁴⁻¹⁶⁷. In our combined SICM approach, we integrate a custom-made SOFI optimized for live cell imaging through self-blinking dyes and 3D reconstruction¹⁶⁸⁻¹⁷¹. Moreover, SOFI achieves lateral resolution in the same range as SICM ~50 nm¹⁷⁰.

- SOFI integration into a widefield setup in the SICM system (Figure 4.1a). The custom-made SOFI can be easily implemented on a widefield setup, yielding high-resolution imaging¹⁶⁹. Paired with self-blinking dyes, SOFI does not require high-intensity laser illumination making it the ideal SR technique to combine with the non-invasive SICM for live cell imaging.
- Demonstration of correlative 3D imaging of cell topography and cytoskeletal protein (Figure 4.1b). We implement 3D super-resolution with an image-splitting prism to acquire 8 physical planes at the same time¹⁶⁸. With this method we can generate 22 total planes spaced 116 nm apart after 3rd order SOFI computation, giving a 3D volume of 50 μm x 60 μm x 2.45 μm . We show combined SICM imaging to correlate several membrane structures with actin and tubulin cytoskeletal proteins. For example, to resolve microvilli structures (~ 200 nm range) with SICM and actin filaments with SOFI.
- Demonstration of live cell imaging with combined SICM and SR microscopy. We demonstrate that we can track lamellipodia dynamics with SICM and co-localize actin filament dynamics on the cell periphery, up to 1 hour of consecutive imaging. The system performs a recording of 300 frame-long stacks of the fluorescence signal every 3 minutes, resulting in a combined SICM/SOFI acquisition time of 3 min/frame.

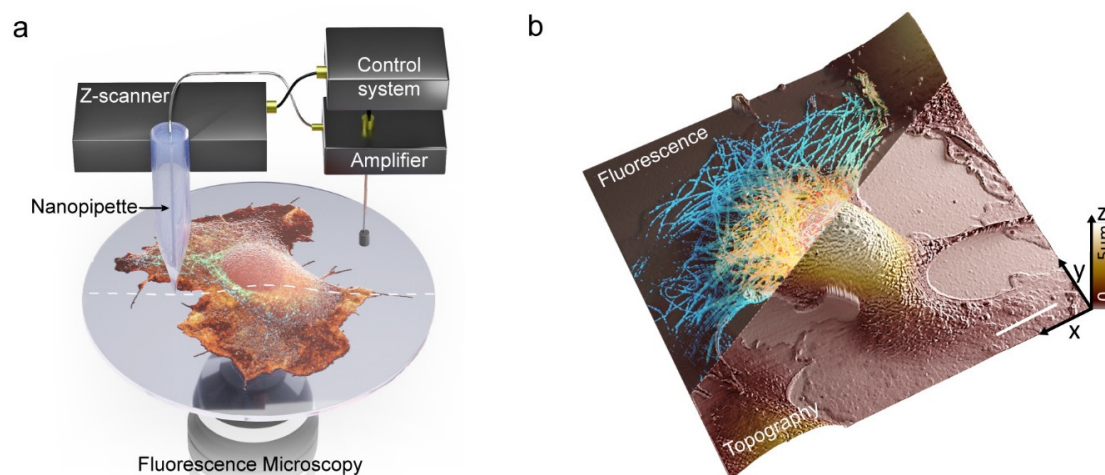


Figure 4.1. Combined SICM and fluorescence and microscopy. a) SICM setup performs topography imaging from the top of the sample, while the fluorescence microscopy setup performs imaging through the bottom. b) Combined 3D imaging with SICM and SOFI on a kidney cell (COS7). Scale bar, 10 μm . Reproduced from^{153,172}.

The integration of the SOFI method with time-resolved SICM, correlative measurements of membrane structures and cytoskeleton proteins, and combined live cell imaging is described in the next **Article-Chapter 5**.

Chapter 5

Correlative 3D Microscopy of Single Cells using Super-Resolution and Scanning Ion-Conductance Microscopy

This is a verbatim copy of an article published in Nature Communication, 2021.

<https://www.nature.com/articles/s41467-021-24901-3>

Navikas, V.^{2*}; **Leitao, M. S.**^{1*}; Grussmayer, K.²; Descloux, A.²; Drake, B.¹; Yserentant, K.³; Werther, P.⁴; Herten, D.³; Wombacher, R.^{4,5}; Radenovic, A.^{2,6}; Fantner, E. G.^{1,6}

*These authors contributed to the manuscript equally: Vytautas Navikas, Samuel M. Leitao. 1: Laboratory for Bio- and Nano-Instrumentation, Institute of Bioengineering, School of Engineering, Swiss Federal Institute of Technology Lausanne (EPFL), Lausanne, Switzerland. 2: Laboratory of Nanoscale Biology, Institute of Bioengineering, School of Engineering, Swiss Federal Institute of Technology Lausanne (EPFL), Lausanne, Switzerland. 3: College of Medical and Dental Sciences, Medical School and School of Chemistry, University of Birmingham, Birmingham, United Kingdom. 4: Institute of Pharmacy and Molecular Biotechnology, Heidelberg University, Heidelberg, Germany. 5: Department of Chemical Biology, Max Planck Institute for Medical Research, Heidelberg, Germany. 6: Corresponding author.

Author contribution: I equally contributed to this paper in collaboration with Dr. Vytautas Navikas from the Radenovic lab at EPFL. We conceived the idea with Prof. Georg Fantner and Prof. Aleksandra Radenovic and wrote the final manuscript. I integrated the optical SOFI system, developed by Dr. Kristin Grussmayer and Dr. Adrian Descloux, into the time-resolved SICM setup with Vytautas Navikas. For SOFI imaging, the dyes were produced by Dr. Yserentant, Dr. Werther, Prof. Herten and Prof. Wombacher. I performed SICM experiments and combined SICM/SOFI imaging followed by data processing and analysis. The SICM system used is the same as presented in Article-Chapter 3, with a modified method for combined SICM/SOFI recordings.

5.1. Abstract

High-resolution live-cell imaging is necessary to study complex biological phenomena. Modern fluorescence microscopy methods are increasingly combined with complementary, label-free techniques to put the fluorescence information into the cellular context. The most common high-resolution imaging approaches used in combination with fluorescence imaging are electron microscopy and atomic-force microscopy (AFM), originally developed for solid-state material characterization. AFM routinely resolves atomic steps, however on soft biological samples, the forces between the tip and the sample deform the fragile membrane, thereby distorting the otherwise high axial resolution of the technique. Here we present scanning ion-conductance microscopy (SICM) as an alternative approach for topographical imaging of soft biological samples, preserving high axial resolution on cells. SICM is complemented with live-cell compatible super-resolution optical fluctuation imaging (SOFI). To demonstrate the capabilities of our method we show correlative 3D cellular maps with SOFI implementation in both 2D and 3D with self-blinking dyes for two-color high-order SOFI imaging. Finally, we employ correlative SICM/SOFI microscopy for visualizing actin dynamics in live COS-7 cells with subdiffractional resolution.

5.2. Introduction

Imaging living cells *in vitro* is crucial in deciphering the biochemical mechanisms underlying complex cellular activity such as cell motility¹, differentiation², membrane trafficking³, and cell-to-cell communication⁴. Our knowledge about the ultra-structure of a cell is almost exclusively derived from high-resolution electron microscopy (EM) on fixed and sectioned cells. Modern EM techniques can routinely reach sub-nm resolution and even provide the atomic structures of macromolecular complexes such as ribosomes¹⁷³ or lately even whole viruses¹⁷⁴. The function of the structures is typically inferred from the presence of specific molecules of interest by performing targeted expression or immunolabelling, followed by fluorescence microscopy techniques thus resulting in correlative light and electron microscopy (CLEM)¹⁷⁵. Axial information can be obtained from EM images through serial sectioning¹⁷⁶, however obtaining unperturbed 3D information about the shape of the cell membrane remains difficult and low throughput.

The portfolio of fluorescence imaging techniques has been expanded with multiple so-called super-resolution microscopy techniques, that circumvent the traditional diffraction limit of optical microscopy¹⁷⁷. Many of these techniques trade-off temporal resolution for lateral resolution, and often require high light intensities causing light-induced cell damage in live cells¹⁷⁸. An approach named super-resolution optical fluctuation imaging (SOFI)¹⁶³ was developed to mitigate the negative phototoxic effects of long-term imaging by increasing acquisition speeds. SOFI relies on stochastic temporal

fluctuations of the signal in independently blinking emitters and is less sensitive to varying fluorophore density and different blinking conditions, compared to localization microscopy approaches¹⁷⁹. SOFI was demonstrated as a powerful imaging method which goes well beyond the diffraction limit and can be extended for live-cell 3D imaging¹⁶⁷ or combined with self-blinking dyes¹⁷⁰, simplifying the image acquisition pipeline.

On the other hand, scanning probe microscopy (SPM) can obtain nanometer resolution images of the 3D surface of unlabeled living cells in its physiological environment¹⁸⁰. It has been proven as a versatile tool for biological imaging, and is often combined with fluorescence microscopy methods¹⁸¹. The most commonly used SPM technique, atomic-force microscopy (AFM), enables the study of the mechanobiology of fixed or living cells¹⁸², to image biological membranes¹⁸³ and even track the dynamics of molecular assembly processes¹⁸⁴. Label-free AFM methods combined with label-specific super-resolution fluorescence microscopy tools can provide maps of single-cells in unprecedented detail not only in fixed, but also in living samples^{185,186}. AFM relies on the direct physical interaction with a sample, which usually deforms sensitive biological specimens and causes height artifacts in live-cell imaging¹⁸⁷. To perform truly non-contact imaging in physiological conditions a scanning modality based on ionic current sensing was developed a few decades ago¹⁷ and was significantly improved with further developments for robust live-cell imaging¹⁹. Scanning-ion conductance microscopy (SICM) relies on the ionic current flowing through a nanocapillary in electrolyte. The ionic current strongly depends on the presence of a surface in the vicinity of the probe tip, hence the nanocapillary can be used as a nanoscale proximity sensor, without ever touching the sample. The sensing distance where the current drops is dependent on the pipette's pore diameter⁶¹. SICM is therefore suitable for sensitive biological systems such as neurons, even with high-aspect ratio topographies with the invention of the hopping mode scanning modality¹⁹.

The use of combined SICM and stimulated emission depletion microscopy for topographical imaging was demonstrated to provide additional information about the structure of cytoskeletal components¹⁴⁸, but lacked the ability to perform the complementary correlative recording on the same setup. Here we present a combined SICM-SOFI approach for in-situ, correlative single-cell imaging.

5.3. Results

5.3.1. Combined SICM/SOFI system

Our pipeline for a combined SICM/SOFI approach is based on correlative imaging with a home-built high-speed SICM setup (Figure 5.1a), operating in hopping mode¹⁹, combined with a SOFI workflow for either two- or three-dimensional sample imaging. SOFI increases the resolution of the widefield microscope by using the statistical

information from stochastic intensity fluctuations and calculating the cumulants of the intensities between the individual pixels and image planes for resolution improvement in 2D and 3D respectively¹⁶⁶, (Figure 5.1b). The lateral resolution of SICM is approximately equal to three times the radius of the pipette⁶¹. In this work, we exclusively use nanocapillaries with a radius of 40-60 nm, which results in a lateral resolution comparable to SOFI. For increased resolution, glass nanocapillaries smaller than 10 nm radius can be fabricated¹²⁷. Such nanocapillaries are however highly susceptible to clogging and are therefore not suitable for long-term measurements.

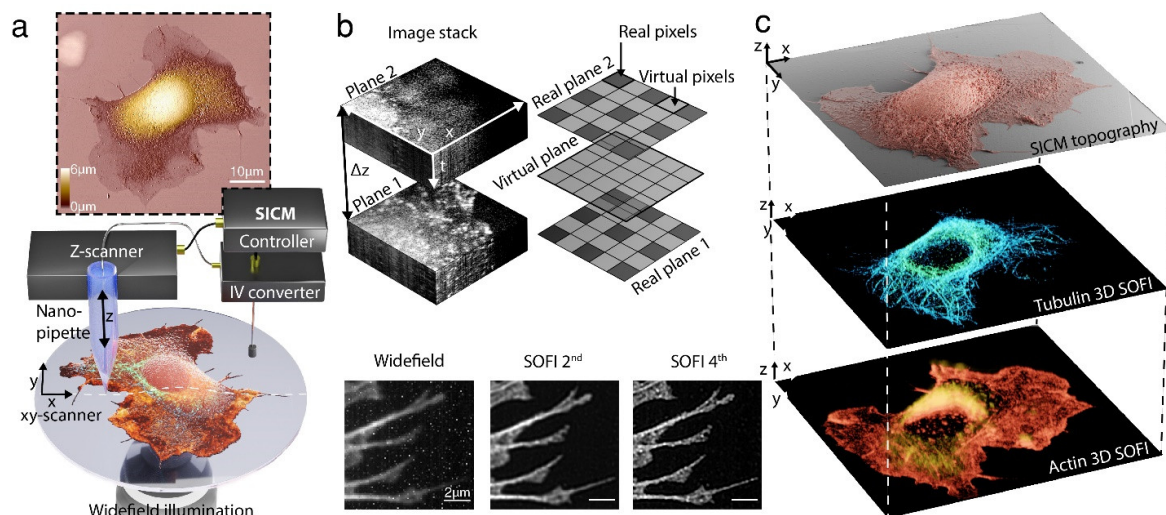


Figure 5.1. Combined scanning ion conductance microscopy (SICM) and super-resolution optical fluctuation imaging (SOFI) for three-dimensional topography-fluorescence correlative imaging. (a) Schematic illustration of the SICM-SOFI setup. In SICM, a current is generated through a nanopipette and modulated as a function of the z-position. The image generated reflects a three-dimensional topographical view of the surface at high lateral and axial resolution (top panel). The lateral resolution in SICM ranges from 150 nm to 30 nm and the axial resolution in the 10 nm range (Figure S5.1). Since the scanning head is mounted on top of the widefield setup, fluorescence imaging can be performed simultaneously. (b) Conceptual visualization of the SOFI principle. The recorded image stack, containing time traces of independently fluctuating fluorophores is used for analysis. A SOFI image is generated by computing cross-cumulants, creating virtual pixels between adjacent real pixels. The cross-cumulant computation principle can be applied in the axial direction as well if multiple sample planes are simultaneously acquired. For the n^{th} order SOFI image, the cumulant PSF volume is raised to n^{th} power thus giving the resolution improvement of a factor of \sqrt{n} . The inset images of the actin structure at the bottom of the (b) panel represent a standard deviation of the image stack (widefield), 2nd and 4th order of linearized SOFI images with corresponding lateral resolution values estimated with an image decorrelation-analysis algorithm of 420 nm, 194 nm, and 93 nm, respectively. (c) Schematics of correlative SICM and two-color 3D SOFI imaging.

To get label-specific information about the cytoskeletal structure of the cells, we performed SOFI with both traditional and self-blinking fluorescent dyes. Self-blinking dyes enable high-order SOFI analysis, that can be applied to various densities of temporally fluctuating fluorophores in order to gain spatial resolution and improve optical sectioning¹⁷⁰. SOFI has the advantage of tolerating higher labelling densities¹⁷⁹ compared to single-molecule localization microscopy, thus decreasing the acquisition time required to the order of 10 s of seconds per SOFI frame¹⁸⁸. Subsequently, we correlated SICM data with two-color 2D and 3D SOFI images, that provided high-resolution single-cell maps showing a distribution of the actin and tubulin cytoskeletal proteins (Figure 5.1c).

5.3.2. Optimizing 2D resolution of fluorescence imaging with SOFI

Before combining the two techniques within one instrument, we tested the 2D SOFI approach with self-blinking dyes on a dedicated setup (Figure 5.2 a-b). We achieved up to 72 ± 3 nm resolution for 4th order SOFI images for microtubules labelled with the commercially available Abberior FLIP-565 dye and 101 ± 9 nm for actin labelled with custom synthesized f-HM-SiR¹⁸⁹, compared to a widefield resolution of 437 ± 106 nm and 480 ± 30 nm (mean \pm s.d., N = 8 images for SOFI 2D resolution measurements) respectively. Resolution was estimated using an image decorrelation analysis algorithm¹⁶¹, which allowed us to estimate the resolution image-wise. The calculated values agreed with theoretical values expected from SOFI analysis (Figure S5.2). Low-intensity (275 W/cm² of 632 nm, 680 W/cm² for 561 nm) illumination was used, resulting in minimal bleaching and long bleaching lifetimes of 406 ± 168 s for Abberior FLIP-565 and 625 ± 130 s for f-HM-SiR (mean \pm s.d., N=8 images for SOFI 2D bleaching measurements) (Figure S5.3). Labelling density for both dyes was optimized for SOFI imaging, however both datasets were also processed with SMLM software¹⁹⁰, which revealed that SOFI analysis was comparable in terms of resolution to the SMLM approach in low SNR conditions.

Furthermore, analysis showed artefacts in high-density regions, non-optimal for SMLM analysis. The resolution, estimated with an image decorrelation analysis algorithm, was found to be 56 nm for tubulin and 98 nm for actin (Figure S5.4). The excellent optical sectioning and contrast provided by SOFI allowed to routinely resolve individual actin filaments (Figure 5.2a, Figure S5.5). Subsequently, the corresponding cells were imaged in a custom SICM using an adaptive hopping mode¹⁷². This yielded the topographical map of the cell membrane (Figure 5.2c) resolving individual microvilli and filopodia membrane structures. Fluorescence and SICM images were registered based on the features from the topography map and the SOFI actin channel (Figure 5.2d). Filamentous actin (f-actin) is known to be located in the lower part of the cell volume and correlates well with the topography of the cell boundary¹⁹¹ in COS-7 cells, that allowed us to simplify the registration process (Figure S5.6).

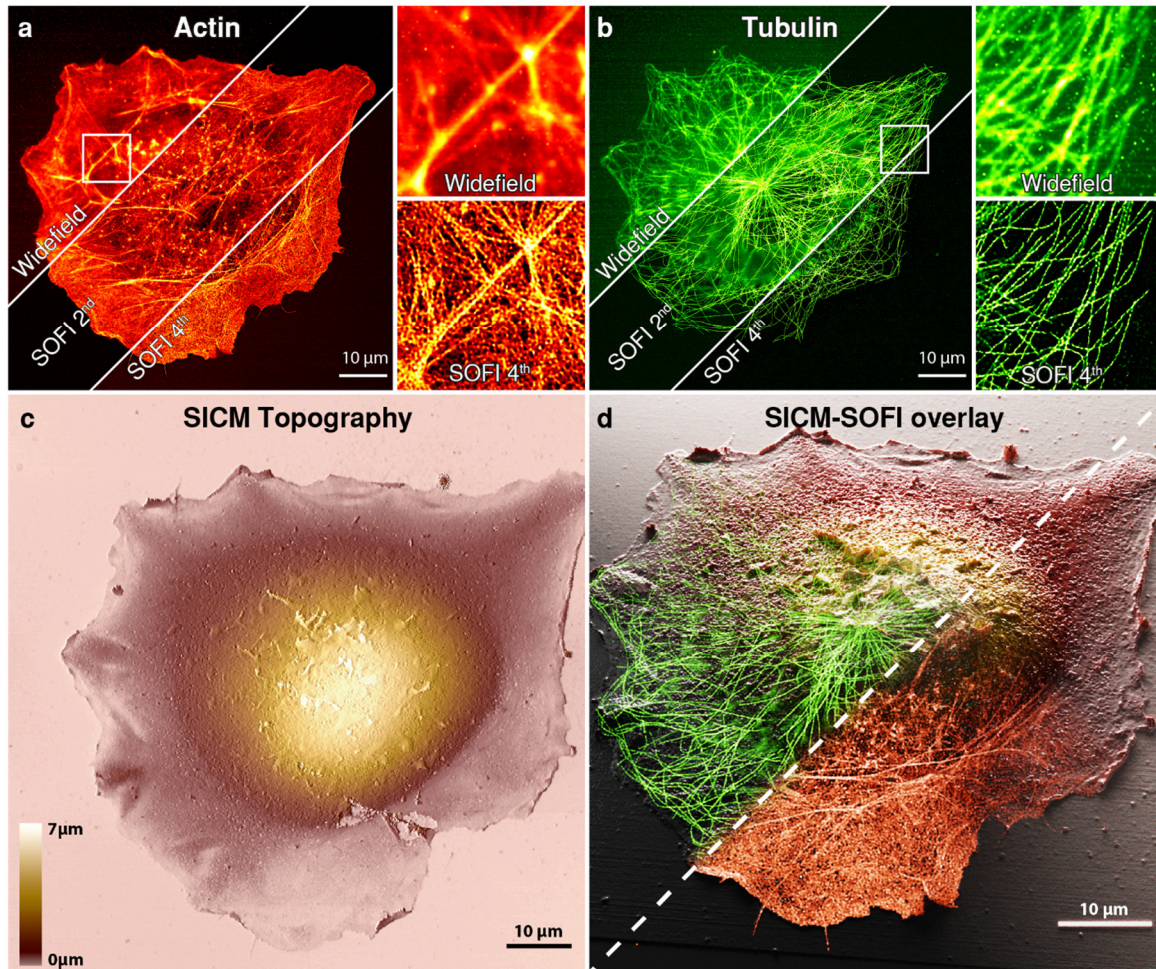


Figure 5.2. Correlative 2D SICM-SOFI imaging cytoskeletal components of a fixed COS-7 cell. (a) Large field of view ($100 \times 100 \mu\text{m}$) 2D SOFI imaging of filamentous actin labeled with a phalloidin-f-HM-SiR self-blinking dye conjugate. (b) Subsequently, immunostained tubulin labelled with the self-blinking Abberior FLIP-565 dye was imaged. $10 \mu\text{m} \times 10 \mu\text{m}$ zoom-ins of the standard deviation of the image stacks (widefield) and 4th order SOFI images are shown for (a) and (b) panels. 635 nm flat-fielded laser excitation was used for imaging f-HM-SiR and a 561 nm laser line for Abberior FLIP-565. Imaging was performed in a 25 % glycerol and PBS mixture at $\text{pH} = 8$. (c) Corresponding topographical SICM image of the same cell acquired on a dedicated SICM setup. 1024×1024 pixels image (78 nm pixel size), acquired at a pixel acquisition rate of 200 Hz with a hopping height of $5 \mu\text{m}$. (d) 3D rendering of a correlative SICM-SOFI overlay. The transparency gradients of tubulin and actin channels are shown as a 2D plane, while topographical SICM information is used for the height representation in the Blender 3D software. The overlay shows that actin is distributed within the boundary of the cell while tubulin displays the canonical cytoskeletal structure.

5.3.3. Optimizing 3D resolution of fluorescence imaging with SOFI

SOFI is not limited in providing the resolution improvement laterally, but it can also be used to improve axial resolution and sectioning by using information from multiple image planes acquired simultaneously. To demonstrate 3D SOFI's capability of volumetric single cell imaging, we performed two-color 3D SOFI imaging on a dedicated setup for the same cytoskeleton components with a multiplane SOFI approach based on an image splitting prism¹⁶⁷ (Figure 5.3a-b), allowing us to calculate cumulants in 3D. However, the trade-off for 3D imaging capability is a reduced signal-to-noise ratio, which makes it difficult to perform high-order SOFI analysis, therefore we only show up to 3rd order 3D SOFI images of microtubules labelled with the Abberior FLIP-565 dye and actin labelled with Alexa-647. (Figure S5.7). The acquired 8 physical planes resulted in 22 total planes spaced 116 nm apart after 3rd order SOFI computation, giving a 3D volume of 50 μm x 60 μm x 2.45 μm with a lateral resolution of 151 ± 34 nm for tubulin structures and 168 ± 34 nm for Alexa 647 labelled f-actin which was comparable to comparable to the 3rd order 2D SOFI results. (Figure S5.2). A single-color 3D SOFI image required as little as 3 min to acquire. This facilitates the screening of a large number of 3D cell volumes (Figure S5.8).

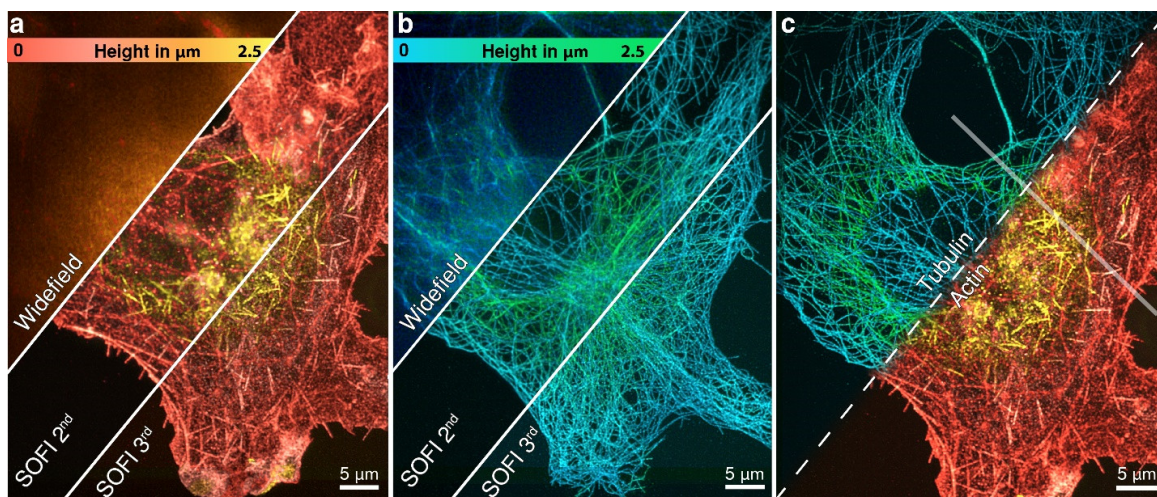


Figure 5.3. Multi-plane 3D SOFI imaging of cytoskeletal components in a fixed COS-7 cell. (a) 3D SOFI imaging of filamentous actin labeled with phalloidin conjugated to Alexa-647 and tubulin (b) labelled with the Abberior FLIP-565 self-blinking dye. A sample volume of 2.45 μm x 65 μm x 55 μm was recorded with 8 equally spaced physical planes, resulting in 22 image planes after 3rd order SOFI processing. Flat-fielded 635 nm and 532 nm laser lines were used for the excitation. Alexa-647 dye was imaged in ROXS imaging buffer with 10 mM MEA, while the Abberior FLIP-565 dye was imaged in a 50% glycerol and PBS solution at pH = 7.5. Height is represented in color scales displayed for each channel. (c) Co-registered 3D 3rd order SOFI volumes of tubulin and filamentous actin. Co-registration was performed based on brightfield microscopy images acquired after recording each

fluorescence channel. Semi-transparent line shows the cross-sections displayed in Figure 5.5a-b.

5.3.4. Correlative SICM and 3D SOFI imaging of cytoskeletal cell structures

We then correlated the 3D SOFI information with the 3D SICM images, which have an order of magnitude higher axial resolution. The samples were moved to the dedicated SICM setup (Figure 5.4a) to resolve microvilli at the surface of the cell (Figure 5.4b-c). Finally, we correlated SICM and 3D SOFI information (Figure 5.4d), which resulted in a detailed picture of the cell volume showing actin colocalized with microvilli protrusions over the whole cell surface (Figure 5.4e).

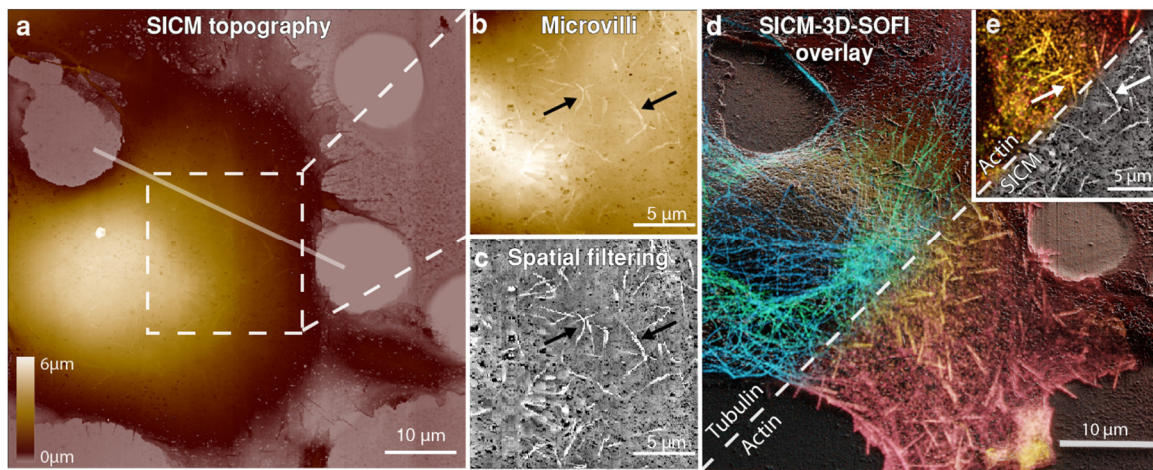


Figure 5.4. Correlative SICM and 3D SOFI imaging of cytoskeletal components in a fixed COS-7 cell. (a) Topographical SICM map of a fixed COS-7 cell imaged on a dedicated SICM setup after two-color 3D-SOFI acquisition. Corresponding fluorescence images are shown in Figure 5.3. The scan resolution is 1024×1024 pixels over an $80 \mu\text{m} \times 80 \mu\text{m}$ area with a corresponding pixel size of 78 nm . The pixel acquisition rate was 200 Hz with a hopping height of $6 \mu\text{m}$. Semi-transparent line shows the cross-section area displayed in Figure 5.5a-b. (b) Leveled zoom-in of the upper part of the cell by mean plane subtraction, showing the topography of microvilli (marked with black arrows) on the surface of the cell. (c) Spatial band-passed filtered SICM image to highlight multiple microvilli structures. (d) 3D rendered correlative SICM and two-color 3D-SOFI overlay. The tubulin and actin channels are rendered as volumes consisting of 22 planes, while topographical SICM information is used for a height representation in the Blender 3D software. (e) Correlative SOFI and SICM overlay (white arrows correspond to the black arrows in b-c).

We have further interpreted the correlative information and compared the topographical maps of multiple cellular structures with two fluorescent channels which we acquired. Taking advantage of a multiplane SOFI approach, we compared the SICM

topography with volumetric localization of actin (Figure 5.5a) and tubulin (Figure 5.5b) in a vertical section, which is marked in Figure 5.3c and Figure 5.4a. Patches of actin are distributed in the top and bottom parts of the cell, while tubulin is distributed homogeneously within the cell volume. We also measured the correlation values for different cellular structures such as filopodia (Figure 5.5c), microvilli (Figure 5.5d) and microtubules (Figure 5.5e) and calculated Pearson correlation coefficients between the pairs of actin, tubulin and SICM topography channels. The physical access to microtubules by SICM was obtained by partially removing the top membrane using Triton X-100 detergent during the permeabilization step¹⁹² (Figure S5.9). We found high correlations between the SICM/actin channels for filopodia and microvilli structures and for SICM/tubulin channels (Figure 5.5f) for the chemically unroofed cell.

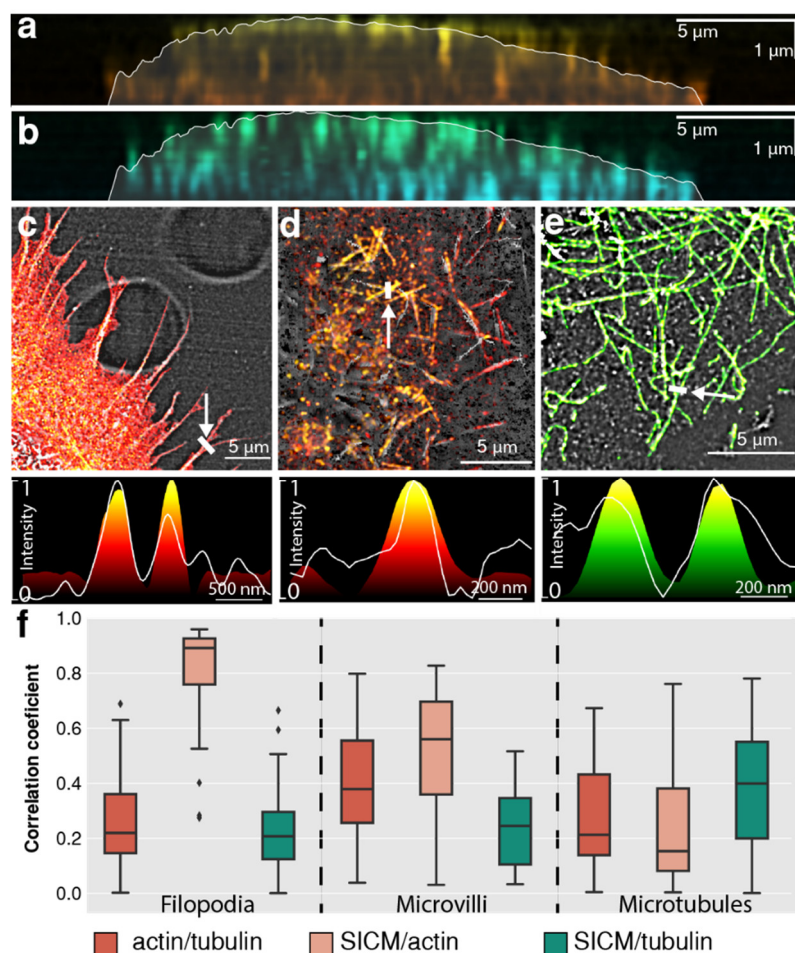


Figure 5.5. Volumetric distribution of cytoskeletal components from correlative SICM-3D-SOFI images. Vertical cross-sections of actin (a) and tubulin (b) in a fixed COS-7 cell marked in Figure 5.3c and Figure 5.4a overlaid with the SICM topography displayed as a semi-transparent contour. (c-e) Correlative imaging of different cellular components resolved by SICM: filopodia overlaid with fluorescently labeled f-actin from 3D-SOFI (c), microvilli overlaid with fluorescently labeled f-actin from 3D-SOFI (d) and microtubules

of chemically unroofed COS-7 cells overlaid with fluorescently labeled tubulin from 3D-SOFI (e). Normalized intensity profiles are displayed below each image. The arrows in (c,d,e) are guides for the eye to indicate the locations of cross sections. For overlays only, the intensity values of SOFI images were projected on spatially filtered SICM images for a better structural representation. (f) Normalized Pearson cross-correlation coefficients of normalized height and intensity cross-sections for both SICM topography and fluorescence channels. Cross-sections ($N = 30$) were manually selected (Figure S5.13) from the SICM image for each of the features. Correlation coefficients were measured on filipodia structures, microvilli structures and microtubules. Significantly higher ($p < 0.05$, two-sided t -test) correlation values were identified for filipodia (SICM)/actin, microvilli (SICM)/actin (3D-SOFI) and microtubules (SICM)/tubulin (3D-SOFI).

5.3.5. Live cell imaging with combined SICM/SOFI

The establishment of a correlative SOFI/SICM pipeline on different instruments paved the way for a combined instrument. For correlative live-cell imaging, we combined the prototype SICM instrument with a 2D SOFI capable widefield microscope. We performed a correlative measurement of cytoskeletal proteins and cell morphology revealing the correlated dynamics of actin and membrane topography at the subcellular level. We transfected COS-7 cells for cytoskeletal proteins of actin filaments (actinin or actin) fused with mEOS-2 photo-switching fluorescent proteins in order to achieve stochastic fluctuations in the fluorescence signal. Cells were then scanned in a consecutive manner with SICM and imaged with SOFI in a custom-design chamber with an environmental control¹⁷² (Figure S5.10). Recordings of 300 frame-long stacks of the fluorescence signal were performed after each SICM frame, resulting in a combined SICM/SOFI acquisition time of 3 min/frame for images of parts of the cell, and 10 min for whole cell imaging (Figure S5.11-12). The 2nd order SOFI images in Figure 5.6a show the actin filaments with a 173 ± 20 nm (mean \pm s.d, $N=6$ images for live-cell SOFI 2D resolution measurements) lateral resolution. After recording, SICM and SOFI images were aligned, revealing correlated dynamics of cytoskeletal proteins and membrane topography (Figure 5.6b-c). During the SICM imaging, there was no laser applied, resulting in two-minute dark intervals between SOFI frames. This significantly reduced the photodamage enabling us to record time-lapse sequences of 10-15 SOFI frames for up to 42 min without observable cell negative phototoxic effects (Figure S5.11).

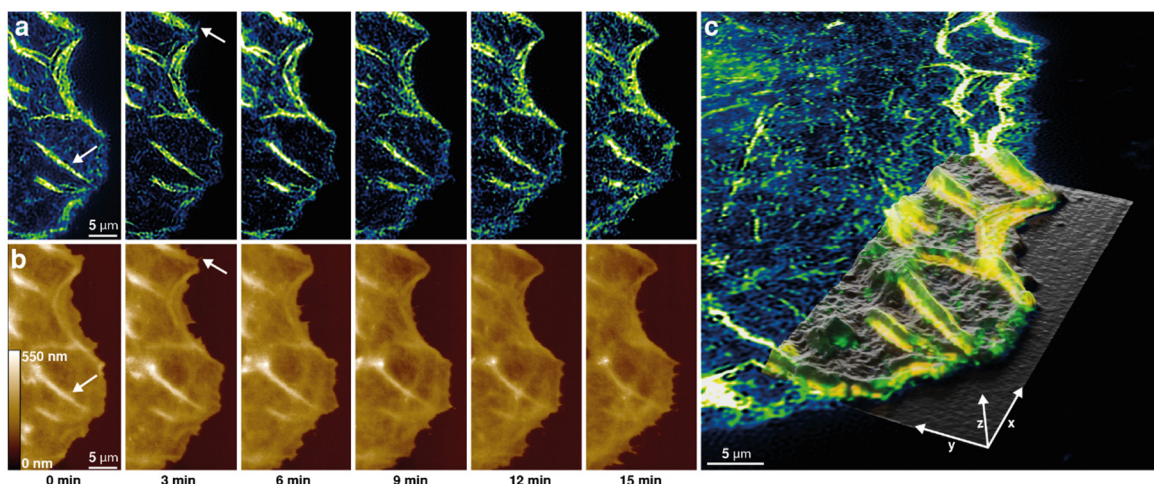


Figure 5.6. Live-cell SICM/SOFI imaging of cytoskeletal actinin dynamics of COS-7 cell. (a) 2nd order SOFI images of actinin-mEOS-2 in transfected COS-7 cells reconstructed from 250 frames each, thus allowing to achieve 12.5 s temporal resolution per SOFI frame. (b) Corresponding SICM height maps (200 x 100 pixels image, with 200 nm pixel size) were acquired at a pixel acquisition rate of 200 Hz with a hopping height of 1 μ m. Correlative SICM/SOFI data was recorded at 180s per frame. The white arrows indicate the corresponding features in SICM and SOFI images. (c) 3D render of SICM height map aligned to the full SOFI image at the start of the recording (0 min) revealing the correlative dynamics of actinin in a livecell.

5.4. Discussion

We have established correlative membrane topography and cytoskeleton imaging provided by combined SICM and SOFI modalities for fixed COS-7 cells both in 2D and 3D on separate imaging setups preserving the state-of-the-art capabilities of both imaging modalities. For imaging densely-labelled samples we used novel self-blinking dyes suitable for high-order SOFI imaging. Additionally, the 3D SOFI approach allowed us to retrieve information about the cytoskeletal protein distribution within the cell volume. Subsequently acquired SICM high-resolution axial topography provided detailed volumetric cell-mapping. Finally, we have performed simultaneous SICM/SOFI live-cell imaging in a combined setup for routinely obtaining correlative measurements in vitro.

Previous studies have demonstrated that a combination of topographical and biochemical sample information is a powerful tool which can provide a comprehensive picture of cellular activity. Correlative SPM and super-resolution microscopy studies, involving techniques such as SMLM¹⁸⁵, stimulated emission depletion (STED)^{148,193}, structured light illumination (SIM)¹⁸⁶ have been demonstrated. SOFI, as a computational method, does not require a complex optical setup design compared to SIM or STED approaches. We show that it can be easily implemented on existing SPM/SICM setups with only few optical components required. Simultaneous SICM measurements can be used to directly detect the

cell topography changes related to apoptosis¹⁹⁴ thus acting as a detector for phototoxicity. Furthermore SICM has been shown to outperform AFM in live-cell imaging¹⁸ due to its non-contact nature, which is crucial in imaging sensitive samples. SICM and confocal microscopy combination was demonstrated to be a versatile tool to study virus-like particle and cell interactions^{160,195}. Small imaging volume, located in the vicinity of the pipette, allows to have superior optical sectioning and colocalized measurement, which is ideal for studying cellular activity near the membrane. On the other hand, AFM has demonstrated its superiority over SICM in terms of imaging resolution⁷¹. AFM is also more versatile in terms of retrieving information about the nanomechanical sample properties¹⁹⁶ and can even be used for molecular-specific imaging¹⁹⁷. Due to the fragile nature of the glass nanocapillary, SICM is less forgiving of imaging mistakes that can lead to fracture of the capillary. This is exacerbated by the fact that no pre-fabricated SICM capillaries are commercially available.

We demonstrated the ability of the combined method for biological studies of the dynamic cell morphology and cytoskeletal architecture inside the cells. This could be used to investigate open questions in membrane trafficking³, cell migration¹⁹⁸ or infection. Due to the electrical nature of SICM measurements, it can also retrieve surface charge information⁷⁴, thus adding a whole new dimension for the measurement. The ability to additionally map the charge of a cell membrane is particularly relevant for problems such as clustering of membrane proteins¹⁹⁹, membrane curvature influence on density of membrane proteins and lipids²⁰⁰, lipid-rafts²⁰¹, behaviour of voltage-gated ion channels²⁰², etc. While there are some remaining technological challenges in terms of usability, the combination of the multimodal SICM and flexible SOFI has the potential to become a routine live-cell imaging modality capable of tackling challenging biological problems.

5.5. Methods

5.5.1. 2D widefield fluorescence imaging setup

A home-built widefield microscopy setup described previously¹⁷⁰ was used (Figure S5.14). The setup has four laser lines for illumination: a 200 mW 405 nm laser (MLL-III-405-200mW, Roithner Lasertechnik), a 1 W 632 nm laser (SD-635-HS-1W, Roithner Lasertechnik), a 350 mW 561 nm laser (Gem561, Laser Quantum) and a 200 mW 488 nm laser (iBEAM-SMART-488-S-HP, Toptica Photonics). The beam of the 635 nm laser is flat fielded by coupling it into the multimode fiber and passed through a speckle reducer (Optotune, LSR-3005-17S-VIS) similarly to that described previously²⁰³. All laser lines are collimated, expanded and focused in the back focal plane of the water immersion 60x objective (Nikon SR Plan Apo IR 60× 1.27 NA WI) resulting in the effective FOV of 100 x 100 μm with a pixel size of 107 nm. Fluorescence signal is then filtered using a quad-line dichroic mirror (ZET405/488/561/640, AHF Analysetechnik) and emission filter (R405/488/561/635 flat, AHF Analysetechnik). Additional band-pass emission filters (596/83 or 685/70, Chroma) were used for sequential two-color imaging. Finally, the light is focused on a sCMOS camera (ORCA Flash 4.0, Hamamatsu; back projected pixel size of 108 nm). Z stabilization is achieved with a PID controller using a total internal reflection from a coverslip using 980 nm laser diode (CPS980, Thorlabs) reflecting from a sample at the critical angle. Axial positioning is achieved with a nano-positioning stage (Nano-Drive, MadCityLabs) using a custom-written software in LabVIEW environment. Lateral sample position is controlled by a Scan-plus IM 120x80 (Marzheuser) stage. Image sequence acquisition is done in Micromanager software.

5.5.2. Multiplane SOFI setup

Multiplane SOFI imaging was performed on a home-built widefield microscope (Figure S5.15) with a simultaneous 8-plane detection system using an image splitting prism²⁰⁴. Four laser lines were used for illumination: a 120 mW 405 nm laser (iBeam smart, Toptica), an 800 mW 635 nm laser (MLL-III-635, Roithner Lasertechnik), 200mW 488nm laser (iBEAM-SMART-488-S-HP, Toptica Photonics) and an 800 mW 532 nm laser (MLL-FN-532, Roithner Lasertechnik). The beam of the 635 nm laser is flat fielded by coupling it into the multimode fiber. All laser lines are collimated, expanded and focused in the back focal plane of the water immersion 60x objective (Olympus UPLSAPO 60XW 1.2 NA). The fluorescence signal is then filtered using a dichroic mirror (zt405/488/532/640/730rpc, Chroma) and quad band emission filter (405/488/532/640m Chroma). Additional band-pass emission filters (582/75 or 685/70, Chroma) were used for sequential two-color imaging. An image-splitting prism was placed behind the last lens and splits the signal into 8 images recorded by two synchronized sCMOS cameras (ORCA

Flash 4.0, Hamamatsu; back projected pixel size of 111 nm). Each image plane is equally spaced 350 nm apart, resulting in a total imaging volume of $50 \times 60 \times 2.45 \mu\text{m}^3$. The sample is positioned in XYZ by using a hybrid piezo nanopositioning stage (3-PT-60-F2,5/5) and Motion-Commander-Piezo controller (Nanos Instruments GmbH). Synchronization of cameras, imaging acquisition and general setup control is done with a custom-written software in LabVIEW environment.

5.5.3. Scanning ion-conductance microscopy setup

Scanning probe microscopy was performed with a custom-made scanning ion conductance microscope. The sample was actuated in X and Y by a piezo-stage (piezosystem Jena TRITOR102SG). The nanocapillary was moved in Z by a home-built actuator¹⁷², operated in hopping mode. Borosilicate and quartz nanopipettes were fabricated with a CO-2 laser puller (Model P-2000, Sutter Instruments) with a radius below 60 nm¹⁵³ (Figure S5.16).

5.5.4. Combined 2D widefield fluorescence /SICM setup

A home-built widefield setup is assembled in combination with a SICM scanner (For more detail see SICM setup) mounted atop an inverted Olympus IX-71 microscope body (Figure S5.17). For sample excitation, a four-color (405 nm, 488 nm 561 nm, 647 nm) pigtailed Monolithic Laser Combiner (400B, Agilent Technologies) is used. Light is collimated and focused to the back focal plane of the oil-immersion high-NA objective (Olympus TIRFM 100x, 1.45 NA) by using a custom built TIRF illuminator. The fluorescence signal is then filtered using a dichroic mirror (493/574 nm BrightLine, Semrock) and a band emission filter (405/488/568 nm stop line, Semrock). Finally, the light is focused on an sCMOS camera (Photometrics, Prime 95B; back projected pixel size of 111 nm). Coarse lateral sample positioning is done with a mechanical stage, while fine positioning is achieved with a SICM XY piezo scanner (Piezosystem Jena TRITOR102SG). Image stacks for SOFI are recorded with a Micromanager software, while laser control and sample positioning are achieved in custom-written LabVIEW software.

5.5.5. Coverslip fabrication

High precision No. 1.5 borosilicate 25 mm coverslips (Marienfeld) were patterned with a custom layout (Figure S5.18) by using a commercial UV excimer laser patterning setup (PTEC LSV3). It allowed to create a user-friendly sample map, which was crucial for further SOFI-SICM correlation experiments while transferring the sample between different setups. After patterning, coverslips were cleaned with piranha solution, washed in MiliQ water, dried with N₂ flow and kept dry for further use. Before use, coverslips were

cleaned with oxygen plasma cleaner (Femto A, Diener electronic GmbH) for 660 s at maximum power setting, washed with PBS (pH = 7.4) once and coated with 50 μ M fibronectin solution in PBS (pH = 7.4) for 30 min at 37° C before seeding the cells.

5.5.6. Cell culture

Cells were cultured at 37 °C and 5% CO₂. DMEM high glucose without phenol red medium (Gibco, Thermo Fisher Scientific) was used, containing 10% fetal bovine serum (Gibco, Thermo Fisher Scientific), 1% penicillin-streptomycin (Gibco, Thermo Fisher Scientific) and 4 mM L-glutamine (Gibco, Thermo Fisher Scientific). Before seeding on coverslips, cells were detached from a flask with TrypLE (Gibco, Thermo Fisher Scientific) and 30 000 cells were seeded on 25 mm coverslips coated with fibronectin. Coverslips were washed twice with PBS before seeding the cells and 2 ml of DMEM medium was used. Cells were grown overnight (12-16 h) before fixation in 6-well plates.

5.5.7. Sample fixation and staining

Cells were washed once with DMEM described previously and incubated for 90 s in a prewarmed microtubule extraction buffer, consisting of 80 mM PIPES, 7 mM MgCl₂, 1 mM EDTA, 150 mM NaCl and 5 mM D-glucose with a pH adjusted to 6.8 using KOH with 0.3% (v/v) Triton X-100 (AppliChem) and 0.25% (v/v) EM-grade glutaraldehyde (Electron Microscopy Sciences). After 90 s the solution was exchanged to pre-warmed 4 % paraformaldehyde dissolved in PBS (pH=7.4) and samples were incubated for 10 min at room temperature. Afterwards, samples were washed thrice for 5 min with PBS on orbital shaker. Cells were kept for 5 min with a freshly prepared 10 mM NaBH₄ solution in PBS on an orbital shaker in order to reduce background fluorescence. Step was followed by one quick wash in PBS, and two washes of 10 min in PBS on an orbital shaker. Samples were then additionally permeabilized to ensure antibody penetration with 0.1% (v/v) Triton X-100 in PBS (pH=7.4) on an orbital shaker followed by additional wash with PBS. Finally, samples were blocked with freshly prepared blocking buffer consisting of 2% (w/v) BSA, 10 mM glycine, 50 mM ammonium chloride NH₄Cl in PBS (pH=7.4) for 60 min at room temperature or stored overnight at 4 °C for further staining. All chemicals were bought from Sigma Aldrich unless stated differently.

5.5.8. Two-color sample staining

For incubation with antibodies and/or phalloidin, coverslips were placed on parafilm in a closed box in the dark, at high humidity to prevent coverslips from drying. 100 μ L of staining solution was typically used for each coverslip. After blocking, samples were incubated with 2 % (v/v) primary anti-tubulin antibody (clone B-5-1-2, Sigma-

Aldrich) in blocking buffer for 60 min at room temperature. Samples were washed with blocking buffer thrice for 5 min on orbital shaker. Coverslips were incubated with 2 % (v/v) secondary donkey anti-mouse-Abberior FLIP-565 antibody, which was labelled as described previously¹⁷⁰. Samples then were kept in blocking buffer for 60 min and washed thrice for 5 min on orbital shaker. Samples were incubated for 10 min in 2% (w/v) PFA in PBS (pH=7.4) as a post-fixation step followed by three 5 min washes with PBS on orbital shaker. After tubulin staining, actin was stained with 500 nM custom synthesized phalloidin-f-HM-SiR (Figure S5.19) or phalloidin-Alexa-647 (Sigma Aldrich) solutions in PBS by incubating for 60 min at room temperature. Samples were washed thrice for 5 min with PBS on orbital shaker and imaged immediately in imaging buffer.

5.5.9. Imaging buffers

2D imaging with self-blinking dyes was performed in 50% glycerol PBS solution at pH=8. The buffer was degassed with N₂ flow for 30 min before use. 3D phalloidin-actin imaging was performed in an imaging buffer described previously²⁰⁵ containing 10% (w/v) D-glucose, 20 % (v/v) glycerol, 50 mM TRIS, 10 mM NaCl, 2 mM COT, 10 mM MEA, 2.5 mM PCA and 50 nM PCD with a pH adjusted with HCl to 7.5. 3D imaging of tubulin labeled with an Abberior FLIP-565 was performed in 50 % (v/v) glycerol solution in PBS (pH = 7.4). All imaging experiments were done in a sealed imaging chamber.

5.5.10. Two-color SOFI imaging

2D SOFI imaging was performed with self-blinking dyes sequentially. Phalloidin-f-HM-SiR labeled actin was imaged first at 275 W/cm² 635 nm excitation, then 680 W/cm² of 561 nm was used to image Abberior FLIP-565 labeled tubulin. The sample was kept on the setup for at least 30 min before imaging, to reduce thermomechanical drift during imaging. 16 000 – 30 000 frames were acquired for each channel for high-order SOFI analysis with minimal photobleaching effects. Sample drift between two-color acquisitions was neglected for further analysis. 3D SOFI imaging was first performed with phalloidin-Alexa-647 labeled actin excited with a 632 nm laser at 3.4 kW/cm² with a low power (5 W/cm²) 405 nm activation laser to increase the population of fluorophores in a bright state. After imaging multiple cells, the oxygen-scavenging imaging buffer was changed to 50 % (v/v) glycerol in PBS for Abberior FLIP-565 labeled tubulin imaging. The sample was then imaged with the 532 nm laser at 3.5 kW/cm². 4 000 frames for each image plane were recorded for high-order 3D-SOFI analysis. After recording each image stack, a subsequent brightfield-image was taken for a further alignment of 2-channel data. 50 ms exposure time was used for all imaging experiments. The data presented in the paper are from two distinct samples.

5.5.11. SICM imaging and processing

The SICM imaging was performed in PBS (pH = 7.4). On fixed cells, SICM images with 1024 x 1024 pixels were acquired at a pixel acquisition rate of 200 Hz with a hopping height of 5 and 6 μm . After performing fluorescence imaging corresponding cells were found using markers described in a coverslip fabrication section. On live cells, SICM images with 512 x 256 and 200 x 100 pixels were acquired at a pixel acquisition rate of 200 Hz with a hopping height of 1 and 3 μm . These experiments were performed in the combined SICM/SOFI system described previously. The current setpoint used in all the SICM measurements was 99 % of the normalized current recorded. SICM images were further processed using Gwyddion¹⁵⁵ and Fiji¹⁵⁶.

5.5.12. SOFI Image analysis and image alignment

2D and 3D SOFI image analysis was performed as described previously^{170,204}. Briefly, the image stack was drift-corrected using cross-correlation between SOFI subsequences before performing cumulant calculation. Different planes of the 3D image stack were registered based on acquired bead stack and images sequence was drift-corrected after the registration, assuming that the drift is homogenous within the volume. 4th order SOFI images were used in 2D SOFI case, while 3rd order SOFI images were taken for 3D SOFI. Images were further deconvolved with a Lucy-Richardson deconvolution algorithm using gaussian PSF model. Deconvolution settings were optimized using decorrelation analysis algorithm for resolution estimation¹⁶¹. 2D and 3D SOFI analysis code was implemented in Matlab and is available upon request. After 2D and 3D SOFI processing, images were aligned with a topographical SICM map using custom-written Python code based on the hand-selected features in the actin channel and SICM image using an affine transformation (Figure S5.6). For two-color 3D SOFI, two-color SOFI stacks were co-registered based on brightfield images and then aligned with SICM image based on the actin channel.

5.5.13. Live-cell SOFI/SICM imaging

COS-7 cells were seeded according to the procedure described previously. After 12-16h cells were transfected with actinin-mEOS2 or Lifeact-mEOS2 (Supplementary information: Plasmid sequences) with a Lipofectamine 3000 (Thermo Fisher) according to the protocol provided by manufacturer. Cells were used for combined SICM-SOFI experiment 24 h after the transfection. Imaging was performed at 37 °C and 5 % CO₂ in a custom-built imaging chamber in FluoroBrite DMEM media (Gibco, Thermo Fisher Scientific) in order to reduce autofluorescence. SICM and SOFI imaging was performed subsequently i.e. after each SICM image, a fluorescent stack of 300 frames with an exposure time of 50 ms was recorded. The first 50 frames were excluded from SOFI processing due to rapid intensity change upon 405 activation and only 250 frames were

used for further SOFI analysis. Live-cell imaging was performed under the low-illumination intensity (500 W/cm^2 of 561 imaging laser and 0.3 W/cm^2 of 405 nm activation laser) in order to reduce phototoxicity.

5.5.14. Correlative 3D SICM/SOFI data rendering

In order to fully expose the correlative 3D data, we have used the advanced open-source 3D rendering tool Blender 3D for data visualization. Normalized topographical SICM data was imported as a height map and scaled in the axial direction. Then, 2D SOFI data was overlaid by importing a co-registered fluorescence image and a custom-written shader was used for volumetric multiplane data rendering (Figure S5.21) to generate the final Figures.

5.6. Supporting information

Figure S5.1. SICM image of a supported lipid bilayer for axial resolution estimation.

Figure S5.2. SOFI resolution estimation for two-color 2D and 3D SOFI images.

Figure S5.3. Labelling density and bleaching kinetics of self-blinking dyes.

Figure S5.4. High order SOFI comparison with SMLM.

Figure S5.5. Multiple two-color 4th order SOFI images.

Figure S5.6. SICM SOFI image co-registration procedure.

Figure S5.7. Comparison of image quality of 3D SOFI orders.

Figure S5.8. Multiple correlative SICM and two-color 3rd order 3D SOFI images.

Figure S5.9. SICM topographical map of microtubules.

Figure S5.10. SICM setup with an environmental control chamber for live cell imaging.

Figure S5.11. Live-cell SICM-SOFI imaging of actin of filopodia for 42 min.

Figure S5.12. Live-cell SICM-SOFI imaging of a single cell.

Figure S5.13. Cross sections used to calculate Pearson-correlation coefficient between different channels.

Figure S5.14. Detailed schematics of 2D SOFI setup.

Figure S5.15. Detailed schematics of 3D SOFI setup.

Figure S5.16. SEM characterization of glass nanocapillaries.

Figure S5.17. Detailed schematics of a combined SICM-SOFI setup.

Figure S5.18. Coverslip fabrication and binary mark map generation.

Figure S5.19. Phalloidin-f-HM-SiR chemical synthesis.

Figure S5.20. Kinetics of self-blinking dyes for high-order SOFI imaging and ON time estimation.

Figure S5.21. Description of final 3D SOFI data visualization in Blender 3D.

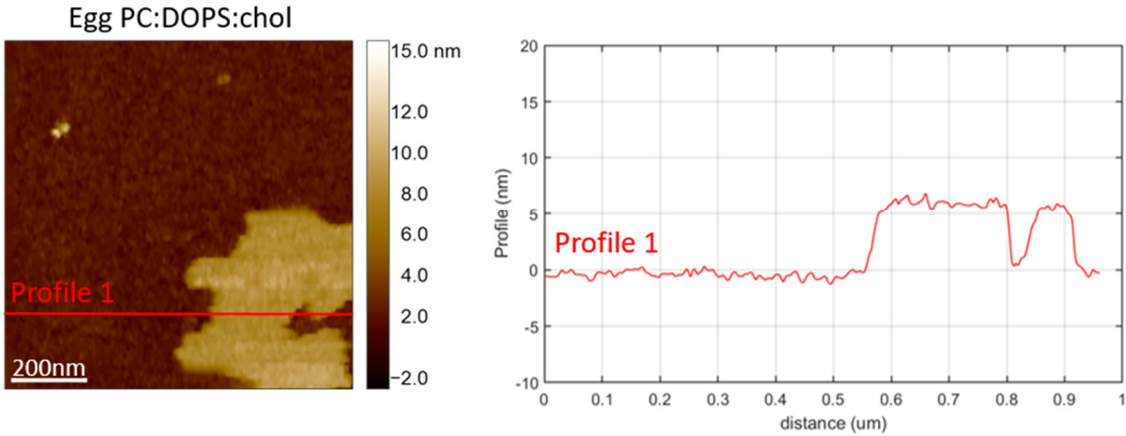


Figure S5.1. SICM image of a supported lipid bilayer (SLB) for axial resolution estimation. (a) SICM image of a SLB, composed of Egg PC:DOPC:chol (3:1:2), deposited on mica acquired using 15 nm radius nanocapillary. 480 x 480 pixels image acquired at pixel acquisition rate of 300 Hz with a hopping height of 100 nm. (b) Height profile of the SLB indicating the axial resolution of SICM below 5 nm.

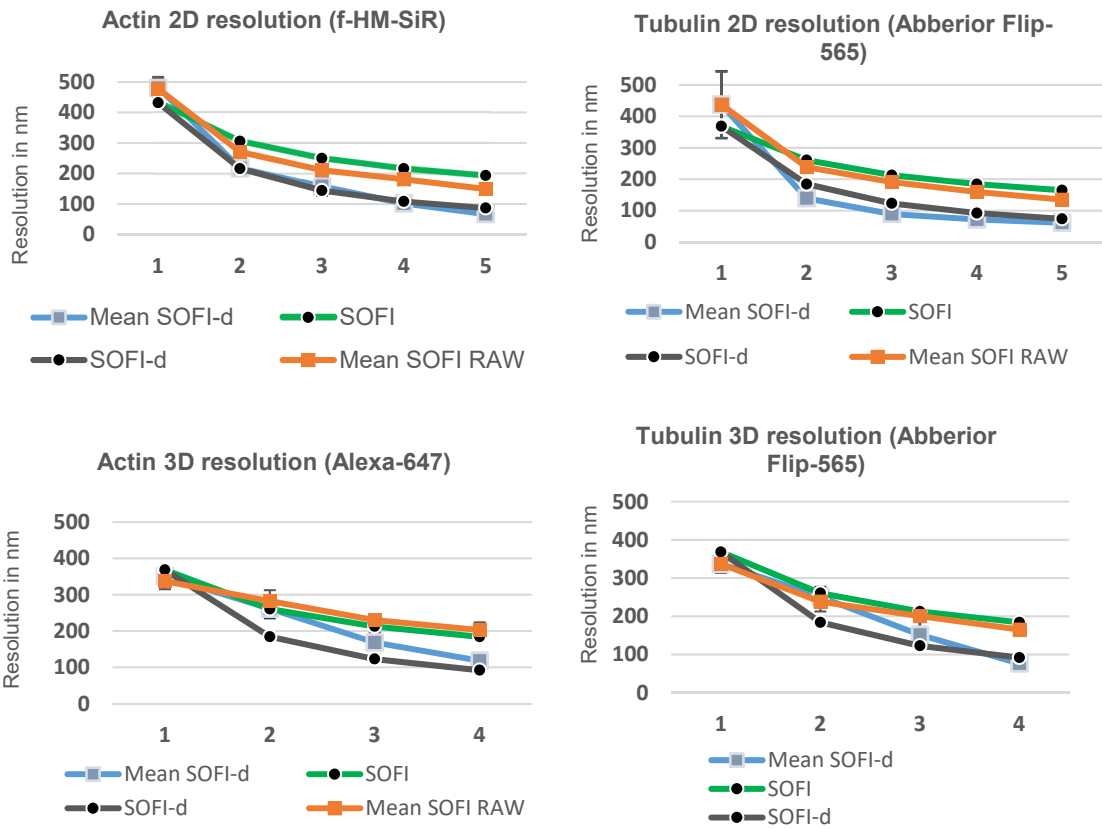


Figure S5.2. SOFI resolution estimation for two-color 2D and 3D SOFI images. Resolution was estimated with a parameter-free image resolution estimation algorithm¹⁶¹. For 2D

images, each value is calculated from 8 images. For 3D SOFI stack resolution was estimated in all planes ($N = 8$, $N = 15$, $N = 22$, $N = 29$) for corresponding SOFI orders. Theoretical values for SOFI and SOFI-d (deconvolved) based on the diffraction limited PSF size are also plotted.

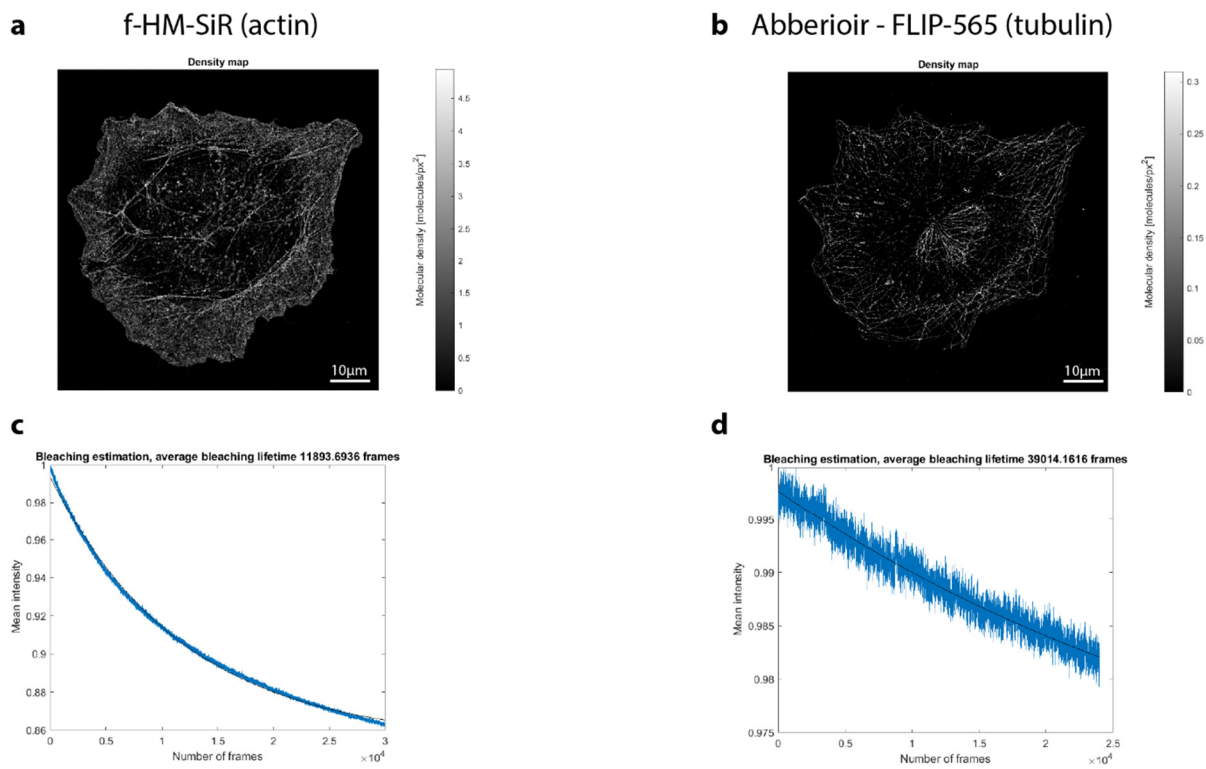


Figure S5.3. Labelling density and bleaching kinetics of self-blinking dyes. Molecular densities of f-HM-SiR (a) and Abberior-FLIP 565 (b) dyes from a representative image, together with bleaching curves estimated from the corresponding image stacks. Calculated average bleaching lifetimes (8 stacks with 30 000 frames) for f-HM-SiR dye was 406 ± 168 s and 625 ± 130 s for Abberior FLIP-565 (mean \pm s.d, $N = 8$ image stacks consisting of 30 000 frames).

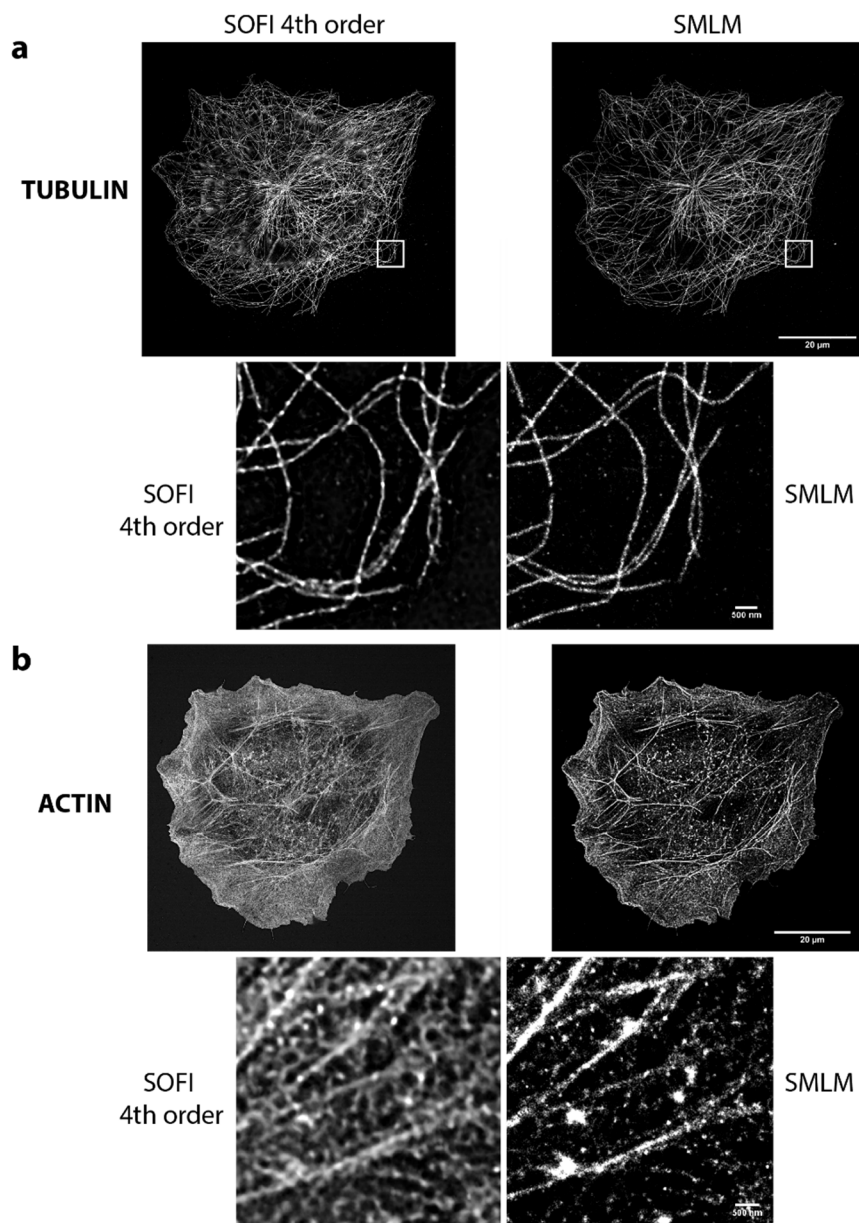


Figure S5.4. High order SOFI comparison with SMLM. a) 4th order SOFI and SMLM (Thunderstorm) image quality comparison. Images stacks were processed with the latest version of Thunderstorm software¹⁹⁰ by using single-emitter fitting function. It is visible that in sparse blinking conditions (Abberior FLIP-565 labelled microtubules) both approaches (SOFI and Thunderstorm) perform similarly, however for f-HM-SiR labelled f-actin SMLM seems to produce localization artifacts, that are expected for high-density data. Resolutions metric stated in the paper were computed with image decorrelation analysis algorithm¹⁶¹. The localization precision might be improved by using multi-emitter fitting or pre-processing tools such as HAWK²⁰⁶, however this is clearly outside of the scope for this study.

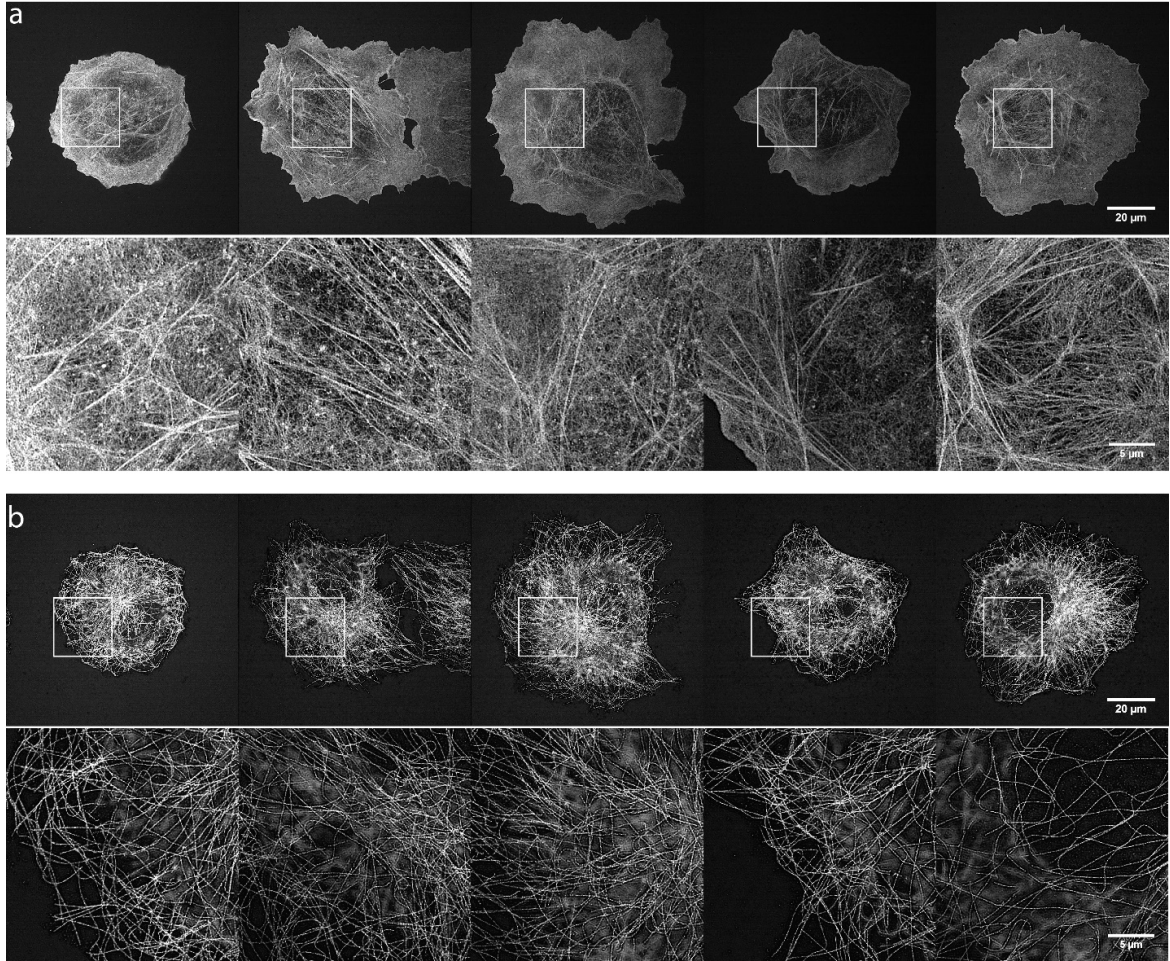


Figure S5.5. Multiple two-color 4th order SOFI images. 4th order SOFI images of phalloidin-fHM-SiR labeled actin (a) and Abberior FLIP-565 immunostained tubulin (b). Zoom-ins of 25 μm are shown together with the whole 90x90 μm field of view images.

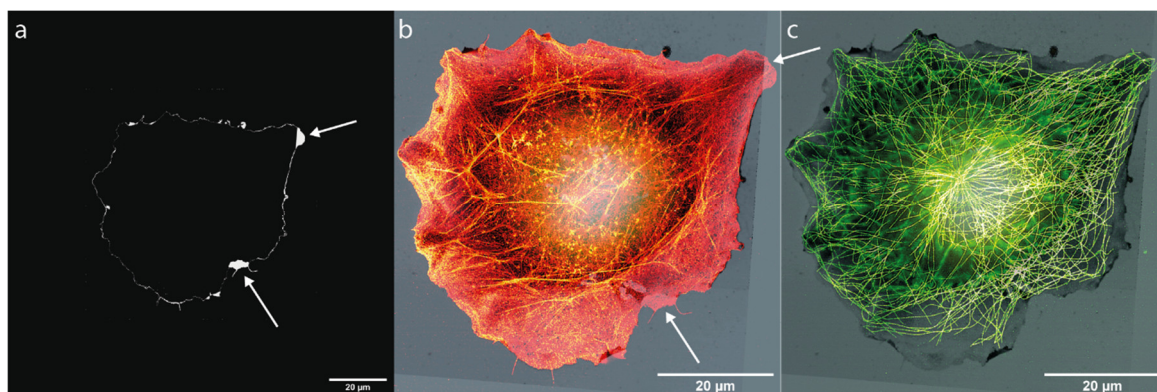


Figure S5.6. SICM SOFI image co-registration procedure. (a) Difference of the thresholded SICM and actin channels revealing the different cell features between SICM and actin channels. (b) SICM image overlaid with actin and (c) channels. Arrows are showing the ambiguities marked in image (a). 2D SOFI images were aligned with SICM topographical map based on the actin channel. Same features were manually depicted in both images and affine transformation matrix was computed using at least 10 corresponding marks. 2D tubulin image was transformed using the same transformation matrix assuming that the lateral drift between two SOFI images is neglectable. 3D SOFI image stacks were processed in the same way expect in this case two-color stacks were aligned based on the brightfield microscopy by phase correlation using the images recorded before acquiring each of the stack.

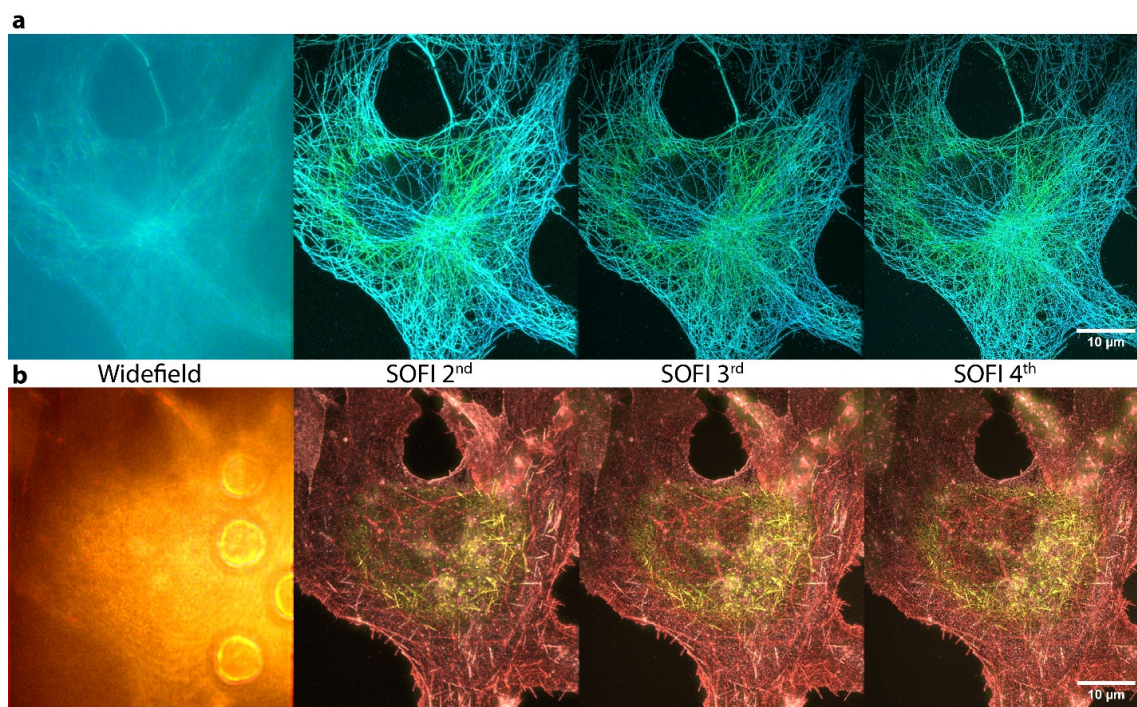


Figure S5.7. Comparison of image quality of 3D SOFI orders. SOFI orders for the two-color 3D SOFI image used in the main text Figure 5.3.

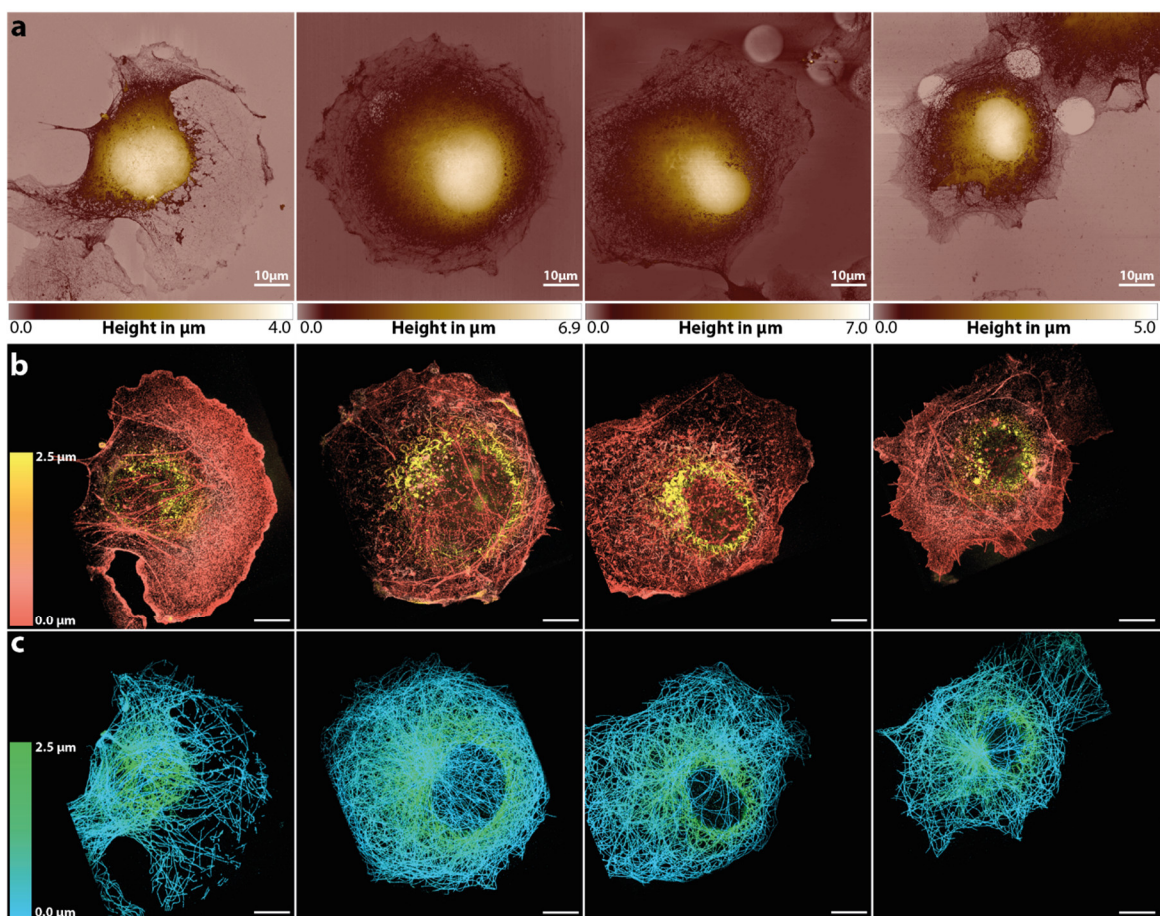


Figure S5.8. Multiple correlative SICM and two-color 3rd order 3D SOFI images. (a) SICM images (1024 x 1024 pixels, 78nm pixel size), acquired at pixel acquisition rate of 200 Hz with a hopping height of 5 μm ; together with a coaligned 3rd order SOFI images of phalloidin-Alexa647 labeled actin (b)) and Abberior FLIP-565 labelled tubulin (c). Axial scales are represented as color bars. Scale bars are 10 μm in all images. All images were correlated according to a procedure described in the Methods section and in (Figure S5.6).

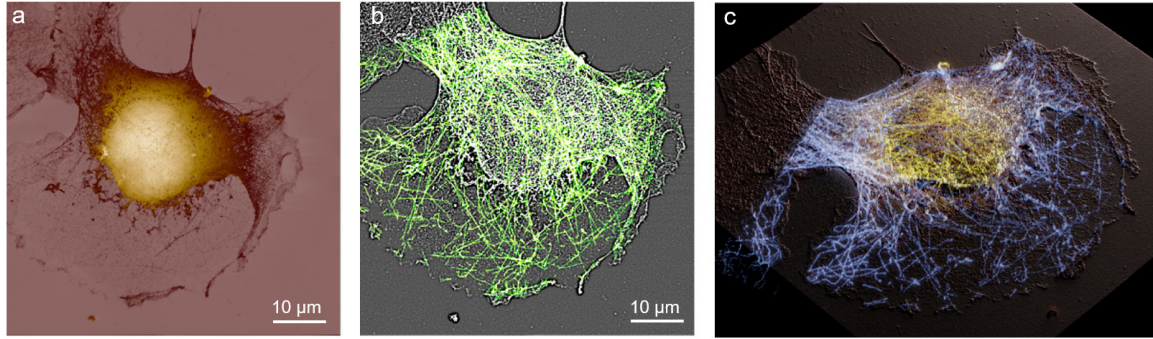


Figure S5.9. SICM topographical map of microtubules. (a) SICM image of a single cell which has part of the membrane removed by permeabilization with Triton X-100. Interestingly, this allows to reveal a preserved microtubular network of the inner part of the cell, which can be better resolved by further spatially filtering the SICM image (b) which is overlaid with a tubulin fluorescence signal from the bottom plane of 3rd order 3D SOFI stack. Bandpass spatial filter with 2-8 px range was used applied on the image (a). (c) Final 3D rendering in Blender 3D software with an overlaid SOFI and SICM data.

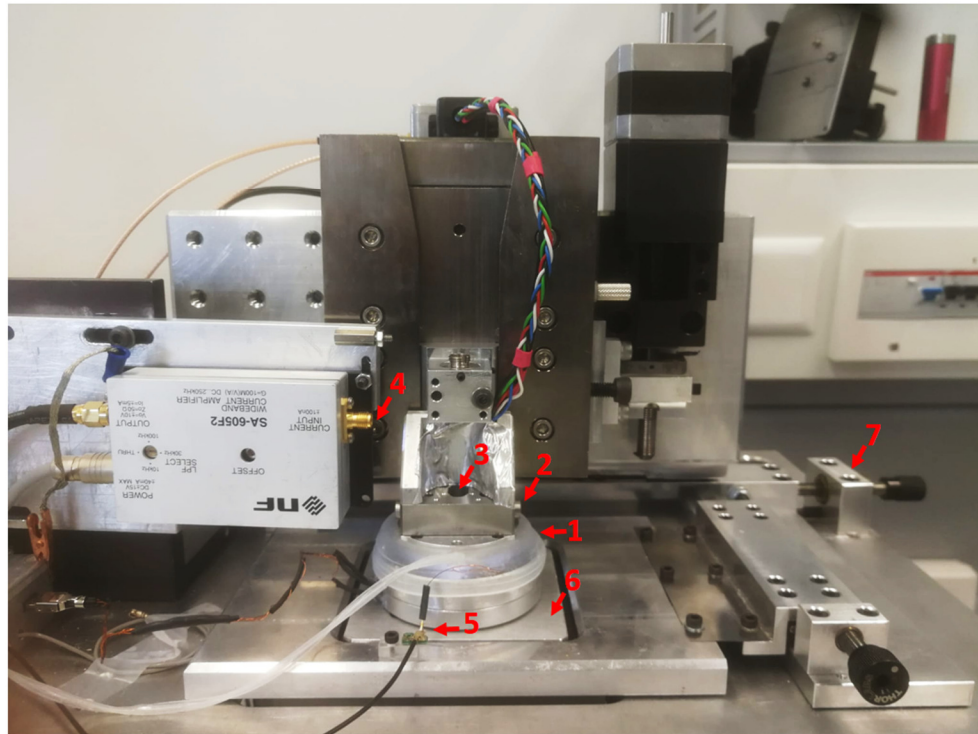


Figure S5.10. SICM setup with an environmental control chamber for live cell imaging described in detail previously¹⁷². 1) Mini-incubator for environmental control. 2) Pipette actuator. 3) Pipette inlet. 4) TIA input for the pipette electrode. 5) Bath electrode. 6) XY scanner. 7) Translation stage.

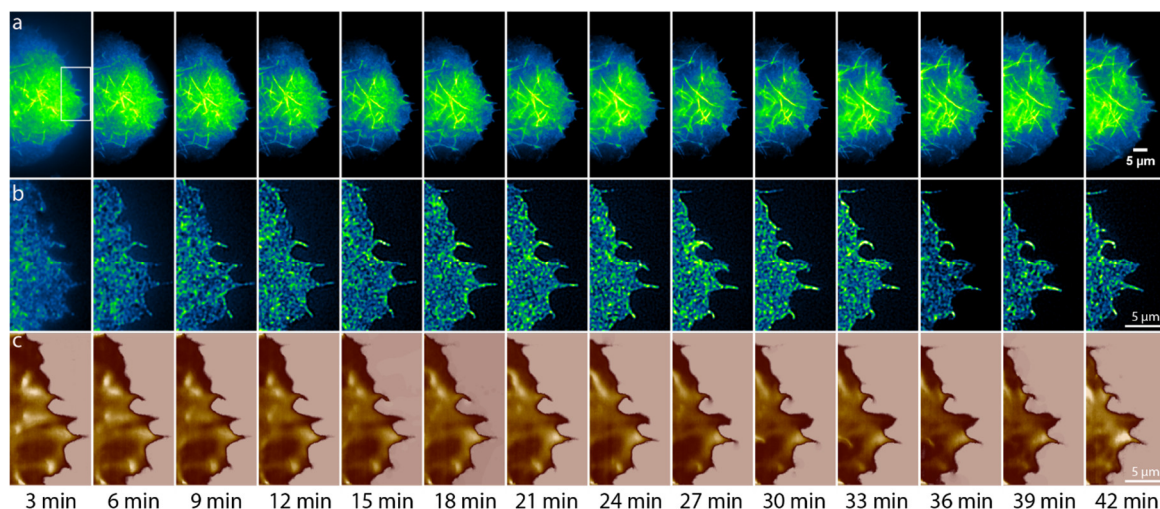


Figure S5.11. Live-cell SICM-SOFI imaging of actin of filopodia for 42 min. Acquisition was performed consequently by recording $10 \times 20 \mu\text{m}$ SICM scans and 300 frame long fluorescence stacks for imaging photoactivated Lifact-mEOS-2. Standard deviation image sequence (a) and 2nd order SOFI (b) aligned with SICM topography images (c) are shown. COS-7 cells were transfected as described in the Methods section by using a Lifact-mEOS-2 plasmid and imaged after 24 h in FluoroBrite medium. 200 W/cm^2 of 561 imaging laser and 0.2 W/cm^2 of 405 nm activation laser were used for illumination with a corresponding exposure time of 50 ms. Corresponding SICM height maps were recorded at 200×100 pixels image (100 nm pixel size), acquired at a pixel acquisition rate of 200 Hz with a hopping height of $1 \mu\text{m}$.

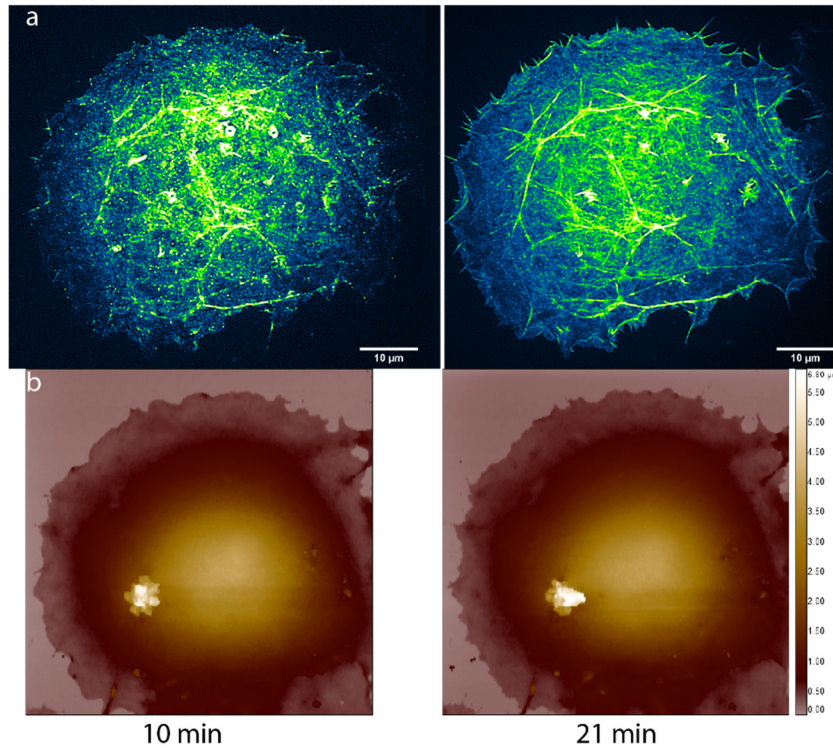


Figure S5.12. Live-cell SICM-SOFI imaging of a single cell. Acquisition was performed consequently by recording $60 \times 60 \mu\text{m}$ SICM scans and 2 fluorescence stacks (300 and 1000 frames long) of photoactivated mEOS-2 for 2nd order SOFI computation. 2nd order SOFI (a) aligned with SICM topography images (b) are showed. COS-7 cells were transfected as described in the Methods section by using a Lifeact-mEOS-2 plasmid and imaged after 24 h in FluoroBrite medium. 200 W/cm^2 of 561 imaging laser and 0.2 W/cm^2 of 405 nm activation laser were used for illumination with a corresponding exposure time of 50 ms. Corresponding SICM height maps recorded at 512×256 pixels image (117 nm pixel size), acquired at a pixel acquisition rate of 200 Hz with a hopping height of $3 \mu\text{m}$. White spot in the SICM image is most likely a particle, attached from the solution.

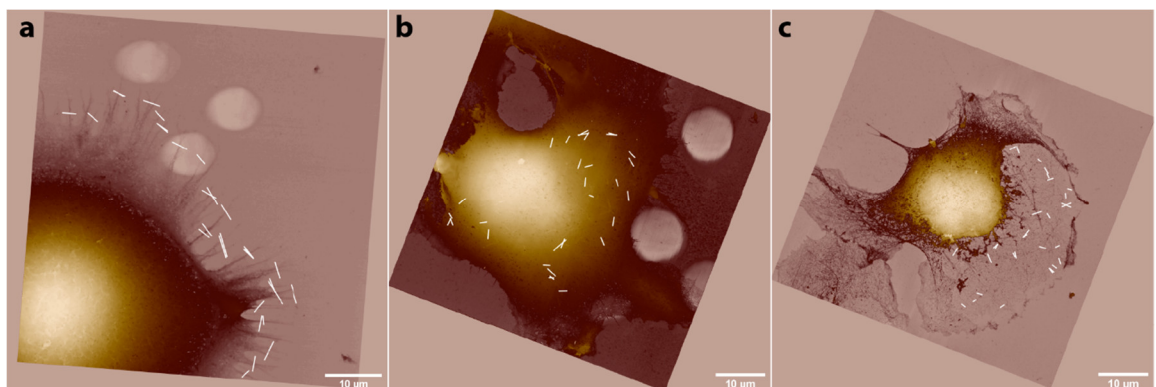


Figure S5.13. Cross sections used to calculate Pearson-correlation coefficient between different channels. For Figure 5.5f 1D cross sections were manually depicted by selecting the structures of interest by hand. Filopodia (a), microvilli (b) and microtubules (c) were selected.

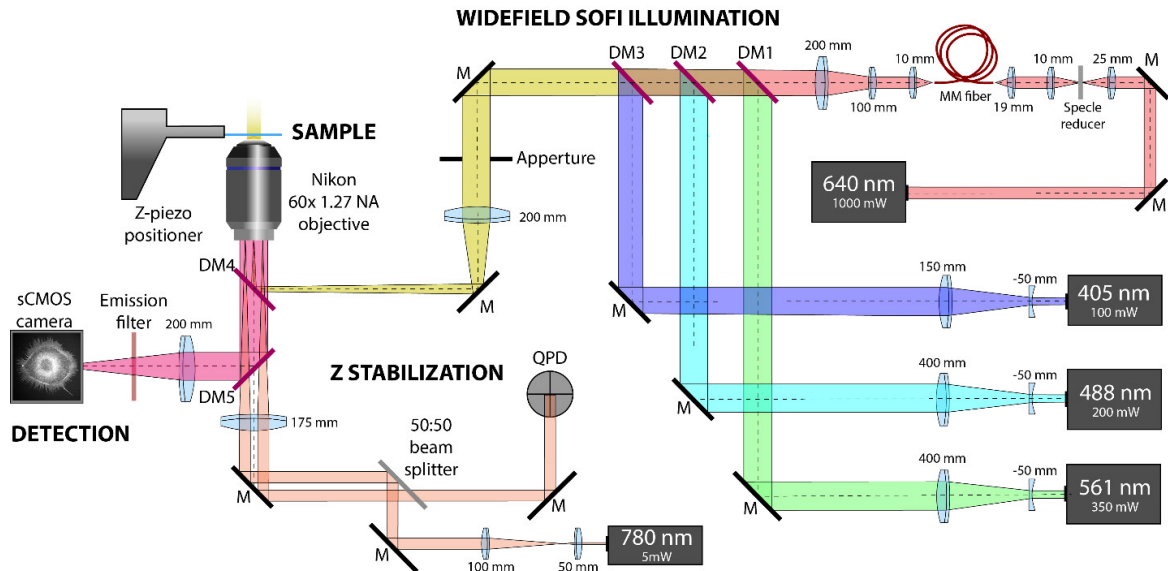


Figure S5.14. Detailed schematics of 2D SOFI setup. Schematics of the setup used for 2D SOFI imaging as described in the Methods section.

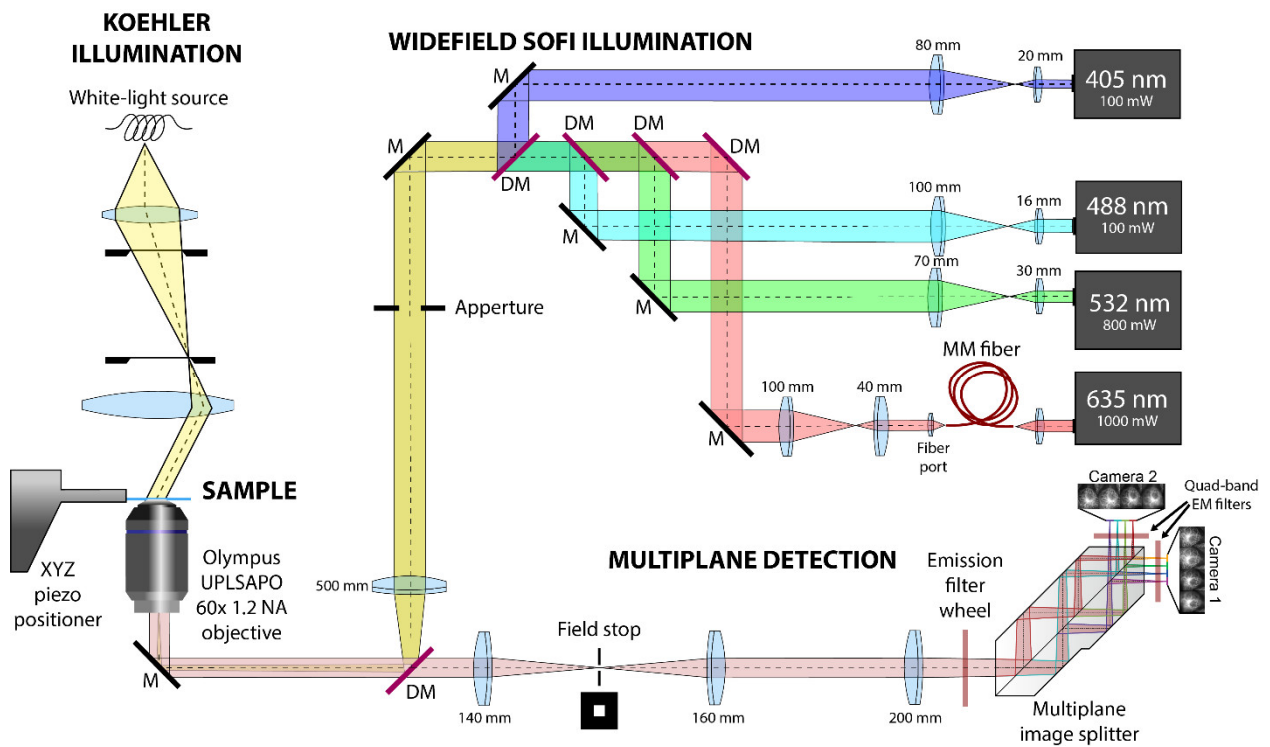


Figure S5.15. Detailed schematics of 3D SOFI setup. Schematics of the setup used for 3D SOFI imaging as described in the Methods section.

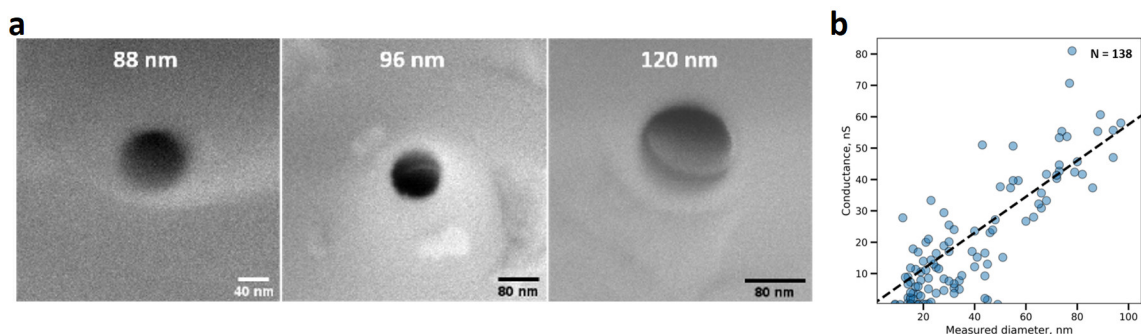


Figure S5.16. SEM characterization of glass nanocapillaries. (a) Selected scanning electron microscope (SEM) images of glass nanocapillaries without conductive coating. (b) Conductance measured in 400 mM KCl solution vs opening diameter measured with SEM. The dashed line represents a least-square fit. The Figure is composed from the data published previously¹⁵³.

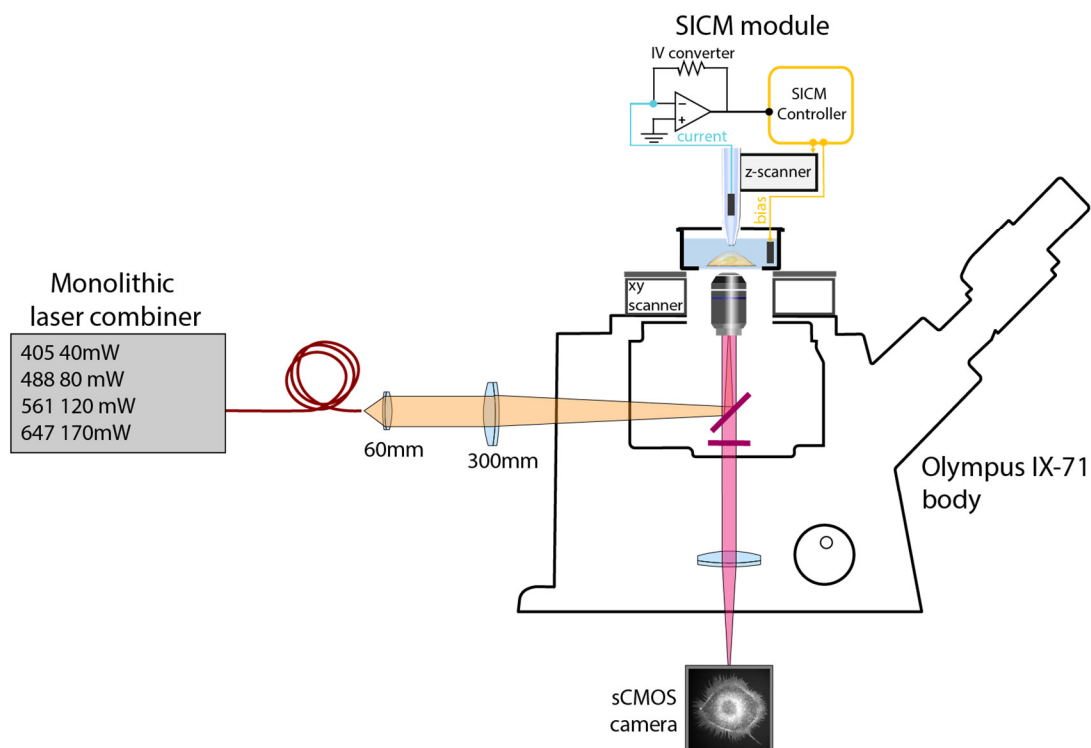


Figure S5.17. Detailed schematics of a combined SICM-SOFI setup.

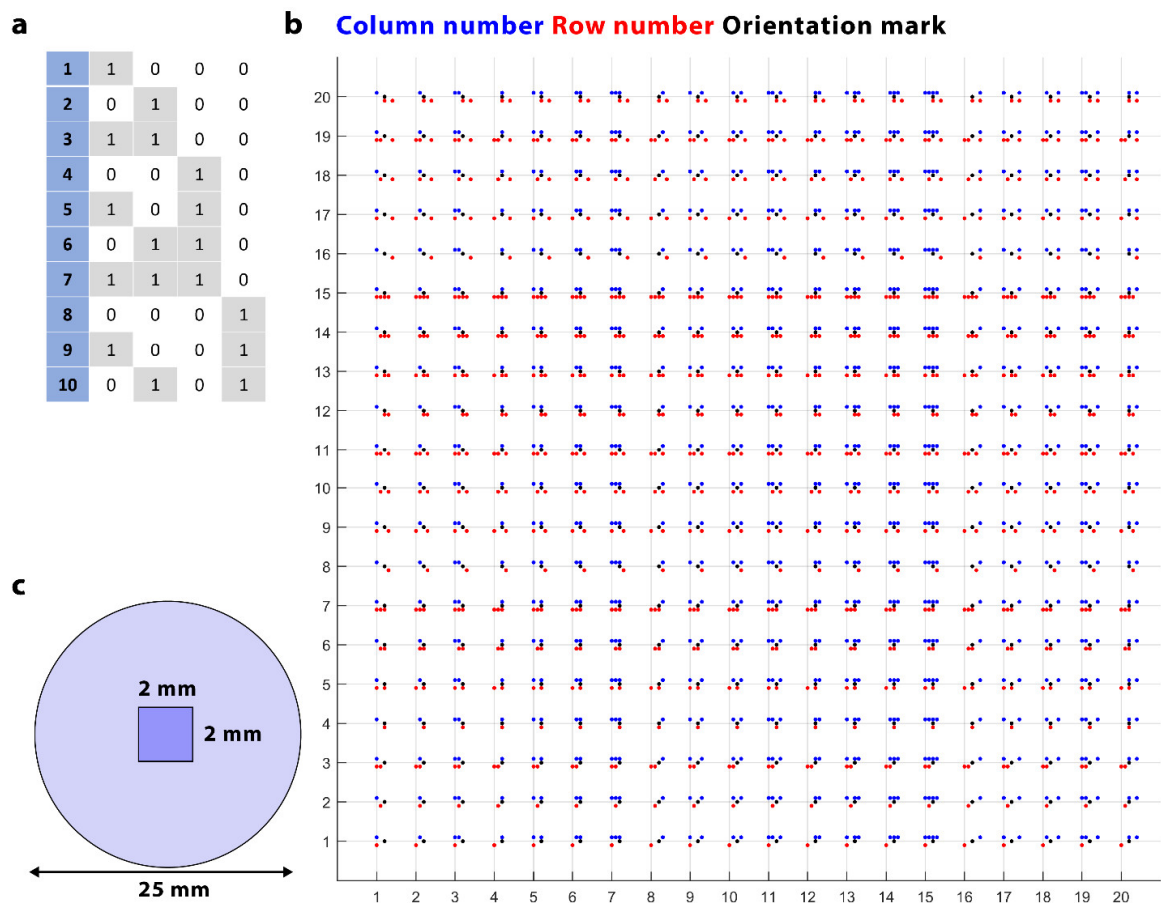


Figure S5.18. Coverslip fabrication and binary mark map generation. (a) The principle of number representation in binary values. 4 binary digits were used to represent numbers from 1 to 20. (b) The final layout of the sample map. Layout was generated with a Matlab code, by using the `dec2bin` function. Binary numbers were used for x and y axis. The static dot in the middle was incorporated for a better determination of the sample orientation. (c) Schematics of the dimensions of the binary digit pattern.

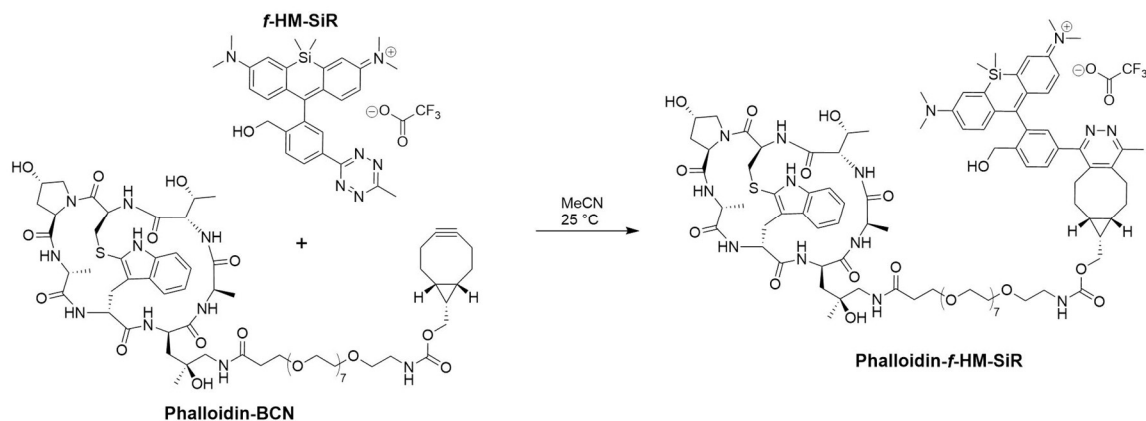
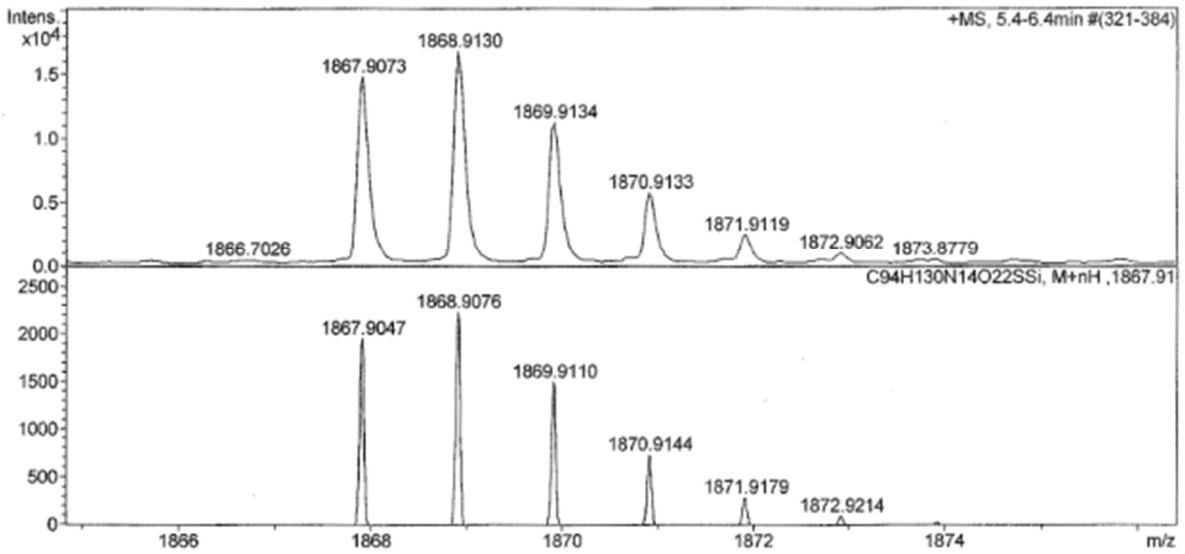
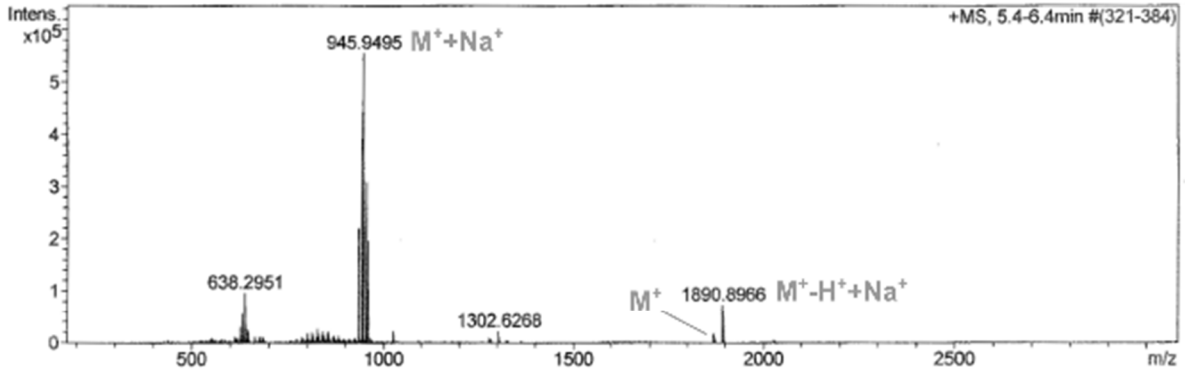
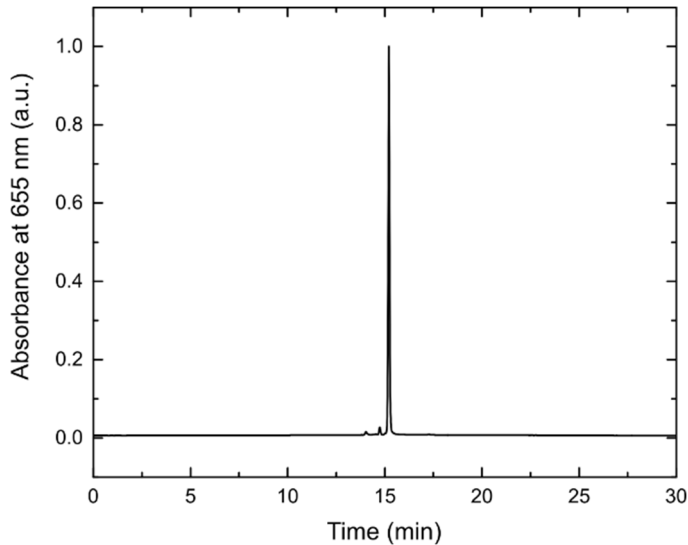


Figure S5.19. Phalloidin-f-HM-SiR chemical synthesis. Reaction scheme of Phalloidin-f-HM-SiR conjugate. Phalloidin-f-HM-SiR was synthesized from f-HM-SiR¹⁸⁹ and Phalloidin-BCN^{171,207}, which were prepared according to literature procedures. In short: Phalloidin-BCN (46 μg) was dissolved in anhydrous MeCN (90 μL) and f-HM-SiR (24.8 μg , 4 μL from 10 mM stock solution) was added at room temperature. The reaction mixture was incubated for 4 h in a thermo-shaker at 700 rpm and subsequently purified by HPLC (gradient 20-90 % solvent B / solvent A ; in 40 min). Phalloidin-f-HM-SiR was afforded as blue solid and after photometric determination of the amount of substance²⁰⁸, a 1 mM stock solution in anhydrous DMSO was prepared. HRMS (ESI⁺) m/z 1867.9047 calculated for $[\text{C}_{94}\text{H}_{131}\text{N}_{14}\text{O}_{22}\text{SSi}]^+$ (M^+), 1867.9073 found; m/z 945.4470 calculated for $[\text{C}_{94}\text{H}_{131}\text{N}_{14}\text{NaO}_{22}\text{SSi}]^{2+}$ ($M^+ + \text{Na}^+$), 945.4482 found. HPLC analytics and semi-preparative purifications were conducted on an Agilent 1100 series HPLC system. Phenomenex Luna 3 μ and 5 μ C18 reversed-phase columns were used for these purposes (Solvent A: H_2O containing 0.1 % TFA; Solvent B: MeCN containing 0.1 % TFA). Collected HPLC fractions were dried by lyophilization. Mass spectrometry was performed on a Bruker microTOF-QII (for ESI-MS) mass spectrometer.



HRMS (ESI⁺) of Phalloidin-*f*-HM-SiR



HPLC chromatogram of Phalloidin-*f*-HM-SiR

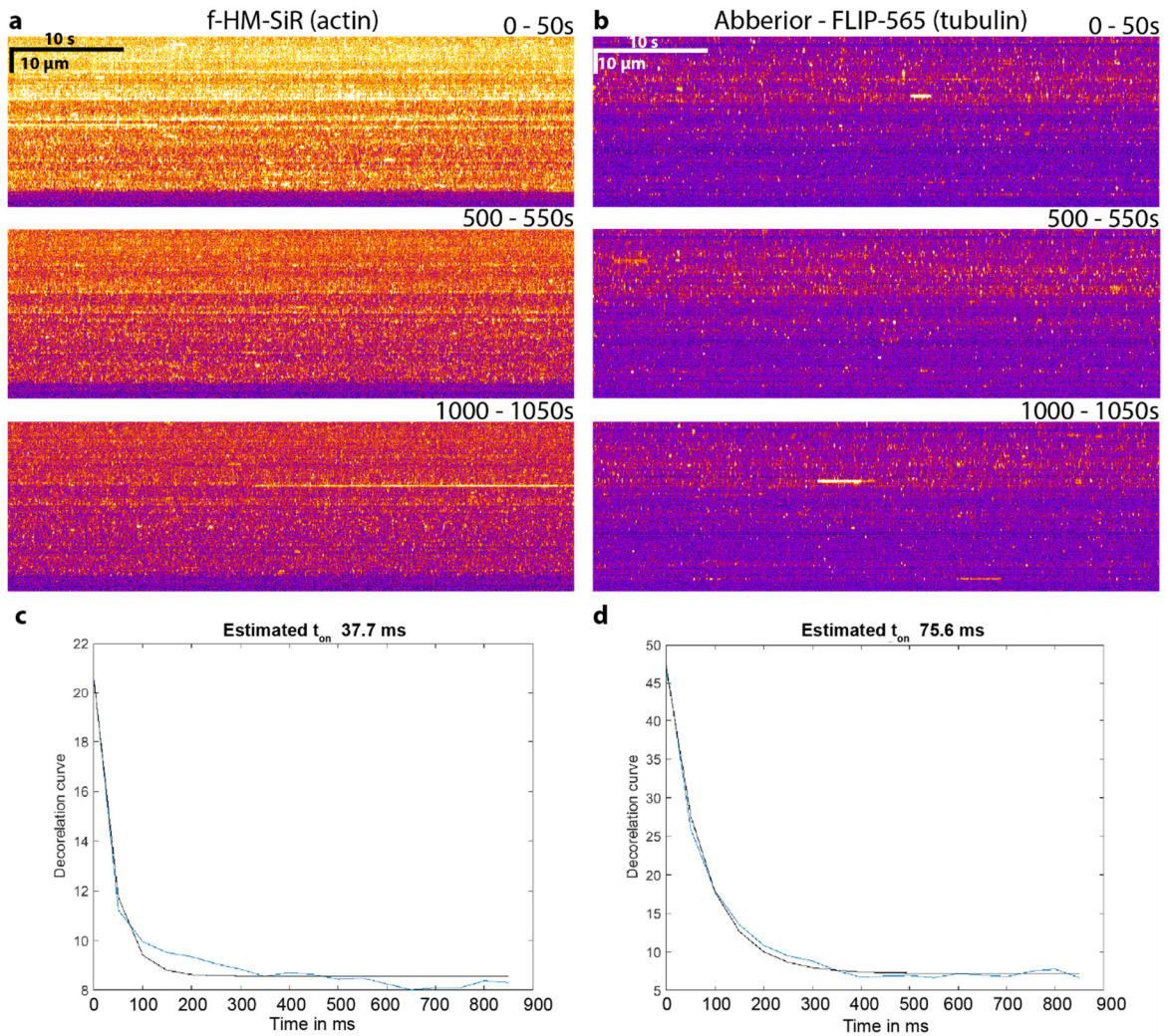


Figure S5.20. Kinetics of self-blinking dyes for high-order SOFI imaging and ON time estimation. Kymographs of signal intensity over time for f-HM-SiR (a) and Abberior-FLIP 565 (b) dyes showing the signal fluctuation over a long-term imaging. Average ON-times were also estimated by computing 2nd order cumulant as a function of time lag and averaging it for subsequences of 500 frames¹⁶⁵. Corresponding lag functions for stacks showed in (a-b) are showed below (c-d). Mean on time for f-HM-SiR dye was estimated to be 38.7 ms and for Abberior-FLIP 565 – 65.75 ms. However, the exposure time of 50 ms might be the limiting factor for the precision of ON-time estimation.

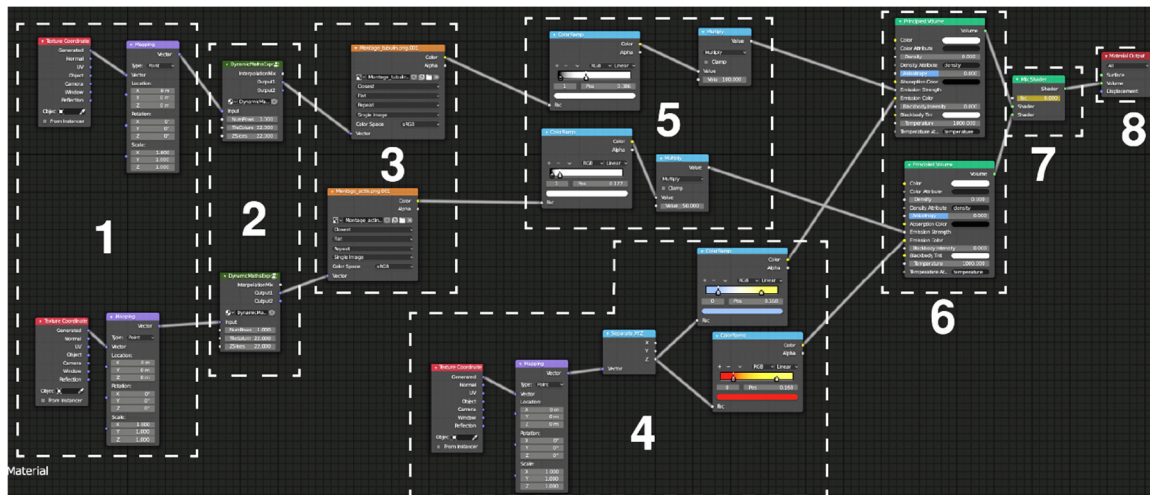


Figure S5.21. Description of final 3D SOFI data visualization in Blender 3D. A simple cube was used as a volume corresponding to the 3D SOFI volume of $2.45 \times 60 \times 60 \mu\text{m}$. Two separate colors were visualized in parallel. Different parts of the shader are explained as follows: 1) Setting up the texture coordinates 2) A script node used to make a 3D volume from the stack of SOFI images. Each image is represented as voxel with dimensions determined by a 3D cube 3) Input of a stack file 4) Color ramps used to represent the height in different colors 5) Contrast and intensity adjustment 6) A principled volume shader 7) A mix shader used to switch between tubulin and actin channels 8) A volume output node.

Chapter 6

Molecular Sensing with Nanopores

6.1. Introduction molecular sensing with nanopores

Although we have used nanocapillaries for SICM imaging, they can be used as a glass nanopore for molecular sensing. The development of nanopore sensing was pioneered by Erwin Neher and Bert Sakmann with the invention of the “patch-clamp” technique for electrical recordings of ion channels (Figure 6.1a), receiving the Nobel prize in 1991^{209–211}. Since then, this method has become routinely used for studying biological membranes and has also inspired the next generation of engineered nanopore systems for molecular sensing using nanopores.

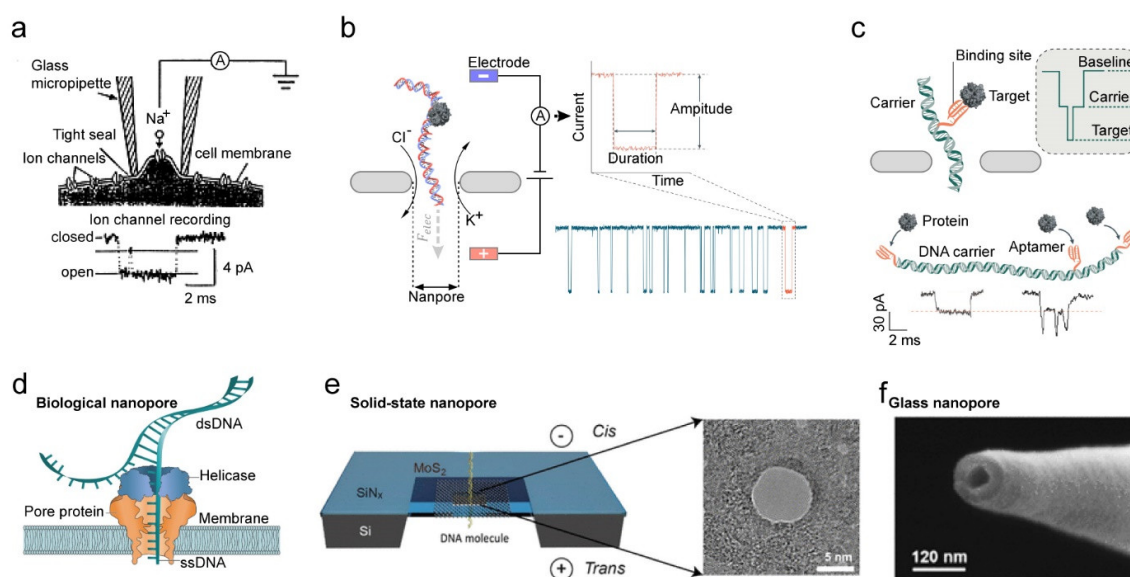


Figure 6.1. Nanopore sensing. a) Electrical recording of a single ion channel with patch-clamp technique²¹¹. b) Principle of single-molecule detection with nanopores, During the passage of an analyte through the pore (often dubbed translocation), the ionic current usually decreases owing to hindered access of ions to the pore volume²¹². c) Schematic illustrating selective target detection using nanopore readout of molecular carriers. Bound targets are confirmed by the presence of one or multiple subpeaks, as shown in the inset²¹². d) Biological nanopore²¹³. e) Solid-state nanopore made out of Silicon dioxide²¹⁴. f) Glass nanopore made of quartz²³.

Nanopores are currently considered one of the most successful label-free single-molecule techniques, with applications to biological screening, diagnostics, and DNA or

protein sequencing. The principle of nanopore sensing is the same as in SICM, where a potential is applied across two electrodes, generating a current through the pore opening that can be measured and analyzed (Figure 6.1b). In nanopore experiments, a charged molecule is detected when it passes through the pore (translocation), mediated by an electrophoretic force (F_{elec}). Keyser et al. estimated the electrophoretic force as:

$$F_{elec} = \frac{2\pi\epsilon(\Psi(a) - \Psi(R))}{\ln(R/a)} \Delta V, \quad (1.7)$$

where ΔV is the applied bias, R and a are the radius of the pore and the molecule respectively ($a = 1.1$ nm for DNA), the $\Psi(a) - \Psi(R)$ are the surface potentials of the DNA and the nanopore, respectively, and ϵ is the dielectric constant of water. This expression is derived from combining Poisson–Boltzmann and Stokes equations to yield an expression for the electrophoretic force on a stationary molecule²¹⁵. This electrophoretic force leads to the molecule translocating through the pore, generating a current decrease that depends on the topological characteristics and charge of the molecule. This current signal enables the detection of topological features on the DNA, such as the binding of a protein (Figure 6.1c).

Several types of nanopores have been engineered for single-molecule sensing (Figure 6.1d-f). Biological nanopores have been effective in sequencing single-stranded DNA and peptides^{216–218}, but the stochastic nature of molecule entry and the fluctuation in protein motor feed rate present challenges. Solid-state nanopores offer the advantage of controlled pore design and stability, allowing for the detection and characterization of various biomolecules^{212,219}. However, speed control using molecular motors has not been achieved with solid-state nanopores, limiting high-fidelity measurements and resolution. Glass nanopores, although limited by the resolution of the large pore size, yield low noise and high-bandwidth properties with promising detection capabilities for applications to a broad range of molecules^{220–223}. Nanopore technology is evolving fast, but the main challenge remains unsolved - controlling the dynamics of the translocation that influences the accuracy of the measurement and could yield higher spatiotemporal detection.

6.2. Thesis approach to molecular sensing with nanopores

The new concept developed in this thesis is to use the time-resolved SICM system to control spatiotemporally the nanopore position instead of letting the molecule diffuse randomly. Dubbed scanning ion conductance spectroscopy (SICS), we trap the DNA molecule that is tethered on the surface with the electrophoretic force generated by the glass nanopore probe. By moving the nanopore with the precision of the piezo actuator along the molecule length, we can generate a conductance signal in function of distance to detect features down to the angstrom range. The time-resolved SICM was adapted to perform SICS measurements as the following

- 3D nanopositioner to control the velocity of the translocation. The use of a SICM system with a piezo stack actuator enables to control of the position of the nanopore with high precision, defining the velocity for the translocation. This approach decouples the translocation velocity from other experimental factors such as the charge density of the molecule under test, the applied bias voltage, salt concentration, and pH.
- Spatial addressability along the DNA molecule for single-molecule sensing. The capability to move the nanopore in XYZ with nanometer precision allows selecting a specific molecule on the surface and performing a translocation on a specific region along the selected molecule.
- Spatial multiplexing, high-throughput, and single-molecule mapping. the ability to deposit different molecules on a surface in an array (Different conditions/molecules), and probe them with the same pipette that allows a fair comparison between molecules. Moreover, the throughput of our method does not depend on the concentration of the analyte as it does for free translocations. We can perform SICS mapping (In the same fashion as AFM force volume mapping) over a X x Y μm^2 area (up to 100 x 100 μm^2 area in our XY scanner) generating controlled translocation on many different molecules.
- Re-reading capability for single-molecule sensing. The measurements on the same single molecule can be repeated an arbitrary number of times. This enables the averaging of multiple signals from the same molecule, increasing the SNR and accuracy of the translocation fingerprint.
- Glass nanopores for single-molecule sensing. For SICS measurements we need to fabricate small nanopores with electron beam radiation, achieving down to 7 nm radius. This method gives the flexibility to accurately fabricate nanopores with different dimensions depending on the applications. For example, DNA-protein complexes require larger pores in the 20 nm radius range to avoid sticking and DNA gaps require nanopores below 10 nm for higher sensitivity measurements.

The creation of the SICS method shows once more the flexibility of the time-resolved SICM system and controller, which can be modified to perform different types of measurements. The following **Article-Chapter 7** show in more detail the development and validation of the SICS method for single-molecule sensing.

Chapter 7

Spatially Multiplexed Single-Molecule Translocations through a Nanopore at Controlled Speeds

This is a verbatim copy of an article published in Nature Nanotechnology, 2023.

<https://www.nature.com/articles/s41565-023-01412-4>

Leitao, M. S.¹; Navikas, V.²; Miljkovic, H.²; Drake, B.¹; Marion, S.²; Pistoletti, G.³; Chen, K.⁴; Mayer, S.²; Keyser, U.⁴; Kuhn, A.³; Fantner, E. G.^{1,5}; Radenovic A.^{2,5}

1: Laboratory for Bio- and Nano-Instrumentation, Institute of Bioengineering, School of Engineering, EPFL, 1015, Lausanne, Switzerland. 2: Laboratory of Nanoscale Biology, Institute of Bioengineering, School of Engineering, EPFL, 1015, Lausanne, Switzerland. 3: HES-SO Valais-Wallis - Haute Ecole d'Ingénierie, 1950, Sion, Switzerland. 4: Cavendish Laboratory, University of Cambridge, CB3 0HE, Cambridge, United Kingdom. 5: Corresponding author.

Author contribution: I conceptualized and developed the SICS method integrated into the time-resolved SICM system described in Article-Chapter 3. The original idea was conceived by Prof. Aleksandra Radenovic, and refined by Prof. Georg Fantner, Dr. Vytautas Navikas, and me. The system used is the same as presented in Article-Chapter 3, with a modified controller for conductance-volume recordings. I performed SICM measurements with glass nanopores fabricated by Dr. Vytautas Navikas and Helena Miljkovic, on samples designed and prepared by Dr. Pistoletti, Dr. Chen, Mayer, Prof. Keyser, and Prof. Khun. I performed SICS experiments, and data analysis with Dr. Vytautas Navikas and Dr. Sanjin Marion. I designed experiments and wrote the manuscript with Prof. Georg Fantner and Prof. Aleksandra Radenovic.

7.1. Abstract

In current nanopore-based label-free single-molecule sensing technologies, stochastic processes influence the selection of the translocating molecule, translocation rate and translocation velocity. As a result, single-molecule translocations are challenging to control spatially and temporally. Here we present a method using a glass nanopore mounted on a 3D nanopositioner to spatially select molecules, deterministically tethered on a glass surface, for controlled translocations. By controlling the distance between the nanopore and the glass surface, we can actively select the region of interest on the molecule and scan it a controlled number of times and at a controlled velocity. Decreasing the velocity and averaging thousands of consecutive readings of the same molecule increases the signal-to-noise ratio (SNR) by two orders of magnitude compared to free translocations. We demonstrate the method's versatility by assessing DNA-protein complexes, DNA rulers, and DNA gaps achieving down to single nucleotide gap detection.

7.2. Introduction

Biological nanopores have been used to successfully sequence single-stranded DNA (ssDNA) and peptides which is made possible by slowing the speed of the translocation with protein motors^{216,224–227}. However, the stochastic nature of which molecule enters the pore at which time, as well as the residual fluctuation in the feed rate of the protein motor remains challenging²²⁸.

Solid-state nanopores have been engineered to attempt the same molecular detectability of biological nanopores while keeping full control of the pore design and properties in a stable system^{212,219,229–231}. Pores can be tuned to the desired size for the molecules in question, enabling the detection and characterization of a broad range of biomolecules such as double-stranded DNA (dsDNA), proteins and DNA-protein complexes^{212,232}. However, speed control with molecular motors has not yet been demonstrated with solid-state nanopores. Even though the conductance drop in solid-state nanopores can be higher than in biological nanopores, the uncontrolled translocation speed hampers the potentially higher SNR^{233,234}. Therefore, the free translocation speed limits high fidelity measurements, making single base pair resolution along freely translocating dsDNA challenging to achieve.

Uncontrolled velocity limits the temporal and spatial resolution due to a finite amplifier bandwidth and the noise density integrated over the measurement bandwidth⁶⁸. This limitation decreases the signal-to-noise ratio (SNR), critical for detecting small features along the DNA nanostructure²²⁸. High translocation speeds and low SNR on single readings have thus far hampered the use of solid-state devices in the study of complex forms of dsDNA.

Nanocapillaries, referred to as glass nanopores, are well suited for the detection of DNA structures^{235,236} since they have good SNR characteristics for high-bandwidth measurements. Glass nanopores can be manufactured to radii below 10 nm by precisely controlling the diameter of the opening with an electron beam irradiation or by depositing the additional coatings by controllable wet-chemical silanization¹²⁷. They can also be integrated with other techniques, such as optical detection, atomic force microscopy (AFM)^{237,238}, and optical tweezers²³⁹. The latter allows probing force during translocation, but the very high force resolution requires low optical trap stiffness and prevents sub-nanometer displacement control.

Scanning Ion Conductance Microscopy (SICM), on the other hand, has very high accuracy displacement control combined with high-bandwidth, low-noise current sensing. SICM uses a glass nanopore as a probe to image biological surfaces by moving the nanocapillary with nanometer precision towards a surface while measuring the current to detect the sample topography^{17,19,59}. This microscopy method reveals the dynamics of nanostructures on the cell membrane and can be combined with super-resolution fluorescence techniques^{149,172}. Here we utilize the benefits of SICM to overcome the limitations of uncontrolled translocation of DNA through glass nanopores by combining the high SNR and high bandwidth of the glass nanopores with the high degree of displacement control of SICM to achieve accurate, repeated control of single-molecule translocation experiments.

7.3. Results

7.3.1. Single-molecule translocations controlled by nanopositioner

We modified our previously developed high-speed scanning ion conductance microscope (HS-SICM) setup¹⁷² with a closed loop, long-range XYZ piezo scanner to accurately control the pipette motion and perform controlled translocations of spatially multiplexed molecules (Figure 7.1a). Analogously to single-molecule force spectroscopy experiments²⁴⁰ performed by AFM that generate force-distance traces, with SICM, we generate conductance-distance traces of single molecules. We, therefore, refer to our measurements as scanning ion conductance spectroscopy (SICS), a nanopore-based method for controlled translocations. To demonstrate the principle of a controlled translocation with SICS, we used a DNA-dCas9 construct to generate a conductance-distance fingerprint of proteins bound to DNA (Figure 7.1b). In the first step, the pipette approaches the surface. The electrophoretic force captures the tethered molecule detected by a conductance drop, stopping at 200 nm from the surface once the molecule is inside the nanopore (Figure 7.1b-1). Due to the molecule entering the pore, the conductance through the glass nanopore drops. Then, the controlled translocation initiates at the start position and the glass nanopore moves backward with sub-nanometer precision by the closed-loop piezo (Figure 7.1b-2). The measured conductance through the nanopore can then be plotted as a function of

distance along the molecule, and structural features along the DNA molecule can be identified (Figure 7.1b-3), until the end position (Figure 7.1b-4). The controlled translocation generated corresponds to a conductance-distance fingerprint that reveals structural features along the translocated molecule, in this case, a DNA-dCas9 complex (red plot in Figure 7.1b). After this, we can go to a different molecule at a different XY position or scan the same molecule again. We can even stop before reaching step 4, and measure the same region of the molecule multiple times without removing the molecule from the pore. As a proof-of-concept, we performed SICS mapping over a $40 \times 40 \mu\text{m}^2$ area generating 100 controlled translocation traces (10 x 10 array with $4 \mu\text{m}$ pitch), detecting dCas9 binding specificity along the DNA contour length (Figure 7.1b and Figure S7.1). This approach also allowed performing combined fluorescence microscopy and operating at a lower ionic strength, while taking advantage of the tunable size of the glass pores to translocate DNA-protein complexes (see Figure S7.2).

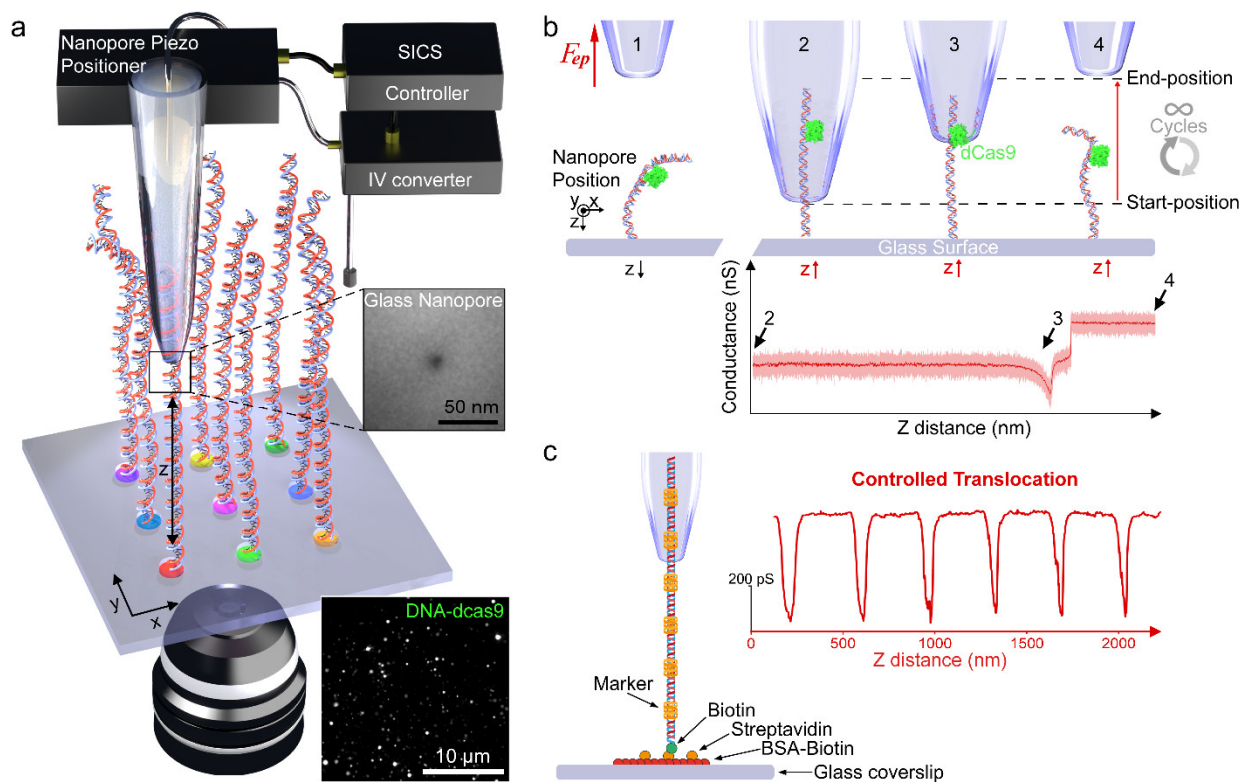


Figure 7.1. Controlled translocations of single molecules with nanopore-based scanning ion conductance spectroscopy (SICS). a) Schematics of the SICS system combined with fluorescence microscopy. Each color represents spatially multiplexed molecules deposited on the glass surface. b) Principle of SICS step-by-step, consisting in the molecule capture (1) followed by controlled translocation (2-4). (1): DNA shortly before capture in the nanopore by an electrophoretic force (F_{ep}) generated by a positive bias (50 – 600 mV). (2): Start-position of the controlled translocation along the DNA length. (3): Identification of a feature. (4): End-position of the controlled translocation followed by thousands of potential translocation cycles on the same molecule or mapping out different molecules upon XY

displacement. The generated data corresponds to a conductance-distance curve revealing the DNA nanostructure, identifying a DNA-dCas9 complex in this case (red curve). 20 nm glass nanopore radius at 1 $\mu\text{m/s}$ translocation velocity, 200 mV bias in 400 mM KCl, pH=7.4. Light red shows a conductance recording at 0.015 samples/nm and dark red trace shows the signal with an average window of 1 nm. c) SICS controlled translocation signature of a DNA ruler in optimal conditions with 8 nm glass nanopore radius at 1 $\mu\text{m/s}$ translocation velocity, signal average window of 1 nm; 300 mV bias in 1 M KCl, pH=7.4. DNA molecules are tethered to a glass surface via biotin-streptavidin binding.

7.3.2. Controlled translocations of molecular rulers

The key difference between our technique and traditional nanopore experiments is how the translocation speed is controlled. In conventional nanopore experiments, the speed of the translocation is determined by the electrophoretic force and the viscous drag of the molecules in the solution and the pore. Translocation speed depends on several factors, such as ionic strength, molecular charge, thermal fluctuations, transient analyte interactions with pore, bias voltage, and nanopore geometry. The result is a stochastic nature of the translocation process. This manifests in non-uniform dwell-time distribution between the detection of equally spaced motifs on a molecule such as a DNA ruler, see Figure S7.3 and 4.4. Free translocations generate conductance signals as a function of time with non-uniform translocation velocity^{236,241}. In addition to stochastic effects influencing the translocation speed, the selection of which molecules are translocated is governed by stochastic factors.

In SICS, however, the molecule of interest is tethered to the surface and the electrophoretic force is countered by a reaction force on the tether, which prevents the molecule from fully translocating. Translocation is solely governed by the motion of the glass nanopore, which can be controlled accurately during the experiment. With the ability to deterministically control the velocity, the conductance traces are now a function of distance instead of time. Figure 7.1c (controlled translocation) shows the equidistant motif on the DNA ruler. This decouples important experimental parameters (ionic strength, bias voltage) and uncontrollable factors (such as nanopore geometry) from the translocation speed and detection bandwidth. We can, therefore, independently optimize experimental parameters to improve the detection limit.

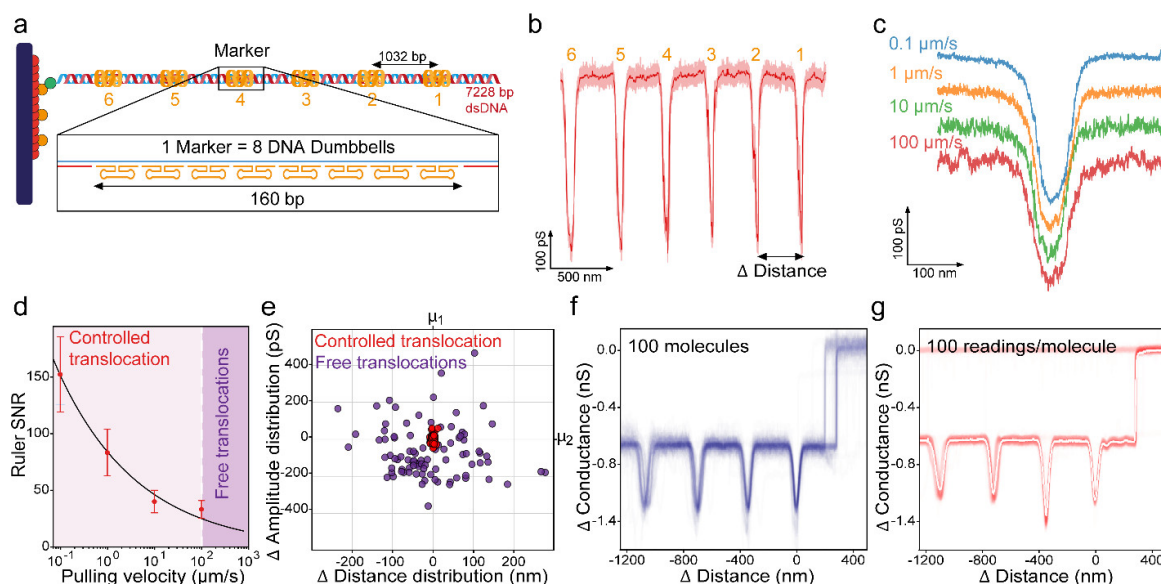


Figure 7.2. Controlled translocation of custom-designed DNA rulers increases SNR, precision, and accuracy. *a)* Design of the DNA ruler construct, composed of 7'228 base pairs with 6 markers containing DNA dumbbell hairpins separated by equal 1032 bp intervals. *b)* Controlled translocation of DNA ruler with 7 nm radius glass nanopore at 1 $\mu\text{m/s}$ translocation velocity. Light red shows a conductance recording at 0.01 samples/nm and dark red trace shows the signal with an average window of 1 nm. Orange numbers above the trace indicate marker location along the DNA ruler. *c)* Controlled translocation at several velocities: 0.1 $\mu\text{m/s}$ (blue), 1 $\mu\text{m/s}$ (orange), 10 $\mu\text{m/s}$ (green) and 100 $\mu\text{m/s}$ (red); 8 nm radius glass nanopore, signal average window of 1 nm. *d)* SNR for the detection of markers at different translocation velocities. The error bars represent the standard deviation and the center is the mean SNR of all markers measured in several molecules ($N = 12, 8, 12, \text{ and } 8$, for 0.1, 1, 10 and 100 $\mu\text{m/s}$ respectively). *e)* Comparison of SICS translocations at 1 $\mu\text{m/s}$ (red) with free translocations (purple) for glass nanopores of the same size (8 nm radius). The plot shows the distribution of the amplitude for marker 1 and the distance between markers 1 and 2 (Black arrows spacing in panel b), centered to the average distance (μ_1) and average amplitude (μ_2), $N = 100$. *f)* Overlay of controlled translocations for several molecules tethered on the surface, $N = 100$; Glass nanopores with radius of 8 nm were used at 1 $\mu\text{m/s}$ translocation velocity, signal average window of 1 nm. Conductance traces were aligned to the first marker from the free-end. *g)* Overlay of controlled translocation of the same molecule (red) and their average (in white), $N = 100$; 8 nm radius glass nanopore at 1 $\mu\text{m/s}$ translocation velocity, signal average window of 1 nm. All controlled translocation experiments were performed with 300 mV bias in 1 M KCl, $\text{pH}=7.4$.

To assess the benefits of SICS we used DNA rulers^{241,242} to characterize the effect of translocation velocity on SNR, precision and repeatability. This DNA ruler is composed of a 7'228 base pair DNA strand (2'458 nm) and 6 markers of DNA dumbbell hairpins which are positioned at 1'032 base pairs intervals along the DNA contour (Figure 7.2a). Figure 7.2b shows the conductance-distance curve generated by SICS, revealing 6 markers.

Controlled translocation with SICS allows decreasing the speed by more than 4 orders of magnitude compared with typical free translocations, leading to an increased SNR (Figure 7.2c). At the lowest velocity of 0.1 $\mu\text{m/s}$, the SNR (conductance amplitude of the ruler divided by the root-mean-square conductance noise of the baseline) measured was 152 ± 33 with an 8 nm glass nanopore radius (Figure 7.2d). This corresponds to an order of magnitude improvement of SNR compared with a free-translocation ($>100 \mu\text{m/s}$ velocity). Figure 7.2e shows a location precision of 1% with controlled translocations, compared with 30% in free translocations with glass nanopores of the same pore size. SICS inherently has lateral control and can map out diverse molecules tethered on the surface (Figure 7.2f) or scan the same molecule again (Figure 7.2g). This spatial addressability allows us to multiplex the measurements to multiple molecular species. In free-translocation, differences in the detected amplitudes cannot be validated at the single molecule level due to the non-uniform translocation speed and limited transimpedance bandwidth (As shown in Figure S7.4). SICS method can identify rare structures and perform several translocations on the same molecule, rather than measuring 100 molecules with assumed identical structure by design (Figure S7.5). If the particular molecule shown in Figure 7.2g had been part of the 100 different molecules measured in Figure 7.2f, the misfolding event would have been lost in the averaging.

7.3.3. Spatial addressability and spatial multiplexing of single molecules

To take advantage of our SICS platform regarding spatial addressability, multiplexing and resolution assessment, we engineered dsDNA that contained single-stranded regions (“DNA gaps”) of various sizes. We custom-designed four different DNA constructs (Figure S7.6) that were 8’750 base pairs in length (2’975 nm) and presented DNA gaps of 80, 40, 20, or 12 nucleotides, corresponding to lengths of 27.2, 13.6, 6.8, and 4.1 nm, respectively (Figure 7.3a). As a proof-of-principle for spatially multiplexed single molecules, we deposited the four different DNA gap constructs in an area of 5 mm \times 5 mm (Figure 7.3b). Within a single experiment, using the same glass nanopore, we detected and discriminated the four different DNA molecules. Figure 7.3c shows distinct conductance amplitudes (ΔG_{gap}) for the different 80, 40, 20, and 12 nucleotides (nt) gaps. Figure 7.3d shows that the measured conductance amplitude of the 80 nt gap (ΔG_{gap}) was half of the dsDNA conductance drop (ΔG_{dsDNA}) as expected, and the measured $\Delta G(\text{dsDNA}/\text{ssDNA})$ ratio was 2.06 ± 0.13 (Figure S7.7). For smaller gap sizes, the measured ΔG_{gap} decreases due to the convolution effects of the pipette geometry with the molecule structure and surface charge. To obtain reliable measurements on the smaller gaps, multiple measurements are desirable.

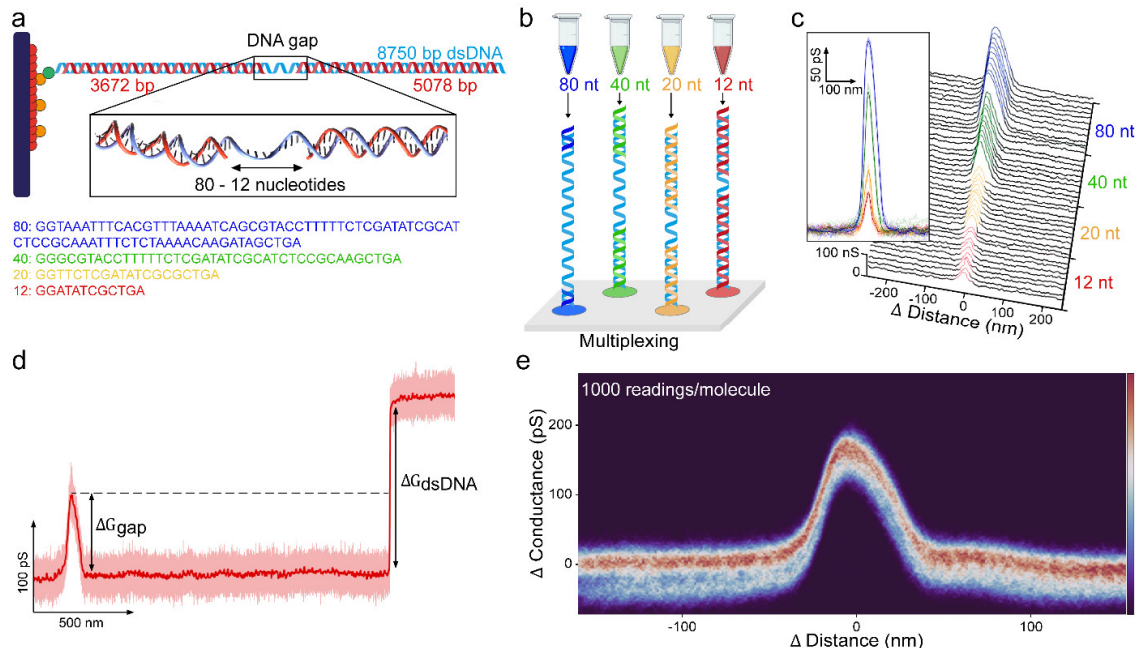


Figure 7.3. Spatial addressability of single-molecule translocations demonstrated on DNA gaps. *a)* Design of DNA gap construct composed of 8750 base pairs and containing a central single-stranded region (“gap”) of 4 different sizes: 80, 40, 20, or 12 nucleotides. *b)* Spatially multiplexed DNA gap molecules. *c)* Controlled translocation signals of DNA constructs with the different nucleotide gaps ($N = 10$ for each gap size molecule with the average in dark color) and corresponding waterfall plot. 8 nm glass nanopore radius at $1 \mu\text{m/s}$ translocation velocity, signal average window of 1 nm. *d)* Controlled translocation of the construct with an 80 nucleotide gap. The conductance amplitude (ΔG_{gap}) of half the dsDNA translocation amplitude (ΔG_{dsDNA}); 12 nm glass nanopore radius at $1 \mu\text{m/s}$ translocation velocity. Light red shows a conductance recording at 0.01 samples/nm and dark red trace shows the signal with an average window of 1 nm. *e)* Probability density map of 1000 readings in the same 80 nucleotide gap region, with a 10 nm glass nanopore radius at $1 \mu\text{m/s}$ translocation velocity, signal average window of 1 nm; the linear colormap represents the normalized probability of occurrence for a conductance value at a corresponding distance, 0 – 1 range. All the experiments were performed with 300 mV bias in 1 M KCl, pH=7.4.

We use the sub-molecular spatial addressability (position the glass nanopore along the single molecule) to scan the same molecular region multiple times, with tunable bias and bi-directional readings (Figure S7.8 and 7.9). Figure 7.3e shows the probability density map of 1000 readings on the same feature (80 nt DNA gap). Asymmetries or differences in the shape of probability density map plots, were more noticeable when smaller diameter pipettes were used and when a large number of curves were recorded for the same molecule. If only 100 curves were used for Figure 7.3e, the asymmetries would be less noticeable (Figure S7.10). By recording and averaging conductance-distance curves of the same feature, we decreased the RMS noise of the averaged signal from 11.2 pS to 0.4 pS,

increasing the SNR 20 times compared with a single reading (Figure S7.11). Moreover, multiple reads of the same feature decreased the measurement error, and obtained an average amplitude of 157.3 pS with a standard error of 0.05 pS (0.03 % error), see Figure S7.11. Thus, our method yielded an SNR of 394 on the DNA gap, corresponding to an improvement of two orders of magnitude compared to free translocations. By accessing specific regions of the DNA molecule and by averaging the conductance fingerprints, we reliably detected gaps as small as 12 nucleotides (4.1 nm) with high SNR. The conductance traces for smaller gap sizes (12 and 20 nucleotides) measured with different pipettes indicate that the dimension of glass nanopores strongly influences the detected conductance drop. Remarkably, we estimated that the pipette's radii below 10 nm hint at an ultimate detection capability down to single nucleotide gaps (Figure S7.12).

7.3.4. Single base gap detection in dsDNA

To have finer control over the gap size, we created a library of oligonucleotides complementary to the DNA gaps (gap adaptors shown in SI Table 1). As a proof-of-concept, we hybridized 79 nt single-stranded DNA (oligonucleotide) to complementary 80 nt DNA gap molecules (DNA gap template) and then deposited the non-hybridized 80 nt DNA gap template on the same area of the substrate (Figure 7.4a). Within a single experiment and the same glass nanopore, we compared controlled translocations on the 80 nt gap template (Figure 7.4b - Top) and the 1 nt gap in the hybridized complex (Figure 7.4b - Bottom). Our results demonstrate the single nt gap detection of SICS, with an average gap amplitude detected of 31.2 pS for a glass nanopore of 7 nm radius. Furthermore, the hybridization does not have to happen before depositing but rather in situ after depositing the template (Figure 7.4c). We demonstrated in-situ hybridization of 19 nt oligo strand with a complementary 20 nt gap, and the subsequent successful detection of the single nucleotide gap with an average gap amplitude detected of 16.9 pS for a glass nanopore of 8 nm radius (Figure 7.4d). This indicates potential applications in diagnostics, DNA data storage and data retrieval²⁴³.

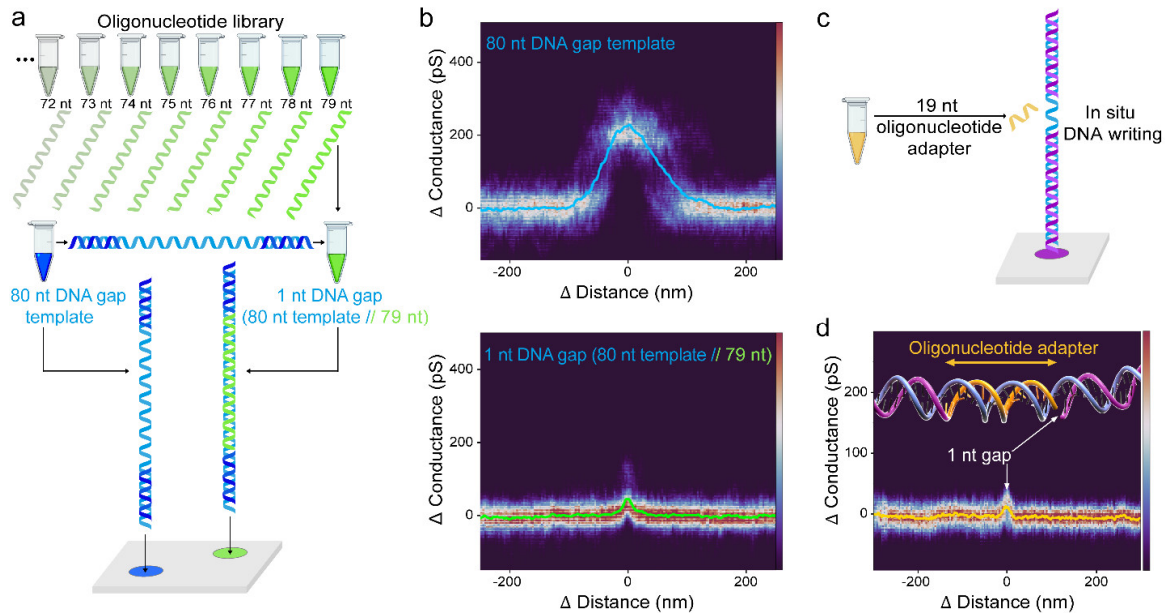


Figure 7.4. Detection of single nucleotide gaps with SICS. *a)* Strategy for creating shorter, variable gap sizes using multi nt gap template and complementary oligonucleotide library. *b)* Detection of an 80 nt DNA gap template (top) and a single nucleotide gap from a complementary 79 nt-long oligonucleotide hybridized to the gap (bottom), with a 7 nm glass nanopore radius at 1 $\mu\text{m/s}$ translocation velocity, 0.01 samples/nm, $N = 10$; the linear colormap represents the normalized probability, 0 – 0.3 range. *c)* In situ hybridization concept for DNA writing, showing a gap template and addition of the complementary oligonucleotide (gap adaptor). *d)* A complementary 19 nt oligonucleotide was hybridized in situ on a 20 nt gap. The colormap represents the normalized probability. Reading of a 1 nt gap with 8 nm glass nanopore radius at 1 $\mu\text{m/s}$ translocation velocity, 0.01 samples/nm, $N = 10$; the linear colormap represents the normalized probability, 0 – 0.5 range. All the experiments were performed with 300 mV bias in 1 M KCl, pH=7.4.

7.4. Discussion

We achieved full control of the translocation speed providing precise spatial and temporal control of the single-molecule experiments, demonstrated in several biomolecule systems such as DNA-protein complexes, molecular rulers, DNA gaps, in-situ oligonucleotide hybridization, and hairpin formation. The translocation control with SICS allows reading the same molecule, or region of a molecule, thousands of times, as well as scanning an array of different types of molecules. This control is independent of experimental parameters (ionic strength, bias voltage) as well as uncontrollable factors (such as nanopore geometry), and it allows for independent optimization of experimental parameters to improve the detection limit, unlocking the use of nanopore sensing in applications that previously required sub-nanometer resolution. For the first time, It was possible to reproducibly scan selected areas of a molecule, thereby addressing specific molecular regions of interest with unprecedented resolution and throughput. We achieved

100'000 readings per experiment and a scanning rate of 4 readings/s on a series of different molecules, each translocated multiple times. The ability to perform experiments with different molecular species within one experiment (see Figure 7.3b), drastically increases the experimental throughput and permits accurate comparison of the results given the identical experimental conditions (same glass nanopore, velocities, and buffer conditions). Besides enabling more detailed biophysical studies, this addressability enables new conceptual approaches to multiplexed diagnostics (multiple analytes on one DNA template) or DNA data storage, where the sample area could be spatially divided into sectors and folders, with the data stored in individual molecules acting as files.

In principle, SICS is able to detect any substrate-conjugated molecule; it has the potential to detect DNA and RNA at very low concentrations. In a diagnostic setting, the main factors determining its concentration detection limit are the efficiency of conjugate binding, the binding kinetics, and the capture efficiency. The demonstrations presented here constitute a fraction of DNA-based systems, and the full extent of molecules and biopolymers that SICS can be applied to are yet to be explored.

Currently, we used glass capillaries shrunken down with SEM to nanopore size. Fabricating these glass nanopores in a reproducible way remains a challenging task. It offers, however, the possibility to tune the nanopore size depending on the application. Whereas we preferred smaller nanopores for our DNA template-based (DNA rulers, DNA gaps) experiments, DNA/protein complexes often require bigger pores. The conical shape of the glass nanopores intrinsically limits the axial resolution of our measurements. Nevertheless, through the drastic increase of SNR, we could detect down to single nucleotide gaps in dsDNA. Additionally, SICS measurements could benefit from the fact that our SICS setup is integrated with a state-of-the-art optical microscope, enabling Förster resonance energy transfer (FRET)²⁴⁴, single-molecule localization microscopy (SMLM)²⁴⁵ and DNA-PAINT (DNA-based Point Accumulation for Imaging in Nanoscale Topography)²⁴⁶ experiments.

Compared to other nanopore detection techniques, glass nanopores are more difficult to parallelize. This drawback, however, is partially mitigated by the ability to do spatial multiplexing, meaning that one glass nanopore could probe thousands of molecules arranged on the surface. The spatial multiplexing combined with the sub-nanometer resolution could be used in conjunction with micro-array technologies to enable screening of DNA, improving point of care devices, or enabling high-density, addressable DNA data storage. The basis of SICS, the mechanical control of the translocation, could also be realized using solid-state nanopores in MEMS devices.

Integrating biological nanopores into the opening of the glass capillary²⁴⁷ could combine the benefits of biological nanopores (high resolution and reproducibility) with the benefits of SICS (molecule independent speed control and multiple readings per molecule). We

expect this to greatly enhance the suitability of nanopores for the sequencing of peptides and proteins.

7.5. Methods

7.5.1. SICS system and controlled translocation measurements

The SICS system is based on a high-speed scanning ion conductance microscope (HS-SICM) that we developed recently¹⁷². We modified our HS-SICM with the addition of a closed loop, long-range XYZ piezo scanner to precisely control the pipette motion and perform mapping curves in a similar way as done in AFM²⁵. This enabled us to spatially select single molecules to translocate them at a controlled speed. In order to capture selected molecules, a bias is applied between two Ag/AgCl electrodes across the glass nanopore used in our system. When a positive bias is applied on the negatively charged DNA molecule tethered on the glass surface, the resulting force will pull the molecule through the nanopore, until the molecule is stretched between the surface and the nanopore. By moving the nanopore with respect to the surface, the conductance signature of the molecule inside the nanopore can be measured as a function of distance along the molecule, detecting specific features on the single molecule. The 3D nanopositioner used to translocate the molecules through the nanopore is a piezo-nanopositioning stage with 10 μm Z travel range and 100 μm X-Y travel range (P-733 Piezo NanoPositioner, Physik Instrumente), driven by a low-voltage piezo amplifier (E-500 Piezo Controller System, Physik Instrumente). The 3D nanopositioner was assembled in a custom-built micro translation stage, mounted atop an inverted Olympus IX71 microscope body. Thus, the SICS system enabled correlative fluorescence microscopy with a four-color (405 nm, 488 nm, 561 nm, 647 nm) pigtailed Monolithic Laser Combiner (400B, Agilent Technologies), controlled by a custom-written LabVIEW software. An integrated sCMOS camera (Photometrics, Prime 95B) and Micromanager software were used to acquire images. The controlled translocation current signal was amplified by a transimpedance amplifier NF-SA-605F2 (100 M Ω gain, NF corporation) with a bandwidth of 10 kHz. The SICS controller was implemented in LabVIEW on a NI USB-7856R OEM R Series (National Instruments, Austin, TX, USA), to perform high-precision conductance-distance measurements and spatial mapping (conductance-volume mapping), similar to AFM force volume mapping²⁴⁰, with a sampling rate up to 1 MHz. The controlled translocations were generated in 0.2 - 1 M KCl solution for bias ranging from 50 mV to 600 mV, while free translocations were generated in 1 M KCl and 4 M LiCl for bias ranging from 500 to 600 mV. Bias below 50 mV prevents the capture of the molecule, while bias above 600 mV leads to frequent contamination events and detachment of molecules.

7.5.2. Data processing and analysis

Controlled translocation curves were processed with a custom-written Python program which was used to automatically filter data, align different molecules, and calculate signal parameters. Single conductance-distance curves were averaged by a savitzky-golay filter with a window size of 1 nm. The root-mean-square conductance noise

(RMS) measured corresponds to the square root of the average squared value of the conductance fluctuations from the mean conductance in a 20 nm range. To calculate the precision and compare controlled translocations with free translocations we used the relative standard deviation: $RSD = (\text{standard deviation} \div \text{average}) \times 100$. Fluorescence image data analysis was performed using Fiji software¹⁵⁶ and AFM images were processed with Gwyddion software¹⁵⁵.

7.5.3. Fabrication and characterization of nanocapillaries

Nanocapillaries were fabricated using a CO₂-laser puller (P-2000, Sutter Instrument). Quartz capillaries with 0.5 mm outer diameter and 0.2 mm inner diameter were bought from (Hilgenberg GmbH). Before the pulling process, all capillaries were cleaned with 99 % acetone, 99 % ethanol, MiliQ water (Millipore Corp), and again with 99 % ethanol by sonication in each solution for at least 10 min. After washing, nanocapillaries were dried in a desiccator for 1-2 h until they were completely dry and cleaned for 10 min in oxygen plasma. After the fabrication, nanocapillaries were characterized by a scanning electron microscope (Zeiss, Merlin). Nanocapillary diameters were confirmed using SEM, and as expected, under relatively high imaging current (400 pA), capillaries under 40 nm shrunk due to electron beam heating-induced effects¹²⁷. Diameters of all nanocapillaries were measured manually based on SEM images, using Fiji software¹⁵⁶. See shrinking procedure and pore radius measurement in Figure S7.13.

7.5.4. Nanocapillary filling procedure

After SEM imaging, nanocapillaries were placed on the cover-glass with double-sided polyimide (Kapton) tape or a specially designed holder fabricated from PEEK plastic. Nanocapillaries were then cleaned with oxygen plasma (Femto A, Diener electronic GmbH) for 300 s at the maximum power setting. Immediately after, the nanocapillaries were immersed in a 400 mM or 1000 mM KCl solution and placed inside the desiccator connected to a vacuum pump. Nanocapillaries were kept under low-pressure (1-10 mbar) for 10 min to pre-fill them and avoid the formation of air bubbles in the thick end of the capillaries. Then they were imaged with an inverted brightfield microscope to confirm pre-filling. After, the nanocapillaries were placed inside a microwave oven (MW 1766 EASY WAVE, P = 700 W, $\lambda = 12.23$ cm). The highest power setting was always used. Microwave radiation was applied in heating cycles to heat the solution until its boiling point. The heating duration varied based on the volume and temperature of the solution. The first heating phase took (30-60 s), and subsequent heating phases were significantly shorter (5-10 s) due to the increased temperature of the capillary immersion solution. Heating was always stopped at the boiling point of a solution in order to minimize evaporation¹²⁷. Short 10-20 s pauses were made in between heating steps to allow for the gas to dissolve into the solution. At least 3 heating cycles were performed to complete the filling of the nanocapillary batch¹⁵³. After the procedure, capillaries were kept at 4 °C and the buffer was exchanged after a few hours to ensure the salt concentration was not affected by evaporation. For storage, nanocapillaries were kept at 4 °C in sealed chambers for up to one year.

7.5.5. Lambda DNA preparation

10 kilobase long λ -DNA was prepared from full-length phage λ -DNA (New England BioLabs) by performing polymerase chain reaction (PCR) using one primer (Microsynth) with a biotin tag on the 5' end and the second one without biotin at the 3'. PCR was performed using a LongAmp DNA polymerase (New England BioLabs) following the protocol from the manufacturer. The reaction mixture was purified using PCR and a Gel Cleanup kit (Qiagen) from the agarose gel according to the protocol from the manufacturer. The length of the 10 kb λ -DNA product was verified with an agarose gel electrophoresis and the concentration was measured with a NanoDrop 1000 spectrometer.

7.5.6. gRNA preparation and immobilization

10kb long λ -DNA was screened for the presence of PAM motifs 5'X20NGG3' and two targets separated by 5374 bp were selected. Single guide RNAs (gRNAs) were designed to be complementary to the 2 adjacent 20 bp PAM motifs previously selected on the λ -DNA. gRNAs were prepared by *in vitro* transcription of dsDNA templates carrying a T7 promoter sequence. Transcription templates were generated by PCR amplification of ssDNA templates containing the T7 binding site, 20 bp sequence complementary to the DNA target site, and sgRNA scaffold sequence using Phusion High-Fidelity DNA Polymerase (New England Biolabs). The gRNAs were synthesized by *in vitro* transcription using the MEGAshortscript T7 Transcription kit (Thermo Fisher) according to the manufacturer's conditions. The gRNAs were treated with Turbo DNase (Thermo Fisher) and MEGAclear Transcription Clean-Up Kit (Thermo Fisher) was used for purification according to the protocol provided by the manufacturer. The concentration of purified gRNAs was measured with a NanoDrop 1000 spectrometer and the length and quality of the sgRNA were estimated by agarose gel electrophoresis. sgRNA samples were kept at -20 °C for a maximum time of 48h until further use.

7.5.7. dCas9-DNA complex formation

A commercially available inactive mutant of Cas9 nuclease (dCas9) with N-terminal SNAP-tag (EnGen Spy dCas9) was acquired from New England Biolabs. The protein was labeled with SNAP-Surface Alexa Fluor 647 labeling kit (New England Biolabs) according to the protocol provided by the manufacturer. The unreacted substrate was removed by the size exclusion column. Finally, fluorescently labeled dCas9 was incubated with gRNA in 1× NEBuffer 3.1 (New England Biolabs). 1 nM dCas9 was incubated with 10 nM gRNA for 30 min at 37 °C on an orbital shaker. 0.5 units of RNase inhibitors (Thermo Fisher) were used to prevent the degradation of RNA. After incubation, DNA was added at the final concentration of 50 pM and the mixture was further kept for 30 min at 37 °C on an orbital shaker. Schematics of the final constructs are shown in Figure S7.1a and dCas9-DNA binding controls were performed with AFM (Figure S7.14).

7.5.8. DNA ruler construct

DNA ruler constructs were prepared using previously published protocol²³⁶. The DNA ruler was synthesized by cutting circular 7249 base M13mp18 ssDNA (New England Biolabs) using the enzymes EcoRI and BamHI to form a linear ssDNA chain 7228 bases in length. The final scaffold was then purified and mixed in a 1:5 ratio with 212 oligonucleotides that formed a double-strand with six equidistant zones of dumbbell hairpins. The mixture is then annealed and purified. The final construct contains 6 markers with 8 dumbbells each. Markers are equally positioned in intervals of 1032 bp (See Figure S7.3).

7.5.9. DNA gap construct

DNA gap constructs were generated using modified 9 kb plasmids. In short, the pPIC9K plasmid (Invitrogen) was mutated using Q5 Site-Directed Mutagenesis (New England BioLabs) to insert two restriction sites specific for the nicking endonuclease Nt.BbvCI (New England BioLabs). Four plasmids were engineered with restriction cut sites that were 80, 40, 20, or 12 nt apart and that flanked an EcoRV restriction site. To generate a specific DNA gap fragment, the corresponding purified plasmid was first linearized by restriction digestion and biotin-labeled using Biotin-11-dUTP (ThermoFisher) and Klenow fragment (New England BioLabs). The DNA fragments were then digested with Nt.BbvCI to obtain single-strand breaks (nicks) and gapped by repeated (3x) heating cycles (90 °C, 60 sec; 60 °C, 10 min; 37 °C, 20 min) in the presence of a single-stranded competitor oligonucleotide (i.e. complementary to the DNA sequence comprised between the nicks)²⁴⁸. Finally, the construct was digested with EcoRV to eliminate ungapped fragments²⁴⁹ analyzed on a 1 % agarose gel and purified (Monarch DNA gel extraction kit, New England BioLabs). The final dsDNA constructs were 8'750 base pairs long with biotin attached on one end, and a gap of 80, 40, 20, or 12 nucleotides (See Figure 7.3 and Figure S7.6). The sequence of the single-stranded stretches in the gap constructs were: 80 nt: GGTAATTTACGTTTAAAATCAGCGTACCTTTTTCTCGATATCGCATCTCCGCAAAATTTCTCTAAAACAAGATAGCTGA; 40 nt: GGGCGTACCTTTTTCTCGATATCGCATCTCCGCAAGCTGA; 20 nt: GGTTCTCGATATCGCGCTGA; 12 nt: GGATATCGCTGA. Occasionally we observed hairpins during SICS experiments in samples measured right after incubation at 4°C (See Figure S7.15).

7.5.10. Oligonucleotide-DNA gap template construct

In order to create gaps of shorter length, we created a library of complementary DNA oligos of different lengths that were hybridized on already existing dsDNA with a gap (See SI Table 1). In this way, we got gaps of smaller sizes that can be found in the table. We hybridized them by mixing the ~9 kb dsDNA gap templates (20, 40, 80) with the oligo (termed gap adaptor) at a 1:100 ratio, and placing it in a thermocycler with the following program: the sample was heated at 70 °C for 5 min and afterward ramped down 1 °C for 1 min per cycle, over 60 cycles.

7.5.11. Imaging chambers for DNA immobilization

The imaging chambers that are compatible with single-molecule fluorescence and single-molecule scanning ion conductance microscopy imaging were fabricated from high precision No. 1.5 borosilicate 25 mm coverslips (Marienfeld). Coverslips were cleaned with ethanol, then MiliQ water, dried with nitrogen flow, and cleaned with oxygen plasma (Femto A, Diener electronic GmbH) at maximum power for 660 s. After cleaning the open circular chamber made from a 1 mL pipette tip was glued on top with polydimethylsiloxane (PDMS), forming the final assembly. Fabricated chambers were kept in sealed petri-dishes until further use. For multiplexing, we made four small chambers (each of 5 μ l volume) located on the same coverslip (see Figure 7.3). In the same way, adopting the robotic spotting methodology used in the preparation of microarrays²⁵⁰, on a single 25 mm coverslip, one could accommodate more than 400 000 samples in the same buffer conditions.

7.5.12. Surface immobilization

100 μ L of 1 mg/ml of BSA-Bt (Sigma-Aldrich) in PBS was incubated for at least 1 h in plasma-cleaned chambers to achieve the full glass surface coverage. Samples then were washed 10 \times with PBS by exchanging half of the solution, but without drying a surface. Samples then were incubated with 0.1 mg/ml of streptavidin (Sigma-Aldrich) for 1 h, followed by a 10 \times wash with PBS. Finally, 10-100 pM of DNA molecules were incubated for 1 h, followed by 10 \times wash with PBS or 3.1 NEBuffer. Samples were kept at 4 $^{\circ}$ C until use. The solution in the imaging chambers was exchanged by performing an additional 10 \times wash before imaging. The final imaging solutions are described in the imaging and SICS sections. We noticed that samples have not shown signs of degradation even after one year if kept at 4 $^{\circ}$ C in sealed petri-dishes that eliminate water evaporation.

7.5.13. Single-molecule fluorescence imaging

To optimize the surface density of DNA and to perform a control of dCas9 binding, samples were first imaged with a single molecule fluorescence microscope¹⁴⁹(See Figure S7.16). For single-molecule imaging and to prevent photobleaching, a reductive/oxidative system (ROXS) based on glucose oxidase and catalase was used. Final buffer composition consisted of 2 mM TROLOX, 40 mM TRIS, 400 mM KCl, 1 % of glucose, 120 units/ml of glucose catalase, 15 units/ml. Buffer was filtered with a 200 nm filter. Imaging was performed in a sealed chamber to avoid oxygen exposure. All chemicals were acquired from (Sigma-Aldrich) unless stated otherwise.

7.6. Supporting information

Figure S7.1. Binding specificity of dCas9 on DNA with SICS.

Figure S7.2. Correlative single-molecule fluorescence and SICS measurement.

Figure S7.3. Design of the DNA ruler construct.

Figure S7.4. Free translocation traces with glass nanopores of a DNA ruler with markers equally spaced along the DNA contour, highlighting the low detectability originated from the uncontrolled velocity.

Figure S7.5. Controlled translocation of 10 molecules, each scanned multiple times. The corresponding average of 10 curves generated in each molecule is shown in white (Averaged to 1 nm).

Figure S7.6. Procedure for custom-designed DNA gaps.

Figure S7.7. Ratio of the dsDNA to ssDNA conductance change for translocations on 80 nt DNA gaps.

Figure S7.8. SICS translocation of the DNA gap construct containing the 80 nt gap, with a tunable bias for a constant speed of 1 $\mu\text{m/s}$.

Figure S7.9. Bidirectional readings with SICS.

Figure S7.10. Probability density map on the same 80 nucleotide gap.

Figure S7.11. Improvement of the translocation SNR and detection of amplitude error by averaging multiple traces from the same feature on the same molecule.

Figure S7.12. Amplitude of the detected gaps (ΔG_{gap}) vs gap length (in nucleotides) with different pipettes represented in different colors.

Figure S7.13. Shrinking procedure and pore radius measurement.

Figure S7.14. Atomic force microscopy imaging of DNA-dCas9 complex.

Figure S7.15. Hairpin formation in DNA gap molecules.

Figure S7.16. Imaging of DNA tethered on a glass coverslip with a widefield fluorescence microscope

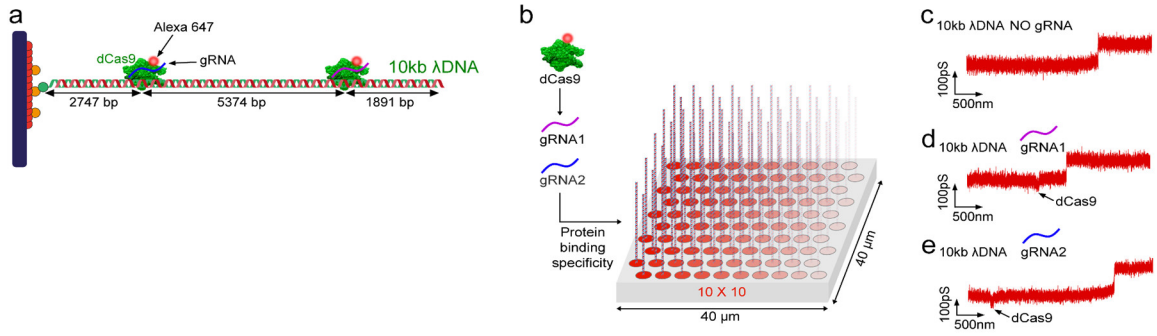


Figure S7.1. Binding specificity of dCas9 on DNA with SICS. a) Design and construct of 10 kb long λ -DNA to test dCas9-DNA complexes with different RNA guides (gRNA). b) SICS mapping (10×10) of DNA-dcas9 complexes over a $40 \times 40 \mu\text{m}^2$ area detecting dCas9 binding specificity. In this proof-of-principle measurement, two gRNA were tested. c) SICS conductance-distance curve of a λ -DNA molecule translocated without dCas9/gRNA. d) Shows the detection of dCas9/gRNA1. e) Shows the detection of dCas9/gRNA2. These experiments were performed with 200 mV bias in 0.4 M KCl, pH=7.4.

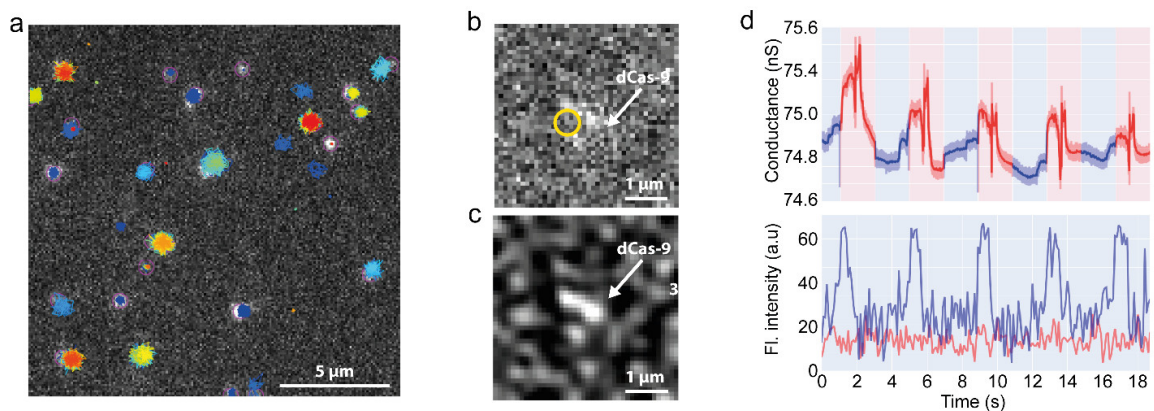


Figure S7.2. Correlative single-molecule fluorescence and SICS measurement. A single widefield image showing the surface-immobilized DNA-dCas9 complex labeled with Alexa-647 dye. a) Single-particle tracks in different colors. b) DNA-dCas9 complex zoom-in. c) Band-passed image from (b) for improved visualization of the protein. d) A repetitive ($n=5$) correlative recording of conductance (top) co-aligned with fluorescence intensity (bottom) measured from the location marked in (b) plotted in blue and fluorescence intensity from the background plotted in red. The conductance signal is inverted in this plot. Light red shows a conductance recording at 0.01 samples/nm and dark red trace shows the signal with an average window of 1 nm. 5 approach-retract curves were acquired at the same spot marked in (b). The yellow circle marked in (b) also signifies the approach point of the glass nanopore. High concentration of free proteins used in the oxygen-scavenging system can influence the conductance signal in SICS, and cause sticking and clogging events.

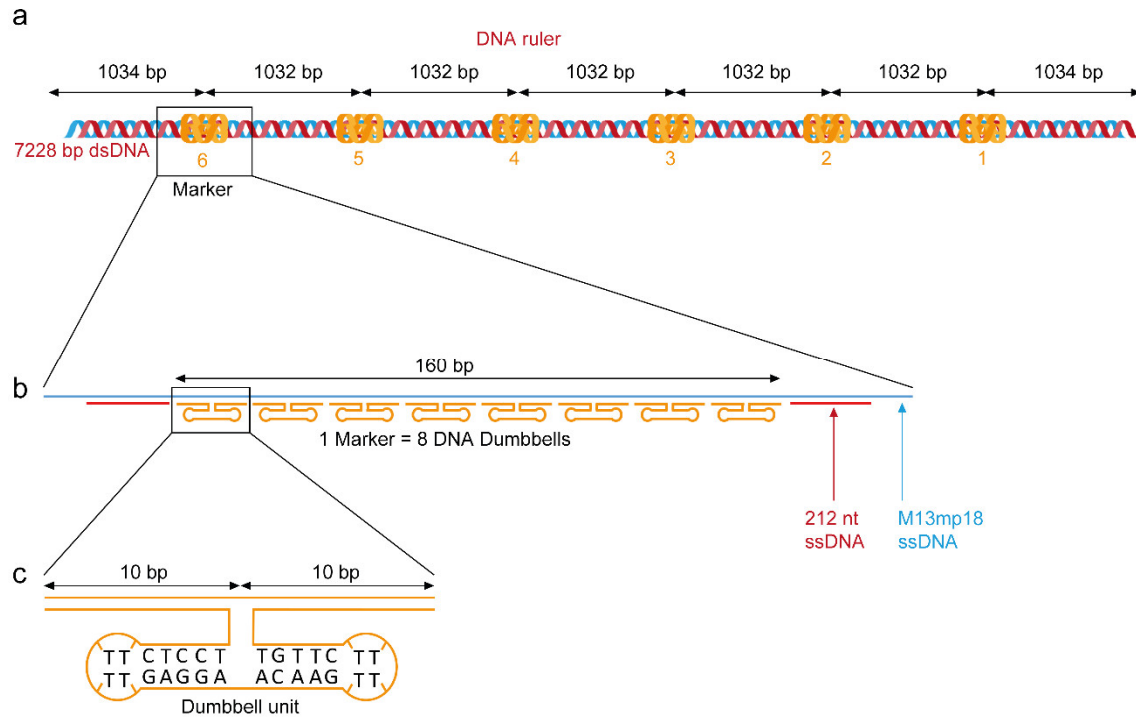


Figure S7.3. Design of the DNA ruler construct. a) Schematic of a DNA structure composed of 7228 base pairs in length with 6 markers separated by equal 1032 bp intervals. b) Each marker contains 8 DNA dumbbell hairpin motifs (in orange), which are joined to the backbone (M13mp18 in blue). The designed dumbbells and the complementary 212 ssDNA (in red) formed the final dsDNA ruler. (see methods section for more details). c) Base sequence of the dumbbell hairpin motif composed of two 10 bp sections.

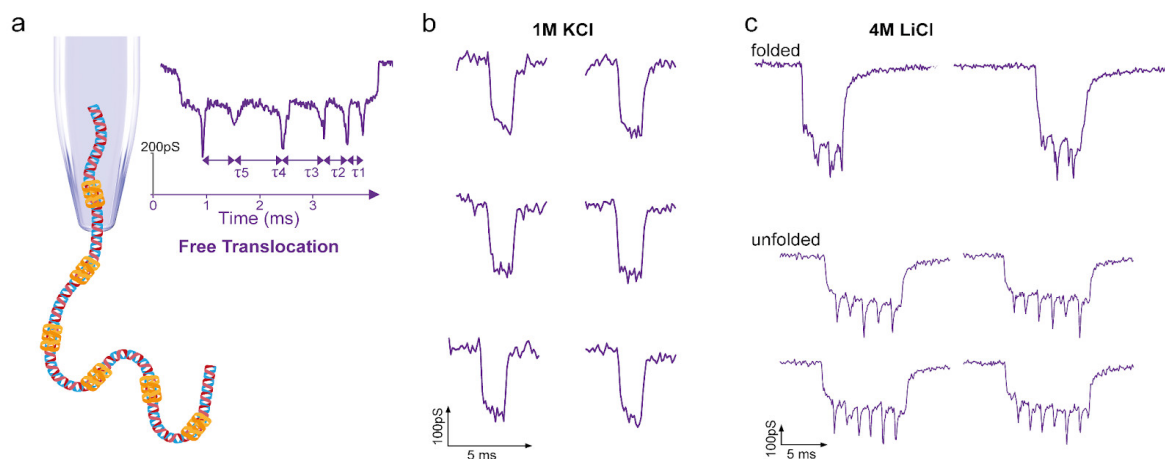


Figure S7.4. Free translocation traces with glass nanopores of a DNA ruler with markers equally spaced along the DNA contour, highlighting the low detectability originated from the uncontrolled velocity. a) Schematic of a free-translocation of a molecule diffused in solution, with the corresponding signature that displays different velocity during translocation (different intra-event intervals τ). b) Free translocations in 1M KCl with 500 mV bias. c) Free translocations in 4 M LiCl. This Figure highlights the challenges of free translocations in detecting topological features along DNA molecules with 600 mV bias. KCl medium has been shown to increase the SNR of the conductance signal compared with other salts (NaCl and LiCl)¹³ but the translocation speed is too high to detect the features. 4M LiCl medium is typically a good alternative to slow down translocation speed, but the detection is still limited and translocations of folded molecules are recurrent (panel b - on top).

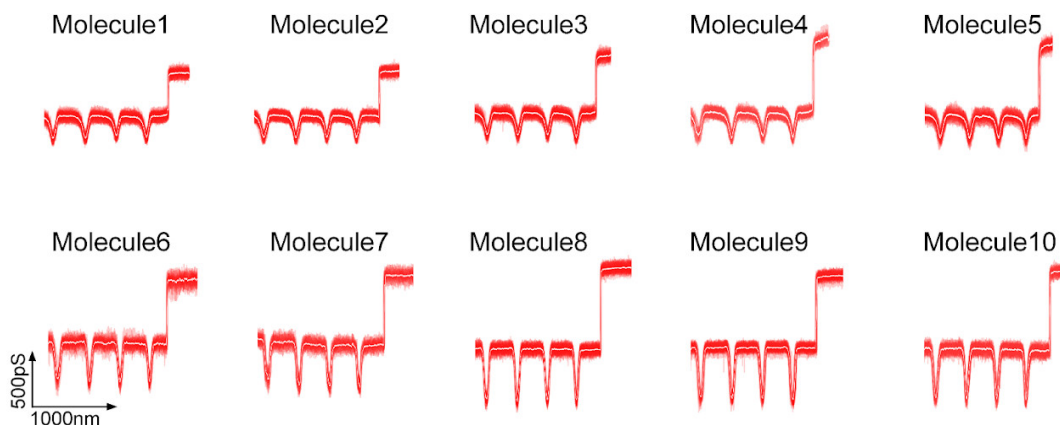
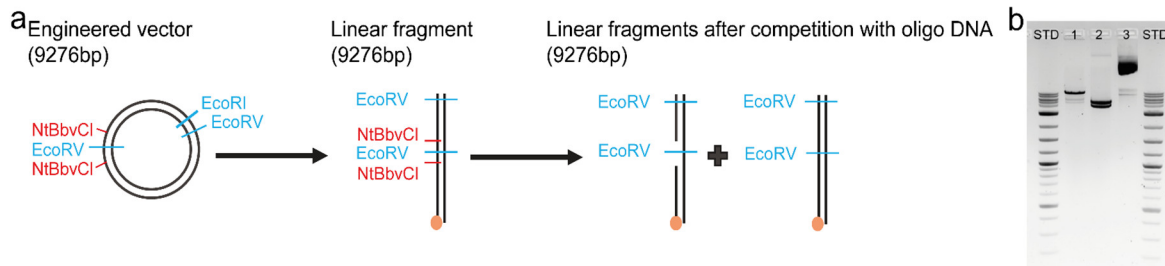


Figure S7.5. Controlled translocation of 10 molecules, each scanned multiple times. The corresponding average of 10 curves generated in each molecule is shown in white (Averaged to 1 nm). Molecules were measured with several pipettes: Molecules 1 and 2 with a 16 nm radius pipette; Molecule 3 with a 14 nm radius pipette; Molecules 4 and 5 were acquired with a 13 nm radius pipette; 6 and 7 with a 10 nm radius pipette; 8, 9 and 10 with a 8 nm radius pipette. Light red shows a conductance recording at 0.01 samples/nm and dark red trace shows the signal with an average window of 1 nm.



*Figure S7.6. Procedure for fustom-designed DNA gaps. a) We modified a 9 kb circular vector to introduce two *Nt.BbvCI* restriction sites flanking an *EcoRV* restriction site. First, the vector is linearized using digestion with *EcoRI*. Digestion with the nicking enzyme *Nt.BbvCI* introduces single-strand breaks in dsDNA and allows for subsequent elimination of the single-stranded DNA comprised between the nicks. The *EcoRV* site between *Nt.BbvCI* sites are used to eliminate ungapped molecules. Indeed, upon successful gap formation, *EcoRV* will not recognize the (now single-stranded) restriction site. In contrast, if gap formation fails and the fragment remains ungapped, digestion with *EcoRV* will generate two fragments of smaller sizes that can easily be eliminated. b) Construct characterization using electrophoresis on an agarose gel. Lane 1: Biotinylated, gapped DNA purified, after additional digestion with *EcoRV*. Additional digestion with *EcoRV* cannot cut DNA at the gap because *EcoRV* only hydrolyzes double-stranded DNA. Thus, the ~9kb fragment is left intact. There might still be a minority fraction of fragments that do not contain the gap which gives rise to two smaller linear fragments (see two faint bands below the main band). Lane 2: If the engineered vector is digested with *EcoRV* before gap formation, it produces two linear fragments, (that appear like a single, thick band on the picture), as expected. Lane 3: Undigested engineered vector.*

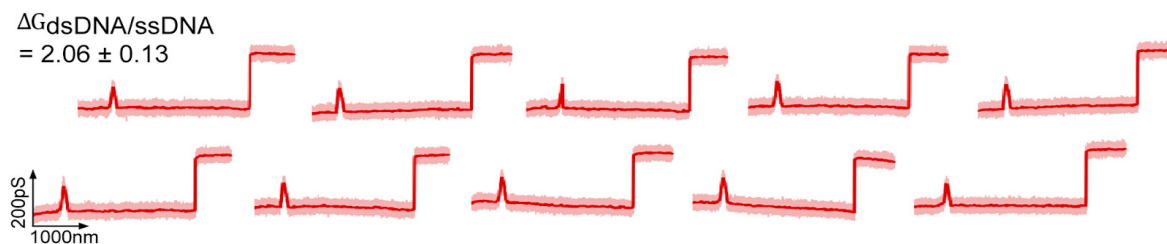


Figure S7.7. Ratio of the dsDNA to ssDNA conductance change for translocations on 80 nt DNA gaps. Light red shows a conductance recording at 0.01 samples/nm and dark red trace shows the signal with an average window of 1 nm. $N=10$.

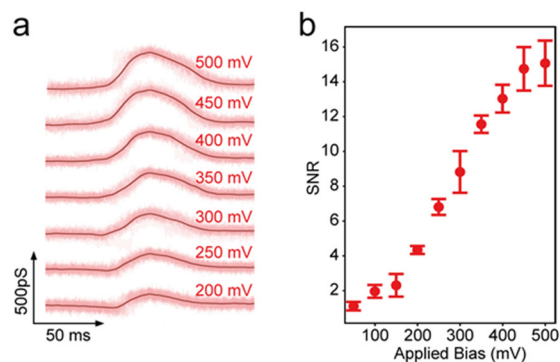


Figure S7.8. SICS translocation of the DNA gap construct containing the 80 nt gap, with a tunable bias for a constant speed of $1 \mu\text{m/s}$. a) SICS curves with a 13 nm radius pipette. In dark red is the average of 10 curves for each bias, and in light red is the overlay of 10 curves, at 0.01 samples/nm. b) SNR of averaged translocations vs applied bias. The error bars represent the standard deviation and the center is the mean SNR of the same detected gap at different bias, $N = 10$ for each bias.

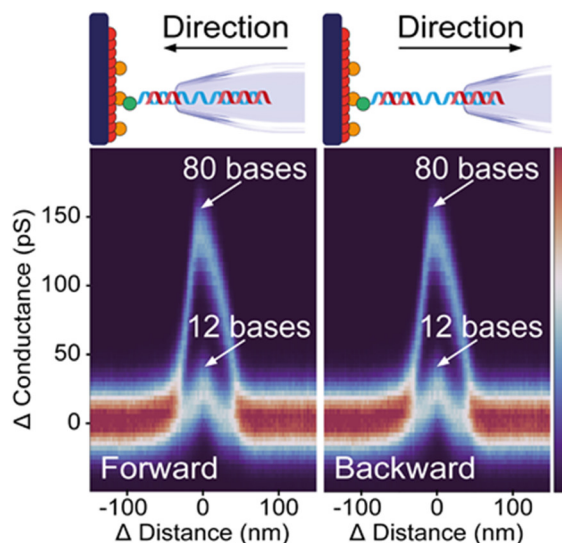


Figure S7.9. Bidirectional readings with SICS. This Figure shows the color-coded probability density map ($N = 100$ curves) of forward (left panel) and backward (right panel) controlled-translocations curves of 80 nt and 12 nt DNA gaps at $1 \mu\text{m/s}$ translocation velocity with 12 nm radius pipette, 0.01 samples/nm, $N = 100$. The colormap represents the normalized probability of occurrence for a conductance value at a corresponding distance, 0 – 0.8 range. The capability to have control over the pulling directionality allowed us to observe DNA hairpins at 4°C see Figure S7.15.

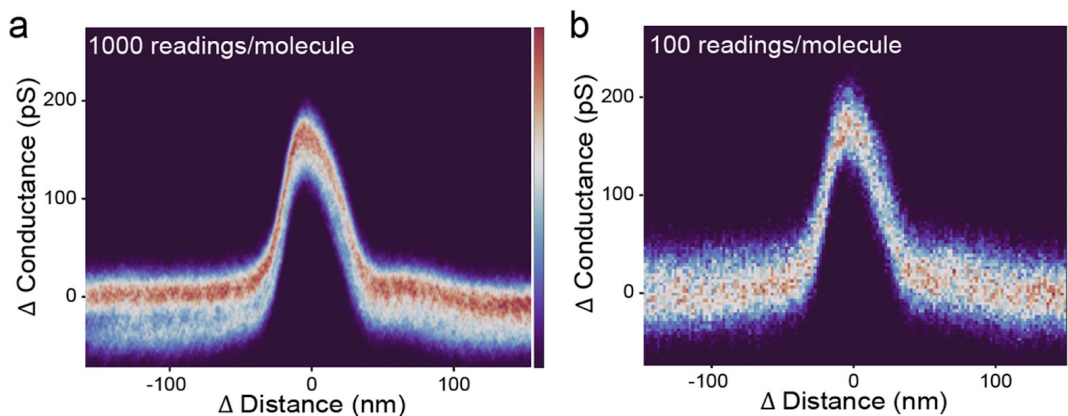


Figure S7.10. Probability density map on the same 80 nucleotide gap. a) 1000 readings/of the same single-molecule molecule. b) 100 readings/of the same single-molecule. The linear colormap represents the normalized probability of occurrence for a conductance value at a corresponding distance, 0 – 1 range. 10 nm glass nanopore radius at 1 $\mu\text{m/s}$ translocation velocity, signal average window of 1 nm.

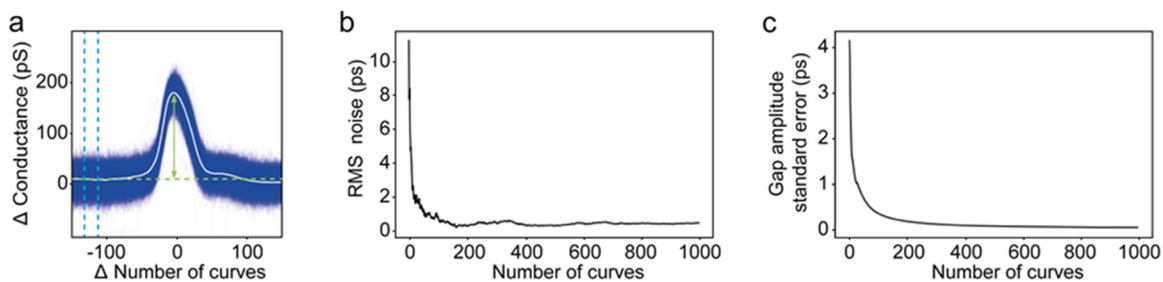


Figure S7.11. Improvement of the translocation SNR and detection of amplitude error by averaging multiple traces from the same feature on the same molecule. a) Average of 1000 curves on the same 80 nt gap at 1 $\mu\text{m/s}$ translocation velocity, recording 0.01 samples/nm with 10 nm radius pipette and 300 mV bias in 1 M KCl. b) RMS noise measured in 20 nm range, blue dashed lines in panel (a). c) Standard error of the detected gap amplitude, green arrows in panel (a).

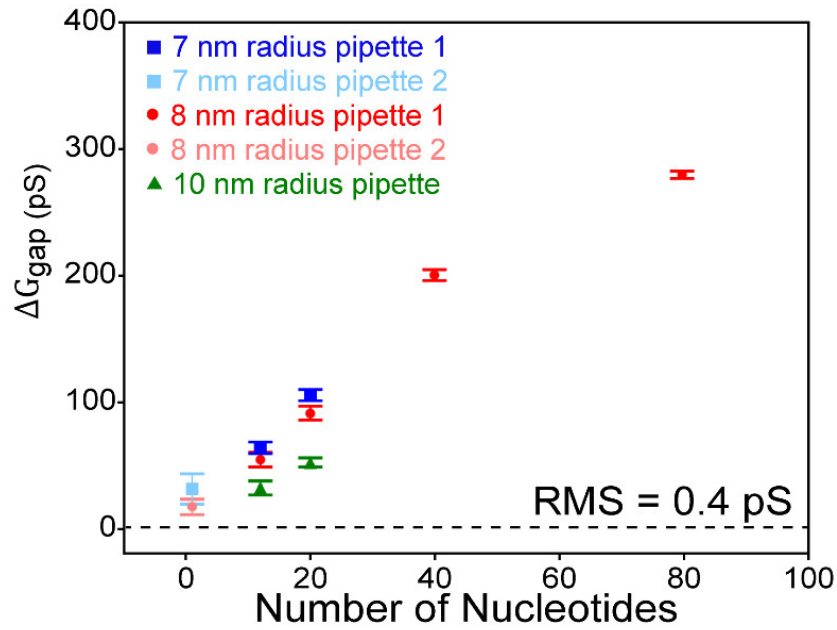


Figure S7.12. Amplitude of the detected gaps (ΔG_{gap}) vs gap length (in nucleotides) with different pipettes represented in different colors. The error bars represent the standard deviation and the center is the mean amplitude of the detected gap ($N = 40$ for 7 nm radius pipette 2, and $N = 10$ for the other pipettes).

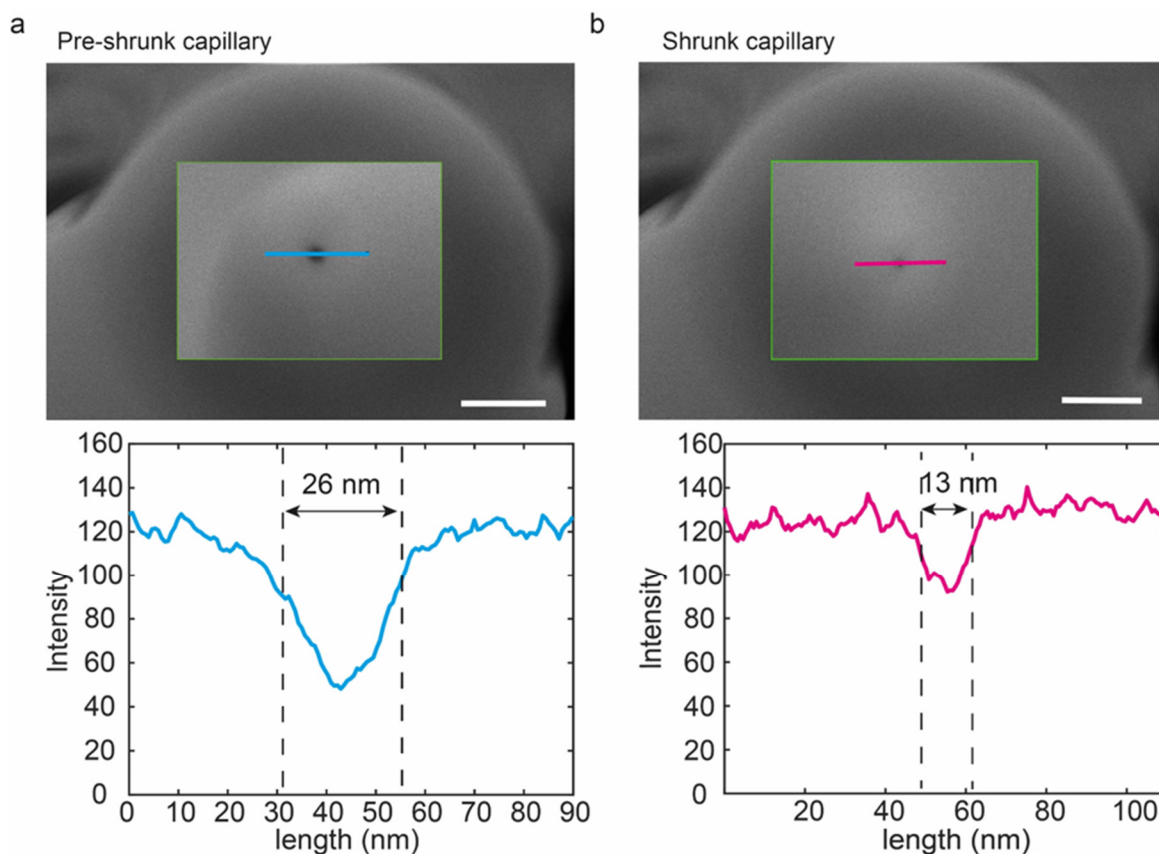


Figure S7.13. Shrinking procedure and pore radius measurement. a) Pre-shrunk capillary and b) Shrunk capillary with their respective intensities across the pore. The pore edge is defined as the point where the intensity drops to 80% of the baseline intensity value. Scale bars = 100 nm.

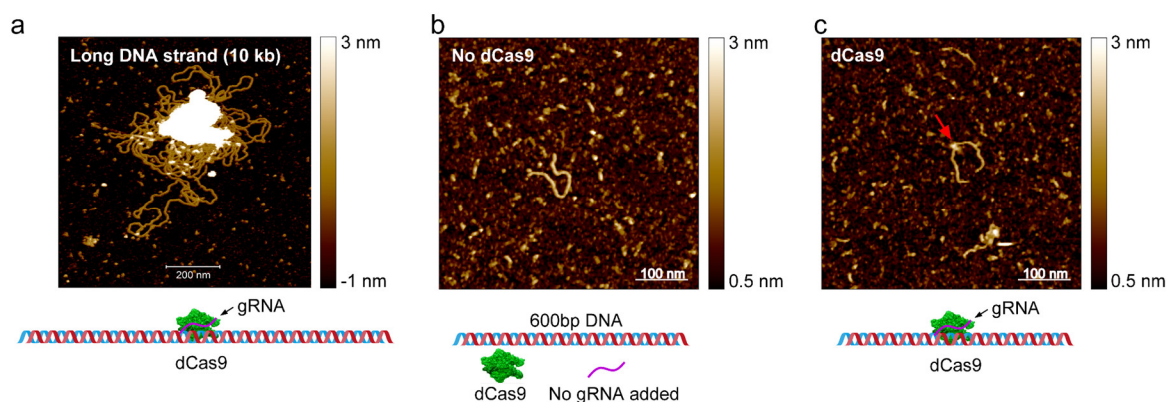


Figure S7.14. Atomic force microscopy imaging of DNA-dCas9 complex. a) AFM image of 10 kb long DNA incubated with dCas9 and gRNA, demonstrating that AFM analysis is not feasible on long DNA molecules. b) A negative control experiment with an absence of gRNA with no observed dCas9 binding. c) A positive control, with gRNA present in a solution with a dCas9 binding event in a field-of-view (red arrow).

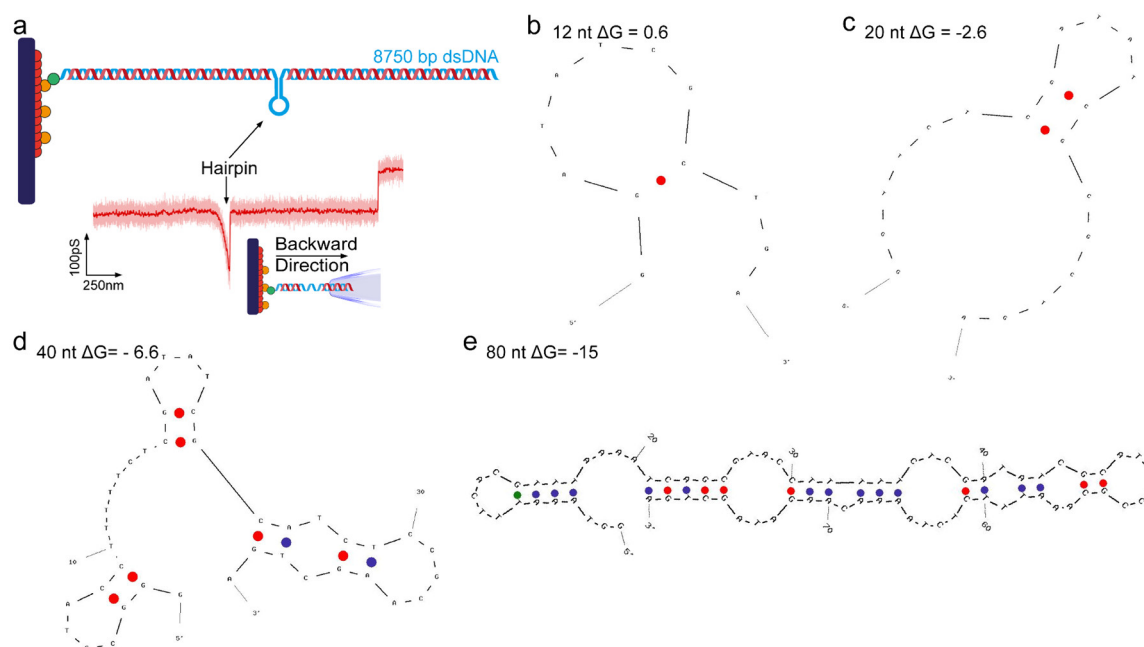


Figure S7.15. Hairpin formation in DNA gap molecules. a) Design of a DNA gap construct (40 nt gap) with the formation of a hairpin and a SICS conductance-distance curve in red. Light red shows a conductance recording at 0.01 samples/nm and dark red trace shows the signal with an average window of 1 nm. Prediction of secondary structures and Gibbs free energy values (ΔG) at 4°C for the sequences of the single-strand DNA stretch in four DNA gap constructs: 12 nucleotide gap b), 20 nucleotide gap c), 40 nucleotide gap d), and 80 nucleotide gap e). This Figure highlights the formation of hairpins that were observed during SICS experiments, in samples measured right after incubation at 4°C. The experiments were performed with 300 mV bias in 1 M KCl. The bidirectional capability of SICS (Figure S7.9) is relevant in this application as it allows us to exploit the balance between drag and electrophoretic force. Decreasing the total force acting on the molecule in the backward direction allowed us to observe a prominent peak (a) that we assigned to the hairpin formation. In forward direction, the total force is high enough that our data are similar to the results shown in the main Figures after samples have been brought to room temperature (Figure 7.3 and 7.4).

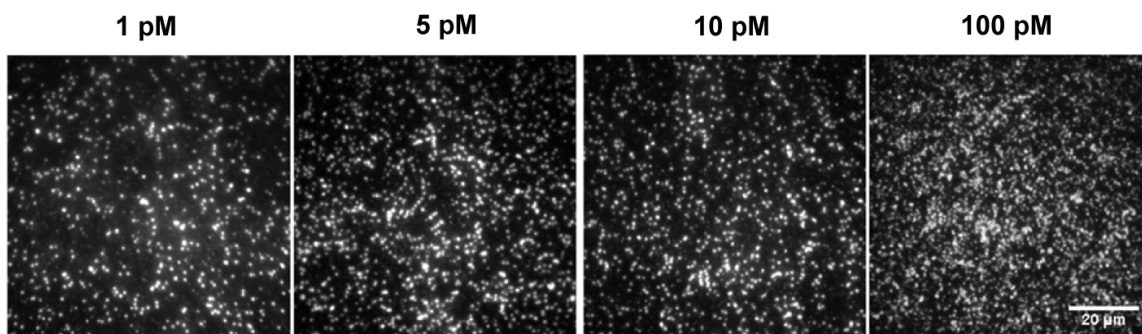


Figure S7.16. Imaging of DNA tethered on a glass coverslip with a widefield fluorescence microscope. The different BSA-Bt tether concentrations indicated above (1, 5, 10, 100 pM). 100 pM DNA solution and 5 nM YOYO-1 dye was used for all experiments. DNA surface densities were calculated using a single-molecule localization approach. DNA surface density values were found to be (from left to right): 0.09, 0.22, 0.24, 0.44 DNA molecules per μm^2 .

Chapter 8

Conclusion and Future Developments

8.1. Time-resolved SICM instrumentation for high-speed imaging

The main achievement of the thesis was the development of a time-resolved SICM microscope from concept to prototype to spatiotemporally resolve biological processes. The new design and instrumentation integration resulted in a microscope that can visualize 3D processes at sub-5nm axial resolution on the cell membrane for temporal ranges of sub-second to days without interfering with the live cell.

Researchers have shown that SICM does not need to be a slow imaging technique, in our high-speed SICM approach I intended to expand other capabilities that are important to study processes on live cells but constraint the high-speed design. The design constraints were addressed by implementing advances in nanopositioning, controls theory, microelectronics, and nanopore fabrication. The nanocapillary probe actuator was designed to maximize the actuation range and the resonance frequency for the probe nanopositioning. To control the probe positioning at high-speed, I implemented an adaptive hopping mode and data-driven controller for fast probe actuation without exciting resonances. In addition, I integrated a high-gain, low input-noise, bandwidth extended CMOS transimpedance amplifier to convert pico-ampere current-to-voltage that improved the setpoint detection on biological surfaces. These implementations enabled large imaging volumes of $100 \times 100 \times 20 \mu\text{m}^3$ in the XYZ dimension while keeping a fast probe actuation. For high-resolution imaging, I utilased glass nanopores with a 10-15 nm radius that were fabricated using an electron beam. The integration of these methods resulted in the development of a high-speed SICM system that can generate images up to 0.5 ms per frame while maintaining cell viability during measurements. With the implementation of this system, I was able to monitor and analyze nanoscale processes through high-speed imaging and gain insights into the intricate dynamics of cellular networks through large imaging volumes.

The ultimate goal of microscopists is to augment human visual capabilities to perceive objects beyond the limits of naked-eye resolution. Remarkable advancements have been made in super-resolution microscopy, electron microscopy, and scanning probe microscopy to achieve exceptional levels of resolution. Nevertheless, many high-resolution imaging techniques generate images that are not readily comprehensible to the human brain. SEM in a noteworthy example of microscopy which produces instantly recognizable 3D images due to our brain's innate ability to interpret them as three-dimensional objects with lighting and shading. This is a key factor contributing to the widespread utilization of SEM as a high-resolution microscope. Thus, another important aspect of the SICM system

presented here is data visualization, as I developed a display process that produces easily recognizable 3D images.

8.2. Time-resolved SICM for studying live cell biology at the nanoscale

To demonstrate the new imaging capabilities of time-resolved SICM, I collaborated with cell biologists and microbiologists to study dynamic processes on cell membranes, morphological changes in cancer cells, and host-mammalian cell infection with bacteria. I was able to track the dynamics of circular dorsal ruffles (CDRs) that impact cell infection and cancer progression but whose mechanisms of formation are poorly understood. I resolved the 3D structure of CDR assembly with unprecedented three-dimensional resolution at fast frame rates, co-localizing the formation of stress fibers with the ring wave's dynamics. Visualizing these structures in great detail opens the doors for comprehensive and quantitative biophysical studies of CDR mechanisms of formation, as previous fluorescence microscopy approaches lacked axial resolution²⁵¹. It will help researchers to better understand how these internalization processes are hijacked by pathogens such as viruses and bacteria to infect humans. In addition, I also followed morphological changes in melanoma cells upon treatment with Forskolin, a drug shown to reduce resistance to immunotherapy¹⁴³. Our data revealed a substantial increase in the surface area after treatment that possibly indicates increased immunogenicity, yielding higher success rates in the treatment. Another relevant application was imaging bacteria-host infection in the human cell membrane. Time-resolved SICM enabled the visualization of bacterial adhering and dividing directly on the host cell membrane. The observations suggest that these engulfment processes could be related to bacteria shape that triggered the internalization through the human cell. It points to a critical role of the 3D structure of bacteria in successfully infecting cells and highlights how time-resolved SICM has the potential to study elusive mechanisms of infection.

8.3. Combined super-resolution optical imaging with time-resolved SICM

Another significant contribution of the thesis was combining time-resolved SICM with super-resolution fluorescence. In this collaborative project with Radenovic lab, I implemented a SR method based on SOFI into the SICM system to perform 3D imaging with mitigated phototoxic effects, requiring low laser intensity and acquisition time. While SOFI provided the visualization of the cytoskeleton protein architecture with a lateral resolution of 72 ± 3 nm, time-resolved SICM provided structural information on cell membrane morphology, such as microvilli and filopodia (with lateral resolution in the same range as SOFI and axial resolution below 5 nm). To demonstrate the capabilities of the combined method, I performed imaging to correlate membrane surface dynamics (TR-SICM) with actin cytoskeleton architecture (SOFI) in living cells with subdiffraction

resolution. I showed that time-resolved SICM could be efficiently combined with SR methods to become a routine tool in studying membrane processes of living cells. However, only short-period processes can be imaged, as the phototoxic effects of SR imaging were still obvious for prolonged imaging time. Hence, the integration of SICM and fluorescence imaging for high-resolution analysis in live cell studies is still in need of significant advancements to effectively investigate extended-time processes, such as morphological changes and cytoskeleton rearrangement in cellular differentiation.

8.4. Single-molecule spectroscopy with time-resolved SICM

The outcome of the thesis goes beyond imaging of living cells with the development of a high-speed SICM system; Time-resolved SICM is also a nanoprobe-positioning platform that can be modified and adapted to a broad range of measurements, from tissue and live cell imaging to single-molecule spectroscopy. The final significant result of the thesis was adapting the time-resolved SICM to control and detect individual molecules with unprecedented precision. This new type of measurement is dubbed scanning ion conductance spectroscopy (SICS). SICS overcomes critical limitations in nanopore technology by enabling a controlled translocation with constant velocity and averaging thousands of readings on the same molecule. I showed that the system can perform up to 100,000 readings per experiment, it can generate translocations at a scanning rate of 4 readings/s, and it can detect features in DNA down to 3-angstrom. I also showed the application of SICS to detecting topological features in complex DNA structures, demonstrated on DNA-dCas9 complexes, hairpin formation, molecular rulers, and dsDNA gaps, achieving single-base gap detection in dsDNA for the first time reported. SICS's precision and detection capabilities promise exciting applications in several fields, from biophysics to diagnostics and peptide sequencing. Nevertheless, in this demonstration, I used the inherent glass nanopore of SICM nanocapillary probe. Macazo et al. and Shi et al. have shown the integration of ion channels into the SICM probe^{252,253} which highlights the possibilities of integrating biopores in the SICS system for expanded the applications such as peptide sequencing.

8.5. Future developments

Time-resolved SICM is a promising tool for studying nanoscale processes in cell biology and single molecules. Nevertheless, the temporal resolution has margin to be improved, as acquiring images at faster frame rates is essential to track biological processes. The mechanical actuator can be redesigned to extend the resonance of 13 kHz, increasing the effective hopping rate without exciting resonances. In addition, the transimpedance amplifier implemented in the system can also be improved in terms of input noise to increase the signal-to-noise (SNR) ratio. Improving the SNR during scanning will benefit the performance of the adaptive hopping and help in integrating efficient SICM scanning

controllers. The implemented adaptive hopping mode scanning controller can also be improved by predicting the approach-curve shape to detect the surface position more accurately. These improvements would ultimately lead to faster image acquisition and higher resolution.

The combination of SICM with super-resolution optical microscopy is a promising area that will offer new insights into eukaryotic membrane processes with three-dimensional nanometer detail. However, SR methods have a significant negative impact on cell viability. Combining SICM with immersing optical techniques that are less phototoxic while keeping a high resolution in the axial direction is the key to future applications in live cell imaging. Additionally, the SICM field has developed rapidly in recent years, with many additional measurement capabilities being added, such as sample stiffness, surface charge, and local pH. Combining these developments with time-resolved SICM will provide further insights into biological processes at the nanoscale.

This thesis also addresses single-molecule detection with SICM. The ability to control the translocation speed and multiple average readings of the same molecule has resulted in two orders of magnitude increase in signal-to-noise ratio compared to conventional free translocation. Nevertheless, the SNR could be potentially improved with AC modulation and the fabrication of smaller pores. Moreover, the increased detection capability with SICS demonstrated with glass nanopores can be transferable to other solid-state and biological nanopore methods, which could significantly improve diagnostic and sequencing applications. Besides enabling more detailed biophysical studies in dsDNA systems, this method will be particularly beneficial for high-throughput screening (HTS) assays, point-of-care devices, and high-density, addressable DNA data storage. SICS also shows great potential for implementation in single protein sequencing and identification of posttranslational modifications.

Another important future direction is turning the time-resolved SICM system into an open-source technology platform. This thesis already shows the flexibility of adapting the time-resolved SICM from topography imaging to multiparametric and single-molecule spectroscopy, which are entirely different measurements, even though implemented in the same system. Sharing designs and documentation with the scientific community will help researchers adapt our microscope to different applications.

Chapter 9

Scientific Contributions

In this section, the description of my scientific contributions during my doctoral studies and thesis work is listed below chronologically.

1. Reducing Uncertainties in Energy Dissipation Measurements in Atomic Force Spectroscopy of Molecular Networks and Cell-Adhesion Studies.

Biswas, S.*; **Leitao, M. S.***; Theillaud, Q.; Erickson, B.; Fantner, E. G.;
Scientific Reports **2018**, 8, 9390.

I am the co-first author of this manuscript. I contributed to the development of the Matlab script for correcting energy dissipation measurement. I designed and performed force spectroscopy experiments on cell-adhesion studies. I performed data analysis and made figures. I wrote the manuscript with Soma Biswas.

2. High-Throughput Nanocapillary Filling Enabled by Microwave Radiation for Scanning Ion Conductance Microscopy Imaging.

Navikas, V.; **Leitao, M. S.**; Marion, S.; Davis, S.; Drake, B.; Fantner, E. G.;
Radenovic, A.;
ACS applied Nano Materials **2020**, 3, 8, 7829-7834. 2020.

I designed experiments to record and understand the process behind the nanocapillary filling process enabled by microwave radiation. I built a custom-made nanocapillary imaging chamber to record in real-time the filling process. I performed electrical characterization of the nanocapillaries and SICM imaging with the small glass nanopores.

3. Time-Resolved Scanning Ion Conductance Microscopy for Three-Dimensional Tracking of Nanoscale Cell Surface Dynamics.

Leitao, M. S.; Drake, B.; Pinjusic, K.; Pierrat, X.; Navikas, V.; Nievergelt, A.;
Brillard, C.; Djekic, D.; Radenovic, A.; Persat, A.; Constam, S.; Anders, J.; Fantner,
E. G.;
ACS Nano **2021**, 15, 11, 17613–17622.

I am the first author of this manuscript, presented as a main contribution in the thesis, **Article-Chapter 3**.

4. Correlative 3D Microscopy of Single Cells using Super-Resolution and Scanning Ion-Conductance Microscopy.

Navikas, V.*; **Leitao, M. S.***; Grussmayer, K.; Descloux, A.; Drake, B.;
Yserentant, K.; Werther, P.; Hertel, D.; Wombacher, R.; Radenovic, A.; Fantner,
E. G.;
Nature Communications **2021**, 12, 4565.

I am the co-first author of this manuscript, presented as a main contribution in the thesis, **Article-chapter 5**.

5. Structural Diversity of Photoswitchable Sphingolipids for Optodynamic Control of Lipid Raft Microdomains.

Hartrampf N.*; **Leitao, M. S.***; Winter N.; Toombs-Ruane, H.; Frank, J.; Schwille, P.; Trauner, D.; Franquelim, H;
Biophysical Journal **2023**, S0006-3495(23)00135-2.

I am the co-first author of this manuscript. I designed the biophysical experiments on biomembrane models with Hartrampf and Franquelim, performed high-speed AFM imaging, and analyzed the data. I developed a custom-made Matlab script to identify and quantify properties in membrane microdomains, from confocal and AFM images.

6. Label-Free Long-Term Methods for Live Cell Imaging of Neurons: New Opportunities.

Baricevic, Z.*; Ayar, Z.*; **Leitao, M. S.**; Mladinic, M.; Fantner, E. G.; Ban, J.;
Biosensors **2023**, 13(3), 404.

I performed correlative microscopy with SICM on neurons, shown in this manuscript. I have also proofread and corrected the manuscript.

7. Spatially Multiplexed Single-Molecule Translocations through a Nanopore at Controlled Speeds.

Leitao, M. S.; Navikas, V.; Miljkovic, H.; Marion, S.; Pistoletti, G.; Chen, K.; Mayer, S.; Keyser, U.; Kuhn, A.; Fantner, E. G.; Radenovic A.;
Nature Nanotechnology **2023**.

I am the first author of this manuscript, presented as a main contribution in the thesis **Article-chapter 7**.

8. OpenSIM: Open Source Microscope Add-On for Structured Illumination Microscopy.

Hannebelle, T. M*; Raeth, E.*; **Leitao, M. S.**; Lukeš, T.; Pospíšil, J.; Toniolo, C.; Venzin, F. O.; Chrisnandy, A.; Bichon, N.; P. Swain, P. P.; Ronceray, N.; Lütolf, P. M.; Oates, C. A.; Hagen, M. G.; Lasser, T.; Radenovic, A.; McKinney, D. J.; Fantner, E. G.;
Under review.

I integrated the structured illumination microscopy (SIM) developed by Hannebelle and Raeth into the time-resolved SICM system and performed correlative imaging. I processed SIM data with denoising artificial intelligence and compared it with traditional SIM reconstruction algorithms. I made figures and contributed to the writing of the manuscript.

9. Open source research-grade Scanning Probe Microscope Controller.

Kangul, M.; Asmari, N.; Penedo, M.; Nievergelt, A.; Brillard, C.; **Leitao, M. S.**;
Hug, H.; Fantner, E. G.;

In preparation.

I integrated the SICM adaptive hopping controller, and other control modules into the open-source hardware developed at LBNI.

10. High-Speed Scanning Ion Conductance Microscopy with Adaptive Hopping-Mode.

Leitao, M. S. *; Drake, B. *; Shih, J.; Asmari, N.; Andany, S.; Nievergelt, A.;
Kangul, M.; Fantner, E. G.;

ACS Nano **2021**, 15, 11, 17613–17622.

In preparation.

I developed the high-speed SICM system with Barney Drake. In this manuscript, we are describing in detail all the mechanical parts of the instrument and the adaptive hopping mode.

*Equal contribution

Bibliography

- (1) Pollard, T. D. Cell Motility and Cytokinesis: From Mysteries to Molecular Mechanisms in Five Decades. *Annual Review of Cell and Developmental Biology*. Annual Reviews Inc. October 7, 2019, pp 1–28. <https://doi.org/10.1146/annurev-cellbio-100818-125427>.
- (2) Alvarado, A. S.; Yamanaka, S. Rethinking Differentiation: Stem Cells, Regeneration, and Plasticity. *Cell* **2014**, *157* (1), 110–119. <https://doi.org/10.1016/j.cell.2014.02.041>.
- (3) Derby, M. C.; Gleeson, P. A. New Insights into Membrane Trafficking and Protein Sorting. *Int. Rev. Cytol.* **2007**, *261*, 47–116. [https://doi.org/10.1016/S0074-7696\(07\)61002-X](https://doi.org/10.1016/S0074-7696(07)61002-X).
- (4) Alberts, B.; Johnson, A.; Lewis, J.; Raff, M.; Roberts, K.; Walter, P. *Molecular Biology of the Cell*, 4th ed.; Garland Science, 2002.
- (5) Bagheri, N.; Carpenter, A. E.; Lundberg, E.; Plant, A. L.; Horwitz, R. The New Era of Quantitative Cell Imaging—Challenges and Opportunities. *Mol. Cell* **2022**, *82* (2), 241–247. <https://doi.org/10.1016/j.molcel.2021.12.024>.
- (6) Wu, Y.; Shroff, H. Multiscale Fluorescence Imaging of Living Samples. *Histochem. Cell Biol.* **2022**, *158* (4), 301–323. <https://doi.org/10.1007/s00418-022-02147-4>.
- (7) Shroff, H.; Galbraith, C. G.; Galbraith, J. A.; Betzig, E. Live-Cell Photoactivated Localization Microscopy of Nanoscale Adhesion Dynamics. *Nat. Methods* **2008**, *5* (5), 417–423. <https://doi.org/10.1038/nmeth.1202>.
- (8) Balzarotti, F.; Eilers, Y.; Gwosch, K. C.; Gynnå, A. H.; Westphal, V.; Stefani, F. D.; Elf, J.; Hell, S. W. Nanometer Resolution Imaging and Tracking of Fluorescent Molecules with Minimal Photon Fluxes. *Science* **2017**, *355* (6325), 606–612. <https://doi.org/10.1126/science.aak9913>.
- (9) Power, R. M.; Huisken, J. A Guide to Light-Sheet Fluorescence Microscopy for Multiscale Imaging. *Nat. Methods* **2017**, *14* (4), 360–373. <https://doi.org/10.1038/nmeth.4224>.
- (10) Keller, P. J.; Schmidt, A. D.; Wittbrodt, J.; Stelzer, E. H. K. Reconstruction of Zebrafish Early Embryonic Development by Scanned Light Sheet Microscopy. *Science* **2008**, *322* (5904), 1065–1069. <https://doi.org/10.1126/science.1162493>.
- (11) Wu, Y.; Ghitani, A.; Christensen, R.; Santella, A.; Du, Z.; Rondeau, G.; Bao, Z.; Colón-Ramos, D.; Shroff, H. Inverted Selective Plane Illumination Microscopy (ISPIM) Enables Coupled Cell Identity Lineaging and Neurodevelopmental Imaging in *Caenorhabditis Elegans*. *Proc. Natl. Acad. Sci. U. S. A.* **2011**, *108* (43), 17708–17713. <https://doi.org/10.1073/pnas.1108494108>.
- (12) Wang, T.; Ouzounov, D. G.; Wu, C.; Horton, N. G.; Zhang, B.; Wu, C.-H.; Zhang, Y.; Schnitzer, M. J.; Xu, C. Three-Photon Imaging of Mouse Brain Structure and Function through the Intact Skull. *Nat. Methods* **2018**, *15* (10), 789–792. <https://doi.org/10.1038/s41592-018-0115-y>.
- (13) Schermelleh, L.; Ferrand, A.; Huser, T.; Eggeling, C.; Sauer, M.; Biehlmaier, O.; Drummen, G. P. C. Super-Resolution Microscopy Demystified. *Nat. Cell Biol.* **2019**, *21* (1), 72–84. <https://doi.org/10.1038/s41556-018-0251-8>.
- (14) Wäldchen, S.; Lehmann, J.; Klein, T.; van de Linde, S.; Sauer, M. Light-Induced Cell Damage in Live-Cell Super-Resolution Microscopy. *Sci. Rep.* **2015**, *5*, 15348. <https://doi.org/10.1038/srep15348>.
- (15) Laissue, P. P.; Alghamdi, R. A.; Tomancak, P.; Reynaud, E. G.; Shroff, H. Assessing Phototoxicity in Live Fluorescence Imaging. *Nat. Methods* **2017**, *14* (7), 657–661. <https://doi.org/10.1038/nmeth.4344>.
- (16) Binnig, G.; Quate, C. F.; Gerber, C. Atomic Force Microscope. *Phys. Rev. Lett.* **1986**, *56* (9), 930–933. <https://doi.org/10.1103/PhysRevLett.56.930>.

- (17) Hansma, P. K.; Drake, B.; Marti, O.; Gould, S. A. C.; Prater, C. B. The Scanning Ion-Conductance Microscope. *Science* **1989**, *243* (4891), 641–643. <https://doi.org/10.1126/science.2464851>.
- (18) Seifert, J.; Rheinlaender, J.; Novak, P.; Korchev, Y. E.; Schäffer, T. E. Comparison of Atomic Force Microscopy and Scanning Ion Conductance Microscopy for Live Cell Imaging. *Langmuir* **2015**, *31* (24), 6807–6813. <https://doi.org/10.1021/acs.langmuir.5b01124>.
- (19) Novak, P.; Li, C.; Shevchuk, A. I.; Stepanyan, R.; Caldwell, M.; Hughes, S.; Smart, T. G.; Gorelik, J.; Ostanin, V. P.; Lab, M. J.; Moss, G. W. J.; Frolenkov, G. I.; Klenerman, D.; Korchev, Y. E. Nanoscale Live-Cell Imaging Using Hopping Probe Ion Conductance Microscopy. *Nat. Methods* **2009**, *6* (4), 279–281. <https://doi.org/10.1038/nmeth.1306>.
- (20) Binnig, G.; Rohrer, H.; Gerber, Ch.; Weibel, E. Tunneling through a Controllable Vacuum Gap. *Appl. Phys. Lett.* **1982**, *40* (2), 178–180. <https://doi.org/10.1063/1.92999>.
- (21) Binnig, G.; Rohrer, H. Scanning Tunneling Microscopy---from Birth to Adolescence. *Rev. Mod. Phys.* **1987**, *59* (3), 615–625. <https://doi.org/10.1103/RevModPhys.59.615>.
- (22) Li, B.; Zhang, Y.; Wang, J.; Jia, Z.; Shi, C.; Ma, Y.; Ma, L. Fabricating Ultra-Sharp Tungsten STM Tips with High Yield: Double-Electrolyte Etching Method and Machine Learning. *SN Appl. Sci.* **2020**, *2* (7), 1246. <https://doi.org/10.1007/s42452-020-3017-4>.
- (23) Gao, T.; Xu, C.; Chen, M.-L.; Wang, J.-H.; Mao, L.; Yu, P. Insights into Surface Charge of Single Particles at the Orifice of a Nanopipette. *Anal. Chem.* **2022**, *94* (23), 8187–8193. <https://doi.org/10.1021/acs.analchem.1c05579>.
- (24) Zhu, C.; Zhou, L.; Choi, M.; Baker, L. A. Mapping Surface Charge of Individual Microdomains with Scanning Ion Conductance Microscopy. *ChemElectroChem* **2018**, *5* (20), 2986–2990. <https://doi.org/10.1002/celec.201800724>.
- (25) Radmacher, M.; Cleveland, J. P.; Fritz, M.; Hansma, H. G.; Hansma, P. K. Mapping Interaction Forces with the Atomic Force Microscope. *Biophys. J.* **1994**, *66* (6), 2159–2165. [https://doi.org/10.1016/S0006-3495\(94\)81011-2](https://doi.org/10.1016/S0006-3495(94)81011-2).
- (26) Štubian, M.; Bobek, J.; Setvin, M.; Diebold, U.; Schmid, M. Fast Low-Noise Transimpedance Amplifier for Scanning Tunneling Microscopy and Beyond. *Rev. Sci. Instrum.* **2020**, *91* (7), 074701. <https://doi.org/10.1063/5.0011097>.
- (27) Enning, R.; Ziegler, D.; Nievergelt, A.; Friedlos, R.; Venkataramani, K.; Stemmer, A. A High Frequency Sensor for Optical Beam Deflection Atomic Force Microscopy. *Rev. Sci. Instrum.* **2011**, *82* (4), 043705. <https://doi.org/10.1063/1.3575322>.
- (28) Fantner, G. E.; Schitter, G.; Kindt, J. H.; Ivanov, T.; Ivanova, K.; Patel, R.; Holten-Andersen, N.; Adams, J.; Thurner, P. J.; Rangelow, I. W.; Hansma, P. K. Components for High Speed Atomic Force Microscopy. *Ultramicroscopy* **2006**, *106* (8), 881–887. <https://doi.org/10.1016/j.ultramic.2006.01.015>.
- (29) Braunsman, C.; Schäffer, T. E. High-Speed Atomic Force Microscopy for Large Scan Sizes Using Small Cantilevers. *Nanotechnology* **2010**, *21* (22), 225705. <https://doi.org/10.1088/0957-4484/21/22/225705>.
- (30) Yong, Y. K.; Aphale, S. S.; Moheimani, S. O. R. Design, Identification, and Control of a Flexure-Based XY Stage for Fast Nanoscale Positioning. *IEEE Trans. Nanotechnol.* **2009**, *8* (1), 46–54. <https://doi.org/10.1109/TNANO.2008.2005829>.
- (31) Watanabe, H.; Uchihashi, T.; Kobashi, T.; Shibata, M.; Nishiyama, J.; Yasuda, R.; Ando, T. Wide-Area Scanner for High-Speed Atomic Force Microscopy. *Rev. Sci. Instrum.* **2013**, *84* (5), 053702. <https://doi.org/10.1063/1.4803449>.
- (32) Kenton, B. J.; Leang, K. K. Design and Control of a Three-Axis Serial-Kinematic High-Bandwidth Nanopositioner. *IEEEASME Trans. Mechatron.* **2012**, *17* (2), 356–369. <https://doi.org/10.1109/TMECH.2011.2105499>.

- (33) Chen, C. J.; Chen, C. J. *Introduction to Scanning Tunneling Microscopy*, Second Edition, Second Edition.; Monographs on the Physics and Chemistry of Materials; Oxford University Press: Oxford, New York, 2015.
- (34) Hölscher, H. AFM, Tapping Mode. In *Encyclopedia of Nanotechnology*; Bhushan, B., Ed.; Springer Netherlands: Dordrecht, 2012; pp 99–99. https://doi.org/10.1007/978-90-481-9751-4_33.
- (35) Kodera, N.; Yamamoto, D.; Ishikawa, R.; Ando, T. Video Imaging of Walking Myosin V by High-Speed Atomic Force Microscopy. *Nature* **2010**, *468* (7320), 72–76. <https://doi.org/10.1038/nature09450>.
- (36) Shibata, M.; Yamashita, H.; Uchihashi, T.; Kandori, H.; Ando, T. High-Speed Atomic Force Microscopy Shows Dynamic Molecular Processes in Photoactivated Bacteriorhodopsin. *Nat. Nanotechnol.* **2010**, *5* (3), 208–212. <https://doi.org/10.1038/nnano.2010.7>.
- (37) Chiaruttini, N.; Redondo-Morata, L.; Colom, A.; Humbert, F.; Lenz, M.; Scheuring, S.; Roux, A. Relaxation of Loaded ESCRT-III Spiral Springs Drives Membrane Deformation. *Cell* **2015**, *163* (4), 866–879. <https://doi.org/10.1016/j.cell.2015.10.017>.
- (38) Dufrêne, Y. F.; Boonaert, C. J. P.; Gerin, P. A.; Asther, M.; Rouxhet, P. G. Direct Probing of the Surface Ultrastructure and Molecular Interactions of Dormant and Germinating Spores of *Phanerochaete chrysosporium*. *J. Bacteriol.* **1999**, *181* (17), 5350–5354.
- (39) Alsteens, D.; Dupres, V.; Yunus, S.; Latgé, J.-P.; Heinisch, J. J.; Dufrêne, Y. F. High-Resolution Imaging of Chemical and Biological Sites on Living Cells Using Peak Force Tapping Atomic Force Microscopy. *Langmuir* **2012**, *28* (49), 16738–16744. <https://doi.org/10.1021/la303891j>.
- (40) Schneider, S. W.; Sritharan, K. C.; Geibel, J. P.; Oberleithner, H.; Jena, B. P. Surface Dynamics in Living Acinar Cells Imaged by Atomic Force Microscopy: Identification of Plasma Membrane Structures Involved in Exocytosis. *Proc. Natl. Acad. Sci. U. S. A.* **1997**, *94* (1), 316–321. <https://doi.org/10.1073/pnas.94.1.316>.
- (41) Dupres, V.; Menozzi, F. D.; Locht, C.; Clare, B. H.; Abbott, N. L.; Cuenot, S.; Bompard, C.; Raze, D.; Dufrêne, Y. F. Nanoscale Mapping and Functional Analysis of Individual Adhesins on Living Bacteria. *Nat. Methods* **2005**, *2* (7), 515–520. <https://doi.org/10.1038/nmeth769>.
- (42) Andre, G.; Kulakauskas, S.; Chapot-Chartier, M.-P.; Navet, B.; Deghorain, M.; Bernard, E.; Hols, P.; Dufrêne, Y. F. Imaging the Nanoscale Organization of Peptidoglycan in Living *Lactococcus lactis* Cells. *Nat. Commun.* **2010**, *1* (1), 27. <https://doi.org/10.1038/ncomms1027>.
- (43) Fantner, G. E.; Barbero, R. J.; Gray, D. S.; Belcher, A. M. Kinetics of Antimicrobial Peptide Activity Measured on Individual Bacterial Cells Using High-Speed Atomic Force Microscopy. *Nat. Nanotechnol.* **2010**, *5* (4), 280–285. <https://doi.org/10.1038/nnano.2010.29>.
- (44) Eskandarian, H. A.; Odermatt, P. D.; Ven, J. X. Y.; Hannebelle, M. T. M.; Nievergelt, A. P.; Dhar, N.; McKinney, J. D.; Fantner, G. E. Division Site Selection Linked to Inherited Cell Surface Wave Troughs in Mycobacteria. *Nat. Microbiol.* **2017**, *2* (9), 1–6. <https://doi.org/10.1038/nmicrobiol.2017.94>.
- (45) Hannebelle, M. T. M.; Ven, J. X. Y.; Toniolo, C.; Eskandarian, H. A.; Vuaridel-Thurre, G.; McKinney, J. D.; Fantner, G. E. A Biphasic Growth Model for Cell Pole Elongation in Mycobacteria. *Nat. Commun.* **2020**, *11* (1), 1–10. <https://doi.org/10.1038/s41467-019-14088-z>.
- (46) Odermatt, P. D.; Hannebelle, M. T. M.; Eskandarian, H. A.; Nievergelt, A. P.; McKinney, J. D.; Fantner, G. E. Overlapping and Essential Roles for Molecular and Mechanical Mechanisms in Mycobacterial Cell Division. *Nat. Phys.* **2020**, *16* (1), 57–62. <https://doi.org/10.1038/s41567-019-0679-1>.

- (47) Penedo, M.; Miyazawa, K.; Okano, N.; Furusho, H.; Ichikawa, T.; Alam, M. S.; Miyata, K.; Nakamura, C.; Fukuma, T. Visualizing Intracellular Nanostructures of Living Cells by Nanoendoscopy-AFM. *Sci. Adv.* **2021**, *7* (52), eabj4990. <https://doi.org/10.1126/sciadv.abj4990>.
- (48) Radmacher, M.; Tillmann, R. W.; Fritz, M.; Gaub, H. E. From Molecules to Cells: Imaging Soft Samples with the Atomic Force Microscope. *Science* **1992**, *257* (5078), 1900–1905. <https://doi.org/10.1126/science.1411505>.
- (49) Radmacher, M.; Fritz, M.; Kacher, C. M.; Cleveland, J. P.; Hansma, P. K. Measuring the Viscoelastic Properties of Human Platelets with the Atomic Force Microscope. *Biophys. J.* **1996**, *70* (1), 556–567. [https://doi.org/10.1016/S0006-3495\(96\)79602-9](https://doi.org/10.1016/S0006-3495(96)79602-9).
- (50) Duf re, Y. F.; Ando, T.; Garcia, R.; Alsteens, D.; Martinez-Martin, D.; Engel, A.; Gerber, C.; M ller, D. J. Imaging Modes of Atomic Force Microscopy for Application in Molecular and Cell Biology. *Nat. Nanotechnol.* **2017**, *12* (4), 295–307. <https://doi.org/10.1038/nnano.2017.45>.
- (51) Schillers, H. Measuring the Elastic Properties of Living Cells. In *Atomic Force Microscopy: Methods and Protocols*; Santos, N. C., Carvalho, F. A., Eds.; Methods in Molecular Biology; Springer: New York, NY, 2019; pp 291–313. https://doi.org/10.1007/978-1-4939-8894-5_17.
- (52) Duf re, Y. F.; Viljoen, A.; Mignolet, J.; Matheli -Guinlet, M. AFM in Cellular and Molecular Microbiology. *Cell. Microbiol.* **2021**, *23* (7), e13324. <https://doi.org/10.1111/cmi.13324>.
- (53) Cross, S. E.; Jin, Y.-S.; Rao, J.; Gimzewski, J. K. Nanomechanical Analysis of Cells from Cancer Patients. *Nat. Nanotechnol.* **2007**, *2* (12), 780–783. <https://doi.org/10.1038/nnano.2007.388>.
- (54) Plodinec, M.; Loparic, M.; Monnier, C. A.; Obermann, E. C.; Zanetti-Dallenbach, R.; Oertle, P.; Hyotyla, J. T.; Aebi, U.; Bentires-Alj, M.; Lim, R. Y. H.; Schoenenberger, C.-A. The Nanomechanical Signature of Breast Cancer. *Nat. Nanotechnol.* **2012**, *7* (11), 757–765. <https://doi.org/10.1038/nnano.2012.167>.
- (55) Meister, A.; Gabi, M.; Behr, P.; Studer, P.; V r s, J.; Niedermann, P.; Bitterli, J.; Polesel-Maris, J.; Liley, M.; Heinzelmann, H.; Zambelli, T. FluidFM: Combining Atomic Force Microscopy and Nanofluidics in a Universal Liquid Delivery System for Single Cell Applications and Beyond. *Nano Lett.* **2009**, *9* (6), 2501–2507. <https://doi.org/10.1021/nl901384x>.
- (56) Li, M.; Liu, L.; Zambelli, T. FluidFM for Single-Cell Biophysics. *Nano Res.* **2022**, *15* (2), 773–786. <https://doi.org/10.1007/s12274-021-3573-y>.
- (57) Chen, W.; Guillaume-Gentil, O.; Rainer, P. Y.; G belein, C. G.; Saelens, W.; Gardeux, V.; Klaeger, A.; Dainese, R.; Zachara, M.; Zambelli, T.; Vorholt, J. A.; Deplancke, B. Live-Seq Enables Temporal Transcriptomic Recording of Single Cells. *Nature* **2022**, *608* (7924), 733–740. <https://doi.org/10.1038/s41586-022-05046-9>.
- (58) <https://www.parksystems.com/>.
- (59) Korchev, Y. E.; Bashford, C. L.; Milovanovic, M.; Vodyanoy, I.; Lab, M. J. Scanning Ion Conductance Microscopy of Living Cells. *Biophys. J.* **1997**, *73* (2), 653–658. [https://doi.org/10.1016/S0006-3495\(97\)78100-1](https://doi.org/10.1016/S0006-3495(97)78100-1).
- (60) Chen, K.; Choudhary, A.; Sandler, S. E.; Maff o, C.; Ducati, C.; Aksimentiev, A.; Keyser, U. F. Super-Resolution Detection of DNA Nanostructures Using a Nanopore. *Adv. Mater.* **2023**, *35* (12), 2207434. <https://doi.org/10.1002/adma.202207434>.
- (61) Rheinlaender, J.; Sch ffer, T. E. Image Formation, Resolution, and Height Measurement in Scanning Ion Conductance Microscopy. *J. Appl. Phys.* **2009**, *105* (9). <https://doi.org/10.1063/1.3122007>.
- (62) Chen, C.; Zhou, Y.; Baker, L. A. Scanning Ion Conductance Microscopy. **2012**. <https://doi.org/10.1146/annurev-anchem-062011-143203>.

- (63) Happel, P.; Thatenhorst, D.; Dietzel, I. D. Scanning Ion Conductance Microscopy for Studying Biological Samples. **2012**, 14983–15008. <https://doi.org/10.3390/s121114983>.
- (64) Chowdhury, T. K. Fabrication of Extremely Fine Glass Micropipette Electrodes. *J. Phys. [E]* **1969**, 2 (12), 1087. <https://doi.org/10.1088/0022-3735/2/12/319>.
- (65) von Eysmond, H.; Schäffer, T. E. Scanning Ion Conductance Microscopy and Atomic Force Microscopy: A Comparison of Strengths and Limitations for Biological Investigations. In *Scanning Ion Conductance Microscopy*; Schäffer, T. E., Ed.; Bioanalytical Reviews; Springer International Publishing: Cham, 2022; pp 23–71. https://doi.org/10.1007/11663_2022_15.
- (66) Smeets, R. M. M.; Keyser, U. F.; Dekker, N. H.; Dekker, C. Noise in Solid-State Nanopores. *Proc. Natl. Acad. Sci.* **2008**, 105 (2), 417–421. <https://doi.org/10.1073/pnas.0705349105>.
- (67) Hoogerheide, D. P.; Garaj, S.; Golovchenko, J. A. Probing Surface Charge Fluctuations with Solid-State Nanopores. *Phys. Rev. Lett.* **2009**, 102 (25), 256804. <https://doi.org/10.1103/PhysRevLett.102.256804>.
- (68) Rosenstein, J. K.; Wanunu, M.; Merchant, C. A.; Drndic, M.; Shepard, K. L. Integrated Nanopore Sensing Platform with Sub-Microsecond Temporal Resolution. *Nat. Methods* **2012**, 9 (5), 487–492. <https://doi.org/10.1038/nmeth.1932>.
- (69) Levis, R. A.; Rae, J. L. The Use of Quartz Patch Pipettes for Low Noise Single Channel Recording. *Biophys. J.* **1993**, 65 (4), 1666–1677.
- (70) Cheng, L.; Zhuang, J.; Wang, T.; Liao, X.; Yu, J. 500kHz Bandwidth Feedback for Scanning Ion Conductance Microscopy With Nano-Resolution. *IEEE Trans. Ind. Electron.* **2023**, 1–10. <https://doi.org/10.1109/TIE.2023.3250764>.
- (71) Rheinlaender, J.; Schäffer, T. E. Lateral Resolution and Image Formation in Scanning Ion Conductance Microscopy. *Anal. Chem.* **2015**, 87 (14), 7117–7124. <https://doi.org/10.1021/acs.analchem.5b00900>.
- (72) Gorelik, J.; Zhang, Y.; Shevchuk, A. I.; Frolenkov, G. I.; Sánchez, D.; Lab, M. J.; Vodyanoy, I.; Edwards, C. R. W.; Klenerman, D.; Korchev, Y. E. The Use of Scanning Ion Conductance Microscopy to Image A6 Cells. *Mol. Cell. Endocrinol.* **2004**, 217 (1), 101–108. <https://doi.org/10.1016/j.mce.2003.10.015>.
- (73) Shevchuk, A. I.; Frolenkov, G. I.; Sánchez, D.; James, P. S.; Freedman, N.; Lab, M. J.; Jones, R.; Klenerman, D.; Korchev, Y. E. Imaging Proteins in Membranes of Living Cells by High-Resolution Scanning Ion Conductance Microscopy. *Angew. Chem. Int. Ed.* **2006**, 45 (14), 2212–2216. <https://doi.org/10.1002/anie.200503915>.
- (74) Klausen, L. H.; Fuhs, T.; Dong, M. Mapping Surface Charge Density of Lipid Bilayers by Quantitative Surface Conductivity Microscopy. *Nat. Commun.* **2016**, 7, 12447. <https://doi.org/10.1038/ncomms12447>.
- (75) Li, C.; Johnson, N.; Ostanin, V.; Shevchuk, A.; Ying, L.; Korchev, Y.; Klenerman, D. High Resolution Imaging Using Scanning Ion Conductance Microscopy with Improved Distance Feedback Control. *Prog. Nat. Sci.* **2008**, 18 (6), 671–677. <https://doi.org/10.1016/j.pnsc.2008.01.011>.
- (76) Shevchuk, A. I.; Gorelik, J.; Harding, S. E.; Lab, M. J.; Klenerman, D.; Korchev, Y. E. Simultaneous Measurement of Ca²⁺ and Cellular Dynamics: Combined Scanning Ion Conductance and Optical Microscopy to Study Contracting Cardiac Myocytes. *Biophys. J.* **2001**, 81 (3), 1759–1764.
- (77) Pastré, D.; Iwamoto, H.; Liu, J.; Szabo, G.; Shao, Z. Characterization of AC Mode Scanning Ion-Conductance Microscopy. *Ultramicroscopy* **2001**, 90 (1), 13–19. [https://doi.org/10.1016/s0304-3991\(01\)00096-1](https://doi.org/10.1016/s0304-3991(01)00096-1).
- (78) McKelvey, K.; Perry, D.; Byers, J. C.; Colburn, A. W.; Unwin, P. R. Bias Modulated Scanning Ion Conductance Microscopy. *Anal. Chem.* **2014**, 86 (7), 3639–3646. <https://doi.org/10.1021/ac5003118>.

- (79) Li, P.; Liu, L.; Wang, Y.; Yang, Y.; Zhang, C.; Li, G. Phase Modulation Mode of Scanning Ion Conductance Microscopy. *Appl. Phys. Lett.* **2014**, *105* (5), 053113. <https://doi.org/10.1063/1.4891571>.
- (80) Proksch, R.; Lal, R.; Hansma, P. K.; Morse, D.; Stucky, G. Imaging the Internal and External Pore Structure of Membranes in Fluid: Tapping-Mode Scanning Ion Conductance Microscopy. *Biophys. J.* **1996**, *71* (4), 2155–2157. [https://doi.org/10.1016/S0006-3495\(96\)79416-X](https://doi.org/10.1016/S0006-3495(96)79416-X).
- (81) Mann, S. A.; Hoffmann, G.; Hengstenberg, A.; Schuhmann, W.; Dietzel, I. D. Pulse-Mode Scanning Ion Conductance Microscopy--a Method to Investigate Cultured Hippocampal Cells. *J. Neurosci. Methods* **2002**, *116* (2), 113–117. [https://doi.org/10.1016/S0165-0270\(02\)00023-7](https://doi.org/10.1016/S0165-0270(02)00023-7).
- (82) Happel, P.; Dietzel, I. D. Backstep Scanning Ion Conductance Microscopy as a Tool for Long Term Investigation of Single Living Cells. *J. Nanobiotechnology* **2009**, *7*, 7. <https://doi.org/10.1186/1477-3155-7-7>.
- (83) Happel, P.; Hoffmann, G.; Mann, S. A.; Dietzel, I. D. Monitoring Cell Movements and Volume Changes with Pulse-Mode Scanning Ion Conductance Microscopy. *J. Microsc.* **2003**, *212* (Pt 2), 144–151. <https://doi.org/10.1046/j.1365-2818.2003.01248.x>.
- (84) Novak, P.; Li, C.; Shevchuk, A. I.; Stepanyan, R.; Caldwell, M.; Hughes, S.; Smart, T. G.; Gorelik, J.; Ostanin, V. P.; Lab, M. J.; Moss, G. W. J.; Frolenkov, G. I.; Klenerman, D.; Korchev, Y. E. Correction: Corrigendum: Nanoscale Live-Cell Imaging Using Hopping Probe Ion Conductance Microscopy. *Nat. Methods* **2009**, *6* (12), 935–935. <https://doi.org/10.1038/nmeth1209-935a>.
- (85) Zhuang, J.; Wang, Z.; Li, Z.; Liang, P.; Vincent, M. Smart Scanning Ion-Conductance Microscopy Imaging Technique Using Horizontal Fast Scanning Method. *Microsc. Microanal.* **2018**, *24* (3), 264–276. <https://doi.org/10.1017/S1431927618000375>.
- (86) Ida, H.; Takahashi, Y.; Kumatani, A.; Shiku, H.; Matsue, T. High Speed Scanning Ion Conductance Microscopy for Quantitative Analysis of Nanoscale Dynamics of Microvilli. *Anal. Chem.* **2017**, *89* (11), 6015–6020. <https://doi.org/10.1021/acs.analchem.7b00584>.
- (87) Takahashi, Y.; Zhou, Y.; Miyamoto, T.; Higashi, H.; Nakamichi, N.; Takeda, Y.; Kato, Y.; Korchev, Y.; Fukuma, T. High-Speed SICM for the Visualization of Nanoscale Dynamic Structural Changes in Hippocampal Neurons. *Anal. Chem.* **2020**, *92* (2), 2159–2167. <https://doi.org/10.1021/acs.analchem.9b04775>.
- (88) Zhang, S.; Cho, S.-J.; Busuttill, K.; Wang, C.; Besenbacher, F.; Dong, M. Scanning Ion Conductance Microscopy Studies of Amyloid Fibrils at Nanoscale. *Nanoscale* **2012**, *4* (10), 3105–3110. <https://doi.org/10.1039/c2nr12049f>.
- (89) Ushiki, T.; Nakajima, M.; Choi, M.; Cho, S.-J.; Iwata, F. Scanning Ion Conductance Microscopy for Imaging Biological Samples in Liquid: A Comparative Study with Atomic Force Microscopy and Scanning Electron Microscopy. *Micron* **2012**, *43* (12), 1390–1398. <https://doi.org/10.1016/j.micron.2012.01.012>.
- (90) Zhou, Y.; Saito, M.; Miyamoto, T.; Novak, P.; Shevchuk, A. I.; Korchev, Y. E.; Fukuma, T.; Takahashi, Y. Nanoscale Imaging of Primary Cilia with Scanning Ion Conductance Microscopy. *Anal. Chem.* **2018**, *90* (4), 2891–2895. <https://doi.org/10.1021/acs.analchem.7b05112>.
- (91) Nakajima, M.; Mizutani, Y.; Iwata, F.; Ushiki, T. Scanning Ion Conductance Microscopy for Visualizing the Three-Dimensional Surface Topography of Cells and Tissues. *Semin. Cell Dev. Biol.* **2018**, *73*, 125–131. <https://doi.org/10.1016/j.semcdb.2017.09.024>.
- (92) Simeonov, S.; Schäffer, T. E. Ultrafast Imaging of Cardiomyocyte Contractions by Combining Scanning Ion Conductance Microscopy with a Microelectrode Array. *Anal. Chem.* **2019**, *91* (15), 9648–9655. <https://doi.org/10.1021/acs.analchem.9b01092>.
- (93) Zhu, C.; Huang, K.; Siepser, N. P.; Baker, L. A. Scanning Ion Conductance Microscopy. *Chem. Rev.* **2021**, *121* (19), 11726–11768. <https://doi.org/10.1021/acs.chemrev.0c00962>.

- (94) Sánchez, D.; Johnson, N.; Li, C.; Novak, P.; Rheinlaender, J.; Zhang, Y.; Anand, U.; Anand, P.; Gorelik, J.; Frolenkov, G. I.; Benham, C.; Lab, M.; Ostanin, V. P.; Schäffer, T. E.; Klenerman, D.; Korchev, Y. E. Noncontact Measurement of the Local Mechanical Properties of Living Cells Using Pressure Applied via a Pipette. *Biophys. J.* **2008**, *95* (6), 3017–3027. <https://doi.org/10.1529/biophysj.108.129551>.
- (95) Pellegrino, M.; Orsini, P.; Pellegrini, M.; Baschieri, P.; Dinelli, F.; Petracchi, D.; Tognoni, E.; Ascoli, C. Weak Hydrostatic Forces in Far-Scanning Ion Conductance Microscopy Used to Guide Neuronal Growth Cones. *Neurosci. Res.* **2011**, *69* (3), 234–240. <https://doi.org/10.1016/j.neures.2010.11.009>.
- (96) Rheinlaender, J.; Schäffer, T. E. Mapping the Mechanical Stiffness of Live Cells with the Scanning Ion Conductance Microscope. *Soft Matter* **2013**, *9* (12), 3230–3236. <https://doi.org/10.1039/c2sm27412d>.
- (97) Clarke, R. W.; Novak, P.; Zhukov, A.; Tyler, E. J.; Cano-Jaimez, M.; Drews, A.; Richards, O.; Volynski, K.; Bishop, C.; Klenerman, D. Low Stress Ion Conductance Microscopy of Sub-Cellular Stiffness. *Soft Matter* **2016**, *12* (38), 7953–7958. <https://doi.org/10.1039/c6sm01106c>.
- (98) Rheinlaender, J.; Vogel, S.; Seifert, J.; Schächtele, M.; Borst, O.; Lang, F.; Gawaz, M.; Schäffer, T. E. Imaging the Elastic Modulus of Human Platelets during Thrombin-Induced Activation Using Scanning Ion Conductance Microscopy. *Thromb. Haemost.* **2015**, *113* (2), 305–311. <https://doi.org/10.1160/TH14-05-0414>.
- (99) Baumann, J.; Sachs, L.; Otto, O.; Schoen, I.; Nestler, P.; Zaninetti, C.; Kenny, M.; Kranz, R.; von Eysmond, H.; Rodriguez, J.; Schäffer, T. E.; Nagy, Z.; Greinacher, A.; Palankar, R.; Bender, M. Reduced Platelet Forces Underlie Impaired Hemostasis in Mouse Models of MYH9-Related Disease. *Sci. Adv.* **2022**, *8* (20), eabn2627. <https://doi.org/10.1126/sciadv.abn2627>.
- (100) Swiatlowska, P.; Sanchez-Alonso, J. L.; Mansfield, C.; Scaini, D.; Korchev, Y.; Novak, P.; Gorelik, J. Short-Term Angiotensin II Treatment Regulates Cardiac Nanomechanics via Microtubule Modifications. *Nanoscale* **2020**, *12* (30), 16315–16329. <https://doi.org/10.1039/D0NR02474K>.
- (101) Rheinlaender, J.; Wirbel, H.; Schäffer, T. E. Spatial Correlation of Cell Stiffness and Traction Forces in Cancer Cells Measured with Combined SICM and TFM. *RSC Adv.* **2021**, *11* (23), 13951–13956. <https://doi.org/10.1039/D1RA01277K>.
- (102) Kolmogorov, V. S.; Erofeev, A. S.; Barykin, E. P.; Timoshenko, R. V.; Lopatukhina, E. V.; Kozin, S. A.; Salikhov, S. V.; Klyachko, N. L.; Mitkevich, V. A.; Edwards, C. R. W.; Korchev, Y. E.; Makarov, A. A.; Gorelkin, P. V. Scanning Ion-Conductance Microscopy for Studying β -Amyloid Aggregate Formation on Living Cell Surface. *bioRxiv* June 30, 2022, p 2022.06.30.498242. <https://doi.org/10.1101/2022.06.30.498242>.
- (103) Sa, N.; Baker, L. A. Rectification of Nanopores at Surfaces. *J. Am. Chem. Soc.* **2011**, *133* (27), 10398–10401. <https://doi.org/10.1021/ja203883q>.
- (104) McKelvey, K.; Kinnear, S. L.; Perry, D.; Momotenko, D.; Unwin, P. R. Surface Charge Mapping with a Nanopipette. *J. Am. Chem. Soc.* **2014**, *136* (39), 13735–13744. <https://doi.org/10.1021/ja506139u>.
- (105) Fuhs, T.; Klausen, L. H.; Sønderkov, S. M.; Han, X.; Dong, M. Direct Measurement of Surface Charge Distribution in Phase Separating Supported Lipid Bilayers. *Nanoscale* **2018**, *10* (9), 4538–4544. <https://doi.org/10.1039/C7NR09522H>.
- (106) Page, A.; Perry, D.; Young, P.; Mitchell, D.; Frenguelli, B. G.; Unwin, P. R. Fast Nanoscale Surface Charge Mapping with Pulsed-Potential Scanning Ion Conductance Microscopy. *Anal. Chem.* **2016**, *88* (22), 10854–10859. <https://doi.org/10.1021/acs.analchem.6b03744>.

- (107) Perry, D.; Paulose Nadappuram, B.; Momotenko, D.; Voyias, P. D.; Page, A.; Tripathi, G.; Frenguelli, B. G.; Unwin, P. R. Surface Charge Visualization at Viable Living Cells. *J. Am. Chem. Soc.* **2016**, *138* (9), 3152–3160. <https://doi.org/10.1021/jacs.5b13153>.
- (108) Cremin, K.; Jones, B. A.; Teahan, J.; Meloni, G. N.; Perry, D.; Zerfass, C.; Asally, M.; Soyer, O. S.; Unwin, P. R. Scanning Ion Conductance Microscopy Reveals Differences in the Ionic Environments of Gram-Positive and Negative Bacteria. *Anal. Chem.* **2020**, *92* (24), 16024–16032. <https://doi.org/10.1021/acs.analchem.0c03653>.
- (109) Actis, P.; Tokar, S.; Clausmeyer, J.; Babakinejad, B.; Mikhaleva, S.; Cornut, R.; Takahashi, Y.; López Córdoba, A.; Novak, P.; Shevchuk, A. I.; Dougan, J. A.; Kazarian, S. G.; Gorelkin, P. V.; Erofeev, A. S.; Yaminsky, I. V.; Unwin, P. R.; Wolfgang Schuhmann, X.; Klenerman, D.; Dmitri Rusakov, O. A.; Sviderskaya, E. V.; Korchev, Y. E. Electrochemical Nanoprobes for Single-Cell Analysis. **2013**. <https://doi.org/10.1021/nn405612q>.
- (110) Takahashi, Y.; Shevchuk, A. I.; Novak, P.; Murakami, Y.; Shiku, H.; Korchev, Y. E.; Matsue, T. Simultaneous Noncontact Topography and Electrochemical Imaging by SECM/SICM Featuring Ion Current Feedback Regulation. *J. Am. Chem. Soc.* **2010**, *132* (29), 10118–10126. <https://doi.org/10.1021/ja1029478>.
- (111) Morris, C. A.; Chen, C.-C.; Ito, T.; Baker, L. A. Local PH Measurement with Scanning Ion Conductance Microscopy. *J. Electrochem. Soc.* **2013**, *160* (8), H430. <https://doi.org/10.1149/2.028308jes>.
- (112) Nadappuram, B. P.; McKelvey, K.; Al Botros, R.; Colburn, A. W.; Unwin, P. R. Fabrication and Characterization of Dual Function Nanoscale PH-Scanning Ion Conductance Microscopy (SICM) Probes for High Resolution PH Mapping. *Anal. Chem.* **2013**, *85* (17), 8070–8074. <https://doi.org/10.1021/ac401883n>.
- (113) Zhang, Y.; Takahashi, Y.; Hong, S. P.; Liu, F.; Bednarska, J.; Goff, P. S.; Novak, P.; Shevchuk, A.; Gopal, S.; Barozzi, I.; Magnani, L.; Sakai, H.; Suguru, Y.; Fujii, T.; Erofeev, A.; Gorelkin, P.; Majouga, A.; Weiss, D. J.; Edwards, C.; Ivanov, A. P.; Klenerman, D.; Sviderskaya, E. V.; Edel, J. B.; Korchev, Y. High-Resolution Label-Free 3D Mapping of Extracellular PH of Single Living Cells. *Nat. Commun.* **2019**, *10* (1), 5610. <https://doi.org/10.1038/s41467-019-13535-1>.
- (114) Shevchuk, A. I.; Novak, P.; Taylor, M.; Diakonov, I. A.; Ziyadeh-Isleem, A.; Bitoun, M.; Guicheney, P.; Gorelik, J.; Merrifield, C. J.; Klenerman, D.; Korchev, Y. E. An Alternative Mechanism of Clathrin-Coated Pit Closure Revealed by Ion Conductance Microscopy. **2012**, *197* (4), 499–508. <https://doi.org/10.1083/jcb.201109130>.
- (115) Bednarska, J.; Pelchen-Matthews, A.; Novak, P.; Burden, J. J.; Summers, P. A.; Kuimova, M. K.; Korchev, Y.; Marsh, M.; Shevchuk, A. Rapid Formation of Human Immunodeficiency Virus-like Particles. *Proc. Natl. Acad. Sci. U. S. A.* **2020**, *117* (35), 21637–21646. <https://doi.org/10.1073/pnas.2008156117>.
- (116) Seifert, J.; Rheinlaender, J.; Lang, F.; Gawaz, M.; Schäffer, T. E. Thrombin-Induced Cytoskeleton Dynamics in Spread Human Platelets Observed with Fast Scanning Ion Conductance Microscopy. *Sci. Rep.* **2017**, *7* (1), 4810. <https://doi.org/10.1038/s41598-017-04999-6>.
- (117) Simeonov, S.; Schäffer, T. E. High-Speed Scanning Ion Conductance Microscopy for Sub-Second Topography Imaging of Live Cells. *Nanoscale* **2019**, *11* (17), 8579–8587. <https://doi.org/10.1039/c8nr10162k>.
- (118) Watanabe, S.; Kitazawa, S.; Sun, L.; Kodera, N.; Ando, T. Development of High-Speed Ion Conductance Microscopy. *Rev. Sci. Instrum.* **2019**, *90* (12), 123704. <https://doi.org/10.1063/1.5118360>.
- (119) Watanabe, S.; Ando, T. High-Speed XYZ-Nanopositioner for Scanning Ion Conductance Microscopy. **2017**, No. September, 1–5.

- (120) Novak, P.; Shevchuk, A.; Ruenraroengsak, P.; Miragoli, M.; Thorley, A. J.; Klenerman, D.; Tetley, T. D.; Gorelik, J.; Korchev, Y. E. Imaging Single Nanoparticle Interactions with Human Lung Cells Using Fast Ion Conductance Microscopy. **2014**. <https://doi.org/10.1021/nl404068p>.
- (121) Jung, G. E.; Noh, H.; Shin, Y. K.; Kahng, S. J.; Baik, K. Y.; Kim, H. B.; Cho, N. J.; Cho, S. J. Closed-Loop ARS Mode for Scanning Ion Conductance Microscopy with Improved Speed and Stability for Live Cell Imaging Applications. *Nanoscale* **2015**, *7* (25), 10989–10997. <https://doi.org/10.1039/c5nr01577d>.
- (122) Nievergelt, A. P.; Andany, S. H.; Adams, J. D.; Hannebelle, M. T.; Fantner, G. E. Components for High-Speed Atomic Force Microscopy Optimized for Low Phase-Lag. *IEEEASME Int. Conf. Adv. Intell. Mechatron. AIM* **2017**, 731–736. <https://doi.org/10.1109/AIM.2017.8014104>.
- (123) Kammer, C.; Nievergelt, A. P.; Fantner, G. E.; Karimi, A. Data-Driven Controller Design for Atomic-Force Microscopy. *IFAC-Pap.* **2017**, *50* (1), 10437–10442. <https://doi.org/10.1016/j.ifacol.2017.08.1972>.
- (124) Djekic, D.; Ortmanns, M.; Fantner, G.; Anders, J. A Tunable, Robust Pseudo-Resistor with Enhanced Linearity for Scanning Ion-Conductance Microscopy. In *Proceedings - IEEE International Symposium on Circuits and Systems*; Institute of Electrical and Electronics Engineers Inc., 2016; Vol. 2016-July, pp 842–845. <https://doi.org/10.1109/ISCAS.2016.7527372>.
- (125) Djekic, D.; Fantner, G.; Behrends, J.; Lips, K.; Ortmanns, M.; Anders, J. A Transimpedance Amplifier Using a Widely Tunable PVT-Independent Pseudo-Resistor for High-Performance Current Sensing Applications. In *ESSCIRC 2017 - 43rd IEEE European Solid State Circuits Conference*; Institute of Electrical and Electronics Engineers Inc., 2017; pp 79–82. <https://doi.org/10.1109/ESSCIRC.2017.8094530>.
- (126) Djekic, D.; Fantner, G.; Lips, K.; Ortmanns, M.; Anders, J. A 0.1% THD, 1-M Ω to 1-G Ω Tunable, Temperature-Compensated Transimpedance Amplifier Using a Multi-Element Pseudo-Resistor. *IEEE J. Solid-State Circuits* **2018**, *53* (7), 1913–1923. <https://doi.org/10.1109/JSSC.2018.2820701>.
- (127) Steinbock, L. J.; Steinbock, J. F.; Radenovic, A. Controllable Shrinking and Shaping of Glass Nanocapillaries under Electron Irradiation. *Nano Lett.* **2013**, *13* (4), 1717–1723. <https://doi.org/10.1021/nl400304y>.
- (128) Yamashita, H.; Kodera, N.; Miyagi, A.; Uchihashi, T.; Yamamoto, D.; Ando, T. Tip-Sample Distance Control Using Photothermal Actuation of a Small Cantilever for High-Speed Atomic Force Microscopy. *Rev. Sci. Instrum.* **2007**, *78* (8), 083702. <https://doi.org/10.1063/1.2766825>.
- (129) Kolmogorov, V. S.; Erofeev, A. S.; Woodcock, E.; Efremov, Y. M.; Iakovlev, A. P.; Savin, N. A.; Alova, A. V.; Lavrushkina, S. V.; Kireev, I. I.; Prelovskaya, A. O.; Sviderskaya, E. V.; Scaini, D.; Klyachko, N. L.; Timashev, P. S.; Takahashi, Y.; Salikhov, S. V.; Parkhomenko, Y. N.; Majouga, A. G.; Edwards, C. R. W.; Novak, P.; Korchev, Y. E.; Gorelkin, P. V. Mapping Mechanical Properties of Living Cells at Nanoscale Using Intrinsic Nanopipette–Sample Force Interactions. *Nanoscale* **2021**, *13* (13), 6558–6568. <https://doi.org/10.1039/D0NR08349F>.
- (130) Baker, M. Taking a Long, Hard Look. *Nature* **2010**, *466* (7310), 1137–1140. <https://doi.org/10.1038/4661137a>.
- (131) Noctor, S. C.; Martínez-Cerdeño, V.; Ivic, L.; Kriegstein, A. R. Cortical Neurons Arise in Symmetric and Asymmetric Division Zones and Migrate through Specific Phases. *Nat. Neurosci.* **2004**, *7*, 136–144 (2), 136–144. <https://doi.org/10.1038/nn1172>.
- (132) Sauvanet, C.; Wayt, J.; Pelaseyed, T.; Bretscher, A. Structure, Regulation, and Functional Diversity of Microvilli on the Apical Domain of Epithelial Cells. *Annu. Rev. Cell Dev. Biol.* **2015**, *31*, 593–621. <https://doi.org/10.1146/annurev-cellbio-100814-125234>.

- (133) Innocenti, M. New Insights into the Formation and the Function of Lamellipodia and Ruffles in Mesenchymal Cell Migration. *Cell Adhes. Migr.* **2018**, *12* (5), 401–416. <https://doi.org/10.1080/19336918.2018.1448352>.
- (134) Jones, S. A.; Shim, S. H.; He, J.; Zhuang, X. Fast, Three-Dimensional Super-Resolution Imaging of Live Cells. *Nat. Methods* **2011**, *8* (6), 499–505. <https://doi.org/10.1038/nmeth.1605>.
- (135) Tian, T.; Wang, Y.; Wang, H.; Zhu, Z.; Xiao, Z. Visualizing of the Cellular Uptake and Intracellular Trafficking of Exosomes by Live-Cell Microscopy. *J. Cell. Biochem.* **2010**, *111* (2), 488–496. <https://doi.org/10.1002/jcb.22733>.
- (136) Eghiaian, F.; Rigato, A.; Scheuring, S. Structural, Mechanical, and Dynamical Variability of the Actin Cortex in Living Cells. *Biophys. J.* **2015**, *108* (6), 1330–1340. <https://doi.org/10.1016/j.bpj.2015.01.016>.
- (137) Jung, G.-E.; Noh, H.; Shin, Y. K.; Kahng, S.-J.; Baik, K. Y.; Kim, H.-B.; Cho, N.-J.; Cho, S.-J. Nanoscale Closed-Loop ARS Mode for Scanning Ion Conductance Microscopy with Improved Speed and Stability for Live Cell Imaging Applications Closed-Loop ARS Mode for Scanning Ion Conductance Microscopy with Improved Speed and Stability for Live Cell Imaging Applications. **2015**, *7* (7), 10989. <https://doi.org/10.1039/c5nr01577d>.
- (138) Valdivia, A.; Goicoechea, S. M.; Awadia, S.; Zinn, A.; Garcia-Mata, R. Regulation of Circular Dorsal Ruffles, Macropinocytosis, and Cell Migration by RhoG and Its Exchange Factor, Trio. *Mol. Biol. Cell* **2017**, *28* (13), 1768–1781. <https://doi.org/10.1091/mbc.E16-06-0412>.
- (139) Hoon, J.-L.; Wong, W.-K.; Koh, C.-G. Functions and Regulation of Circular Dorsal Ruffles. *Mol. Cell. Biol.* **2012**, *32* (21), 4246–4257. <https://doi.org/10.1128/mcb.00551-12>.
- (140) Bernitt, E.; Döbereiner, H. G.; Gov, N. S.; Yochelis, A. Fronts and Waves of Actin Polymerization in a Bistability-Based Mechanism of Circular Dorsal Ruffles. *Nat. Commun.* **2017**, *8* (1), 1–8. <https://doi.org/10.1038/ncomms15863>.
- (141) Irshad, H.; Veillard, A.; Roux, L.; Racoceanu, D. Methods for Nuclei Detection, Segmentation, and Classification in Digital Histopathology: A Review-Current Status and Future Potential. *IEEE Rev. Biomed. Eng.* **2014**, *7*, 97–114. <https://doi.org/10.1109/RBME.2013.2295804>.
- (142) Johannessen, C. M.; Johnson, L. A.; Piccioni, F.; Townes, A.; Frederick, D. T.; Donahue, M. K.; Narayan, R.; Flaherty, K. T.; Wargo, J. A.; Root, D. E.; Garraway, L. A. A Melanocyte Lineage Program Confers Resistance to MAP Kinase Pathway Inhibition. *Nature* **2013**, *504* (7478), 138–142. <https://doi.org/10.1038/nature12688>.
- (143) Englaro, W.; Bertolotto, C.; Buscà, R.; Brunet, A.; Pagès, G.; Ortonne, J. P.; Ballotti, R. Inhibition of the Mitogen-Activated Protein Kinase Pathway Triggers B16 Melanoma Cell Differentiation. *J. Biol. Chem.* **1998**, *273* (16), 9966–9970. <https://doi.org/10.1074/jbc.273.16.9966>.
- (144) Cho, D. H.; Bae, C. D.; Juhn, Y. S. Multi-Facet Expressions of Adenylate Cyclase Isoforms in B16-F10 Melanoma Cells Differentiated by Forskolin Treatment. *Experimental and Molecular Medicine*, **2000**, *32*, 235–242. <https://doi.org/10.1038/emm.2000.39>.
- (145) Chang, C. H.; Lee, H. H.; Lee, C. H. Substrate Properties Modulate Cell Membrane Roughness by Way of Actin Filaments. *Sci. Rep.* **2017**, *7* (1), 1–11. <https://doi.org/10.1038/s41598-017-09618-y>.
- (146) Wang, Y.; Xu, C.; Jiang, N.; Zheng, L.; Zeng, J.; Qiu, C.; Yang, H.; Xie, S. Quantitative Analysis of the Cell-Surface Roughness and Viscoelasticity for Breast Cancer Cells Discrimination Using Atomic Force Microscopy. *Scanning* **2016**, *38* (6), 558–563. <https://doi.org/10.1002/sca.21300>.

- (147) Rheinlaender, J.; Schäffer, T. E. Lateral Resolution and Image Formation in Scanning Ion Conductance Microscopy. *Anal. Chem.* **2015**, *87* (14), 7117–7124. <https://doi.org/10.1021/ACS.ANALCHEM.5B00900>.
- (148) Hagemann, P.; Gesper, A.; Happel, P. Correlative Stimulated Emission Depletion and Scanning Ion Conductance Microscopy. *ACS Nano* **2018**, *12*, 5807–5815. <https://doi.org/10.1021/acsnano.8b01731>.
- (149) Navikas, V.; Leitao, S. M.; Grussmayer, K. S.; Descloux, A.; Drake, B.; Yserentant, K.; Werther, P.; Hertel, D.-P.; Wombacher, R.; Radenovic, A.; Fantner, G. E. Correlative 3D Microscopy of Single Cells Using Super-Resolution and Scanning Ion-Conductance Microscopy. *Nat. Commun.* **2021**, *12* (1), 4565. <https://doi.org/10.1038/s41467-021-24901-3>.
- (150) Doyon, J. B.; Zeitler, B.; Cheng, J.; Cheng, A. T.; Cherone, J. M.; Santiago, Y.; Lee, A. H.; Vo, T. D.; Doyon, Y.; Miller, J. C.; Paschon, D. E.; Zhang, L.; Rebar, E. J.; Gregory, P. D.; Urnov, F. D.; Drubin, D. G. Rapid and Efficient Clathrin-Mediated Endocytosis Revealed in Genome-Edited Mammalian Cells. *Nat. Cell Biol.* **2011**, *13* (3), 331–337. <https://doi.org/10.1038/ncb2175>.
- (151) Pierrat, X.; Wong, J. P. H.; Al-Mayyah, Z.; Persat, A. The Membrane Microenvironment Regulates the Sequential Attachment of Bacteria to Host Cells. *bioRxiv*. bioRxiv November 25, 2020, p 2020.11.25.397950. <https://doi.org/10.1101/2020.11.25.397950>.
- (152) Glass, D. S.; Riedel-Kruse, I. H. A Synthetic Bacterial Cell-Cell Adhesion Toolbox for Programming Multicellular Morphologies and Patterns. *Cell* **2018**, *174* (3), 649-658.e16. <https://doi.org/10.1016/j.cell.2018.06.041>.
- (153) Navikas, V.; Leitão, S. M.; Marion, S.; Davis, S. J.; Drake, B.; Fantner, G. E.; Radenovic, A. High-Throughput Nanocapillary Filling Enabled by Microwave Radiation for Scanning Ion Conductance Microscopy Imaging. *ACS Appl. Nano Mater.* **2020**, *3* (8), 7829–7834. <https://doi.org/10.1021/acsanm.0c01345>.
- (154) Nievergelt, A. P.; Kammer, C.; Brillard, C.; Kurisinkal, E.; Bastings, M. M. C.; Karimi, A.; Fantner, G. E. Large-Range HS-AFM Imaging of DNA Self-Assembly through In Situ Data-Driven Control. *Small Methods* **2019**, *3* (7), 1900031. <https://doi.org/10.1002/smt.201900031>.
- (155) Nečas, D.; Klapetek, P. Gwyddion: An Open-Source Software for SPM Data Analysis. *Open Phys.* **2012**, *10* (1), 181–188. <https://doi.org/10.2478/s11534-011-0096-2>.
- (156) Schindelin, J.; Arganda-Carreras, I.; Frise, E.; Kaynig, V.; Longair, M.; Pietzsch, T.; Preibisch, S.; Rueden, C.; Saalfeld, S.; Schmid, B.; Tinevez, J.-Y.; White, D. J.; Hartenstein, V.; Eliceiri, K.; Tomancak, P.; Cardona, A. Fiji: An Open-Source Platform for Biological-Image Analysis. *Nat. Methods* **2012**, *9* (7), 676–682. <https://doi.org/10.1038/nmeth.2019>.
- (157) Yildiz, A.; Forkey, J. N.; McKinney, S. A.; Ha, T.; Goldman, Y. E.; Selvin, P. R. Myosin V Walks Hand-Over-Hand: Single Fluorophore Imaging with 1.5-Nm Localization. *Science* **2003**, *300* (5628), 2061–2065. <https://doi.org/10.1126/science.1084398>.
- (158) Guo, Y.; Li, D.; Zhang, S.; Yang, Y.; Liu, J.-J.; Wang, X.; Liu, C.; Milkie, D. E.; Moore, R. P.; Tulu, U. S.; Kiehart, D. P.; Hu, J.; Lippincott-Schwartz, J.; Betzig, E.; Li, D. Visualizing Intracellular Organelle and Cytoskeletal Interactions at Nanoscale Resolution on Millisecond Timescales. *Cell* **2018**, *175* (5), 1430-1442.e17. <https://doi.org/10.1016/j.cell.2018.09.057>.
- (159) Chalfie, M.; Tu, Y.; Euskirchen, G.; Ward, W. W.; Prasher, D. C. Green Fluorescent Protein as a Marker for Gene Expression. *Science* **1994**, *263* (5148), 802–805. <https://doi.org/10.1126/science.8303295>.
- (160) Shevchuk, A. I.; Hobson, P. Endocytic Pathways : Combined Scanning Ion Conductance and Surface Confocal Microscopy Study. **2008**, 227–235. <https://doi.org/10.1007/s00424-007-0410-4>.

- (161) Descloux, A.; Grubmayer, K. S.; Radenovic, A. Parameter-Free Image Resolution Estimation Based on Decorrelation Analysis. *Nat. Methods* **2019**, *16* (9), 918–924. <https://doi.org/10.1038/s41592-019-0515-7>.
- (162) Betzig, E.; Patterson, G. H.; Sougrat, R.; Lindwasser, O. W.; Olenych, S.; Bonifacino, J. S.; Davidson, M. W.; Lippincott-Schwartz, J.; Hess, H. F. Imaging Intracellular Fluorescent Proteins at Nanometer Resolution. *Science* **2006**, *313* (5793), 1642–1645. <https://doi.org/10.1126/science.1127344>.
- (163) Dertinger, T.; Colyer, R.; Iyer, G.; Weiss, S.; Enderlein, J. Fast, Background-Free, 3D Super-Resolution Optical Fluctuation Imaging (SOFI). *Proc. Natl. Acad. Sci. U. S. A.* **2009**, *106* (52), 22287–22292. <https://doi.org/10.1073/pnas.0907866106>.
- (164) Dertinger, T.; Colyer, R.; Vogel, R.; Enderlein, J.; Weiss, S. Achieving Increased Resolution and More Pixels with Superresolution Optical Fluctuation Imaging (SOFI). *Opt. Express* **2010**, *18* (18), 18875–18885. <https://doi.org/10.1364/OE.18.018875>.
- (165) Geissbuehler, S.; Bocchio, N. L.; Dellagiacomma, C.; Berclaz, C.; Leutenegger, M.; Lasser, T. Mapping Molecular Statistics with Balanced Super-Resolution Optical Fluctuation Imaging (BSOFI). *Opt. Nanoscopy* **2012**, *1* (1), 4. <https://doi.org/10.1186/2192-2853-1-4>.
- (166) Dertinger, T.; Colyer, R.; Iyer, G.; Weiss, S.; Enderlein, J. Fast, Background-Free, 3D Super-Resolution Optical Fluctuation Imaging (SOFI). *Proc. Natl. Acad. Sci. U. S. A.* **2009**, *106* (52), 22287–22292. <https://doi.org/10.1073/pnas.0907866106>.
- (167) Geissbuehler, S.; Sharipov, A.; Godinat, A.; Bocchio, N. L.; Sandoz, P. A.; Huss, A.; Jensen, N. A.; Jakobs, S.; Enderlein, J.; Gisou van der Goot, F.; Dubikovskaya, E. A.; Lasser, T.; Leutenegger, M. Live-Cell Multiplane Three-Dimensional Super-Resolution Optical Fluctuation Imaging. *Nat. Commun.* **2014**, *5*, 5830. <https://doi.org/10.1038/ncomms6830>.
- (168) Descloux, A.; Grubmayer, K. S.; Bostan, E.; Lukes, T.; Bouwens, A.; Sharipov, A.; Geissbuehler, S.; Mahul-Mellier, A.-L.; Lashuel, H. A.; Leutenegger, M.; Lasser, T. Combined Multi-Plane Phase Retrieval and Super-Resolution Optical Fluctuation Imaging for 4D Cell Microscopy. *Nat. Photonics* **2018**, *12* (3), 165–172. <https://doi.org/10.1038/s41566-018-0109-4>.
- (169) Grubmayer, K. S.; Geissbuehler, S.; Descloux, A.; Lukes, T.; Leutenegger, M.; Radenovic, A.; Lasser, T. Spectral Cross-Cumulants for Multicolor Super-Resolved SOFI Imaging. *Nat. Commun.* **2020**, *11* (1), 3023. <https://doi.org/10.1038/s41467-020-16841-1>.
- (170) Grubmayer, K.; Lukes, T.; Lasser, T.; Radenovic, A. Self-Blinking Dyes Unlock High-Order and Multiplane Super-Resolution Optical Fluctuation Imaging. *ACS Nano* **2020**. <https://doi.org/10.1021/acsnano.0c04602>.
- (171) Werther, P.; Yserentant, K.; Braun, F.; Grubmayer, K.; Navikas, V.; Yu, M.; Zhang, Z.; Ziegler, M. J.; Mayer, C.; Gralak, A. J.; Busch, M.; Chi, W.; Rominger, F.; Radenovic, A.; Liu, X.; Lemke, E. A.; Backup, T.; Herten, D.-P.; Wombacher, R. Bio-Orthogonal Red and Far-Red Fluorogenic Probes for Wash-Free Live-Cell and Super-Resolution Microscopy. *ACS Cent. Sci.* **2021**, *7* (9), 1561–1571. <https://doi.org/10.1021/acscentsci.1c00703>.
- (172) Leitao, S. M.; Drake, B.; Pinjusic, K.; Pierrat, X.; Navikas, V.; Nievergelt, A. P.; Brillard, C.; Djekic, D.; Radenovic, A.; Persat, A.; Constam, D. B.; Anders, J.; Fantner, G. E. Time-Resolved Scanning Ion Conductance Microscopy for Three-Dimensional Tracking of Nanoscale Cell Surface Dynamics. *ACS Nano* **2021**, *15* (11), 17613–17622. <https://doi.org/10.1021/acsnano.1c05202>.
- (173) Ban, N.; Nissen, P.; Hansen, J.; Moore, P. B.; Steitz, T. A. The Complete Atomic Structure of the Large Ribosomal Subunit at 2.4 Å Resolution. *Science* **2000**, *289* (5481), 905–920. <https://doi.org/10.1126/science.289.5481.905>.

- (174) Fang, Q.; Zhu, D.; Agarkova, I.; Adhikari, J.; Klose, T.; Liu, Y.; Chen, Z.; Sun, Y.; Gross, M. L.; Van Etten, J. L.; Zhang, X.; Rossmann, M. G. Near-Atomic Structure of a Giant Virus. *Nat. Commun.* **2019**, *10* (1), 1–11. <https://doi.org/10.1038/s41467-019-08319-6>.
- (175) Bharat, T. A. M.; Kukulski, W. Cryo-Correlative Light and Electron Microscopy. In *Correlative Imaging*; Wiley, 2019; pp 137–153.
- (176) Neumüller, J. Electron Tomography—a Tool for Ultrastructural 3D Visualization in Cell Biology and Histology. *Wien. Med. Wochenschr.* **2018**, *168* (11–12), 322–329. <https://doi.org/10.1007/s10354-018-0646-y>.
- (177) Sahl, S. J.; Hell, S. W.; Jakobs, S. Fluorescence Nanoscopy in Cell Biology. *Nat. Rev. Mol. Cell Biol.* **2017**, *18* (11), 685–701. <https://doi.org/10.1038/nrm.2017.71>.
- (178) Waldchen, S.; Lehmann, J.; Klein, T.; Van De Linde, S.; Sauer, M. Light-Induced Cell Damage in Live-Cell Super-Resolution Microscopy. *Sci. Rep.* **2015**, *5* (1), 1–12. <https://doi.org/10.1038/srep15348>.
- (179) Geissbuehler, S.; Dellagiacomma, C.; Lasser, T. Comparison between SOFI and STORM. *Biomed. Opt. Express* **2011**, *2* (3), 408. <https://doi.org/10.1364/boe.2.000408>.
- (180) Shibata, M.; Watanabe, H.; Uchihashi, T.; Ando, T.; Yasuda, R. High-Speed Atomic Force Microscopy Imaging of Live Mammalian Cells. *Biophys. Physicobiology* **2017**, *14* (0), 127–135. https://doi.org/10.2142/biophysico.14.0_127.
- (181) Moreno Flores, S.; Toca-Herrera, J. L. The New Future of Scanning Probe Microscopy: Combining Atomic Force Microscopy with Other Surface-Sensitive Techniques, Optical Microscopy and Fluorescence Techniques. *Nanoscale* **2009**, *1* (1), 40–49. <https://doi.org/10.1039/b9nr00156e>.
- (182) Krieg, M.; Fläschner, G.; Alsteens, D.; Gaub, B. M.; Roos, W. H.; Wuite, G. J. L.; Gaub, H. E.; Gerber, C.; Dufrene, Y. F.; Müller, D. J. Atomic Force Microscopy-Based Mechanobiology. *Nature Reviews Physics*. Springer Nature January 1, 2019, pp 41–57. <https://doi.org/10.1038/s42254-018-0001-7>.
- (183) Frederix, P. L. T. M.; Bosshart, P. D.; Engel, A. Atomic Force Microscopy of Biological Membranes. *Biophysical Journal*. Biophysical Society January 21, 2009, pp 329–338. <https://doi.org/10.1016/j.bpj.2008.09.046>.
- (184) Nievergelt, A. P.; Banterle, N.; Andany, S. H.; Gönczy, P.; Fantner, G. E. High-Speed Photothermal off-Resonance Atomic Force Microscopy Reveals Assembly Routes of Centriolar Scaffold Protein SAS-6. *Nat. Nanotechnol.* **2018**, *13* (8), 696–701. <https://doi.org/10.1038/s41565-018-0149-4>.
- (185) Odermatt, P. D.; Shivanandan, A.; Deschout, H.; Jankele, R.; Nievergelt, A. P.; Feletti, L.; Davidson, M. W.; Radenovic, A.; Fantner, G. E. High-Resolution Correlative Microscopy: Bridging the Gap between Single Molecule Localization Microscopy and Atomic Force Microscopy. *Nano Lett.* **2015**, *15* (8), 4896–4904. <https://doi.org/10.1021/acs.nanolett.5b00572>.
- (186) Gómez-Varela, A. I.; Stamov, D. R.; Miranda, A.; Alves, R.; Barata-Antunes, C.; Dambournet, D.; Drubin, D. G.; Paiva, S.; De Beule, P. A. A. Simultaneous Co-Localized Super-Resolution Fluorescence Microscopy and Atomic Force Microscopy: Combined SIM and AFM Platform for the Life Sciences. *Sci. Rep.* **2020**, *10* (1), 1–10. <https://doi.org/10.1038/s41598-020-57885-z>.
- (187) Seifert, J.; Rheinlaender, J.; Novak, P.; Korchev, Y. E.; Schäffer, T. E. Comparison of Atomic Force Microscopy and Scanning Ion Conductance Microscopy for Live Cell Imaging. *Langmuir* **2015**, *31* (24), 6807–6813. <https://doi.org/10.1021/acs.langmuir.5b01124>.
- (188) Deschout, H.; Lukes, T.; Sharipov, A.; Szlag, D.; Feletti, L.; Vandenberg, W.; Dedecker, P.; Hofkens, J.; Leutenegger, M.; Lasser, T.; Radenovic, A. Complementarity of PALM and SOFI for Super-Resolution Live-Cell Imaging of Focal Adhesions. *Nat. Commun.* **2016**, *7*, 13693. <https://doi.org/10.1038/ncomms13693>.

- (189) Werther, P.; Yserentant, K.; Braun, F.; Kaltwasser, N.; Popp, C.; Baalman, M.; Herten, D.; Wombacher, R. Live-Cell Localization Microscopy with a Fluorogenic and Self-Blinking Tetrazine Probe. *Angew. Chem. Int. Ed.* **2020**, *59* (2), 804–810. <https://doi.org/10.1002/anie.201906806>.
- (190) Ovesný, M.; Křížek, P.; Borkovec, J.; Svindrych, Z.; Hagen, G. M. ThunderSTORM: A Comprehensive ImageJ Plug-in for PALM and STORM Data Analysis and Super-Resolution Imaging. *Bioinforma. Oxf. Engl.* **2014**, *30* (16), 2389–2390. <https://doi.org/10.1093/bioinformatics/btu202>.
- (191) Henderson, E.; Sakaguchi, D. S. Imaging F-Actin in Fixed Glial Cells with a Combined Optical Fluorescence/Atomic Force Microscope. *NeuroImage* **1993**, *1* (2), 145–150. <https://doi.org/10.1006/nimg.1993.1007>.
- (192) Berdyeva, T.; Woodworth, C. D.; Sokolov, I. Visualization of Cytoskeletal Elements by the Atomic Force Microscope. *Ultramicroscopy* **2005**, *102* (3), 189–198. <https://doi.org/10.1016/j.ultramic.2004.09.008>.
- (193) Cosentino, M.; Canale, C.; Bianchini, P.; Diaspro, A. AFM-STED Correlative Nanoscopy Reveals a Dark Side in Fluorescence Microscopy Imaging. *Sci. Adv.* **2019**, *5* (6), eaav8062. <https://doi.org/10.1126/sciadv.aav8062>.
- (194) Tanaka, A.; Tanaka, R.; Kasai, N.; Tsukada, S.; Okajima, T.; Sumitomo, K. Time-Lapse Imaging of Morphological Changes in a Single Neuron during the Early Stages of Apoptosis Using Scanning Ion Conductance Microscopy. *J. Struct. Biol.* **2015**, *191* (1), 32–38. <https://doi.org/10.1016/j.jsb.2015.06.002>.
- (195) Gorelik, J.; Shevchuk, A. I.; Frolenkov, G. I.; Diakonov, I. A.; Lab, M. J.; Kros, C. J.; Richardson, G. P.; Vodyanoy, I.; Edwards, C. R. W.; Klenerman, D.; Korchev, Y. E. Dynamic Assembly of Surface Structures in Living Cells. *Proc. Natl. Acad. Sci.* **2003**, *100* (10), 5819–5822. <https://doi.org/10.1073/pnas.1030502100>.
- (196) Garcia, R. Nanomechanical Mapping of Soft Materials with the Atomic Force Microscope: Methods, Theory and Applications. *Chem. Soc. Rev.* **2020**, *49* (16), 5850–5884. <https://doi.org/10.1039/D0CS00318B>.
- (197) Hinterdorfer, P.; Dufrêne, Y. F. Detection and Localization of Single Molecular Recognition Events Using Atomic Force Microscopy. *Nature Methods*. Nature Publishing Group May 20, 2006, pp 347–355. <https://doi.org/10.1038/nmeth871>.
- (198) Yamada, K. M.; Sixt, M. Mechanisms of 3D Cell Migration. *Nature Reviews Molecular Cell Biology*. Nature Research December 1, 2019, pp 738–752. <https://doi.org/10.1038/s41580-019-0172-9>.
- (199) Johannes, L.; Pezeshkian, W.; Ipsen, J. H.; Shillcock, J. C. Clustering on Membranes: Fluctuations and More. *Trends in Cell Biology*. Elsevier Ltd May 1, 2018, pp 405–415. <https://doi.org/10.1016/j.tcb.2018.01.009>.
- (200) Yesylevskyy, S. O.; Rivel, T.; Ramseyer, C. The Influence of Curvature on the Properties of the Plasma Membrane. Insights from Atomistic Molecular Dynamics Simulations. *Sci. Rep.* **2017**, *7* (1), 1–13. <https://doi.org/10.1038/s41598-017-16450-x>.
- (201) Sezgin, E.; Levental, I.; Mayor, S.; Eggeling, C. The Mystery of Membrane Organization: Composition, Regulation and Roles of Lipid Rafts. *Nature Reviews Molecular Cell Biology*. Nature Publishing Group June 1, 2017, pp 361–374. <https://doi.org/10.1038/nrm.2017.16>.
- (202) Heine, M.; Ciuraszkiewicz, A.; Voigt, A.; Heck, J.; Bikbaev, A. Surface Dynamics of Voltage-Gated Ion Channels. *Channels*. Taylor and Francis Inc. July 3, 2016, pp 267–281. <https://doi.org/10.1080/19336950.2016.1153210>.
- (203) Deschamps, J.; Rowald, A.; Ries, J. Efficient Homogeneous Illumination and Optical Sectioning for Quantitative Single-Molecule Localization Microscopy. *Opt. Express* **2016**, *24* (24), 28080. <https://doi.org/10.1364/oe.24.028080>.

- (204) Descloux, A.; Größmayer, K. S.; Bostan, E.; Lukes, T.; Bouwens, A.; Sharipov, A.; Geissbuehler, S.; Mahul-Mellier, A. L.; Lashuel, H. A.; Leutenegger, M.; Lasser, T. Combined Multi-Plane Phase Retrieval and Super-Resolution Optical Fluctuation Imaging for 4D Cell Microscopy. *Nat. Photonics* **2018**, *12* (3), 165–172. <https://doi.org/10.1038/s41566-018-0109-4>.
- (205) Olivier, N.; Keller, D.; Gönczy, P.; Manley, S. Resolution Doubling in 3D-STORM Imaging through Improved Buffers. *PLoS ONE* **2013**, *8* (7), e69004. <https://doi.org/10.1371/journal.pone.0069004>.
- (206) Marsh, R. J.; Pfisterer, K.; Bennett, P.; Hirvonen, L. M.; Gautel, M.; Jones, G. E.; Cox, S. Artifact-Free High-Density Localization Microscopy Analysis. *Nat. Methods* **2018**, *15* (9), 689–692. <https://doi.org/10.1038/s41592-018-0072-5>.
- (207) Textor, Marcus.; Grandin, H. Michelle. *Intelligent Surfaces in Biotechnology : Scientific and Engineering Concepts, Enabling Technologies, and Translation to Bio-Oriented Applications*; John Wiley & Sons, 2012.
- (208) Meimetis, L. G.; Carlson, J. C. T.; Giedt, R. J.; Kohler, R. H.; Weissleder, R. Ultrafluorogenic Coumarin-Tetrazine Probes for Real-Time Biological Imaging. *Angew. Chem. - Int. Ed.* **2014**, *53* (29), 7531–7534. <https://doi.org/10.1002/anie.201403890>.
- (209) Sigworth, F. J.; Neher, E. Single Na⁺ Channel Currents Observed in Cultured Rat Muscle Cells. *Nature* **1980**, *287* (5781), 447–449. <https://doi.org/10.1038/287447a0>.
- (210) Sakmann, B.; Neher, E. Patch Clamp Techniques for Studying Ionic Channels in Excitable Membranes. *Annu. Rev. Physiol.* **1984**, *46* (1), 455–472. <https://doi.org/10.1146/annurev.ph.46.030184.002323>.
- (211) *Single-Channel Recording*; Sakmann, B., Neher, E., Eds.; Springer US: Boston, MA, 1995. <https://doi.org/10.1007/978-1-4419-1229-9>.
- (212) Xue, L.; Yamazaki, H.; Ren, R.; Wanunu, M.; Ivanov, A. P.; Edel, J. B. Solid-State Nanopore Sensors. *Nat. Rev. Mater.* **2020**, *5* (12), 931–951. <https://doi.org/10.1038/s41578-020-0229-6>.
- (213) Sutton, M. A.; Burton, A. S.; Zaikova, E.; Sutton, R. E.; Brinckerhoff, W. B.; Bevilacqua, J. G.; Weng, M. M.; Mumma, M. J.; Johnson, S. S. Radiation Tolerance of Nanopore Sequencing Technology for Life Detection on Mars and Europa. *Sci. Rep.* **2019**, *9* (1), 5370. <https://doi.org/10.1038/s41598-019-41488-4>.
- (214) Liu, K.; Feng, J.; Kis, A.; Radenovic, A. Atomically Thin Molybdenum Disulfide Nanopores with High Sensitivity for DNA Translocation. *ACS Nano* **2014**, *8* (3), 2504–2511. <https://doi.org/10.1021/nn406102h>.
- (215) Ghosal, S. Electrokinetic-Flow-Induced Viscous Drag on a Tethered DNA inside a Nanopore. *Phys. Rev. E* **2007**, *76* (6), 061916. <https://doi.org/10.1103/PhysRevE.76.061916>.
- (216) Brinkerhoff, H.; Kang, A. S. W.; Liu, J.; Aksimentiev, A.; Dekker, C. Multiple Rereads of Single Proteins at Single-Amino Acid Resolution Using Nanopores. *Science* **2021**, *374* (6574), 1509–1513. <https://doi.org/10.1126/science.abl4381>.
- (217) Deamer, D.; Akeson, M.; Branton, D. Three Decades of Nanopore Sequencing. *Nat. Biotechnol.* **2016**, *34* (5), 518–524. <https://doi.org/10.1038/nbt.3423>.
- (218) Wang, Y.; Zhao, Y.; Bollas, A.; Wang, Y.; Au, K. F. Nanopore Sequencing Technology, Bioinformatics and Applications. *Nat. Biotechnol.* **2021**, *39* (11), 1348–1365. <https://doi.org/10.1038/s41587-021-01108-x>.
- (219) Dekker, C. Solid-State Nanopores. *Nat. Nanotechnol.* **2007**, *2* (4), 209–215. <https://doi.org/10.1038/nnano.2007.27>.
- (220) Li, W.; Bell, N. A. W.; Hernández-Ainsa, S.; Thacker, V. V.; Thackray, A. M.; Bujdoso, R.; Keyser, U. F. Single Protein Molecule Detection by Glass Nanopores. *ACS Nano* **2013**, *7* (5), 4129–4134. <https://doi.org/10.1021/nn4004567>.

- (221) Bell, N. A. W.; Keyser, U. F. Digitally Encoded DNA Nanostructures for Multiplexed, Single-Molecule Protein Sensing with Nanopores. *Nat. Nanotechnol.* **2016**, *11* (7), 645–651. <https://doi.org/10.1038/nnano.2016.50>.
- (222) Bošković, F.; Keyser, U. F. Nanopore Microscope Identifies RNA Isoforms with Structural Colours. *Nat. Chem.* **2022**, *14* (11), 1258–1264. <https://doi.org/10.1038/s41557-022-01037-5>.
- (223) Bošković, F.; Zhu, J.; Tivony, R.; Ohmann, A.; Chen, K.; Alawami, M. F.; Đorđević, M.; Ermann, N.; Pereira-Dias, J.; Fairhead, M.; Howarth, M.; Baker, S.; Keyser, U. F. Simultaneous Identification of Viruses and Viral Variants with Programmable DNA Nanobait. *Nat. Nanotechnol.* **2023**, *18* (3), 290–298. <https://doi.org/10.1038/s41565-022-01287-x>.
- (224) Branton, D.; Deamer, D. W.; Marziali, A.; Bayley, H.; Benner, S. A.; Butler, T.; Di Ventra, M.; Garaj, S.; Hibbs, A.; Huang, X.; Jovanovich, S. B.; Krstic, P. S.; Lindsay, S.; Ling, X. S.; Mastrangelo, C. H.; Meller, A.; Oliver, J. S.; Pershin, Y. V.; Ramsey, J. M.; Riehn, R.; Soni, G. V.; Tabard-Cossa, V.; Wanunu, M.; Wiggin, M.; Schloss, J. A. The Potential and Challenges of Nanopore Sequencing. *Nat. Biotechnol.* **2008**, *26* (10), 1146–1153. <https://doi.org/10.1038/nbt.1495>.
- (225) Schneider, G. F.; Dekker, C. DNA Sequencing with Nanopores. *Nat. Biotechnol.* **2012**, *30* (4), 326–328. <https://doi.org/10.1038/nbt.2181>.
- (226) Manrao, E. A.; Derrington, I. M.; Laszlo, A. H.; Langford, K. W.; Hopper, M. K.; Gillgren, N.; Pavlenok, M.; Niederweis, M.; Gundlach, J. H. Reading DNA at Single-Nucleotide Resolution with a Mutant MspA Nanopore and Phi29 DNA Polymerase. *Nat. Biotechnol.* **2012**, *30* (4), 349–353. <https://doi.org/10.1038/nbt.2171>.
- (227) Derrington, I. M.; Craig, J. M.; Stava, E.; Laszlo, A. H.; Ross, B. C.; Brinkerhoff, H.; Nova, I. C.; Doering, K.; Tickman, B. I.; Ronaghi, M.; Mandell, J. G.; Gunderson, K. L.; Gundlach, J. H. Subangstrom Single-Molecule Measurements of Motor Proteins Using a Nanopore. *Nat. Biotechnol.* **2015**, *33* (10), 1073–1075. <https://doi.org/10.1038/nbt.3357>.
- (228) Fragasso, A.; Schmid, S.; Dekker, C. Comparing Current Noise in Biological and Solid-State Nanopores. *ACS Nano* **2020**, *14* (2), 1338–1349. <https://doi.org/10.1021/acsnano.9b09353>.
- (229) Li, J.; Stein, D.; McMullan, C.; Branton, D.; Aziz, M. J.; Golovchenko, J. A. Ion-Beam Sculpting at Nanometre Length Scales. *Nature* **2001**, *412* (6843), 166–169. <https://doi.org/10.1038/35084037>.
- (230) Storm, A. J.; Chen, J. H.; Ling, X. S.; Zandbergen, H. W.; Dekker, C. Fabrication of Solid-State Nanopores with Single-Nanometre Precision. *Nat. Mater.* **2003**, *2* (8), 537–540. <https://doi.org/10.1038/nmat941>.
- (231) Garaj, S.; Hubbard, W.; Reina, A.; Kong, J.; Branton, D.; Golovchenko, J. A. Graphene as a Subnanometre Trans-Electrode Membrane. *Nature* **2010**, *467* (7312), 190–193. <https://doi.org/10.1038/nature09379>.
- (232) Yusko, E. C.; Bruhn, B. R.; Eggenberger, O. M.; Houghtaling, J.; Rollings, R. C.; Walsh, N. C.; Nandivada, S.; Pindrus, M.; Hall, A. R.; Sept, D.; Li, J.; Kalonia, D. S.; Mayer, M. Real-Time Shape Approximation and Fingerprinting of Single Proteins Using a Nanopore. *Nat. Nanotechnol.* **2017**, *12* (4), 360–367. <https://doi.org/10.1038/nnano.2016.267>.
- (233) Lu, B.; Albertorio, F.; Hoogerheide, D. P.; Golovchenko, J. A. Origins and Consequences of Velocity Fluctuations during DNA Passage through a Nanopore. *Biophys. J.* **2011**, *101* (1), 70–79. <https://doi.org/10.1016/j.bpj.2011.05.034>.
- (234) Plesa, C.; van Loo, N.; Ketterer, P.; Dietz, H.; Dekker, C. Velocity of DNA during Translocation through a Solid-State Nanopore. *Nano Lett.* **2015**, *15* (1), 732–737. <https://doi.org/10.1021/nl504375c>.

- (235) Steinbock, L. J.; Otto, O.; Chimere, C.; Gornall, J.; Keyser, U. F. Detecting DNA Folding with Nanocapillaries. *Nano Lett.* **2010**, *10* (7), 2493–2497. <https://doi.org/10.1021/nl100997s>.
- (236) Bell, N. A. W.; Chen, K.; Ghosal, S.; Ricci, M.; Keyser, U. F. Asymmetric Dynamics of DNA Entering and Exiting a Strongly Confining Nanopore. *Nat. Commun.* **2017**, *8* (1), 380. <https://doi.org/10.1038/s41467-017-00423-9>.
- (237) Aramesh, M.; Forró, C.; Dorwling-Carter, L.; Lüchtfeld, I.; Schlotter, T.; Ihle, S. J.; Shorubalko, I.; Hosseini, V.; Momotenko, D.; Zambelli, T.; Klotzsch, E.; Vörös, J. Localized Detection of Ions and Biomolecules with a Force-Controlled Scanning Nanopore Microscope. *Nat. Nanotechnol.* **2019**, *14* (8), 791–798. <https://doi.org/10.1038/s41565-019-0493-z>.
- (238) Yuan, Z.; Liu, Y.; Dai, M.; Yi, X.; Wang, C. Controlling DNA Translocation Through Solid-State Nanopores. *Nanoscale Res. Lett.* **2020**, *15* (1), 80. <https://doi.org/10.1186/s11671-020-03308-x>.
- (239) Rahman, M.; Sampad, M. J. N.; Hawkins, A.; Schmidt, H. Recent Advances in Integrated Solid-State Nanopore Sensors. *Lab. Chip* **2021**, *21* (16), 3030–3052. <https://doi.org/10.1039/D1LC00294E>.
- (240) Rief, M.; Oesterhelt, F.; Heymann, B.; Gaub, H. E. Single Molecule Force Spectroscopy on Polysaccharides by Atomic Force Microscopy. *Science* **1997**, *275* (5304), 1295–1297. <https://doi.org/10.1126/science.275.5304.1295>.
- (241) Chen, K.; Jou, I.; Ermann, N.; Muthukumar, M.; Keyser, U. F.; Bell, N. A. W. Dynamics of Driven Polymer Transport through a Nanopore. *Nat. Phys.* **2021**, *17* (9), 1043–1049. <https://doi.org/10.1038/s41567-021-01268-2>.
- (242) Chen, K.; Kong, J.; Zhu, J.; Ermann, N.; Predki, P.; Keyser, U. F. Digital Data Storage Using DNA Nanostructures and Solid-State Nanopores. *Nano Lett.* **2019**, *19* (2), 1210–1215. <https://doi.org/10.1021/acs.nanolett.8b04715>.
- (243) Tabatabaei, S. K.; Wang, B.; Athreya, N. B. M.; Enghiad, B.; Hernandez, A. G.; Fields, C. J.; Leburton, J.-P.; Soloveichik, D.; Zhao, H.; Milenkovic, O. DNA Punch Cards for Storing Data on Native DNA Sequences via Enzymatic Nicking. *Nat. Commun.* **2020**, *11* (1), 1742. <https://doi.org/10.1038/s41467-020-15588-z>.
- (244) Clegg, R. M. Fluorescence Resonance Energy Transfer and Nucleic Acids. *Methods Enzymol.* **1992**, *211*, 353–388. [https://doi.org/10.1016/0076-6879\(92\)11020-j](https://doi.org/10.1016/0076-6879(92)11020-j).
- (245) Lelek, M.; Gyparaki, M. T.; Beliu, G.; Schueder, F.; Griffié, J.; Manley, S.; Jungmann, R.; Sauer, M.; Lakadamyali, M.; Zimmer, C. Single-Molecule Localization Microscopy. *Nat. Rev. Methods Primer* **2021**, *1* (1), 1–27. <https://doi.org/10.1038/s43586-021-00038-x>.
- (246) Jungmann, R.; Steinhauer, C.; Scheible, M.; Kuzyk, A.; Tinnefeld, P.; Simmel, F. C. Single-Molecule Kinetics and Super-Resolution Microscopy by Fluorescence Imaging of Transient Binding on DNA Origami. *Nano Lett.* **2010**, *10* (11), 4756–4761. <https://doi.org/10.1021/nl103427w>.
- (247) Zhu, C.; Huang, K.; Wang, Y.; Alanis, K.; Shi, W.; Baker, L. A. Imaging with Ion Channels. *Anal. Chem.* **2021**, *93* (13), 5355–5359. <https://doi.org/10.1021/acs.analchem.1c00224>.
- (248) Wang, H.; Hays, J. B. Simple and Rapid Preparation of Gapped Plasmid DNA for Incorporation of Oligomers Containing Specific DNA Lesions. *Mol. Biotechnol.* **2001**, *19* (2), 133–140. <https://doi.org/10.1385/MB:19:2:133>.
- (249) Jozwiakowski, S. K.; Connolly, B. A. Plasmid-Based LacZalpha Assay for DNA Polymerase Fidelity: Application to Archaeal Family-B DNA Polymerase. *Nucleic Acids Res.* **2009**, *37* (15), e102. <https://doi.org/10.1093/nar/gkp494>.
- (250) Auburn, R. P.; Kreil, D. P.; Meadows, L. A.; Fischer, B.; Matilla, S. S.; Russell, S. Robotic Spotting of cDNA and Oligonucleotide Microarrays. *Trends Biotechnol.* **2005**, *23* (7), 374–379. <https://doi.org/10.1016/j.tibtech.2005.04.002>.

- (251) Bernitt, E.; Döbereiner, H. G.; Gov, N. S.; Yochelis, A. Fronts and Waves of Actin Polymerization in a Bistability-Based Mechanism of Circular Dorsal Ruffles. *Nat. Commun.* **2017**, *8* (May). <https://doi.org/10.1038/ncomms15863>.
- (252) Macazo, F. C.; White, R. J. Bioinspired Protein Channel-Based Scanning Ion Conductance Microscopy (Bio-SICM) for Simultaneous Conductance and Specific Molecular Imaging. *J. Am. Chem. Soc.* **2016**, *138* (8), 2793–2801. <https://doi.org/10.1021/jacs.5b13252>.
- (253) Shi, W.; Zeng, Y.; Zhu, C.; Xiao, Y.; Cummins, T. R.; Hou, J.; Baker, L. A. Characterization of Membrane Patch-Ion Channel Probes for Scanning Ion Conductance Microscopy. *Small* **2018**, *14* (18), 1702945. <https://doi.org/10.1002/sml.201702945>.

Curriculum Vitae

SAMUEL M. LEITAO

PhD Candidate in Biotechnology and Bioengineering
Swiss Federal Institute of Technology Lausanne (EPFL)
Lausanne 1015, Switzerland;
Email: samuel.mendesleitao@epfl.ch; Phone: +41 762 802 660



Education

- 2018-Now **Swiss Federal Institute of Technology Lausanne (EPFL), Switzerland**
Ph.D. Candidate, Doctoral Program in Biotechnology and Bioengineering.
School of Engineering, Laboratory for Bio- and Nano-Instrumentation. @ Prof. Georg Fantner.
Thesis title: Time-Resolved Ion Conductance Microscopy and Single-Molecule Spectroscopy.
- 2015 **University of Lisbon, Portugal**
Msc degree in Bioengineering and Nanosystems, Highest Honors Diploma.

Research Experience

- 2016-2017 **Max Planck Institute of Biochemistry, Germany**
Scientist at Dept. of Cellular and Molecular Biophysics. @ Prof. Petra Schwille.
Project: Structural diversity of photoswitchable sphingolipids for optodynamic control of lipid raft microdomains.
- 2014 **INESC-MN and Iberian Nanotechnology Laboratory (INL), Portugal**
Research intern at Dept. of Nanodevices. @ Prof. Paulo Freitas.
Project: Spintronic biochip sensor for molecular detection in lateral flow immunoassays.
- 2013 **Federal University of Rio de Janeiro (UFRJ), Brazil**
Research intern at the Biophysics Institute (CCFBI). @ Prof. Paulo Bisch.
Project: Mechanical properties of *klebsiella pneumonia* cell capsule with atomic force microscopy.

Awards, Honors, and Merit Scholarships

- 2022 Best Oral Presentation, International symposium in Neuroscience and Microscopy, Italy.
- 2022 Young Researcher Travel Award, AFM BioMed, Japan.
- 2022 Best Oral Presentation sponsored by Nano Letters, Nano In Bio conference, France.
- 2016 Fellowship, Nanoagents for the spatiotemporal control of molecular and cellular reaction (SFB), Center for Nanoscience initiative LMU Munich/Max Planck Institute, Germany.
- 2015 Highest Honors Master Degree Diploma, University of Lisbon, Portugal.
- 2015 Merit Scholarship, Swiss-European mobility program for my MSc thesis, Switzerland.
- 2013 Merit Scholarship, Excellence academic exchange program Santander for my BSc thesis, Brazil.

First author Publications

Leitao, M. S.; Navikas, V.; Miljkovic, H.; Drake, B.; Marion, S.; Pistoletti, G.; Chen, K.; Mayer, S.; Keyser, U.; Kuhn, A.; Fantner, E. G.; Radenovic, A.; Spatially Multiplexed Single-Molecule Translocations through a Nanopore at Controlled Speeds. *Nature Nanotechnology* 2023.

Hartrampf N.*; **Leitao, M. S. (Co-first author);** Winter N.; Toombs-Ruane, H.; Frank, J.; Schwille, P.; Trauner, D.; Franquelim, H.; Structural Diversity of Photoswitchable Sphingolipids for Optodynamic Control of Lipid Raft Microdomains. *Biophysical J.* 2023 Jun 6;122(11):2325-2341.

Leitao, M. S.; Drake, B.; Pinjusic, K.; Pierrat, X.; Navikas, V.; Nievergelt, A.; Brillard, C.; Djekic, D.; Radenovic, A.; Persat, A.; Constam, S.; Anders, J.; Fantner, E. G.; Time-Resolved Scanning Ion Conductance Microscopy for Three-Dimensional Tracking of Nanoscale Cell Surface Dynamics. *ACS Nano* 2021, 15, 11, 17613–17622.

Navikas, V.*; **Leitao, M. S. (Co-first author);** Grussmayer, K.; Descloux, A.; Drake, B.; Yserentant, K.; Werther, P.; Hertel, D.; Wombacher, R.; Radenovic, A.; Fantner, E. G.; Correlative 3D Microscopy of Single Cells using Super-Resolution and Scanning Ion-Conductance Microscopy. *Nature Communications* 2021, 12, 4565.

Biswas, S.*; **Leitao, M. S. (Co-first author);** Theillaud, Q.; Erickson, B.; Fantner, E. G.; Reducing Uncertainties in Energy Dissipation Measurements in Atomic Force Spectroscopy of Molecular Networks and Cell-Adhesion Studies. *Scientific Reports* 2018, 8, 9390.

Co-author Publications

Hannebelle, T. M.*; Raeth, E.*; **Leitao, M. S.;** Lukeš, T.; Pospíšil, J.; Toniolo, C.; Venzin, F. O.; Chrisnandy, A.; Bichon, N.; P. Swain, P. P.; Ronceray, N.; Lütolf, P. M.; Oates, C. A.; Hagen, M. G.; Lasser, T.; Radenovic, A.; McKinney, D. J.; Fantner, E. G.; OpenSIM: Open Source Microscope Add-On for Structured Illumination Microscopy. *bioRxiv* 2023.06.16.545316;

Baricevic, Z.*; Ayar, Z.*; **Leitao, M. S.;** Mladinic, M.; Fantner, E. G.; Ban, J.; Label-Free Long-Term Methods for Live Cell Imaging of Neurons: New Opportunities. *Biosensors* 2023, 13(3).

Navikas, V.; **Leitao, M. S.;** Marion, S.; Davis, S.; Drake, B.; Fantner, E. G.; Radenovic, A.; High-Throughput Nanocapillary Filling Enabled by Microwave Radiation for Scanning Ion Conductance Microscopy Imaging. *ACS Applied Nano Materials* 2020, 3, 8, 7829-7834. 2020.

*Equal contribution

Patents

2022 Nanopore-based scanning system and method, Patent application PCT/IB2022/055136, Switzerland.

International Conferences – Oral Presentations

2023 Invited Speaker | **Time-Resolved Scanning Ion Conductance Microscopy and Single-Molecule Spectroscopy** Correlative Microscopy Summer School ETH-EPFL 2023, Lausanne, Switzerland.

2022 Talk | **Nanopore-Based Scanning Probe Technology for Controlled-Translocations of DNA** NanoBioTech-Montreux Conference 2022, Montreux, Switzerland.

2022 Talk | **3D Imaging of Cells with Super-Resolution Scanning Ion Conductance Microscopy** International symposium in Neuroscience and Microscopy, FNIP day 2022, Padua, Italy.

2022 Talk | **Scanning Ion Conductance Microscopy and Spectroscopy**, AFM BioMed 2022, Nagoya, Japan.

2022 Talk | **Correlative 3D Imaging of Cells using Scanning Ion Conductance and Super-Resolution Microscopy** Nanosciences for Life & Materials Sciences, Nano In Bio 2022, Guadeloupe, France.

2021 Talk | **Time-Resolved Scanning Ion Conductance Microscopy for 3D Tracking of Nanoscale Cell Surface Dynamics**; Materials Research Society Fall Meeting 2021, Boston, USA.

2021 Invited Speaker | **Time-Resolved Scanning Ion Conductance Microscopy and Super-Resolution Imaging of Living Cells**; Scanning Probe Microscopy for Biological Systems, bioSPM 2021, Moscow, Russia.

Research highlights in the media, printed magazines and interviews

- 2023 **Researchers control individual molecules for precision sensing**
EPFL article, June 2023 <https://actu.epfl.ch/news/researchers-control-individual-molecules-for-pre-2/>
Nature Reviews Materials <https://www.nature.com/articles/s41578-023-00584-8>
Nature Nanotechnology News&Views <https://www.nature.com/articles/s41565-023-01477-1>
- 2022 **New imaging method gives a live glimpse into how cells work**
BBC News - Technology show *4Tech* airing on BBC Arabic, July 2022
https://www.youtube.com/watch?v=Zq0eQPmJOtk&list=PL63lwGZ_8vsk6CkJcDW4KU9hn0gWUC9K_&index=26
- 2021 **New views of how cells work**
Front cover in *Wiley Microscopy and Analysis Magazine* November/December 2021
<https://analyticalscience.wiley.com/do/10.1002/was.00020440> &
<https://analyticalscience.wiley.com/do/10.1002/was.00170312/>

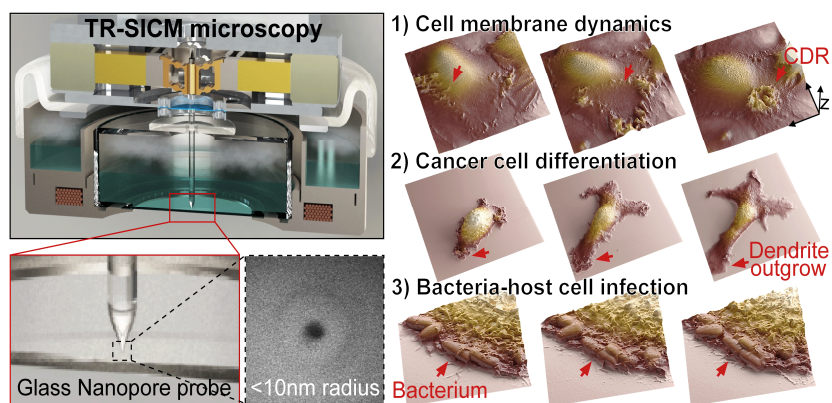
Research summary

I develop microscopes that enable 3D imaging of cellular membrane processes with nanoscale resolution in living cells and new single-molecule detection methods.

A novel scanning probe microscope based on ion conductance reveals nanoscale 3D processes in membranes of living cells

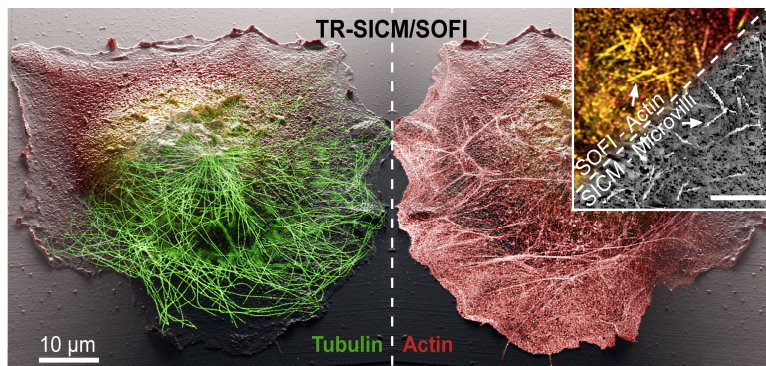
During my Ph.D., I developed a microscope that uses the flow of ions through a glass nanopore to visualize 3D processes on the cell membrane. It generates images at sub-5nm resolution without perturbing the live cell. It's called time-resolved scanning ion conductance microscope (TR-SICM). I demonstrated applications to several biological systems: 1) Biophysical properties of dynamic circular dorsal ruffles (CDR), which are poorly understood membrane events with a role in cell infection; 2) Morphological changes in human melanoma cells upon treatment with a drug known to reduce resistance to immunotherapy; 3) Mechanisms of bacteria-host infection in the human cell membrane. This microscope can potentially impact infection biology, immunology, and neurobiology – fields where it is crucial to understand how a cell interacts, communicates and reacts in real-time to an outside stimulus.

Leitao et al. ACS Nano 2021.



Correlative 3D imaging of single cells using super-resolution microscopy and TR-SICM

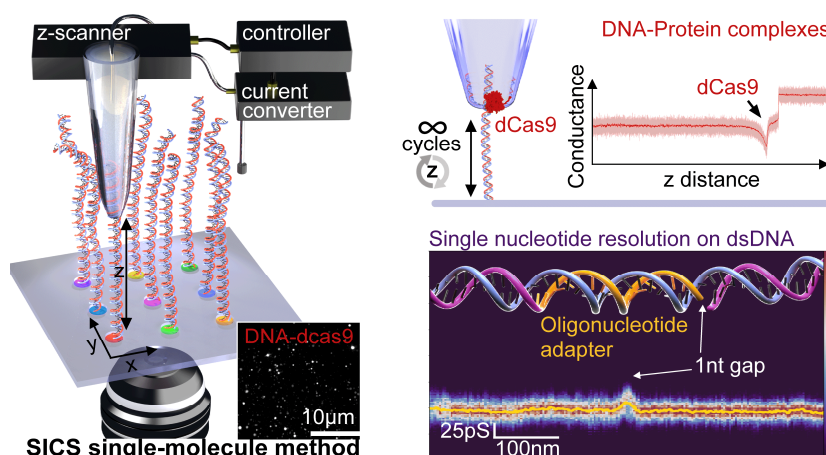
I collaborated with Prof. Radenovic's group (EPFL) to integrate the TR-SICM into a custom-built super-resolution optical fluctuation microscope (SOFI). To demonstrate the capabilities of our method, we performed correlative SICM/SOFI microscopy for visualizing the membrane surface and cytoskeleton dynamics in live cells with subdiffraction resolution. The combination of the multimodal SICM and flexible SOFI approach has the potential to become a routine imaging modality that will offer new insights into membrane processes in living cells. Navikas*, Leitao* et al. Nature Comm 2021.



The combination of the multimodal SICM and flexible SOFI approach has the potential to become a routine imaging modality that will offer new insights into membrane processes in living cells. Navikas*, Leitao* et al. Nature Comm 2021.

A new nanopore-based method to control single molecules for precision sensing

I devised a single-molecule method dubbed scanning ion conductance spectroscopy (SICS) that provides full control over the translocation speed of molecules through glass nanopores, yielding angstrom resolution. SICS overcomes critical limitations in nanopore technology by enabling a controlled translocation with constant velocity and averaging many thousands of readings on the same molecule region. SICS unlocks many applications that were not reachable by existing methods, demonstrated in DNA-protein complexes, DNA rulers, DNA gaps, and hairpins. Besides enabling more detailed biophysical studies in complex DNA systems, this method will be particularly beneficial for high-throughput screening (HTS) assays, point-of-care devices, and high-density, addressable DNA data storage. SICS also shows great potential for implementations in single protein sequencing and identification of post-translational modifications. Leitao et al. Nature Nanotechnology 2023.



SICS unlocks many applications that were not reachable by existing methods, demonstrated in DNA-protein complexes, DNA rulers, DNA gaps, and hairpins. Besides enabling more detailed biophysical studies in complex DNA systems, this method will be particularly beneficial for high-throughput screening (HTS) assays, point-of-care devices, and high-density, addressable DNA data storage. SICS also shows great potential for implementations in single protein sequencing and identification of post-translational modifications. Leitao et al. Nature Nanotechnology 2023.